

SEISMIC PERFORMANCE EVALUATION OF ROLLER COMPACTED  
CONCRETE GRAVITY DAMS BY PSEUDO DYNAMIC TESTING

A THESIS SUBMITTED TO  
THE GRADUATE SCHOOL OF NATURAL AND APPLIED SCIENCES  
OF  
MIDDLE EAST TECHNICAL UNIVERSITY

BY

ALPER ALDEMIR

IN PARTIAL FULFILLMENT OF THE REQUIREMENTS  
FOR  
THE DEGREE OF DOCTOR OF PHILOSOPHY  
IN  
CIVIL ENGINEERING

AUGUST 2016



Approval of the thesis:

**SEISMIC PERFORMANCE EVALUATION OF ROLLER COMPACTED  
CONCRETE GRAVITY DAMS BY PSEUDO DYNAMIC TESTING**

submitted by **ALPER ALDEMİR** in partial fulfillment of the requirements for the degree of **Doctor of Philosophy in Civil Engineering Department, Middle East Technical University** by,

Prof. Dr. Gülbin Dural Ünver  
Dean, Graduate School of **Natural and Applied Sciences**

Prof. Dr. İsmail Özgür Yaman  
Head of Department, **Civil Engineering**

Prof. Dr. Barış Binici  
Supervisor, **Civil Engineering Dept., METU**

**Examining Committee Members:**

Prof. Dr. Polat Gülkan  
Civil Engineering Dept., Cankaya University

Prof. Dr. Barış Binici  
Civil Engineering Dept., METU

Prof. Dr. Erdem Canbay  
Civil Engineering Dept., METU

Assoc. Prof. Dr. Yalın Arıcı  
Civil Engineering Dept., METU

Prof. Dr. Özgür Anıl  
Civil Engineering Dept., Gazi University

**Date:** Aug 22, 2016

**I hereby declare that all information in this document has been obtained and presented in accordance with academic rules and ethical conduct. I also declare that, as required by these rules and conduct, I have fully cited and referenced all material and results that are not original to this work.**

Name, Last name : Alper ALDEMIR

Signature :



## **ABSTRACT**

### **SEISMIC PERFORMANCE EVALUATION OF ROLLER COMPACTED CONCRETE GRAVITY DAMS BY PSEUDO DYNAMIC TESTING**

Aldemir, Alper

Ph.D., Department of Civil Engineering

Supervisor: Prof. Dr. Barış Binici

August 2016, 254 pages

The energy demands throughout the world have reached a level that could create irreversible impacts on the environment unless an overall energy policy to reduce the energy production relying on fossil fuels is implemented. The apparent effects of global warming enforced countries to take precautions and to set limits on the fossil fuel consumption. Thus, the renewable energy sources like hydropower, solar energy, biomass, etc. have, nowadays, been encouraged to generate electricity. Certainly, dams are excellent options to generate energy from renewable sources. Yet, they also supply fresh water for dwelling or agricultural usage. Unfortunately, the seismic behavior of dam structures has not been unveiled yet due to the complications stemmed from the interaction of dams with their surrounding media, i.e. flexible foundation and water in reservoir, and due to the complex valley geometries, which requires the consideration of higher mode effects. To solve the complex interaction of dam structures, numerous finite element modeling strategies

along with special boundary elements have been proposed in literature. However, the experimental works on dams are constrained with a limited number of shake table experiments. Therefore, in this dissertation, a methodology to adapt pseudo dynamic testing scheme to gravity dam structures is generated.

Firstly, the numerical background on the applicability of pseudo dynamic test to distributed mass system is introduced. Then, this methodology is applied to three different specimens consisting of one conventional concrete (CVC) and two roller-compacted concrete (RCC) with different compressive strengths. The prototype specimen was selected as Melen Dam, the highest RCC dam designed in Turkey and the laboratory specimens have a scale factor of 1/75. Each specimen was tested under the effect of three different hazard level earthquakes consecutively. After the completion of earthquake tests, the capacity curve of each specimen was obtained from a pushover experiment. The experiments show that there were no base sliding and stability problems under the effect of each hazard level for none of the specimens. However, the failure of the second specimen (RCC15) was observed during the pushover experiment caused by a body crack reaching the downstream toe of the specimen.

Secondly, the numerical ability of current advanced finite element techniques to estimate both the overall demand criteria like base shear, tip displacement, etc. and the crack propagations was investigated. In this part, two different strategies were utilized to model the boundary conditions of the dam specimen. In the first method, the base of the dam specimen was modeled as fixed base and base springs were placed under the foundation block of the dam specimen in the second method. The results reveal that no method was successful enough to predict the correct crack pattern of the dam specimens. However, both methods were convincing for estimating the overall demand parameters. Therefore, it is suggested that the overall demand parameters should be utilized while designing the concrete gravity dams.

**Keywords:** Pseudo Dynamic Test, Gravity Dams, RCC, CVC, Numerical Models, Crack Prediction

## ÖZ

### SİLİNDİRLE SIKIŞTIRILMIŞ BETON AĞIRLIK BARAJLARIN SİSMİK PERFORMANSLARININ BELİRLENMESİ İÇİN DİNAMİK BENZERİ DENEY UYGULAMALARI

Aldemir, Alper

Doktora, İnşaat Mühendisliği Bölümü

Tez Yöneticisi: Prof. Dr. Barış Binici

Ağustos 2016, 254 sayfa

Fosil yakıtlarından üretilen enerji miktarını azaltacak enerji politikaları yürürlüğe koyulmadığı sürece, dünyadaki enerji talepleri çevreye geri dönüşümsüz etkiler bırakacak bir seviyeye ulaşmıştır. Küresel ısınmanın belirgin etkileri, ülkeleri önlemler almaya ve fosil yakıt tüketimine sınırlar koymaya zorlamaktadır. Bu nedenle, hidroelektrik enerjisi, güneş enerjisi, katı atık enerjisi gibi yenilenebilir enerji kaynaklarının günümüzde elektrik üretiminde kullanılması teşvik edilmektedir. Kuşkusuz yenilenebilir kaynaklardan enerji üretimi için barajlar mükemmel bir seçenektir. Ayrıca, barajlar konut ve tarımsal kullanım için su da tedarik etmektedir. Maalesef barajların sismik davranışları tam anlamıyla çözülememiştir. Bunun nedenleri arasında barajların çevreleriyle (esnek zemin ve rezervuar suyu) etkileşimi veya karmaşık vadi geometrilerinden kaynaklı yüksek mod etkilerinin göz önünde bulundurulmasının zorunluluğu sayılabilir. Literatürde barajların karmaşık

etkileşimlerini çözmek için özel sınır elemanlarıyla birlikte birçok sonlu eleman modelleme stratejileri önerilmiştir. Fakat barajlar üzerine deneysel çalışmalar az sayıda sarsma tablası deneyleriyle sınırlıdır. Bu nedenle, bu tezde dinamik benzeri deney metodunu ağırlık barajlara uygulayabilmek için bir yöntem geliştirilmiştir.

İlk olarak, dinamik benzeri deney yönteminin yayılı kütleyle sahip bir sisteme uygulanabilirliğine dair sayısal altyapı sunulacaktır. Sonra, bu yöntem üç farklı numuneye uygulanacaktır. Bu numunelerden biri klasik betondan (KB) diğer ikisi ise farklı dayanımlara sahip silindire sıkıştırılmış betondan (SSB) imal edilecektir. Prototip numune olarak Türkiye’de tasarlanmış en yüksek SSB baraj olan Melen Barajı seçilmiştir. Laboratuvar numuneleri 1/75 ölçeğe sahiptir. Her numune üç farklı tehlike etkisi altında ardıl olarak test edilmiştir. Deprem testleri bittikten sonra, her numunenin kapasite eğrisi itme deneyi vasıtasıyla elde edilmiştir. Deney sonuçlarına göre, hiçbir numunede üç tehlike etkisi altında da taban kayması ya da stabilite kaybı olmamıştır. Fakat, ikinci numunenin (SSB15) itme deneyi esnasında mansap topuğuna ulaşan bir gövde çatlğından kaynaklı göçtüğü gözlemlenmiştir.

İkinci olarak, güncel gelişmiş sonlu eleman tekniklerinin çatlak dağılımı ve taban kesme kuvveti, tepe deplasmanı vb. genel talep kriterlerini tahmin etmekteki becerileri incelenmiştir. Bu kısımda, baraj numunelerinin sınır koşullarını modellerken iki farklı yaklaşım kullanılmıştır. Birinci yöntemde, baraj numunesinin tabanı ankastre mesnet olarak alınmıştır. İkinci yöntemde ise temel bloğunun altına taban yayları yerleştirilmiştir. Sonuçlara göre doğru çatlama tipini öngörmeye hiçbir yöntem başarılı olamamıştır. Fakat, her iki yöntem de genel talep parametrelerini tahmin etmede ikna edicidir. Bu nedenle, beton ağırlık barajların tasarımında genel talep parametrelerinin kullanılması önerilmektedir.

Anahtar Kelimeler: Dinamik Benzeri Deney, Ağırlık Barajlar, SSB, KB, Sayısal Modeller, Çatlak Tahmini

*To My Family*

## ACKNOWLEDGMENT

I want to express my profound gratitude to my supervisor Prof. Dr. Barış Binici, whose knowledge, criticism, patience and support enabled me to develop the ideas behind this dissertation. From him, I have learned not only how to become a researcher but also how to have a strong character. I will always admire his attitude towards his students and carry the honor of working with him all my life.

Besides my advisor, I would like to thank Assoc. Prof. Dr. Yalın Arıcı, Prof. Dr. Erdem Canbay, Prof. Dr. Özgür Anıl and Assoc. Prof. Dr. Özgür Kurç for their insightful comments.

I owe special thanks to METU Structural Mechanics Laboratory staff; Hasan Metin, Murat Demirel, Osman Keskin and Barış Esen. I also thank deeply Salim Azak for his valuable help in the experimental part of this study.

I would also like to thank to METU Materials of Construction Laboratory staff; Cuma Yıldırım. I would like to present my gratitude to Burhan Alam for the invaluable support during material testing.

My thanks go to my office mates, Erhan Budak, Gizem Mestav Sarıca, Ali Gharibdoust, Beyazıt Bestami Aydın, Naz Topkara Özcan and Dr. Ali Karimzadeh Naghshineh. I will always remember with pleasure the inspiring discussions and activities we had.

My special thank goes to my nine-year office mate and my eternal friend İsmail Ozan Demirel. I think it was one of my luckiest times in my life when I had the chance to meet him. Because he proved me that good and unselfish guys still exist.

I remember tough times during the preparation of this dissertation but I will never forget the sorrow I have felt when I lost my father, Cengiz Aldemir, who was not only my physiological father but also my only mentor. I hope I could accomplish to be a son worthy of you. I wish we would meet in heaven.

I would like to express my sincere gratitude to my beloved mother Tlay Aldemir for her eternal love, encouragement and trust.

The author wishes to thank in particular all those people whose friendly assistance and wise guidance supported him throughout the duration of this research.

The financial support from the Scientific and Technical Research Council of Turkey (TUBITAK – 111M712) is gratefully acknowledged.

## TABLE OF CONTENTS

<b>ABSTRACT .....</b>	<b>V</b>
<b>ÖZ .....</b>	<b>vii</b>
<b>ACKNOWLEDGMENT .....</b>	<b>x</b>
<b>TABLE OF CONTENTS.....</b>	<b>xii</b>
<b>LIST OF TABLES .....</b>	<b>xvi</b>
<b>LIST OF FIGURES .....</b>	<b>xviii</b>
<b>LIST OF SYMBOLS / ABBREVIATIONS.....</b>	<b>xxix</b>
<b>CHAPTERS</b>	
<b>1 INTRODUCTION.....</b>	<b>1</b>
1.1 GENERAL.....	1
1.2 RCC DAMS .....	3
1.3 LITERATURE REVIEW .....	6
1.3.1 Linear Elastic Analysis of Dam-Foundation-Reservoir Interaction .....	6
1.3.2 Nonlinear Simulations.....	17
1.3.3 Seismic Design of Dams.....	21
1.3.4 Experimental Work.....	22
1.4 OBJECT AND SCOPE .....	33
<b>2 APPLICATION OF PSEUDODYNAMIC TESTING FOR DAMS .....</b>	<b>35</b>
2.1 SINGLE DEGREE OF FREEDOM APPROACH.....	35
2.2 RIGOROUS APPROACH.....	40
2.3 PSEUDO DYNAMIC TESTING OF A GRAVITY DAM MONOLITH .....	44
2.3.1 Assumptions involved in Testing Procedure .....	44
2.3.2 The Outline of the Testing Procedure .....	50
2.3.2.1 Specimen 1: CVC Gravity Dam.....	53
2.3.2.2 Specimen 2: RCC Gravity Dam 1 .....	57
2.3.2.3 Specimen 3: RCC Gravity Dam 2 .....	61
2.3.3 Concluding Remarks .....	62
<b>3 MATERIALS.....</b>	<b>63</b>
3.1 AGGREGATES AND SIEVE ANALYSIS RESULTS .....	63



3.1.1 Sieve Analysis Results .....	63
3.1.2 Specific Gravity and Water Absorption Capacity Experiments.....	67
3.2 CHEMICAL PROPERTIES OF CEMENT AND POZZOLAN .....	68
3.3 WATER-CEMENT RATIO.....	69
3.4 CONCRETE MIXTURE RESULTS .....	72
3.4.1 Unscaled CVC Results .....	73
3.4.2 Scaled CVC Results.....	75
3.4.3 Scaled RCC15 Results.....	77
3.4.4 Scaled RCC25 Results.....	78
3.4.5 Unscaled RCC15 Results .....	79
3.4.6 Unscaled RCC25 Results .....	80
3.5 DISCUSSION OF RESULTS.....	81
<b>4 TEST SETUP AND INSTRUMENTATION OF SPECIMENS.....</b>	<b>85</b>
4.1 TEST SETUP.....	85
4.2 VALIDATION OF THE PSD SYSTEM.....	89
4.3 INSTRUMENTATION .....	94
4.4 SPECIMENS .....	97
4.4.1 Specimen 1: CVC Gravity Dam .....	98
4.4.2 Specimen 2: RCC Gravity Dam 1 .....	100
4.4.3 Specimen 3: RCC Gravity Dam 2 .....	102
4.5 TESTING .....	103
<b>5 EXPERIMENTAL RESULTS.....</b>	<b>107</b>
5.1 SPECIMEN 1: CVC GRAVITY DAM .....	107
5.1.1 Hydrostatic Loading .....	107
5.1.2 PSD Testing.....	108
5.1.2.1 OBE.....	108
5.1.2.2 MDE.....	111
5.1.2.3 MCE .....	115
5.1.2.4 Pushover Experiment .....	119
5.1.3 Identification of the Dynamic Parameters .....	121
5.2 SPECIMEN 2: RCC GRAVITY DAM 1.....	123
5.2.1 Hydrostatic Loading .....	123

5.2.2 PSD Testing.....	123
5.2.2.1 OBE.....	123
5.2.2.2 MDE.....	126
5.2.2.3 MCE.....	129
5.2.2.4 Pushover Experiment .....	134
5.2.3 Strain Gage Recordings .....	135
5.2.4 Identification of Dynamic Parameters of the Specimen.....	139
5.3 SPECIMEN 3: RCC GRAVITY DAM.....	140
5.3.1 Hydrostatic Loading.....	140
5.3.2 PSD Testing.....	141
5.3.2.1 OBE.....	141
5.3.2.2 MDE.....	144
5.3.2.3 MCE.....	146
5.3.2.4 Pushover Experiment .....	151
5.3.3 Identification of the Dynamic Parameters of the Specimen.....	152
5.4 DISCUSSION OF TEST RESULTS .....	153
<b>6 NUMERICAL SIMULATIONS .....</b>	<b>161</b>
6.1 BRIEF INFORMATION ON THE CONCRETE CONSTITUTIVE MODEL IN ANSYS..	162
6.1.1 Modeling the Cracking and Crushing of Concrete .....	162
6.1.2 Concrete Material .....	165
6.2 MODELING TECHNIQUES USED TO SIMULATE EXPERIMENTAL BEHAVIOR .....	167
6.3 NUMERICAL SIMULATION RESULTS FOR MODEL 1 .....	170
6.3.1 CVC Gravity Dam : Specimen 1 .....	170
6.3.2 RCC Gravity Dam : Specimen 2 .....	174
6.3.3 RCC Gravity Dam : Specimen 3 .....	180
6.4 NUMERICAL SIMULATION SUMMARIES FOR MODEL 2 .....	184
6.4.1 CVC Gravity Dam : Specimen 1 .....	184
6.4.2 RCC Gravity Dam : Specimen 2 .....	189
6.4.3 RCC Gravity Dam : Specimen 3 .....	194
6.5 DISCUSSION OF NUMERICAL SIMULATION RESULTS.....	199
<b>7 CONCLUSION.....</b>	<b>203</b>
7.1 SUMMARY .....	203

7.2 CONCLUSIONS .....	204
7.3 FUTURE STUDY .....	207
<b>REFERENCES .....</b>	<b>209</b>
<b>APPENDIX A .....</b>	<b>221</b>
<b>A. FORMULATIONS FOR SIMPLIFIED METHOD FOR DAMS .....</b>	<b>221</b>
A.1. SEPARATE HYDRODYNAMIC EFFECTS .....	221
A.2. SEPARATE FOUNDATION FLEXIBILITY EFFECTS .....	223
A.3. COMBINED HYDRODYNAMIC AND FOUNDATION FLEXIBILITY EFFECTS .....	226
<b>APPENDIX B .....</b>	<b>233</b>
<b>B. DEMAND HISTORIES FOR CVC SPECIMEN .....</b>	<b>233</b>
B.1. OBE MOTION .....	233
B.2. MDE MOTION .....	236
B.3. MCE MOTION .....	237
<b>APPENDIX C .....</b>	<b>239</b>
<b>C. DEMAND HISTORIES FOR RCC SPECIMEN .....</b>	<b>239</b>
C.1. OBE MOTION .....	239
C.2. MDE MOTION .....	242
C.3. MCE MOTION .....	243
<b>APPENDIX D .....</b>	<b>245</b>
<b>D. DETAILS FOR PUSHOVER TESTS .....</b>	<b>245</b>
<b>APPENDIX E .....</b>	<b>247</b>
<b>E. DETAILS FOR THE FAILURE SURFACE .....</b>	<b>247</b>
E.1. CCC DOMAIN .....	247
E.2. CCT DOMAIN .....	248
E.3. CTT DOMAIN .....	249
E.4. TTT DOMAIN .....	249
<b>CURRICULUM VITAE .....</b>	<b>251</b>

## LIST OF TABLES

### TABLES

Table 1.1. Concrete Dams Subjected to Significant Shaking .....	5
Table 2.1. Comparisons of the SDFS and Exact Solutions .....	35
Table 2.2. Comparisons of the Errors in the Response Quantities for Scaled Dam Models of Specimen 1 with Different Mass $m$ for OBE motion .....	56
Table 2.3. Comparisons of the Errors in the Response Quantities for Scaled Dam Models of Specimen 1 with Different Mass $m$ for MDE motion.....	56
Table 2.4. Comparisons of the Errors in the Response Quantities for Scaled Dam Models of Specimen 1 with Different Mass $m$ for MCE motion.....	57
Table 2.5. Comparisons of the Errors in the Response Quantities for Scaled Dam Models of Specimen 2 with Different Mass $m$ for OBE motion .....	60
Table 2.6. Comparisons of the Errors in the Response Quantities for Scaled Dam Models of Specimen 2 with Different Mass $m$ for MDE motion.....	60
Table 2.7. Comparisons of the Errors in the Response Quantities for Scaled Dam Models of Specimen 2 with Different Mass $m$ for MCE motion.....	61
Table 3.1. Aggregate Mixtures with 0-3 mm Stream Sand.....	65
Table 3.2. Aggregate Mixtures with 0-3 mm Gravel .....	66
Table 3.3. Unit Weights and Water Absorption Capacities for Fine Aggregates .....	68
Table 3.4. Unit Weights and Water Absorption Capacities for Coarse Aggregates ..	68
Table 3.5. Chemical Composition of Cement .....	69
Table 3.6. Chemical Composition of Fly Ash.....	70
Table 3.7. Compressive Strength Values of Unscaled CVC Specimens .....	74
Table 3.8. Split Tensile Strength Values of Unscaled CVC Specimens .....	75
Table 3.9. Compressive Strength Values of Scaled CVC Specimens.....	75
Table 3.10. Split Tensile Strength Values of Scaled CVC Specimens .....	76
Table 3.11. Compressive Strength Values of Scaled RCC15 Specimens .....	77
Table 3.12. Split Tensile Strength Values of Scaled RCC15 Specimens .....	78

Table 3.13. Compressive Strength Values of Scaled RCC25 Specimens.....	78
Table 3.14. Split Tensile Strength Values of Scaled RCC25 Specimens .....	79
Table 3.15. Compressive Strength Values of the Unscaled RCC15 Specimens.....	80
Table 3.16. Split Tensile Strength Values of the Unscaled RCC15 Specimens .....	80
Table 3.17. Compressive Strength Values of Unscaled RCC25 Specimens.....	81
Table 3.18. Split Tensile Strength Values of Unscaled RCC25 Specimens .....	81
Table 3.19. Summary of Test Specimens and Test Results .....	82
Table 4.1. Specifications of Compaction Machines.....	101
Table 5.1. Summary of All Tests .....	154
Table 5.2. Damping Ratios calculated by the Method proposed by Chopra (2012)	157
Table 6.1. Parameters to define Willam-Warnke Failure Surface .....	165
Table 6.2. Comparison of Base Shear Forces of Specimen 1 for Model 1 .....	174
Table 6.3. Comparison of Tip Displacement of Specimen 1 for Model 1 .....	174
Table 6.4. Comparison of Base Shear Forces of Specimen 2 for Model 1 .....	179
Table 6.5. Comparison of Tip Displacement of Specimen 2 for Model 1 .....	179
Table 6.6. Comparison of Base Shear Forces of Specimen 3 for Model 1 .....	182
Table 6.7. Comparison of Tip Displacement of Specimen 3 for Model 1 .....	182
Table 6.8. Comparison of Base Shear Forces of Specimen 1 for Model 2 .....	187
Table 6.9. Comparison of Tip Displacement of Specimen 1 for Model 2 .....	187
Table 6.10. Comparison of Base Shear Forces of Specimen 2 for Model 2 .....	191
Table 6.11. Comparison of Tip Displacement of Specimen 2 for Model 2 .....	191
Table 6.12. Comparison of Base Shear Forces of Specimen 3 for Model 2 .....	196
Table 6.13. Comparison of Tip Displacement of Specimen 3 for Model 2 .....	196

## LIST OF FIGURES

### FIGURES

Figure 1.1. Steps in RCC Construction .....	7
Figure 1.2. Illustration of Hydrodynamic Pressure .....	8
Figure 1.3. Typical Finite Element Mesh with Nodal Point and Element Numbers in Program EAD .....	10
Figure 1.4. Principal Stresses over Koyna Dam Body .....	11
Figure 1.5. Details of Program ADAP .....	11
Figure 1.6. Different Substructures for Dam and Reservoir .....	12
Figure 1.7. Substructure Representation of the Dam-Reservoir-Foundation System .....	13
Figure 1.8. Dam-Reservoir-Foundation System in Program EAGD .....	14
Figure 1.9. Dam-Reservoir-Foundation System in the Program EACD .....	15
Figure 1.10. Finite Element Mesh for Dam and Near Field, and Layer Discretization of Far Field .....	17
Figure 1.11. Meshes for Foundation, Dam Body and Reservoir.....	19
Figure 1.12. Details of Tests conducted in Fronteddu et al (1998).....	20
Figure 1.13. Basis for Upper Limit Demand-Capacity Ratio and Cumulative Inelastic Duration.....	22
Figure 1.14. Segmented Arch Model on Shaking Table .....	24
Figure 1.15. Koyna Dam Model with Reservoir Tank.....	25
Figure 1.16. Crack Distribution after Test .....	26
Figure 1.17. Observed Cracks in Different Experiments .....	26
Figure 1.18. Test Setup .....	28
Figure 1.19. Centrifuge Test Results.....	29
Figure 1.20. Dynamic Test inside Centrifuge Machine .....	31
Figure 1.21. Observed Cracks during the Second Specimen .....	32
Figure 1.22. Numerical Model in Sevim et al (2012) .....	32
Figure 1.23. Comparison of Crack Patterns .....	33

Figure 2.1. Simplification of the Dam-Water-Foundation Rock System.....	36
Figure 2.2. Comparison of Horizontal Acceleration Responses of Equivalent SDFS and Exact System due to Harmonic Horizontal Ground Motions.....	38
Figure 2.3. Comparison of Horizontal Acceleration Responses of Equivalent SDFS and Exact System with Empty Reservoir Condition due to Harmonic Horizontal Ground Motions .....	39
Figure 2.4. Idealization of Dam-Foundation-Reservoir System in EAGD .....	40
Figure 2.5. Substructures Representation of Dam-Reservoir-Foundation System ....	42
Figure 2.6. Models used in Validation of Pseudo Dynamic Tests .....	45
Figure 2.7. Seismicity of Prototype Dam.....	46
Figure 2.8. Analytical Results .....	48
Figure 2.9. Flowchart Explaining the Testing Procedure .....	52
Figure 2.10. Determination of Effective Height for Specimen 1 .....	53
Figure 2.11. Preliminary Test for Lateral Stiffness Determination of Specimen 1 ..	54
Figure 2.12. Comparison of the Analysis Results of Specimen 1 for the OBE ground motion .....	55
Figure 2.13. Comparison of the Analysis Results of Specimen 1 for the MDE ground motion .....	55
Figure 2.14. Comparison of the Analysis Results of Specimen 1 for the MCE ground motion .....	56
Figure 2.15. Determination of Effective Height for Specimen 2.....	58
Figure 2.16. Preliminary Test for Lateral Stiffness Determination of Specimen 2 ..	58
Figure 2.17. Comparison of the Analysis Results of Specimen 2 for the OBE ground motion .....	59
Figure 2.18. Comparison of the Analysis Results of Specimen 2 for the MDE ground motion .....	59
Figure 2.19. Comparison of the Analysis Results of Specimen 2 for the MCE ground motion .....	60
Figure 2.20. Preliminary Test for Lateral Stiffness Determination .....	62
Figure 3.1. Different Batches of Aggregates .....	64
Figure 3.2. Gradation Curves for the Different Batches of Aggregates.....	65
Figure 3.3. Gradation Curves for Concrete Mixtures .....	66

Figure 3.4. Gradation Curves for Concrete Mixtures.....	67
Figure 3.5. Curves Used in RCC Mixture Design.....	71
Figure 3.6. Apparatus Used in RCC Placement .....	72
Figure 3.7. Stages in RCC Placement .....	72
Figure 3.8. MTS Testing Machine .....	73
Figure 3.9. Stress-Strain Curves of the Unscaled 100x200mm CVC Specimens.....	74
Figure 3.10. Stress-Strain Curves of Scaled 100x200mm CVC Specimens.....	76
Figure 3.11. Stress-Strain Curves of 100x200mm Scaled RCC15 Specimens .....	77
Figure 3.12. Stress-Strain Curves of 100x200mm Scaled RCC25 Specimens .....	79
Figure 3.13. Comparisons of Strength Normalized Stress-Strain Curves of Scaled CVC and Scaled RCC25 .....	83
Figure 3.14. The Effect of Scaling on Stress-Strain Curve of CVC .....	83
Figure 4.1. Formwork Drawings .....	85
Figure 4.2. Test Setup (Isometric View) .....	86
Figure 4.3. Test Setup (Side View) .....	87
Figure 4.4. Test Setup (Top View).....	87
Figure 4.5. Change in Axial Load .....	88
Figure 4.6. Transfer Plate.....	88
Figure 4.7. Intentionally Roughened Foundation Concrete .....	89
Figure 4.8. Verification Frame .....	92
Figure 4.9. Ground Motions.....	92
Figure 4.10. Fourier Amplitude Spectrums.....	93
Figure 4.11. Verification Frame Photos .....	93
Figure 4.12. Feedback Point.....	93
Figure 4.13. Comparison of Tip Displacements .....	94
Figure 4.14. Comparison of Base Shears .....	94
Figure 4.15. Test Setup and Instrumentation .....	95
Figure 4.16. Strain Rosettes at the Dam Base .....	96
Figure 4.17. Test Setup and LVDT's for Tip Displacement Recording in Specimen 3 .....	97
Figure 4.18. Preparation of Specimen .....	98
Figure 4.19. Transfer Plate.....	99



Figure 4.20. Curing .....	99
Figure 4.21. Preparation of Specimen.....	100
Figure 4.22. Transfer Plate.....	103
Figure 4.23. Preparation of Specimen.....	104
Figure 5.1. Base Shear – Tip Displacement and Base Shear – Base Displacement Curves during Hydrostatic Loading for Specimen 1 .....	107
Figure 5.2. Cracks Formed during Hydrostatic Loading for Specimen 1 .....	108
Figure 5.3. Force and Displacement Demands during OBE Experiment for Specimen 1 .....	109
Figure 5.4. Base Uplift and Rotation Demands during OBE Experiment for Specimen 1 .....	110
Figure 5.5. Cracks Formed during the OBE motion for Specimen 1.....	111
Figure 5.6. Base Uplift and Rotation Demands during MDE Experiment for Specimen 1 .....	112
Figure 5.7. Force and Displacement Demands during MDE Experiment for Specimen 1 .....	113
Figure 5.8. Cracks Formed during the MDE motion for Specimen 1 .....	114
Figure 5.9. Force and Displacement Demands during MCE Experiment for Specimen 1 .....	115
Figure 5.10. Base Uplift and Rotation Demands during MCE Experiment for Specimen 1 .....	116
Figure 5.11. Cracks Formed in Specimen 1 during the MCE motion 1.....	117
Figure 5.12. Cracks Formed in Specimen 1 during the MCE motion 2.....	118
Figure 5.13. Base Deformations and Pushover Curve for Specimen 1.....	119
Figure 5.14. Cracks Formed during Pushover Experiment for Specimen 1 .....	120
Figure 5.15. Variation of the Fundamental Period and Damping Ratio during the Experiment for Specimen 1.....	122
Figure 5.16. Base Shear – Tip Displacement and Base Shear – Base Displacement Curves during Hydrostatic Loading for Specimen 2 .....	123
Figure 5.17. Force and Displacement Demands during OBE Experiment for Specimen 2 .....	124
Figure 5.18. Cracks Formed during the OBE motion for Specimen 2.....	125

Figure 5.19. Base Uplift and Rotation Demands during OBE Experiment for Specimen 2 .....	126
Figure 5.20. Base Uplift and Rotation Demands during MDE Experiment for Specimen 2 .....	126
Figure 5.21. Force and Displacement Demands during MDE Experiment for Specimen 2 .....	127
Figure 5.22. Cracks Formed during the MDE motion for Specimen 2 .....	128
Figure 5.23. Base Shear versus Base Displacement Curve during the MDE motion for Specimen 2 .....	129
Figure 5.24. Force and Displacement Demands during MCE Experiment for Specimen 2 .....	130
Figure 5.25. Cracks Formed in Specimen 2 during the MCE motion 1 .....	131
Figure 5.26. Cracks Formed in Specimen 2 during the MCE motion 2 .....	132
Figure 5.27. Base Uplift and Rotation Demands during MCE Experiment for Specimen 2 .....	133
Figure 5.28. Base Shear versus Base Displacement Curve during MCE motion for Specimen 2 .....	134
Figure 5.29. Base Sliding and Pushover Curve for Specimen 2 .....	135
Figure 5.30. Cracks Formed in Specimen 2 during Pushover Experiment 1 .....	136
Figure 5.31. Cracks Formed in Specimen 2 during Pushover Experiment 2 .....	137
Figure 5.32. Cracks Formed in Specimen 2 during Pushover Experiment 3 .....	138
Figure 5.33. Principal Strain Distributions over the Base of Dam Specimen for Specimen 2 .....	139
Figure 5.34. Variation of the Fundamental Period and Damping Ratio during the Experiment for Specimen 2 .....	140
Figure 5.35. Base Shear – Tip Displacement and Base Shear – Base Displacement Curves during Hydrostatic Loading for Specimen 3 .....	141
Figure 5.36. Force and Displacement Demands during OBE Experiment for Specimen 3 .....	142
Figure 5.37. Cracks Formed during OBE motion for Specimen 3 .....	143
Figure 5.38. Base Uplift and Rotation Demands during OBE Experiment for Specimen 3 .....	143

Figure 5.39. Force and Displacement Demands during MDE Experiment for Specimen 3 .....	144
Figure 5.40. Base Uplift and Rotation Demands during MDE Experiment for Specimen 3 .....	145
Figure 5.41. Cracks Formed during MDE motion for Specimen 3.....	146
Figure 5.42. Force and Displacement Demands during MCE Experiment for Specimen 3 .....	147
Figure 5.43. Cracks Formed in Specimen 3 during the MCE motion 1.....	148
Figure 5.44. Cracks Formed in Specimen 3 during the MCE motion 2.....	149
Figure 5.45. Base Uplift and Rotation Demands during MCE Experiment for Specimen 3 .....	150
Figure 5.46. Base Shear versus Base Displacement Curve during MCE motion for Specimen 3 .....	150
Figure 5.47. Pushover Curve for Specimen 3 .....	151
Figure 5.48. Cracks Formed During Pushover Experiment for Specimen 3 .....	152
Figure 5.49. Variation of the Fundamental Period and Damping Ratio during the Experiment for Specimen 3.....	153
Figure 5.50. Comparison of Capacity Curves of All Specimens .....	155
Figure 5.51. Total Dissipated Energies for All Specimens and Hysteretic Damping Plot from Megally (1998).....	156
Figure 5.52. Base Displacement recorded in the Research conducted by Binici et al 2016.....	158
Figure 5.53. Results of Pushover Experiment from the Research conducted by Binici et al 2016 .....	159
Figure 5.54. Comparison of the Base Shear Values obtained from EAGD and Experiments.....	160
Figure 6.1. Description for Stress Relaxation after Cracking .....	163
Figure 6.2. 3D Failure Surface in Dimensionless Principal Stress Axes .....	166
Figure 6.3. 2D Failure Surface in Principal Stress Space for Biaxial Stress State ..	167
Figure 6.4. Different Numerical Models.....	168
Figure 6.5. Numerical Model 1 .....	169
Figure 6.6. Numerical Model 2 .....	169

Figure 6.7. Comparison of Base Shear Demand Histories for Specimen 1 under the Effect of OBE, MDE and MCE Scenarios for Model 1 .....	171
Figure 6.8. Comparison of Tip Displacement Demand Histories for Specimen 1 under the Effect of OBE, MDE and MCE Scenarios for Model 1 .....	171
Figure 6.9. Comparison of Base Shear versus Tip Displacement Demand Histories for Specimen 1 under the Effect of OBE, MDE and MCE Scenarios for Model 1 .	172
Figure 6.10. Comparison of Crack Patterns for Specimen 1 under the Effect of OBE, MDE and MCE Scenarios for Model 1 .....	173
Figure 6.11. Comparison of Pushover Experiment for Specimen 1 from Model 1 .....	175
Figure 6.12. Comparison of Base Shear Demand Histories for Specimen 2 under the Effect of OBE, MDE and MCE Scenarios for Model 1 .....	176
Figure 6.13. Comparison of Tip Displacement Demand Histories for Specimen 2 under the Effect of OBE, MDE and MCE Scenarios for Model 1 .....	177
Figure 6.14. Comparison of Base Shear versus Tip Displacement Demand Histories for Specimen 2 under the Effect of OBE, MDE and MCE Scenarios for Model 1 .....	177
Figure 6.15. Comparison of Crack Patterns for Specimen 2 under the Effect of OBE, MDE and MCE Scenarios for Model 1 .....	178
Figure 6.16. Comparison of Pushover Experiment for Specimen 2 from Model 1 .	179
Figure 6.17. Comparison of Base Shear Demand Histories for Specimen 3 under the Effect of OBE, MDE and MCE Scenarios for Model 1 .....	180
Figure 6.18. Comparison of Tip Displacement Demand Histories for Specimen 3 under the Effect of OBE, MDE and MCE Scenarios for Model 1 .....	181
Figure 6.19. Comparison of Base Shear versus Tip Displacement Demand Histories for Specimen 3 under the Effect of OBE, MDE and MCE Scenarios for Model 1 .....	181
Figure 6.20. Comparison of Crack Patterns for Specimen 3 under the Effect of OBE, MDE and MCE Scenarios for Model 1 .....	183
Figure 6.21. Comparison of Pushover Experiment for Specimen 3 from Model 1 .....	184

Figure 6.22. Comparison of Base Shear Demand Histories for Specimen 1 under the Effect of OBE, MDE and MCE Scenarios for Model 2.....	185
Figure 6.23. Comparison of Tip Displacement Demand Histories for Specimen 1 under the Effect of OBE, MDE and MCE Scenarios for Model 2.....	186
Figure 6.24. Comparison of Base Shear versus Tip Displacement Demand Histories for Specimen 1 under the Effect of OBE, MDE and MCE Scenarios for Model 2 .....	187
Figure 6.25. Comparison of Crack Patterns for Specimen 1 under the Effect of OBE, MDE and MCE Scenarios for Model 2.....	188
Figure 6.26. Comparison of Pushover Experiment for Specimen 1 from Model 2 .....	189
Figure 6.27. Comparison of Base Shear Demand Histories for Specimen 2 under the Effect of OBE, MDE and MCE Scenarios for Model 2.....	190
Figure 6.28. Comparison of Tip Displacement Demand Histories for Specimen 2 under the Effect of OBE, MDE and MCE Scenarios for Model 2.....	191
Figure 6.29. Comparison of Base Shear versus Tip Displacement Demand Histories for Specimen 2 under the Effect of OBE, MDE and MCE Scenarios for Model 2 .....	192
Figure 6.30. Comparison of Crack Patterns for Specimen 2 under the Effect of OBE, MDE and MCE Scenarios for Model 2.....	193
Figure 6.31. Comparison of Pushover Experiment for Specimen 2 from Model 2 .....	194
Figure 6.32. Comparison of Base Shear Demand Histories for Specimen 3 under the Effect of OBE, MDE and MCE Scenarios for Model 2.....	195
Figure 6.33. Comparison of Tip Displacement Demand Histories for Specimen 3 under the Effect of OBE, MDE and MCE Scenarios for Model 2.....	195
Figure 6.34. Comparison of Base Shear versus Tip Displacement Demand Histories for Specimen 3 under the Effect of OBE, MDE and MCE Scenarios for Model 2 .	196
Figure 6.35. Comparison of Crack Patterns for Specimen 3 under the Effect of OBE, MDE and MCE Scenarios for Model 2.....	197
Figure 6.36. Comparison of Pushover Experiment for Specimen 3 from Model 2 .....	198

Figure 6.37. Comparison of Base Shear Demand Histories obtained from Model 1 and Model 2 for Specimen 1 .....	200
Figure 6.38. Comparison of Base Shear Demand Histories obtained from Model 1 and Model 2 for Specimen 2 .....	200
Figure 6.39. Comparison of Base Shear Demand Histories obtained from Model 1 and Model 2 for Specimen 3 .....	201
Figure A.1. Effect of Coupling Impedance on Response of Dams on Flexible Foundation Due to Harmonic Ground Excitation .....	225
Figure A.2. Additional Damping for $E_s=27,500$ MPa and $\eta_f=0.10$ due to Dam-Reservoir and Dam-Foundation Interactions .....	229
Figure A.3. Comparison of Equivalent SDFS Response due to Harmonic Horizontal Ground Motions using Exact Damping and Simplified Damping .....	230
Figure A.4. Comparison of Horizontal Acceleration Responses of Equivalent SDFS and Exact System due to Harmonic Horizontal Ground Motions.....	231
Figure B.1. Comparison of the Analysis Results for OBE Motion with Numerical Mass of 20t.....	233
Figure B.2. Comparison of the Analysis Results for OBE Motion with Numerical Mass of 30t.....	233
Figure B.3. Comparison of the Analysis Results for OBE Motion with Numerical Mass of 35t.....	234
Figure B.4. Comparison of the Analysis Results for OBE Motion with Numerical Mass of 40t.....	234
Figure B.5. Comparison of the Analysis Results for OBE Motion with Numerical Mass of 45t.....	235
Figure B.6. Comparison of the Analysis Results for OBE Motion with Numerical Mass of 55t.....	235
Figure B.7. Comparison of the Analysis Results for MDE Motion with Numerical Mass of 30t.....	236
Figure B.8. Comparison of the Analysis Results for MDE Motion with Numerical Mass of 37.5t.....	236
Figure B.9. Comparison of the Analysis Results for MDE Motion with Numerical Mass of 50t.....	237

Figure B.10. Comparison of the Analysis Results for MDE Motion with Numerical Mass of 45t.....	237
Figure B.11. Comparison of the Analysis Results for MCE Motion with Numerical Mass of 65t.....	238
Figure B.12. Comparison of the Analysis Results for MCE Motion with Numerical Mass of 75t.....	238
Figure C.1. Comparison of the Analysis Results for OBE Motion with Numerical Mass of 20t.....	239
Figure C.2. Comparison of the Analysis Results for OBE Motion with Numerical Mass of 30t.....	239
Figure C.3. Comparison of the Analysis Results for OBE Motion with Numerical Mass of 35t.....	240
Figure C.4. Comparison of the Analysis Results for OBE Motion with Numerical Mass of 40t.....	240
Figure C.5. Comparison of the Analysis Results for OBE Motion with Numerical Mass of 45t.....	241
Figure C.6. Comparison of the Analysis Results for OBE Motion with Numerical Mass of 50t.....	241
Figure C.7. Comparison of the Analysis Results for MDE Motion with Numerical Mass of 30t.....	242
Figure C.8. Comparison of the Analysis Results for MDE Motion with Numerical Mass of 37.5t.....	242
Figure C.9. Comparison of the Analysis Results for MDE Motion with Numerical Mass of 50t.....	243
Figure C.10. Comparison of the Analysis Results for MCE Motion with Numerical Mass of 45t.....	243
Figure C.11. Comparison of the Analysis Results for MCE Motion with Numerical Mass of 65t.....	244
Figure C.12. Comparison of the Analysis Results for MCE Motion with Numerical Mass of 75t.....	244
Figure D.1. Pushover Curve for Specimen 1 .....	245
Figure D.2. Base Shear versus Base Displacement Curve for Specimen 1 .....	246

Figure E.1. Profile Views of the Failure Surface .....	248
--	-----



## LIST OF SYMBOLS / ABBREVIATIONS

ACI	American Concrete Institute
ADAP	A Computer Program for Static and Dynamic Analysis of Arch Dams
$a_g^i$	Ground Acceleration at Time $i$
$a^i$	Acceleration of the Associated Degree of Freedom
$a(n)$	Acceleration for $n^{\text{th}}$ Time Interval
ASTM	American Standard for Testing and Materials
$a_x$	Horizontal Acceleration
$b$	Width of the Base
$C_1$	Generalized Damping of the Fundamental Mode
$c$	Velocity of Pressure Waves in Water
CFD	Computational Fluid Dynamics
CFRD	Concrete-faced Rock-fill Dams
CRCM	Coaxial Rotating Crack Model
C-S-H	Calcium-Silicate-Hydrate Gel (Concrete Paste)
CVC	Conventionally Vibrated Concrete
DCR	Demand-Capacity Ratio
$d_i$	Opening Size of $i^{\text{th}}$ Sieve
$D_{\max}$	Maximum Aggregate Size
$D_n$	Displacements at Time Step $n$
$e$	Effective Height
EACD	A Computer Program for Three-dimensional Earthquake Analysis of Concrete Dams
EAD	Earthquake Analysis of Dams
EAGD	A Computer Program for Earthquake Response Analysis of Concrete Gravity Dams
EFDD	Enhanced Frequency Domain Decomposition
ELSA	European Laboratory for Structural Assessment

EoUCA	Compaction Energy on a Unit Concrete Area
$E_r$	Modulus of Elasticity of the Sediment
$E_s$	Modulus of Elasticity of Dam Structure
F	Externally Applied Force
$f_1$	Compressive Strength for a State of Biaxial Compression superimposed on Hydrostatic Stress State
$f_2$	Compressive Strength for a State of Uniaxial Compression superimposed on Hydrostatic Stress State
$f_c$	Uniaxial Crushing Strength of a Material
$f_{cb}$	Biaxial Compressive Strength of a Material
FCM	Fixed Crack Model with a Variable Shear Resistance
FERC	Federal Energy Regulatory Commission
$F_h$	Lateral Force
$f(n)$	Force for $n^{\text{th}}$ Time Interval
$f_t$	Uniaxial Tensile Strength
$F_v$	Vertical Force
GDSHW	General Directorate of State Hydraulic Works
$G_f$	Fracture Energy
H	Depth of Water in Reservoir
Heidenhain	High Precision Displacement Transducer
$h_p$	Critical Height
ICOLD	International Commission on Large Dams
$I_t$	Mass Moment of Inertia of the Dam Monolith about the Centroid of its Base
k	Stiffness Sub-matrices for Dam
$k_b$	Stiffness Sub-matrices for Dam-Foundation Rock Interface
$K_1$	Generalized Stiffness of the Fundamental Mode
LVDT	Linear Variable Differential Transducer
M	Overturning Moment
m	Concentrated Numerical Mass

$M_1$	Generalized Mass of the Fundamental Mode
$m_a$	Complex-valued Mass for Absorptive Reservoir Bottom
MAS	Maximum Aggregate Size
$m_b$	Mass Sub-matrices for Dam Base
MCE	Maximum Characteristic Earthquake
MDE	Maximum Design Earthquake
$m_t$	Total Mass of the Dam Monolith
$m_x$	Density of Dam Material in x Direction
$m_y$	Density of Dam Material in y Direction
NLFM	Nonlinear Fracture Mechanics
$N_s$	Total Number of Strokes
OBE	Operational Based Earthquake
$\bar{p}_0(y, \omega)$	Response Function for Hydrodynamic Pressure on the Upstream Face due to Horizontal Ground Acceleration of a Rigid Dam
$\bar{p}_1(y, \omega)$	Response Function for Hydrodynamic Pressure on the Upstream Face due to its First Fundamental Mode of Vibration
PGA	Peak Ground Accelerations
PHGA	Peak Horizontal Ground Accelerations
$p_i$	Percentage Passing $i^{\text{th}}$ Sieve
PID	Proportional-Integral-Derivative Control Algorithm
PSD	Pseudo-Dynamic Testing
$p_x$	Hydrodynamic Pressure
$q$	Damping Coefficient for the Sediments
$\bar{Q}_h(\omega)$	Hydrodynamic Forces at the Reservoir Bottom
$\bar{q}(\omega)$	Relative Displacements at the Reservoir Bottom
$\bar{r}^l(\omega)$	Relative Displacements for Nodes above the Base
$\bar{r}_b^l(\omega)$	Relative Displacements for Nodes at the Base
$\bar{R}_b(\omega)$	Forces on the Bottom of Dam at Dam-Foundation Intersection

RCC	Roller Compacted Concrete
RCD	Rolled Compacted Dam
$\bar{\mathbf{r}}_f(\omega)$	Relative Displacements for Nodes on the Surface of Foundation
$\bar{\mathbf{R}}_f(\omega)$	Forces on the Surface of the Foundation
$\bar{\mathbf{R}}_h^1(\omega)$	Hydrodynamic Forces at the Upstream Face
$\mathbf{R}^i$	Restoring Force Vector
$r(n)$	Restoring Force for $n^{\text{th}}$ Time Interval
$\mathbf{R}_{n+1}$	Restoring Force at Time $n+1$
$\mathbf{R}^t$	Cracking Factor
$\mathbf{S}$	Failure Surface
SDFS	Single Degree of Freedom System
$\underline{\mathbf{S}}_f(\omega)$	Condensed Dynamic Stiffness Matrix of the Foundation
$\mathbf{S}_{qq}$	Sub-matrices in the Force-displacement Relation of the Foundation Rock Substructure
$\mathbf{S}_{rq}$	Sub-matrices in the Force-displacement Relation of the Foundation Rock Substructure
$T_1^p$	First Fundamental Frequency of Prototype Specimen
$T_1^s$	First Fundamental Frequency of Scaled Specimen
TCMA	Turkish Cement Manufacturers' Association
$u_o$	Horizontal Translation
USACE	United States Army Corps of Engineering
$u_x$	Translational Degrees of Freedom in x Direction
$u_y$	Translational Degrees of Freedom in y Direction
$u_z$	Translational Degrees of Freedom in z Direction
$\mathbf{V}$	Base Shear
$\mathbf{v}^i$	Velocity of the Associated Degree of Freedom
$\mathbf{V}_n$	Velocities at Time Step $n$
$w$	Unit Weight of Water
$\bar{\mathbf{Y}}_1(\omega)$	Modal Coordinates

$z$	Vertical Coordinate of any Point at which the Pressure Value is sought
$\underline{1}$	Directional Unit Vector
$\alpha$	Wave Reflection Coefficient
$\beta_c$	Closed Crack Shear Factor
$\beta_t$	Open Crack Shear Factor
$\gamma$	Unit Weight
$\Delta t$	Time Step Size
$\zeta_1$	Equivalent Viscous Damping Ratio (Or Simply Damping Ratio) at the First Mode
$\eta$	Angle of Similarity
$\eta_s$	Constant Hysteretic Damping for the Concrete in Dam Body
$\theta$	Rotation
$\mu_n(\omega)$	Complex-valued and Frequency Dependent Eigenvalues of the Impounded Water
$\xi_1$	Damping Ratio of the Fundamental Vibration Mode
$\xi_f$	Added Damping due to Foundation Flexibility
$\xi_r$	Added Damping due to both Reservoir Interaction and Reservoir Bottom Absorption
$\xi_s$	Viscous Damping Ratio
$\rho$	Density of Water
$\rho_r$	Density of the Sediment
$\sigma$	Axial Stress
$\sigma_h$	Hydrostatic Stress State
$\omega$	Excitation Frequency
$\omega_1$	Fundamental Natural Vibration Frequency of the Dam on Rigid Foundation
$\bar{\omega}_r$	Frequency of the Equivalent System



## **CHAPTER 1**

### **INTRODUCTION**

#### **1.1 General**

Societies have struggled to find water resources to maintain their lives since the beginning of civilization. Search of proper and efficient water for usage and energy production has recently become more challenging due to the rise of population and global warming, which necessitates more water storage for both agricultural and energy generation purposes. In addition, the fossil fuel resources have lost their popularity due to their environmental hazard as they release greenhouse gases in the energy production process. Consequently, the clean energy technologies like hydroelectric power plants come into prominence in developing countries with population growth. Evidently, dams are one of the most suitable structures that could serve for both water storage and energy generation.

According to the International Commission on Large Dams (ICOLD), the number of functional dams in its 95 member countries is 57,651 (ICOLD). The interesting fact about this statistics is that 41.4% of the total number of dams are now in China. In this statistics, Turkey is also ranked tenth with its 936 dams. In another statistics presented by the General Directorate of State Hydraulic Works (GDSHW), Turkey has 595 dams having a height taller than 10m. According to GDSHW, the earth/rock fill dams have a large share in this amount and concrete dams prior to 2010 are not the preferred alternative. Number of concrete gravity dams have not increased after 2000; conversely, there is an apparent increase in the number of Roller Compacted Concrete (RCC) and Concrete-faced Rock-fill dams (CFRD). This statistics reveal that, in the last 50 years, clay core rock-fill dams have been preferred by GDSHW for cases where clay stocks exist in a close proximity to the construction site, resulting in economical solutions. Similarly, RCC dams seem to be an attractive alternative with increasing numbers especially after the deregulation law in 2005, which allowed the private sector to build and operate dams and hydropower plants. Both design and construction practices in Turkey have a lot of experience with earth

fill dams. However, the experience in the design and construction of the other alternatives (RCC and CFRD) were quite limited since they have not been built in Turkey before 1990's.

Lately, RCC dams have gained popularity over the Conventionally Vibrated Concrete (CVC) due to the following reasons: i- this type of construction does not require costly formwork, which reduces workmanship and increases the construction speed with no slump concrete, ii- it has a low water-cement ratio, controlling the heat of hydration of mass concrete, iii- it has large aggregates leading to more economical concrete and iv- it has a reduced heat of hydration due to the addition of pozzolan to the mixture (ACI 207). In Turkey, although there are only 3 functional RCC dams namely Suçatı, Cindere and Çine Dams, several RCC dams are currently being built. In fact, some RCC dams are about to be taken in service or they are well into their construction and design stage. The number of RCC dams around the world before 2009 is more than 250 (Ozcan 2008). Therefore, this dam body type has started to supersede the other dam types.

Naturally, dams are constructed on rivers flowing through large or deep valleys so as to amass water in their artificially created reservoir. As stated by Carter (2008) "Faults crop out as linear features along the Earth's surface and usually provide an easily eroded zone between harder, unfaulted rock, so they can localize narrow linear valleys such as the San Andreas Rift Zone, separating Pt. Reyes Peninsula to the west from mainland California to the east". Therefore, the probable construction zones for dams usually lie in earthquake-prone regions. For example, 98.6 percent of the dams being constructed in Western China are located in high to moderate seismic hazard zones (Jackson 2012). A similar situation is valid for Turkey, where 90% of the dams are in earthquake prone zones. Thus, there is a serious risk of damage for these facilities that might endanger both the health and wealth of the society. Although dams are prone to earthquake excitation effects, they have usually performed better than the buildings in the last century. A study by Nuss and his colleagues (Nuss et al. 2012) investigated seismic performances of functional dams shaken by earthquakes having peak horizontal ground accelerations (PHGA) of larger than 0.3g. This study presents the observed performance of the selected



concrete dams, including RCC and arch ones, throughout the world (Table 1.1). In this table, it is apparent that one total collapse, namely Shih Kang Dam, has been observed. Also, some dams like the Koyna Dam, the Rapel Dam, etc. lost their functionalities after the earthquake as they had some major cracks in their body and/or some damage in their appurtenant structures. These observations should not make design engineers overconfident of the seismic performances of dams as these huge structures require special attention both at the design and construction stages (Nuss et al 2012).

The behaviour of dams, especially under the effect of seismic actions, is one of the most complicated problems in earthquake engineering. This is because; dams usually rest on flexible foundations and interact with the reservoir water, which necessitates taking the dam-foundation-reservoir interaction into account for determining their seismic behaviour. Furthermore, the compressibility of the water plays an important role considering the fundamental frequency of the reservoir and the dam, which necessitates the use of rigorous analysis techniques in the design process of these special structures. Also, the complex geometry of the valley and the dam necessitate considering the higher mode effects. The crack initiation and propagation on the dam body further complicates the multiphysics problem. Based on these arguments, further research is still needed in the area of seismic response and risk estimation of the dams.

## **1.2 RCC Dams**

By definition, RCC is a kind of concrete having no slump. This property gives the opportunity to place and compact this type of concrete by utilizing usual earth-fill equipment (Mehta and Monteiro 2014). This property speeds up the slow nature of concrete placement. In other words, CVC procedure is composed of concrete placement, consolidation and compaction, resulting in significant labor work. RCC procedure increases the cost-effectiveness of CVC over the earth-fill dams, which are known to be faster-to-build due to the advances in earth-placement and in compaction equipment over the last few decades. RCC combines the advantages of CVC with the easy-to-place property of earth-fill dams. Consequently, RCC has been replacing CVC for mass concrete (Mehta and Monteiro 2014). The idea of RCC is

based on the fact that the unhardened composition should sustain the weight of a compaction device as the placement of this material without formwork is only possible if large amount of compaction energy is transferred to the concrete batch (Mehta and Monteiro 2014). Consequently, CVC and RCC are different in their consistency requirements. Unlike CVC, RCC should adequately be dry to carry the vibrating cylinder for compaction and should have enough water for hydration process.

RCC technology was first utilized in the Tarbela Dam, Pakistan. In this application, more than 2.5 million m<sup>3</sup> of concrete was placed between 1974 and 1982 (Klieger and Lamond 1994). In 1996, there were approximately 200 RCC dams completed, under construction or in design stage in the world. Recently, there exists more than 300 RCC dams functional in the USA alone (Nawy 2008). Although RCC was more commonly used in the USA at the beginning, it has become more popular in China, Brazil, Spain, etc. Rolled Compacted Dam (RCD), a different version of RCC, has become more prevalent in Japan. In this construction technique, a shell of at least 3m thickness comprised of CVC is used around a low-cement RCC core. This shell mainly cover the faces including upstream, downstream, bottom and top of the dam body. In a new trend, it is common to use more RCC than CVC in RCD construction. This construction type did not find widespread use in countries other than Japan (Nawy 2008).

Similar to CVC, RCC could be obtained by utilizing any type of cement and cement-pozzolan mixture. However, cement-pozzolan mixtures, i.e. cementitious material, are preferred to reduce the heat of hydration in mass concrete applications. The RCC strength is mainly dependent on the compaction quality and effort, water – cementitious material ratios and the aggregate quality. The construction procedure of RCC is summarized in Figure 1.1 adapted from Uji (2010). It is apparent from Figure 1.1 that the placement of RCC is different than CVC. While placing RCC, the aim is to form a sufficient bond between the successive layers. This goal is generally accomplished by restricting the time between two successive layer placements, which prevents cold-joint formation between the lifts. This precaution is vital for both increased strength and reduced permeation (Ozcan 2008).

**Table 1.1.** Concrete Dams Subjected to Significant Shaking [Nuss et al. 2000]

Dam (completed)	Country	Height (m)	Crest (m)	Earthquake	Dist. To Fault (km)	Mag.	PHGA (g)	Remarks
<b>Concrete Gravity Dams</b>								
Lower Crystal Springs (1890)	USA	47	183	San Francisco (1906)	0.4	8.3	0.52 – 0.68	Not the slightest crack
Koyna (1963)	India	103	853	Koyna (1967)	3	6.5	0.63	Cracks in both faces
Williams (1895)	USA	21	27	Loma Prieta (1989)	9.7	7.1	0.6	No damage
Bear Valley (1912, 1988)	USA	28	110	Landers (1992)	45	7.4	0.18	Multiple arch modified to gravity dam in 1988.
				Big Bear (1992)	14.5	6.6	0.57	No damage, except slight displacement of crest bridge girders
Gohonmatsu (1900)	Japan	33	110	Kobe (1995)	1	7.2	0.83	No damage of this masonry dam
Shih Kang (1977)	Taiwan	21.4	357	Chi Chi (1999)	0	7.6	0.51	Vertical disp. of (9 m), Rupture of concrete.
Mingtian (1990)	Taiwan	82	-	Chi Chi (1999)	12	7.6	0.4 – 0.5	No damage
Kasho (1989)	Japan	46.4	174	Western Tottori (2000)	3 or 8	7.3	0.54	Cracks in Control Building at crest
Uh (-)	Japan	14	34	Western Tottori (2000)	1 or 3	7.3	1.16	Small crack at spillway base
Takou (2007)	Japan	77	322	Tohoku (2011)	109	9	0.38	Cracking of gatehouse walls at crest
Miyatoko (1993)	Japan	48	-	Tohoku (2011)	135	9	0.32	No damage
<b>Concrete Arch Dams</b>								
Gibraltar (1920, 1990)	USA	52	183	Santa Barbara (1925)	-	6.3	> 0.3	No damage. Modified in 1990 with RCC
Pacoima (1929)	USA	113	180	San Fernando (1971)	5	6.6	0.6 – 0.8	No cracks in arch. Open joint between arch and thrust block
				Northridge (1994)	18	6.8	0.53	Open joint (5cm) between arch and thrust block
Ambiesta (1956)	Italy	59	145	Gemona-Friuli (1976)	20	6.5	0.36	No damage
Rapel (1968)	Chili	111	270	Santiago (1985)	45	7.8	0.31	Damage to spillway and intake tower.
				Maule (2010)	232	8.8	0.302	Dam performed well. Cracked pavement.
Techi (1974)	Taiwan	185	290	Chi Chi (1999)	85	7.6	0.5	Local cracking of curb at dam crest
Shapai RCC (2003)	China	132	250	Wenchuan (2008)	32	8	0.25 – 0.50	No damage
<b>Concrete Buttress Dams</b>								
Hsinfengkiang (1959)	China	105	440	Reservoir (1962)	1.1	6.1	0.54	Horiz cracks in top part of dam
Sefid Rud (1962)	Iran	106	417	Manjil (1990)	Near dam site	7.7	0.71	Horiz cracks near crest, minor disp of blocks

Notes: Mag.= Magnitude ( $M_L$  or  $M_b$  for less than 6.5 and  $M_S$  above 6.5), PHGA= Peak horizontal ground acceleration

The use of roller compacted concrete has gained popularity since the development of the material in the early 1970's (Raphael 1971). The ease and speed of construction, the reduction in the quantity of cement used, and the corresponding decrease in the heat of hydration are the primary advantages that led to an increased use of RCC in dam construction. When fly ash or pozzolans are available nearby the construction site, the use of RCC results in a much more economical solution compared to the placement of CVC. Such benefits of employing RCC in dam construction were also recognized in Turkey (Dursun and Gokcol, 2011).

The main disadvantage, if to mention one, of RCC is that RCC loses its cost-effectiveness in some projects if the appropriate aggregates could not be found in close proximity to the construction site and if available foundation is poor in quality or foundation rock is not close to the surface (ACI 207). However, due to the significant reduction in the cement amount, some designers managed to employ RCC with fly ash delivered from over few hundred kms (Kagan Solmaz from Dolsar, personal communication, 2015).

### **1.3 Literature Review**

This section presents the important studies on seismic response of concrete gravity dams focusing both on numerical simulations and laboratory experiments.

#### **1.3.1 Linear Elastic Analysis of Dam-Foundation-Reservoir Interaction**

From the beginning of 1900's, significant amount of research have been carried out to investigate the behavior of gravity dams under the effect of ground excitations. The challenges of these special structures for the researchers includes i- modeling an extremely complex and uncertain interaction problem of dam-reservoir-foundation, ii- proposing design methods to maintain the functionality of dams due to their importance to sustain life, iii- preventing the possible risks related to the complete or partial collapse of dams.

The first attempts were to clarify the earthquake effects of the reservoir on dams, which has been one of the most popular topics in dam engineering. In order to have a better understanding on the interaction of dam with its reservoir, Westergaard (1933)

proposed a simplified method in his groundbreaking study. In this method, the hydrodynamic pressure is calculated by Eq. 1.1 illustrated in Figure 1.2.

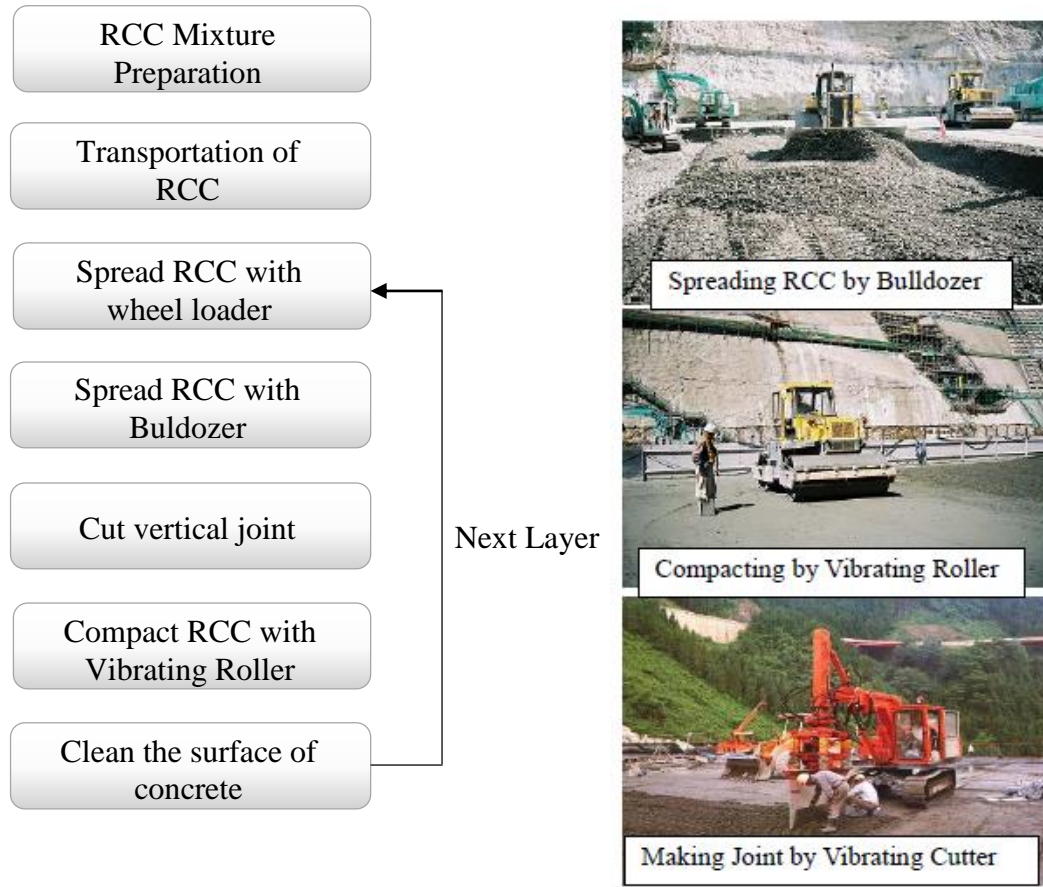


**Figure 1.1.** Steps in RCC Construction [Uji 2010]

$$p_x = \frac{7}{8} a_x w \sqrt{H(H-z)} = a_x m_{add} \quad 1.1$$

where  $p_x$  is the hydrodynamic pressure,  $w$  is the unit weight of water,  $H$  is the reservoir height,  $a_x$  and  $z$  are the horizontal acceleration and the vertical coordinate of any point at which the pressure value is sought, respectively.

In Eq. 1.1,  $a_x$  should be determined from the expected ground acceleration. In dam engineering practice, it became common to define additional masses at upstream face of gravity dams and to perform a dynamic analysis (spectrum or time history) to calculate the hydrodynamic pressures.

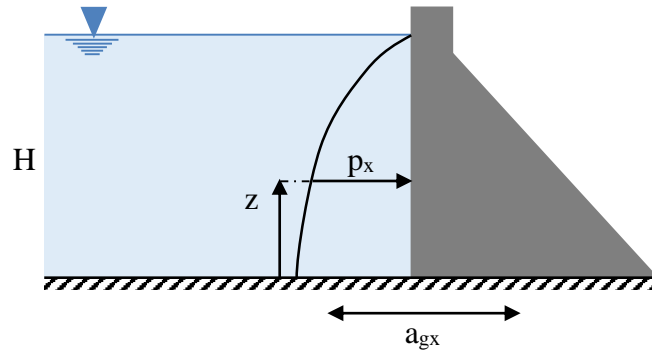


**Figure 1.2.** Illustration of Hydrodynamic Pressure

The main assumptions of Westergaard's added mass concept are :

- The water compressibility is neglected.
- The upstream face is assumed to be vertical.
- The dam base is assumed to be fixed (no reservoir-foundation interaction).
- Surface waves are ignored.

This concept was modified by Kuo (1982) to eliminate the upstream geometry restriction by reformulating the hydrodynamic pressure calculations. In Kuo's formulation, local total normal acceleration instead of the global horizontal one was employed, which helped to remove the restraint on the vertical upstream face geometry.

After the pioneering work of Westergaard (1933) on calculating the hydrodynamic pressure during the earthquake excitation, the seismic analyses and design of concrete gravity dams were studied in detail by Chopra and his colleagues starting in 1960s. At their first attempt, the effect of water compressibility was considered while determining the hydrodynamic effects by Chopra (1967), which removed one more constraint on the hydrodynamic effects. In this method, the hydrodynamic pressure histories were computed under the effect of horizontal and vertical ground excitations for rigid-based gravity dams and these pressures were detected to be significantly different than the ones proposed by Westergaard (1933) due to the compressibility of water. Therefore, the inclusion of the effect of water compressibility was deemed to be necessary for the hydrodynamic calculations and Eq. 1.1 was also claimed to be ineffective during dynamic analysis (Chopra 1967).

Chopra and Chakrabarti (1970) developed a finite-element-based program called Earthquake Analysis of Dams (EAD) to analyze dam bodies under the effect of both horizontal and vertical ground excitations. This program used 4-node plane stress quadrilateral elements in its element library (Figure 1.3). However, it could not combine the foundation-dam interaction as it only had the capability of modelling the foundation as a different layer. Therefore, it was incapable of accounting for the radiation damping due to the infinite foundation layer. One year later, Chopra and Chakrabarti (1971) had used this program to investigate the reason of damage to Koyna Dam during the large magnitude Koyna earthquake in 1967. In their work, they had used the recorded ground motion on the Koyna Dam body and claimed that the reason for the observed damage was due to the fact that

- i- the concrete strength was altered over the height of the dam as a common practice in India, i.e. the highest strength concrete is used in the lower parts of the dam and the strength gradually decreases at higher elevations, which was a logical approach as far as static loading conditions were considered. However, the dynamic load application would dictate larger stresses in higher elevations.
- ii- Koyna earthquake ground motions had high-frequency dominant nature which increased the demands on the dam body.
- iii- The design change during the construction phase of Koyna Dam compelled an uncustomarily large section, causing higher demands and stress concentrations.

This program was also utilized to examine the typical gravity dam sections in the vicinity of California. Pine Flat Dam was selected as the representative section. From the dynamic analyses of this dam, they had concluded that the upper parts of dam body were more likely to undergo larger tensile stresses. This conclusion was just the opposite of the commonly utilized design criteria, i.e. simulating the effects of earthquake excitations by laterally applied static forces, represented by a seismic coefficient.

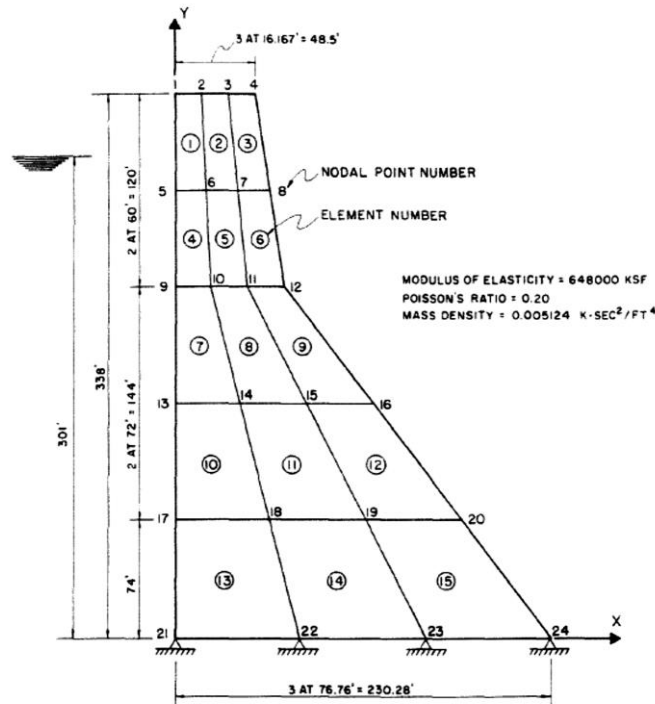


**Figure 1.3.** Typical Finite Element Mesh with Nodal Point and Element Numbers in Program EAD [Chopra and Chakrabarti 1970]

Clough et al (1973) prepared a finite element based program, ADAP, to conduct both static and dynamic analysis of arch dams. In their program, they had formulated curved shell, solid and thick shell elements to model dam body and foundation media (Figure 1.5). Foundation effects were taken into account by using Vogt flexibility method. In this method, flexibility coefficients related the normal, shear and moments applied on a semi-infinite elastic body to unit normal, shear and moment. However, in their method, the proper simulation of the hydrodynamic effects were missing while the hydrostatic effects were considered during the static analysis.

Gutierrez and Chopra (1976) proposed a substructuring method to analyze dam bodies composed of different parts like the foundation and reservoir media. In this study, it was claimed that the error introduced by substructuring the whole structure was negligible. This study formed the theoretical basis of the frequency-based substructure dynamic simulations from 1980's to 2010.



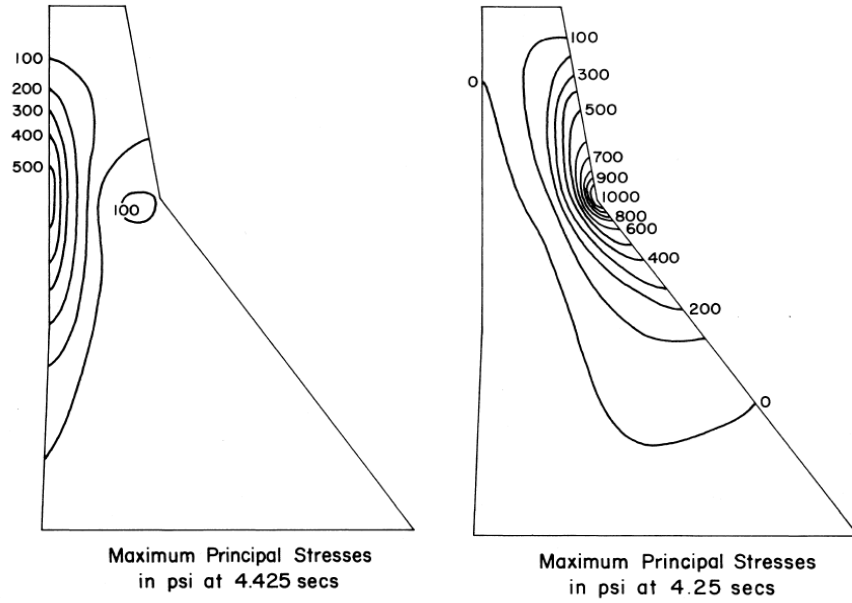


**Figure 1.4.** Principal Stresses over Koyna Dam body [Chopra and Chakrabarti 1971]

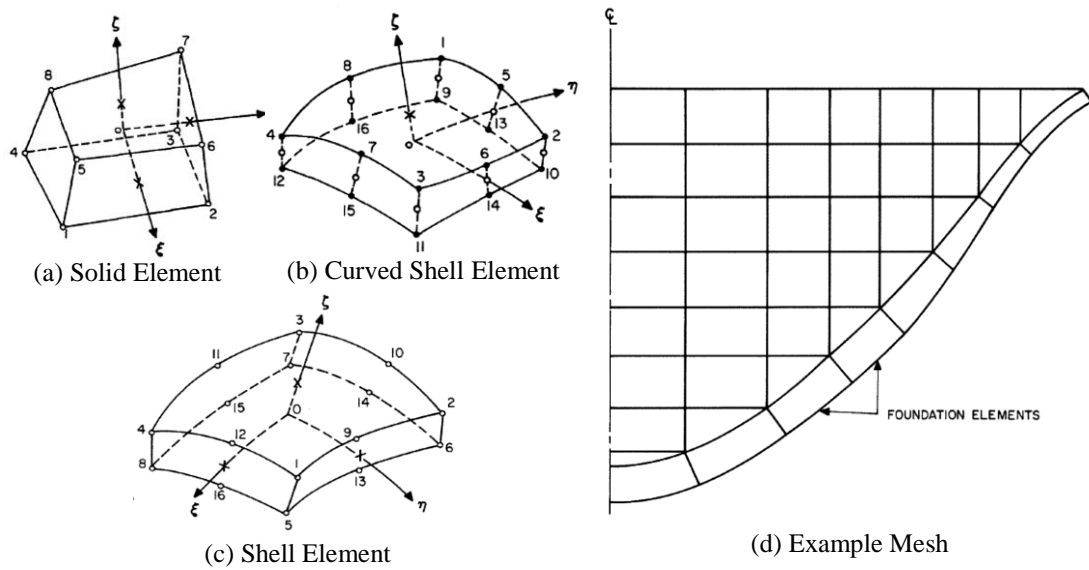


**Figure 1.5.** Details of Program ADAP [Clough et al 1973]

Dasgupta and Chopra (1977) presented a mathematical formulation for the inclusion of the dam-foundation interaction while performing dynamic analysis. In this research, a complex-valued stiffness matrix for the foundation rock was developed. This matrix was determined to be frequency-dependent and was derived by assuming a half-space foundation rock media. Also, the foundation rock was assumed as isotropic, homogeneous and viscoelastic. The nonlinear behaviour of foundation rock was not taken into account. That study was another step to have a semi-analytical

tool capable of analyzing dam bodies without the rigid foundation and incompressible reservoir assumptions.

Hall and Chopra (1980) developed an analysis procedure that accounted for the dam-reservoir interaction including water compressibility. The procedure was applicable in the frequency domain as the hydrodynamic response was determined to be frequency-dependent. Inspired by the work of Gutierrez and Chopra (1976), different substructures were defined for the dam body and reservoir by using finite elements (Figure 1.6). An infinite reservoir region was also defined to consider the radiation damping. The only restriction on the infinite region was the constant depth assumption. In this approach, the foundation was assumed as a rigid media. Dam-reservoir interaction was taken into account by utilizing the common nodes at the upstream face of the dam body. At those nodes, additional loads were calculated due to hydrodynamic effects and those loads were also considered while solving the equation of motion (Eq. 1.2). The hydrodynamic pressures,  $F_h$ , were obtained by solving the two-dimensional wave equation given in Eq.1.3, which was valid for small displacements, irrotational and inviscid fluids.

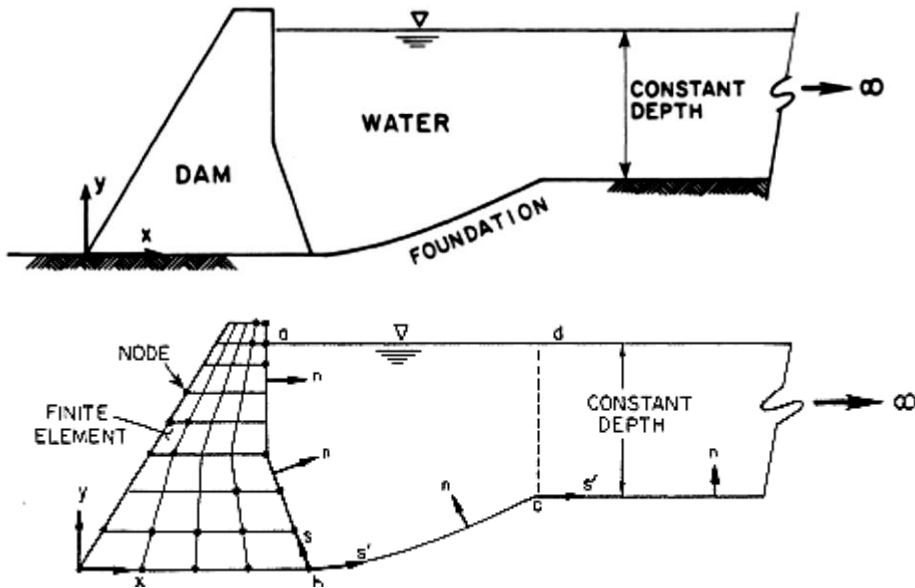


**Figure 1.6.** Different Substructures for Dam and Reservoir [Hall and Chopra 1980]

$$m * a + c * v + k * u = -m * a_g - F_h \quad (1.2)$$

$$\frac{\partial^2 p}{\partial x^2} + \frac{\partial^2 p}{\partial y^2} = \frac{1}{c^2} \frac{\partial^2 p}{\partial t^2} \quad (1.3)$$

where  $p$  is the pressure,  $c$  is the velocity of the compression waves in water.

Chopra et al (1980) combined the works of Dasgupta and Chopra (1977), Hall and Chopra (1980) and Gutierrez and Chopra (1976) to propose an analytical method to determine the dam-reservoir-foundation interaction during seismic excitation. In this method, substructuring methodology was also utilized to define the dam, reservoir and foundation parts. In this procedure, the dam body, the fluid domain and the foundation material were modeled as a finite element mesh, infinite-length continuum and viscoelastic half-plane, respectively. Similar to the procedure proposed by Hall and Chopra (1980), the interactions between the dam body and other substructures were simulated by nodal forces on the boundary nodes.

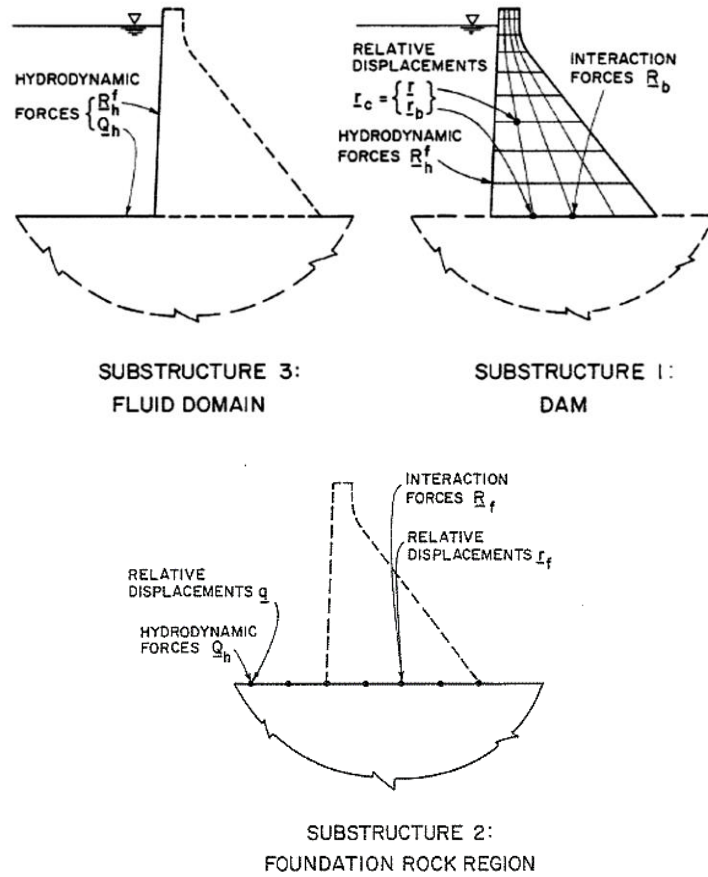


**Figure 1.7.** Substructure Representation of the Dam-Reservoir-Foundation System  
[Chopra et al 1980]

Fenves and Chopra (1984.a) combined the accumulated knowledge and developed a program called EAGD. This approach was capable of performing both static and dynamic analysis of gravity dams in 2D limited to linear analysis. It had both plane stress and plane strain options for the dam body elements considering the dam-reservoir-foundation interaction (Figure 1.8). The basis of this program was actually formed in other studies of Chopra et al (1980), in which an analytical method for the rigorous analysis of gravity dams including dam-foundation-reservoir was proposed.

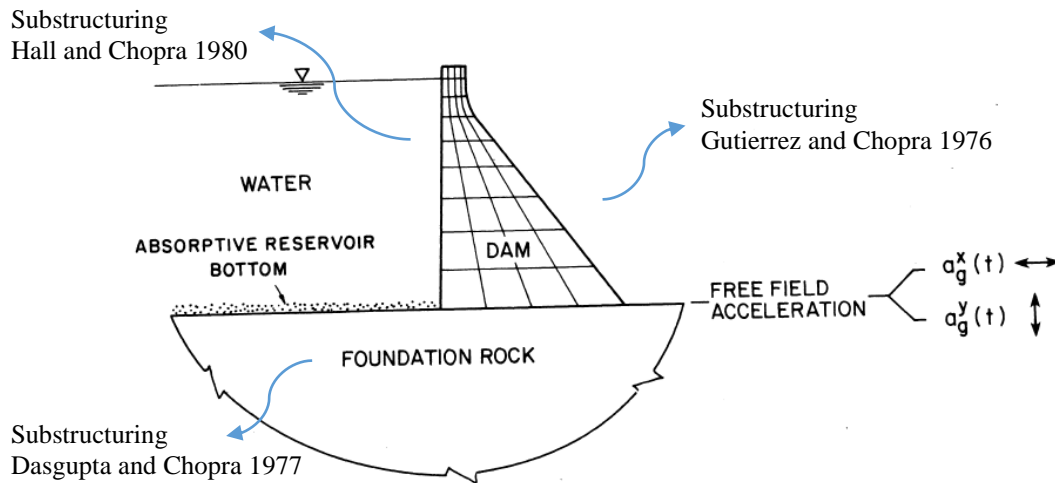


**Figure 1.8.** Dam-Reservoir-Foundation System in Program EAGD [Fenves and Chopra 1984.a]

One year later, Fenves and Chopra (1985.a and 1985.b) developed a simplified dynamic analysis methods for gravity dams. In this method, the dynamic response of stiff structures like gravity dams to ground excitations was assumed to be primarily due to the fundamental mode of vibration (Fenves and Chopra 1985.a). Therefore, response of dam body was determined from the analysis of a single degree of freedom system. Fenves and Chopra (1985.a and 1985.b) proposed the mathematical equations for the dam-foundation-reservoir system and simplified the approach to a simplified single degree of freedom representation of the complex system. In this approach, an equivalent single degree of freedom system was formed to simulate the exact fundamental mode representation of dam-foundation-reservoir system. The equivalent system had its unique period and damping properties that incorporate the effects of added hydrodynamic mass of the impounded water and the enhanced

damping coming from both the foundation and reservoir. The conclusions of those studies were crucial as the dam bodies were, for the first time, treated as a single degree of freedom system, which could really reduce the complexity of experimental studies.

These efforts were taken one step further by Fok et al. (1986) to develop a software to analyze gravity dams in three dimensions (Figure 1.9). A computer program named as Earthquake Analysis of Concrete Dams (EACD) was developed. Similar to EAGD, EACD could perform dynamic analysis of gravity dams by taking dam-reservoir interaction into account. EACD was updated by Tan and Chopra (1995) to include the dam-foundation interaction. Afterwards, Chopra and Wang (2008) appended the analysis capability for spatially-varying ground motions onto EACD.

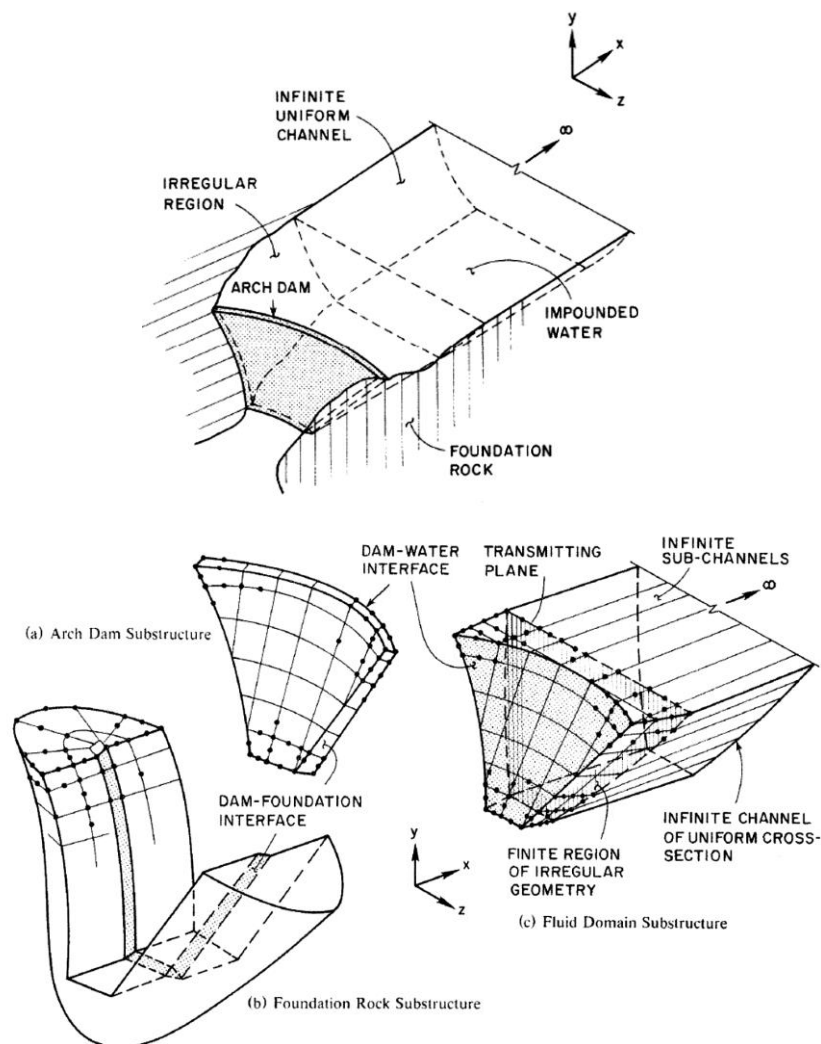


**Figure 1.9.** Dam-Reservoir-Foundation System in the Program EACD [Fok et al 1986]

After deriving the complicated mathematical equation for dam-reservoir-foundation systems, Lokke and Chopra (2013) derived a simplified response spectrum analysis method capable of including dam-reservoir-foundation interaction and higher-mode contributions. In that work, they utilized the conclusions of the previous works of Chopra (1978) and Fenves and Chopra (1985.a and 1985.b) to determine the response of a single-degree-of-freedom system. Then, higher-mode effects were also taken into account by utilizing static correction method presented in Chopra (2012). Lokke and Chopra (2013) showed that this procedure could estimate the dynamic response of a dam accurate enough to be utilized during preliminary and assessment stages. Besides, the reduced computational effort of this analysis technique was noteworthy.

Meanwhile, other researchers like Lotfi et al (1987), Medina and Dominguez (1989) modeled the dam-reservoir-foundation interactions by different techniques. A hyper-element technique capable of considering all possible interactions of a domain composed of dam body, reservoir body and foundation body was proposed by Lotfi et al (1987). At the boundary of the reservoir and dam body, the stress and displacement constraints along normal direction to the upstream face of the dam body were strictly enforced. This new technique could also handle the layered nature of foundation rock. Medina and Dominguez (1989) proposed a new numerical technique to perform 2D analysis of the dam-reservoir-foundation systems by using boundary element method. Boundary element method did not require discretization of interior media, i.e. only boundary mesh was sufficient. Therefore, this method was alluring in models having infinite domains. Just like Fenves and Chopra (1984.b), they also used frequency domain solution and did not include the non-linear behavior of materials. One year later, this method was improved to include sediment effects by Medina et al (1990). This method used boundary element method and could handle both deep-stratum and half-space idealizations of the foundation. They compared their results with the ones provided by Fenves and Chopra (1984.b) who claimed that the sediment effects could be included by an absorptive boundary described by a “wave reflection coefficient”. Medina et al (1990) concluded that the simplification of “wave reflection coefficient” for sediment effects could result in significant

damping especially for full reservoir cases. A similar conclusion was later reached by Bougacha and Tassoulas (1991 and 2006).

Tsai and Lee (1991) attempted to tackle the solution of dam-reservoir interaction problem in the time domain. In their procedure, they also used substructuring method and divided the whole domain into three substructures, i.e. dam body, near-field fluid domain and far-field fluid domain, which was extending to infinity to represent the radiation damping (Figure 1.10). The far-field radiation condition was exactly taken into account by using the formulation proposed by Tsai et al (1990.a and 1990.b).

Aforementioned numerical techniques along with more recent ones such as the perfectly matched layers (Basu and Chopra 2003) demonstrate the enormous efforts and importance of the dam-reservoir-foundation system.

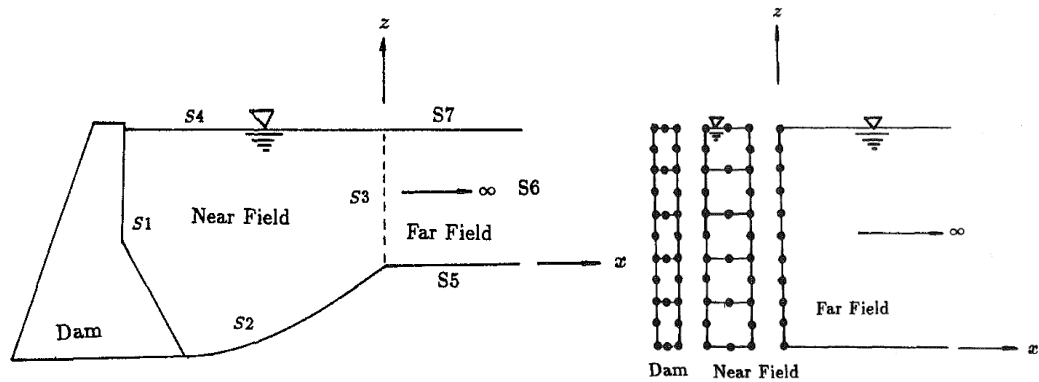


**Figure 1.10.** Finite Element Mesh for Dam and Near Field, and Layer Discretization of Far Field [Tsai and Lee 2007]

### 1.3.2 Nonlinear Simulations

After significant efforts on studying the proper modeling of the interaction of linear dam-reservoir-foundation systems, many researchers attempted to incorporate the nonlinear behavior of concrete in their simulations. Bhattacharjee and Leger (1994) investigated the capabilities of current smeared crack methods in nonlinear fracture mechanics (NLFM), i.e. coaxial rotating crack model (CRCM) and fixed crack model with a variable shear resistance (FCM), to simulate the cracking patterns of concrete dams. That study was concentrated on two-dimensional models and significant number of experiments were simulated to validate the models. The stress-

locking problem common in smeared crack models were suggested to be alleviated more by the CRCM. Bhattacharjee and Leger (1994) asserted that both methods, in general, performed well but the disadvantage of both the CRCM and FCM were that the estimated cracks were mostly dependent on the available mesh geometry. In another study, conducted by Bhattacharjee and Leger (1995), penetrated water inside a crack zone and its extra uplift contribution was modeled by using the effective-porosity concept. The water pressures inside a crack were detected to deteriorate the ultimate capacity of dam body.

Lee and Fenves (1998) proposed a rate-independent concrete model with softening effect for both tension and compression by extending the concrete plasticity model of Lubliner et al (1989). They claimed that the concrete model could simulate the cyclic test results of concrete well. They also used this model to predict the dynamic response of the Koyna Dam to the Koyna Earthquake. They concluded that the damage evolution in the analysis was similar to the observed cracks since the simulations revealed that the cracks formed firstly at the downstream face in the location where the slope changes. After that, the top portion started to rock as a rigid body.

In another study conducted by Hall (1998), a non-linear procedure was generated to analyze arch dams in 3D (Figure 1.11). The proposed method could deal with the opening of contraction joints as well as the previously opened body cracks. The model had some assumptions and simplifications, i.e. treatment of foundation as a massless medium, incompressible water, predetermined crack plane orientations, etc. Despite its major assumptions, this procedure was a significant step towards the development of non-linear analysis tools for dam-reservoir-foundation systems.



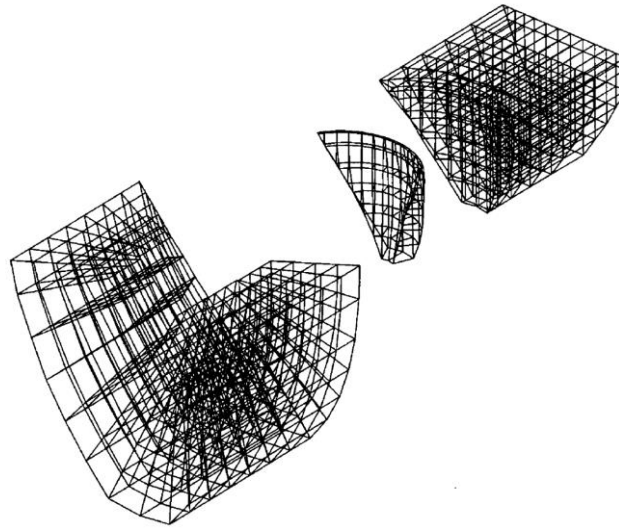


**Figure 1.11.** Meshes for Foundation, Dam Body and Reservoir [Hall 1998]

Fronteddu et al (1998) tried to reveal the behavior of concrete lift joints under both static and dynamic loading conditions. They conducted displacement controlled friction tests on 18 different concrete specimens. Specimens had different surface preparations, i.e. untreated, water-blasted and monolithic. Test results showed that the water-blasted surface behaved similar to the monolithic concrete as the cracks along the water-blasted surface was rough. However, the untreated surface had very flat cracks that resulted in a similar behavior to the independent concrete surfaces. In addition, the cyclic behavior of concrete lift joints was detected to be very stable without significant degradation. Also, the test results revealed that the coefficient of friction was totally dependent on the velocity of the cyclic loading and there was no correlation between coefficient of friction and the frequency content of sliding cyclic displacement.

Slowik and Saouma (2000) and Javanmardi et al (2005) took the idea of including the additional water pressures inside a crack formation one step further and investigated the variations of water pressure inside a crack during a seismic event. The proposed numerical model was compared with the experimental tests and it was concluded that only a small portion of a crack zone was saturated during a seismic event and the uplift force in the cracked portion was determined to be relatively small, verifying the zero uplift force assumption commonly used in the seismic analysis. Furthermore, the rate of crack opening was very influential on the water

penetration into a crack zone. If the rate was fast enough, the water could not penetrate into the crack, which was observed during seismic events. In addition, it was suggested that the factor of safety calculations for the downstream sliding could be performed without including the water pressure in the prescribed crack.

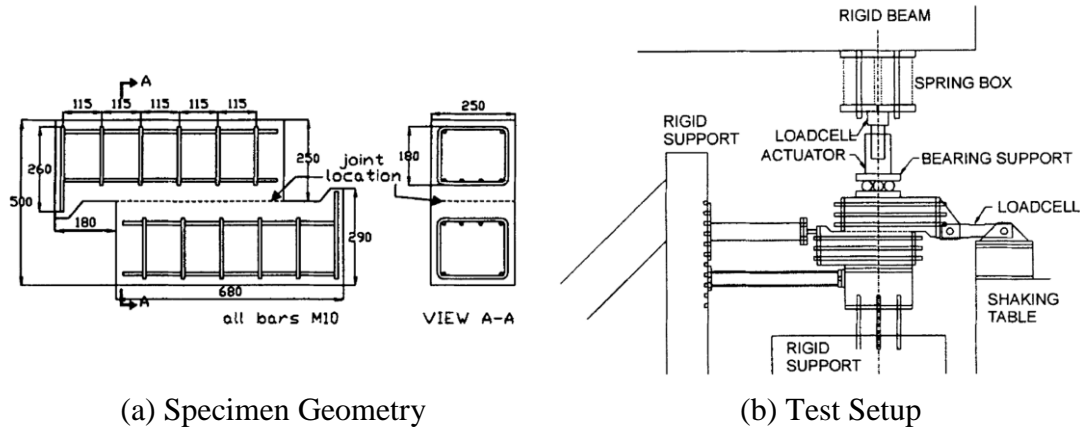


**Figure 1.12.** Details of Tests conducted in Fronteddu et al (1998)

Recently, the researchers have struggled to incorporate the material nonlinearity into the dam-reservoir-foundation interaction problem. However, the mathematical background of this problem was too complicated even for linear systems due to its frequency dependency. Therefore, the new trend was to use multi-physics to perform dynamic analysis. This approach was feasible since finite element software became more efficient and more talented due to the advances in computer technology and improvements in the computational fluid dynamics (CFD) and the structural dynamics. In the multi-physics modelling, two different regions, i.e. fluid and structure, were used to model the fluid pressures and the structural displacements simultaneously (Ghaemian and Ghobarah 1998, Lim et al 2012). The partitioning of the fluid and the dam body was based on the assumption that the solutions for the two media could be achieved asynchronously but the constraint equations at the interface should not be violated, i.e. no fluid penetration inside the dam body. This compatibility equation was required as the fluid elements (Eulerian) had degree of freedoms of pressure, velocity and temperature whereas solid elements had only displacement degree of freedoms (Banerjee et al 2014). The Eulerian fluid elements, also called acoustic elements, could simulate both compressible and incompressible flow of inviscid fluids but the incompatibility of nodal degree of freedoms with the solid elements enforced researchers to propose new element formulations. Therefore,

Lagrangian fluid elements having only displacement degree of freedoms were derived to eliminate the incompatibility of degree of freedoms. Just like Eulerian elements, these elements were suitable to mimic the behavior of inviscid and compressible fluids (Calayir et al 1996). This modeling technique had been utilized by many researchers to investigate the effect of material nonlinearity and the water level in the reservoir on the behavior of the dam body (Arabshahi and Lotfi 2008, Akkose and Simsek 2010, Sevim et al 2011, etc.). Few researchers (Bernal 1998, Ferro 2013) investigated the use of the hybrid frequency time domain solution. However, no significant contribution incorporating rigorous dam-reservoir-foundation interaction along with proper concrete crack modeling is yet to be proposed. Ouzandja et al (2014) conducted a numerical study to investigate the effect of soil-structure interaction on the stress demands by considering the nonlinear behaviour of concrete. In their research, they had used 2D finite element based models with Drucker-Prager (ANSYS 2010.a-2010.d) plasticity for concrete. They claimed that the stress demands were larger when the soil-structure interaction was taken into account.

### **1.3.3 Seismic Design of Dams**

After conducting numerous researches on the new modeling techniques for dams, Ghanaat (2004) presented an assessment method for the safety evaluation of gravity dams to reduce the effect of engineering judgment. In general, USACE (1994) and FERC (1999) suggested a factor of safety of 1.5 and 1.1 in compressive stress for the new design and the evaluation of existing dams, respectively. For the tensile stresses, the limit on maximum tensile stresses is 2 but there is no limit for the overstressed areas in the proposal by USACE (2003). Therefore, a systematic method was proposed relying on demand-capacity ratio (DCR) and cumulative inelastic duration of stresses. In this method, the linear elastic time history results were used to determine the excessive stresses and DCR values. Then, a cumulative inelastic duration versus DCR curve of the dam was depicted and it was compared with the limits (Figure 1.13). If it exceeds the limits, a more rigorous analysis, i.e. nonlinear time history analysis, should be performed to reassess the design or the performance of the dam. The issue of evaluating the safety of existing dams has recently been

investigated by other researches like Gogoi and Maity (2005), Mills-Bria et al. (2008), Yilmazturk et al (2015), etc.

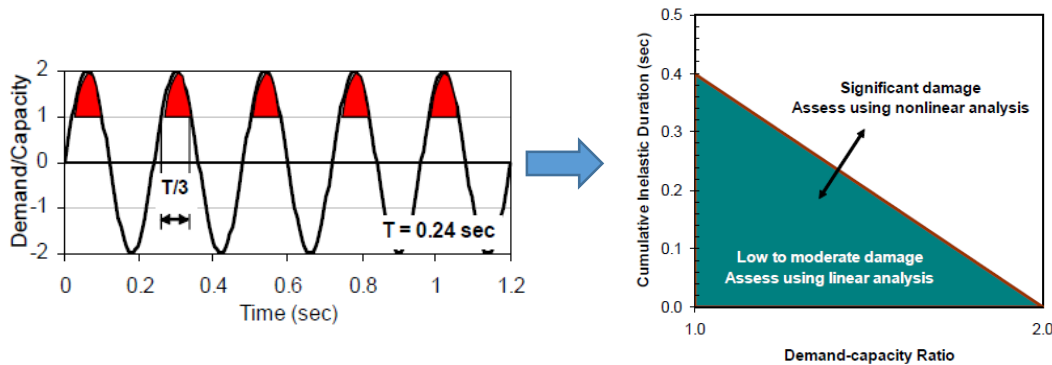


**Figure 1.13.** Basis for Upper Limit Demand-Capacity Ratio and Cumulative Inelastic Duration [USACE 2003]

The state of the art seismic design of dams usually rely on the massless foundation model of Clough (1980) or the simplified approach of Fenves and Chopra (1985.a). Recently, there are suggestions requiring the use of nonlinear time history analysis for the assessment and design of concrete gravity dams (USACE 2003, UBK 2012). These requirements obviously necessitate appropriate modelling techniques and robust constitute models calibrated to the experiments.

#### 1.3.4 Experimental Work

Although there are numerous studies on the simulation of dams, the experimental work is limited due to the tremendous sizes of the dam bodies, restricting the possibility of laboratory testing. This problem was usually overcome by utilizing small scale factors in constructing laboratory specimens or by instrumenting existing dams. While performing laboratory experiments, the important issues were the simulation of hydrodynamic effects and the acquirement of equivalent stress distribution over the dam body. Although the former issue was addressed by placing a reservoir separated by a plastic film from the upstream dam face (Niwa and Clough 1980), the behaviour of dam bodies with empty reservoir cases was investigated in literature with more emphasis. The latter problem was dealt with the utilization of additional external forces, with the scaling of the gravitational acceleration (or density of the material) or by decreasing both the modulus of elasticity and

compressive strength (Niwa and Clough 1980, Donlon and Hall 1991 and Harris et al 2000). In the literature, the scaling of the gravitational effects by utilizing centrifuge machines was favored as this solution allowed to use concrete without changing its physical properties (Uchita et al 2005).

The first attempt to perform a laboratory experiment was the determination of the natural vibration frequency of a scaled earth-fill dam model in Japan (Hatanaka 1955). Hatanaka (1955) prepared a miniature dam model composed of agar-agar, a gelatin-like material obtained from seaweed. These tests were the first of its kind throughout history. The dam model had a base width of 0.33m, height of 0.08m and a downstream/upstream slope of 2:1. The forced-vibration tests were conducted on the specimen. The forced-vibration was generated by executing and stopping the shake-table suddenly. During the experiment, the deformations of some points over the dam model were recorded. The study was quite successful in estimating the vibration frequencies.

Keightley (1964) conducted a study to determine the in-situ dynamic properties of Bouquet Canyon Dam, an earth-fill dam having a height of 61 m and a base width of 396m. Four vibrators were mounted to the crest of the dam body (both in upstream and downstream directions) to induce accelerations on the dam body. In addition, accelerometers were placed to determine the natural vibration frequency as well as the natural vibration shapes of the dam body. The modulus of elasticity and the shear modulus of the dam body were back-calculated by measuring the dilatational and shear wave velocity, respectively, which allowed performing further analytical studies for this dam.

Due to the technological limitations, the first laboratory testing on scaled dam models was performed by utilizing different materials other than concrete to follow the similitude law. However, a few exceptions that did not comply with the material scaling requirements do exist in literature (Baba 1980). One of the first rational attempts to observe the seismic behavior of the concrete dams belonged to Niwa and Clough (1980). In the scope of that study, two different scaled dam specimens were tested to investigate the joint movements between monoliths of arch dams and to detect the cavitation and horizontal cracking effects on gravity dams. Vibration

frequencies of both specimens were detected during each experiment by conducting vibration tests. The similitude laws were enforced during each experiment to have the same strain for both prototype and laboratory specimens. In order to satisfy the similitude law, the density of concrete was set to be constant but the compressive strength and the modulus of elasticity were scaled. Thus, a new material was produced by mixing the plaster-celite-sand with lead powder, which was necessary to increase the unit weight. This material was demonstrated to comply with the similitude requirements, i.e. modulus of elasticity, strength and unit weight. After creating the scaled material, a 1/150-scaled model of the arch dam, the Techí Dam in Taiwan, was constructed. In the first experiment, the possible joint opening effects on the performance of arch dams were investigated. The seven blocks were placed side-by-side on a shake table. The dimensions of the blocks (width-thickness-length) were 0.23m-0.08m-0.34m. These blocks were placed so that the upstream direction faces the negative gravity direction (Figure 1.14).

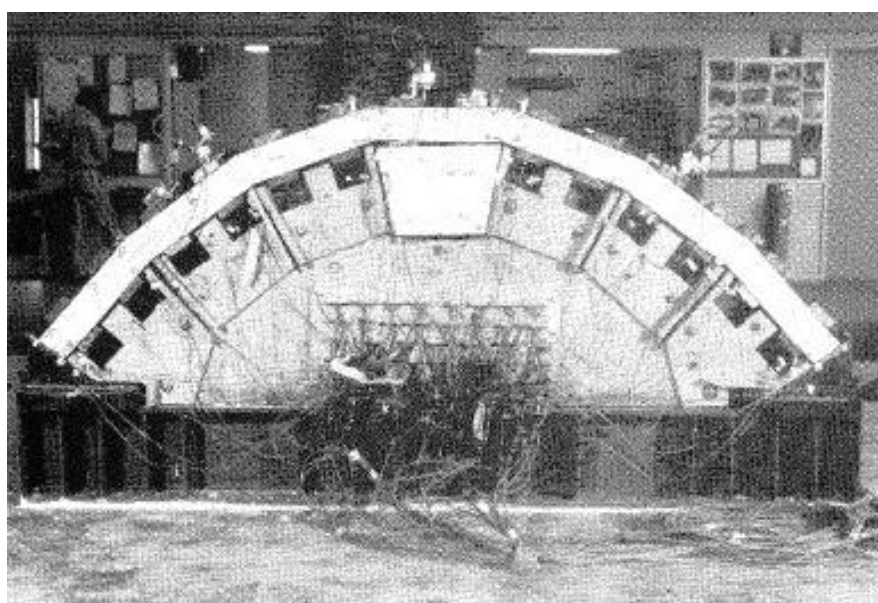


**Figure 1.14.** Segmented Arch Model on Shaking Table [Niwa and Clough 1980]

Lead plates were mounted to simulate the hydrostatic effects on the model, which was necessary to form thrust action. The ground motions were applied in two separate directions, i.e. vertical motions for the upstream-downstream component and the horizontal motions for cross canyon component. The failure was observed due to the crushing of concrete at joint face as a result of the reduced contact area

arising from the joint openings. In the second specimen, the effects of cracking and cavitation on the behavior of the concrete gravity dams were investigated. The 1/150-scaled version of the tallest section of the Koyna Dam located in India and damaged heavily in 1967 was used. A reservoir tank was constructed to include the hydrodynamic effects. The end of the reservoir tank was connected to the upstream face of the dam section by placing a thin plastic layer, which had negligible resistance. First, the forced vibration tests were performed for both the empty and full reservoir cases. The change in frequency due to the reservoir presence was determined as 25%. During the dynamic testing of the structure, body cracks were detected, which were similar to the ones observed in the real structure. However, the post-cracking response of the dam revealed that the dam body could sustain the hydrostatic and gravity effects after dynamic actions although it had large cracks on the body.

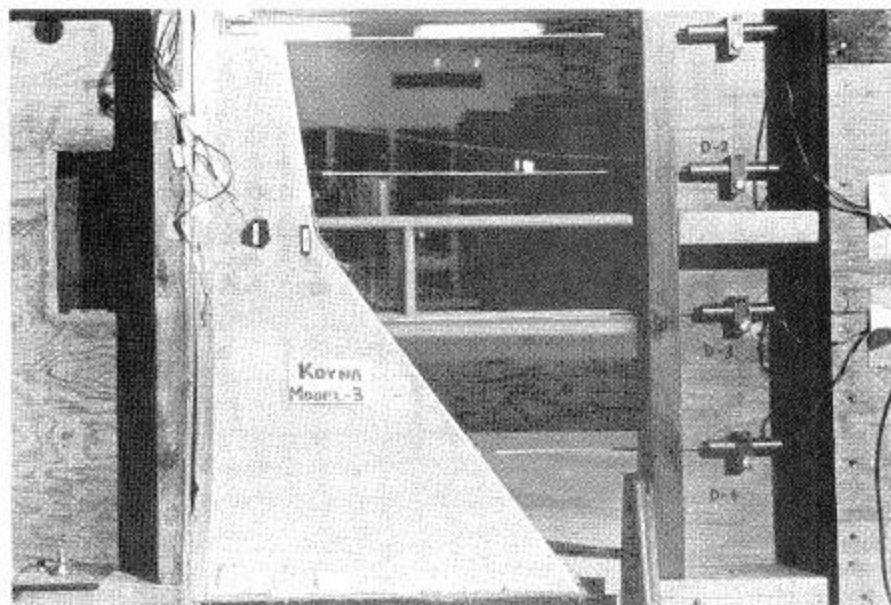


**Figure 1.15.** Koyna Dam Model with Reservoir Tank [Niwa and Clough 1980]

A similar test program was held in the California Institute of Technology by Donlon (1989). This study used Pine Flat Dam as the prototype dam. But, this time, a comparatively larger scale, 1/115, was used. The hydrodynamic effects were also included by using a similar methodology summarized in Niwa and Clough (1980). Polymer and plaster-based materials were employed to comply with the similitude laws during the course of that study. Donlon (1989) claimed that the most crack-

prone region was the neck of the dam body and no collapse was observed during three experiments, which was deemed due to the orientation of formed cracks, i.e v-shaped or up-sloped downstream cracks (Donlon 1989).

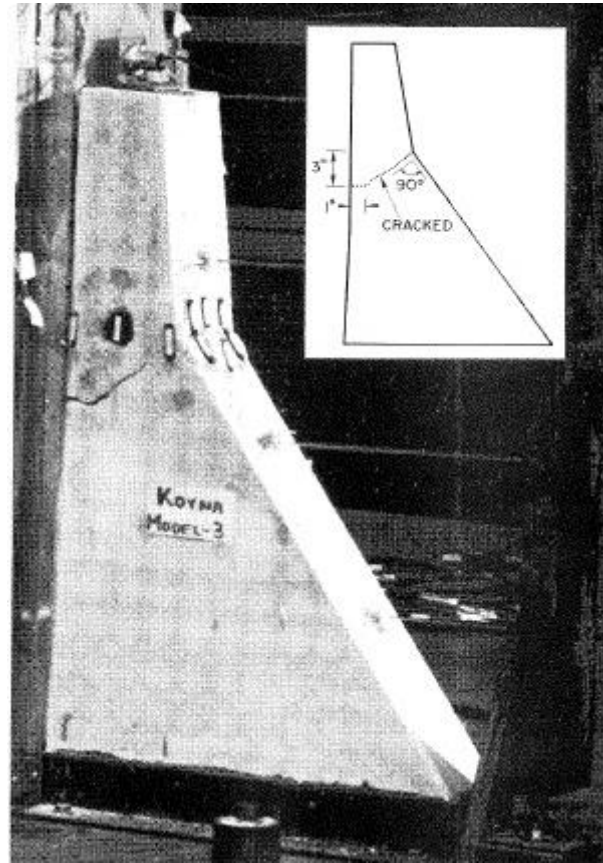
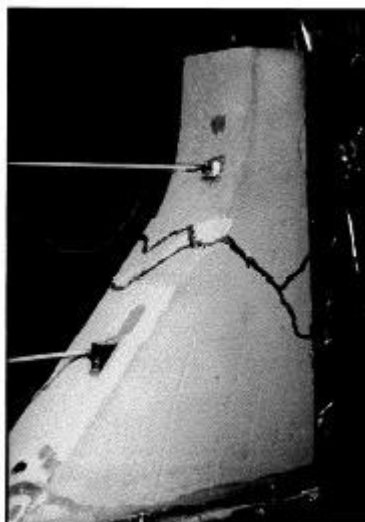
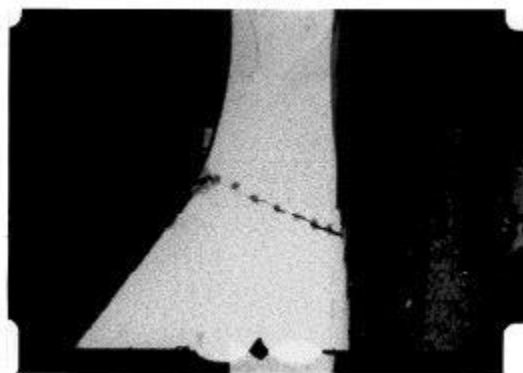


**Figure 1.16.** Crack Distribution after Test [Niwa and Clough 1980]



(a) V-shaped Crack



(b) Up-sloped Crack

**Figure 1.17.** Observed Cracks in Different Experiments [Donlon 1989]



In other studies, the shake table simulations of a gravity dam model of the Koyna Dam were conducted with different scale factors. The focus on the Koyna Dam was due to the fact that this dam was the only one with an observed damage having recorded acceleration histories until 1990's. In all of these studies, the similitude law was satisfied by producing a new material with a higher density. Harris et al (2000) performed the experiment on a 1/50-scale model. In that study, two different tests were conducted, i.e. one with cracks due to shrinkage effects and one without any previously formed cracks. The reservoir effects were excluded to eliminate the water-structure interactions. In another effort, Wilcoski et al (2001) increased the scale to 1/20 and conducted dynamic tests. The model was tested under sinusoidal motions and both the crack pattern and the crack locations at the failure stage of the dam were detected to be similar to the one observed in the real case. In addition, Tinawi et al (2000) performed a study on the investigation of the cracking and sliding behavior of concrete gravity dams under dynamic effects. They utilized a shake table to generate seismic actions on four different specimens having both upstream and downstream notches. Tinawi et al (2000) concluded that the pseudostatic dam seismic safety evaluation for sliding might be performed by 0.5 PGA and 0.67 PGA for high and low frequency earthquakes of USA, respectively.

The sliding behavior of concrete gravity dams was also investigated by Mir and Taylor (1996). Shake table tests were conducted on 6 different specimens with a scale of 1/30. In these tests, the hydrostatic effects were included but the hydrodynamic ones were excluded by using a relatively short tank with a low-stiffness rubber foam liner inside to allow the absorption of hydrodynamic pressures and to avoid the sloshing effects. There was no bond between the specimens and their foundations, so the only base resistance came from the base friction. All specimens were tested consecutively under three different ground motions. Test results revealed that the hydrostatic pressures reduced the downstream sliding resistance and therefore this mode of failure was the dominant one for all specimens. In fact, the upstream sliding and toe overturning would not be expected to occur unless uplift pressures existed or the reservoir was empty.

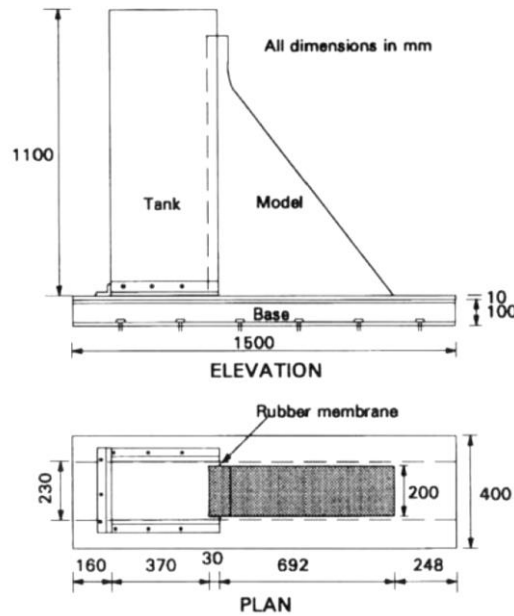


**Figure 1.18.** Test Setup [Mir and Taylor 1996]

In 1995, Plizzari et al (1995) presented a new technique for simulating the failure mechanism of concrete gravity dam models under the effect of hydrostatic forces including dam overtopping effects. Although there were some reported centrifuge testings in Japan up to that date (Takata and Kuribayashi 1961), these attempts were made on plexiglass and the hydrostatic effects were excluded. In this study, a different material was not designed to accommodate the requirements of similitude law. The gravitational acceleration was scaled by increasing the gravitational acceleration with a centrifuge machine to create the same stress distribution over the laboratory model with the prototype one. This technique was commonly used in geotechnical engineering (Ko 1988). However, from the viewpoint of structural engineering, this problem was solved by scaling down both the material strength and modulus of elasticity as explained in the preceding paragraphs. In this research, the crack propagation of gravity dam models under the effect of hydrostatic forces was investigated. Eight 1/100-scaled specimens were tested (Figure 1.19.a). The hydrostatic forces were generated by placing an upstream-wrapped container next to the dam model. The water level was increased till the crest and then the overtopping effects were simulated by exerting air pressure on the top of the dam till the failure. This study revealed that the upstream base cracks may penetrate in the foundation

rock if the connection of dam body and foundation was strong enough (Figure 1.19.b).

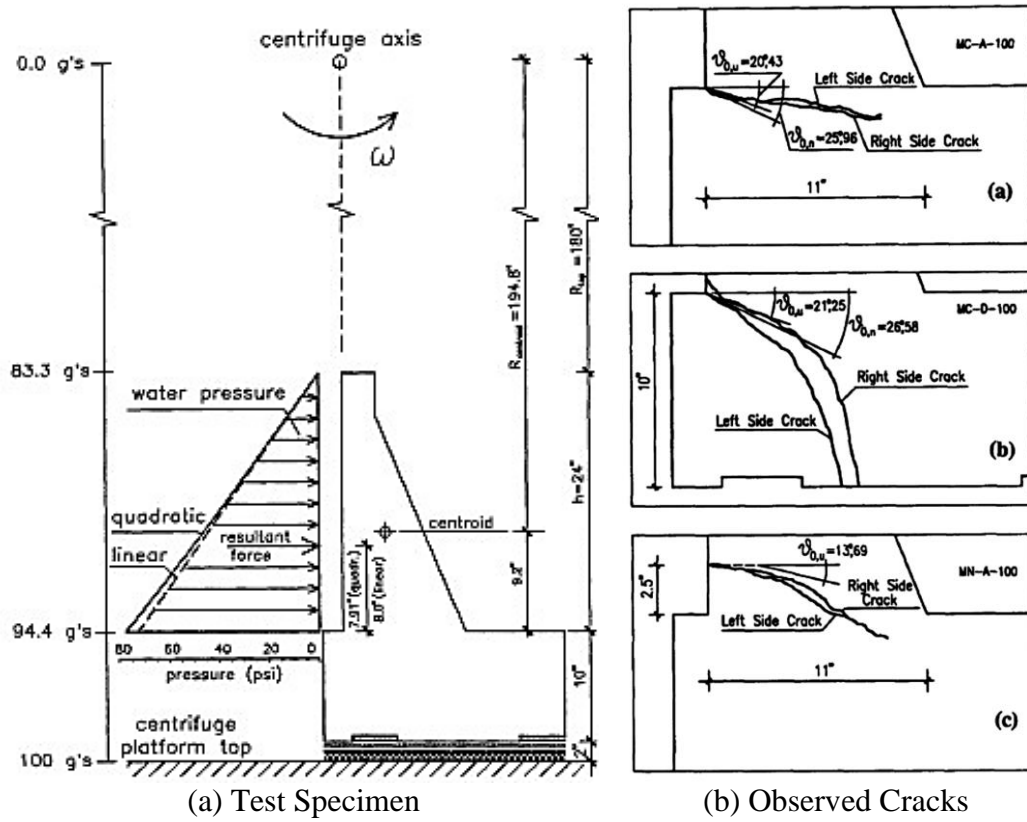


**Figure 1.19.** Centrifuge Test Results [Plizzari et al 1995]

Uchita et al (2005) presented a study on the state-of-the-art of the shake table experiments for dam testing. In their research, they performed a shake table experiment of a concrete dam model of a typical gravity dam cross-section in Japan. The target of this experimental work was to generate experimental data for the verification of numerical tools as they claimed that the linear analysis tools most of the time overestimated the stresses due to the lack of stress redistribution stemming from the joint openings and the crack nucleation and propagations (Uchita et al 2005). It was claimed that proper nonlinear analysis tools were required, which necessitated experimental data for validation. Consequently, for the first time in literature, Uchita et al (2005) placed the shake table inside a centrifuge machine (Figure 1.20) so that the dynamic tests could be conducted without violating the similitude requirements. In other words, the gravitational acceleration was increased according to the applied scale to create the same stress in the scaled specimen. They

used unscaled material properties except the fracture energy. The aggregate sizes were scaled down to reduce the fracture process zone as suggested by Saouma et al (1991). The reservoir effects were also included by placing a water tank inside the centrifuge machine and two specimens were tested. In the first test, foundation failure had occurred so they took precautions in the second specimen by increasing both the width and depth of the foundation and changing the reinforcement detailing at the crack zones. During the second test, some body cracks at the locations where the cross-section changes as well as base cracks were observed (Figure 1.21).

Sevim et al (2012) had used ambient vibration tests to investigate the seismic behavior of the highest arch dam constructed in Turkey, the Berke Dam. They had used the enhanced frequency domain decomposition (EFDD) technique to extract the fundamental frequencies of the tested dam. After determining the fundamental frequencies experimentally, they had examined the capability of a software, ANSYS, to predict the fundamental frequency of the same specimen when the reservoir was full. In their numerical model, they had used Lagrangian fluid elements for modeling the reservoir and 8-node solid elements for dam body and foundation (Figure 1.22). They concluded that the numerical model could estimate the first eight fundamental frequencies with an error of less than 10% after the numerical model was calibrated.

Recently, the shake table efforts made in previously explained studies were repeated for different sections, scales or materials. For instance, Mridha and Maity (2014) investigated the dynamic response of reservoir-dam systems. In that study, 1/150 scaled model of Koyna Dam was used and the mixture was prepared from bentonite, cement, water and sand to obey the similitude law. The experimental behavior was compared with the numerical ones and it was asserted that the estimated cracks matched with the experimentally observed ones (Figure 1.23). In another study, the seismic safety of a newly designed concrete gravity dam was tested under the recommended PGA level for the planned site by using shake table tests, whose scale was set 1/100 for the length (Phansri et al 2015). After determining the fundamental frequencies by conducting resonance and ambient tests, the dynamic tests were performed under the effect of sinusoidal excitations. This study was also used bentonite-based concrete to satisfy the similitude requirements. The maximum base

shear coefficient to cause failure of the dam model was determined and it was suggested that the capacity of the dam model was approximately 1.40 times the PGA of the maximum credible earthquake.

These experimental studies demonstrate that seismic response of concrete dams were almost always investigated by using a shake table with / without centrifuge machine. The other alternative for seismic testing, i.e. the pseudo-dynamic testing procedure developed by Takanashi et al (1975) and further improved by Mahin et al (1989) and Nakashima et al (1990) have never been used in the testing of dams.

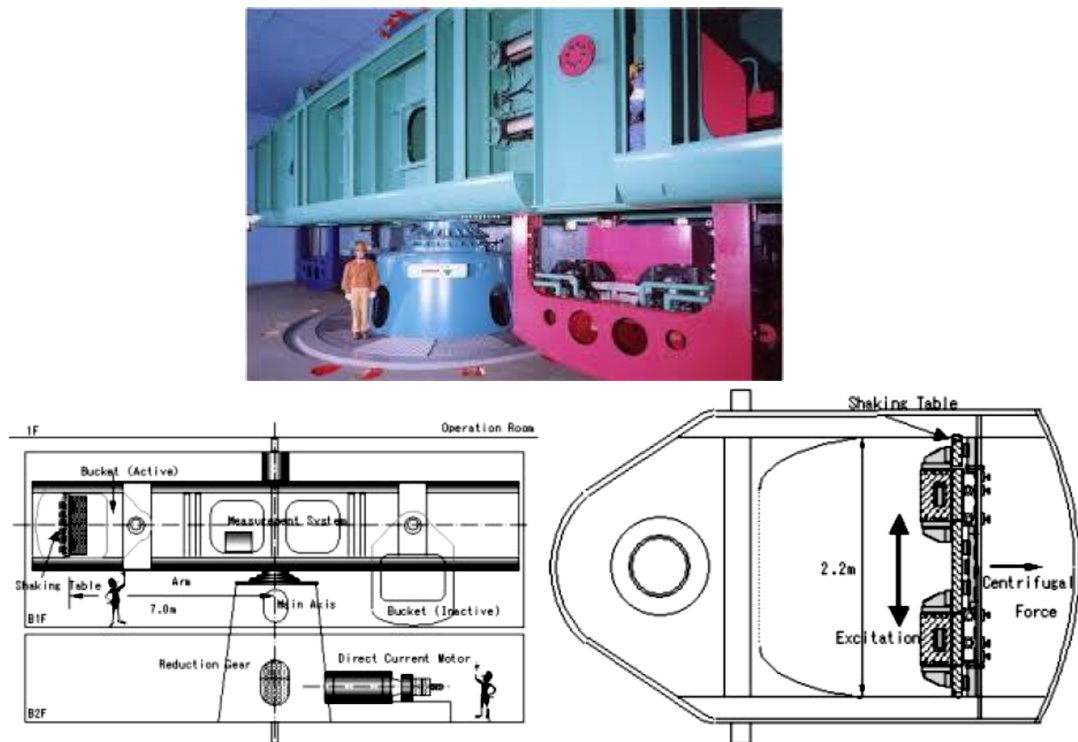


**Figure 1.20.** Dynamic Test inside Centrifuge Machine [Uchita et al 2005]

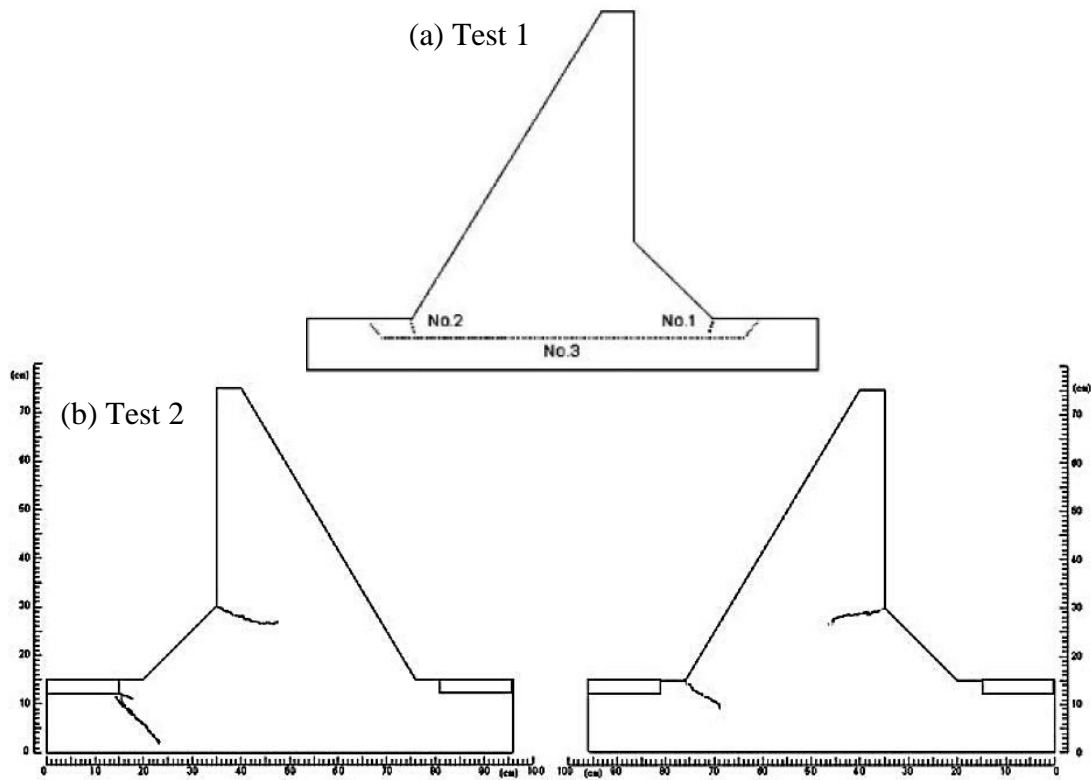


**Figure 1.21.** Observed Cracks during the Second Specimen [Uchita et al 2005]

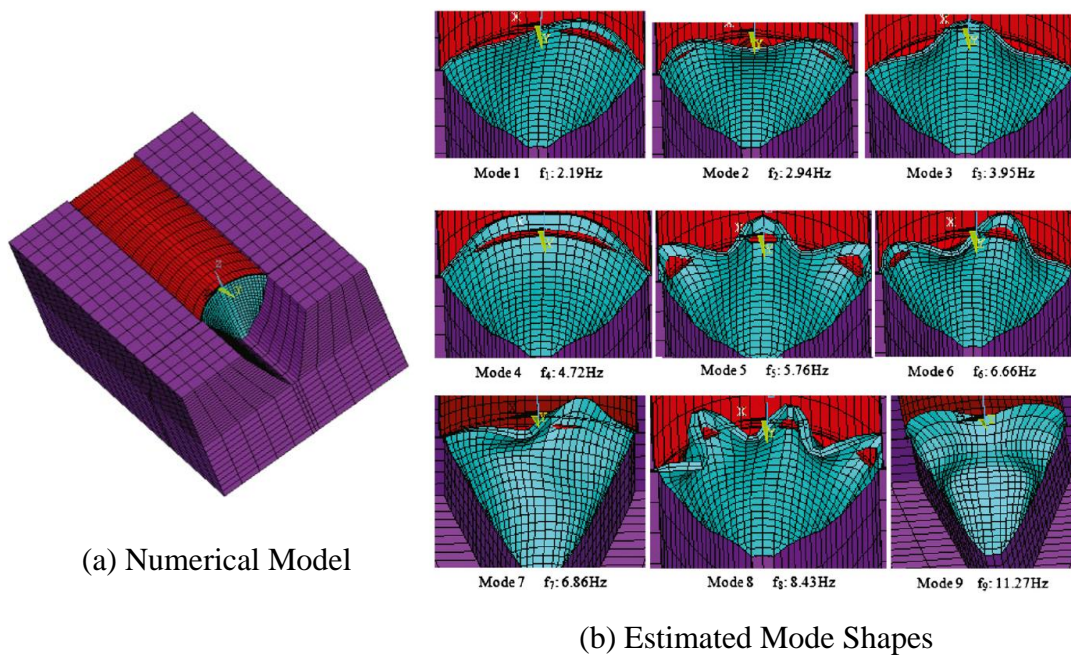


**Figure 1.22.** Numerical Model in Sevim et al (2012)

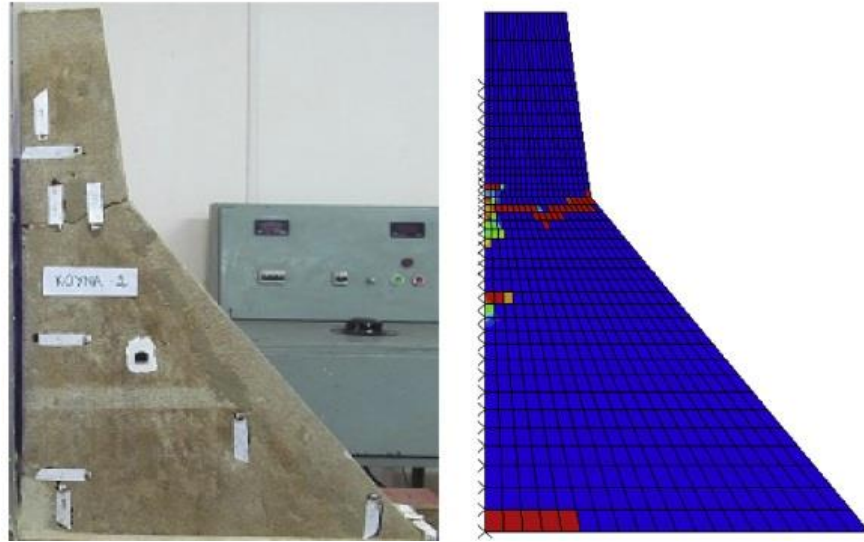


**Figure 1.23.** Comparison of Crack Patterns [Mridha and Maity 2014]

#### 1.4 Object and Scope

In-situ and laboratory experimental studies to better understand the seismic performance of concrete gravity dams are insufficient in number due to the complications regarding the tremendous sizes of dams, their interaction with the reservoir and the high costs of equipment and testing. As explained in the previous subsection, researchers generally opted for laboratory tests on scaled models by using new mixtures for the material or by altering the effects of gravity utilizing centrifuge machines to fulfill the requirements of similitude law. Dynamic loading was mostly simulated by the shake tables. However, one of the most important disadvantage of the shake table tests is the short duration of the ground motion period due to the (time) scaling of the motion. It should be reminded that use of shake tables requires the scaling of the motion by  $1/\sqrt{SF}$  in time, which leads to extremely short testing durations resulting in significant difficulties in the measurement and observation of the seismic response and the crack propagation within the specimen. Based on the shortcomings of the literature on dam testing and necessity of testing the seismic response of CVC and RCC gravity dams, the research presented herein was conducted. The objectives of the study are:

- To present a new approach for the testing of the seismic performance of gravity dams by employing a pseudo-dynamic testing (PSD) method specialized for concrete gravity dams.

- To examine the seismic performance of an RCC dam in Turkey, i.e. the Melen Dam which is under construction.
- To investigate the performance of the existing nonlinear finite element analysis tool to estimate the observed behaviour.
- To compare the seismic performance of CVC and RCC dam sections having similar material strengths.
- To analyze the effect of different material strengths on the seismic performance of the RCC dams.

In the scope of this study, the details of the testing procedure are outlined in Chapter 2. In this chapter, the necessary calculations to form the test specimen and test setup are also summarized. In Chapter 3, the mixture designs for the planned test specimens are presented. In Chapter 4, the details of the test setup including the instrumentation and the verification of test procedure are explained. In Chapter 5, the test results for each specimen are summarized. In Chapter 6, two different numerical techniques to simulate the experimental behavior of each specimen are presented. The abilities of these numerical methods to predict the crack patterns, the force and the displacement demands are discussed. In Chapter 7, the conclusions of this dissertation are drawn.

The tests presented herein are first of its kind in the literature. It is believed that the outcome of this dissertation will help engineers to test dam models economically and to obtain predictions of the expected seismic response of gravity dam monoliths under earthquake effects.



## CHAPTER 2

### APPLICATION OF PSEUDODYNAMIC TESTING FOR DAMS

#### 2.1 Single Degree of Freedom Approach

Existing experimental methods are challenging for simulating the dam systems because these huge structures have complicated interactions of the reservoir, the dam body and the foundation. There has been a constant effort by numerous researchers to simplify the dam analyses and the design problem. In the literature, the distinctive idea of treating dam system as a single mode structure is proposed first by Fenves and Chopra (1984.a, 1985.a, 1985.b and 1986). The method stems from the fact that the dynamic response of stiff structures like gravity dams to ground excitations is primarily due to the fundamental mode of vibration (Fenves and Chopra 1985.a). This statement was verified by comparing the modal responses as well as the principal stresses for Pine Flat Dam section obtained from the single degree of freedom system (SDFS) with the ones determined from rigorous semi-analytical analysis (called as exact solution), explained later in Section 2.2. The results showed that both the first fundamental vibration period and, more importantly, the principal stresses could be predicted by SDFS within an error of less than 10%. This result demonstrated that the SDFS response of Dam structures was dominant in their response and the approach of Fenves and Chopra (1985.a and 1985.b) for treating the dam body as a SDFS was rational.

**Table 2.1.** Comparisons of the SDFS and Exact Solutions  
[Fenves and Chopra 1986]

<i>Case</i>	<i>Foundation</i>	<i>Reservoir</i>	<i>First Fundamental Period (s)</i>		<i>Principal Stresses (MPa)</i>	
			<i>SDFS</i>	<i>Exact</i>	<i>SDFS</i>	<i>Exact</i>
<b>1</b>	Rigid	Empty	0.311	0.317	1.66	1.54
<b>2</b>	Rigid	Full	0.377	0.386	1.81	1.80
<b>3</b>	Flexible	Empty	0.369	0.386	1.08	1.19
<b>4</b>	Flexible	Full	0.448	0.482	1.90	1.50

Fenves and Chopra (1985.a) derived the relevant mathematical equations for the dam-foundation-reservoir system and made some simplifications to derive a simplified single degree of freedom representation of the complex system. In that approach, an equivalent single degree of freedom system was formed to simulate the exact linear elastic fundamental mode response of the dam-foundation-reservoir system. The equivalent system has its unique period and damping properties that interpret the effects of added hydrodynamic mass of the impounded water and the enhanced damping coming from both the foundation and reservoir (Figure 2.1).

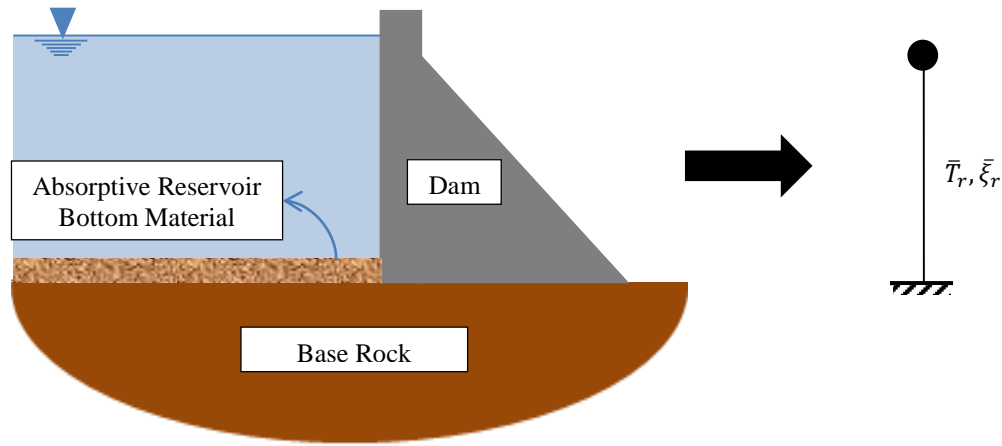


**Figure 2.1.** Simplification of the Dam-Water-Foundation Rock System  
[Fenves and Chopra, 1985.a]

Fenves and Chopra (1985.a) calculated the reservoir-structure and the structure-foundation interactions separately. The dam body, the base rock and the impounded water were all treated as linear elastic media. In addition, the base rock was idealized as a homogeneous, isotropic and viscoelastic half-plane. At the dam base, the deformations other than rigid body ones were ignored. The impounded water in the upstream direction was assumed to have a constant depth and an infinite length. The reservoir materials, i.e. sediments, were integrated to the model by a reservoir bottom damper that partially absorbs incident hydrodynamic waves.

In dealing with the reservoir interaction, the hydrodynamic effects were obtained by solving the two dimensional wave equation. The appropriate boundary conditions for the impounded water were employed for the free surface at the reservoir level, the absorptive boundary at the reservoir base and the dam body at the upstream

direction. Fenves and Chopra (1983) showed that the exact interaction between the dam body and the compressible fluid resulted in the complex-valued frequency response function for the modal coordinates (Eq. 2.4) by solving the equation of motion for SDFS dominant behavior (Eq. 2.1). The steps for the derivation of modal coordinates are summarized below.

$$m * \ddot{u} + c * \dot{u} + k * u = -m * \ddot{u}_g - F_h \quad (2.1)$$

By inserting the equation below into the equation of motion to represent the response as a SDFS dominant one, Then, the equation of motion becomes

$$u(x, y, t) = \phi_1(x, y)^k * Y_1(t) \text{ where } k = x, y \quad (2.2)$$

$$M_1 * \ddot{Y}_1(t) + C_1 * \dot{Y}_1(t) + K_1 * Y_1(t) = L_1 * \ddot{u}_g + \int_0^H p(0, y, t) * \phi_1(0, y)^x * dy \quad (2.3)$$

Fenves and Chopra (1984.b) provided the step-by-step mathematical solution of the above equation. After the necessary mathematical manipulations, the excitation – frequency dependent modal coordinates (  $\bar{Y}_1(\omega)$  ) due to the interaction of the dam body with the impounded water could be found as follows:

$$\bar{Y}_1(\omega) = \frac{-[L_1 + B_o(\omega)]}{-\omega^2\{M_1 + Re[B_1(\omega)]\} + i\omega\{C_1 - Im[B_1(\omega)]\} + K_1} \quad (2.4)$$

where  $M_1$ ,  $C_1$  and  $K_1$  are the generalized mass, damping and stiffness of the fundamental mode summarized in Appendix A. The other terms are also presented in Appendix A.

After the exact derivation of the fundamental modal response (Eq. 2.4), Fenves and Chopra (1985.a) obtained an equivalent single degree of freedom system (SDFS). The properties of SDFS were calculated by modifying the properties of an empty dam-reservoir system. The modifications were due to the added mass and damping caused by the hydrodynamic effects and the foundation flexibility and damping. The frequency dependent hydrodynamic effects were assumed to be frequency-independent and their values were calculated at the frequency of the equivalent system,  $\bar{\omega}_r$ . This assumption was validated by Chopra (1987) for a non-absorptive reservoir bottom. Therefore, the frequency-independent hydrodynamic terms were

assumed to be calculated by rewriting Eq. 2.1 with the help of the standard generalized properties for the fundamental mode (Eq. A.2.6).

Fenves and Chopra (1985.a) verified the effectiveness of the equivalent system by comparing horizontal acceleration responses of simplified and exact SDFS solutions due to the application of harmonic excitations (Figure 2.2). In their comparison, the foundation flexibility was ignored (rigid foundation case). The equivalent SDFS had an acceptable agreement with the exact system for a wide range of dam structure modulus ( $E_s$ ) and wave reflection coefficients ( $\alpha$ ). More details about the validity of the equivalent SDFS can be found in Fenves and Chopra (1985.a).

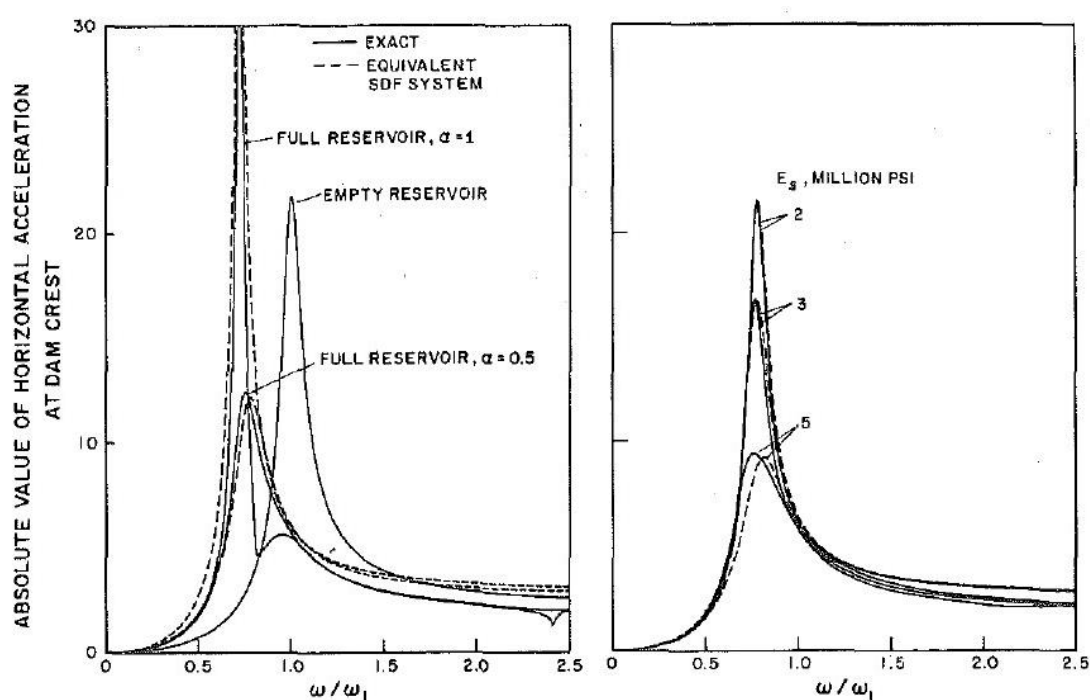


**Figure 2.2.** Comparison of Horizontal Acceleration Responses of Equivalent SDFS and Exact System due to Harmonic Horizontal Ground Motions [Fenves and Chopra 1985.a]

Fenves and Chopra (1985.a) further investigated the foundation flexibility effects on the dam body response in addition to the aforementioned hydrodynamic effects. After formulating the equation of motion to incorporate the translational and rotational degrees of freedoms at the foundation level, the analytical solution for the modal coordinate under the effect of a harmonic ground acceleration was determined. Similar to the reservoir-dam interaction case, Fenves and Chopra (1985.a) made simplifications to obtain an equivalent single degree of freedom

system (SDFS) including foundation flexibility. The properties of the SDFS were calculated by modifying the properties of an empty and rigid based dam-reservoir-foundation system. The modification was due to the added mass and damping caused by the flexible foundation. The frequency dependent foundation flexibility effects were also assumed to be frequency-independent and their values are calculated at the frequency of the equivalent system,  $\bar{\omega}_f$ .

Fenves and Chopra (1985.a) verified the effectiveness of the equivalent system by comparing horizontal acceleration responses of simplified and exact SDFS solutions due to the application of harmonic excitations (Figure 2.3). In this comparison, the reservoir effects were ignored (empty reservoir case). The equivalent SDFS results of the frequency response function were acceptable compared to the exact system for a wide range of dam structure modulus ( $E_s$ ). More details about the validation of the equivalent SDFS can be found in Fenves and Chopra (1985.a).

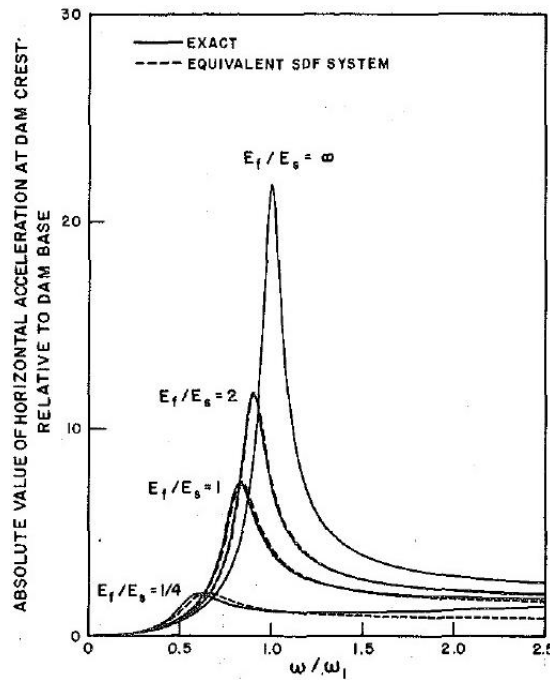


**Figure 2.3.** Comparison of Horizontal Acceleration Responses of Equivalent SDFS and Exact System with Empty Reservoir Condition due to Harmonic Horizontal Ground Motions [Fenves and Chopra 1985.a]

Fenves and Chopra (1985.b) combined their findings for separate actions of the reservoir-dam and the foundation-dam interactions. This remarkable effort forms the basis of the simplified finite element models (massless foundation and added mass)

that are widely used in practice today. The formulations in the previously discussed parts are combined together to include the reservoir-foundation-dam interactions simultaneously. The details on the combined reservoir-dam and foundation-dam interactions are summarized in Appendix A.

The approach of Fenves and Chopra (1985.a) provide a simple sufficiently accurate and elegant approach for dam analysis as demonstrated above. Inspired from this approach, this dissertation attempts to employ single degree of freedom approach for the pseudo-dynamic dam testing.

## 2.2 Rigorous Approach

A semi-analytical finite-element-based procedure for the rigorous analysis of gravity dams including dam-foundation-reservoir was proposed by Fenves and Chopra (1984.b). By utilizing this research, Fenves and Chopra (1984.a) developed a program, EAGD, capable of analyzing gravity dams by considering their interactions with their environment in 2D. An extension of this procedure to 3D, EACD, was proposed by Fok et al (1986).

This approach was suitable for determining the earthquake response of gravity dam monoliths but was limited to the linear elastic response. In the analysis, there exist three different media : the dam body, underlying flexible foundation and the impounded water in reservoir (Figure 2.4). Concrete in the dam body and the reservoir water were idealized as linear elastic materials whereas the foundation rock and sediments were assumed to be viscoelastic half-space materials.

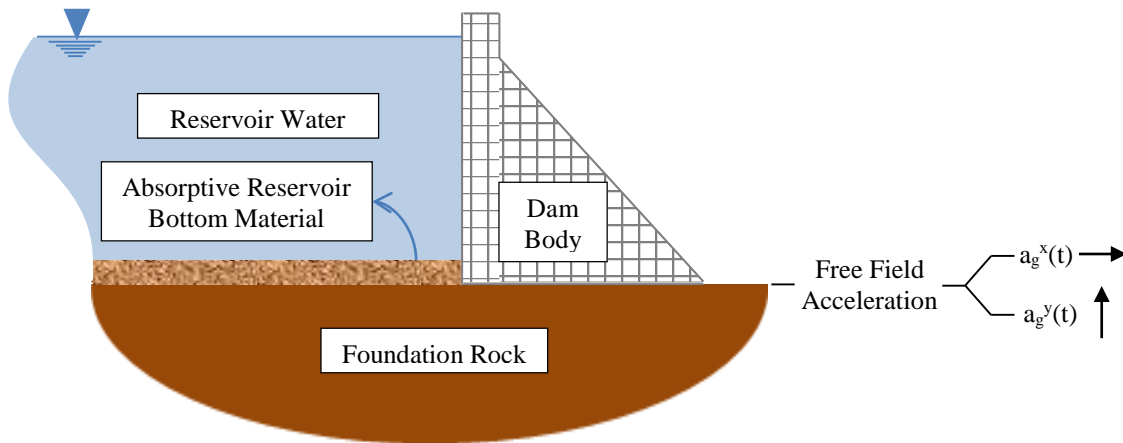


**Figure 2.4.** Idealization of Dam-Foundation-Reservoir System in EAGD  
[Fenves and Chopra 1984.a]

Fenves and Chopra (1984.a) developed a frequency domain hybrid numerical and analytical finite element approach. In their substructure approach, the equation of motion of the dam-reservoir-foundation system is given in Eq. 2.5.

$$\begin{aligned} & \left[ -\omega^2 \begin{bmatrix} \underline{m} & \underline{0} \\ \underline{0} & \underline{m}_b \end{bmatrix} + (1 + i\eta_s) \begin{bmatrix} \underline{k} & \underline{k}_b \\ \underline{k}_b^T & \underline{k}_{bb} \end{bmatrix} + \begin{bmatrix} \underline{0} & \underline{0} \\ \underline{0} & \underline{S}_f(\omega) \end{bmatrix} \right] \begin{Bmatrix} \bar{r}^l(\omega) \\ \bar{r}_b^l(\omega) \end{Bmatrix} \\ & = - \begin{Bmatrix} m \underline{1}^l \\ m_b \underline{1}_b^l \end{Bmatrix} + \begin{Bmatrix} \bar{R}_h^l(\omega) \\ -\underline{S}_{rq} \underline{S}_{qq}^{-1} \bar{Q}_h(\omega) \end{Bmatrix} \end{aligned} \quad (2.5)$$

where  $\omega$  was the excitation frequency,  $m$  and  $m_b$  were mass sub-matrices for the dam and the dam base,  $\eta_s$  was the constant hysteretic damping for the concrete in dam body,  $k$  and  $k_b$  were stiffness sub-matrices for the dam and the dam-foundation rock interface,  $\bar{r}^l(\omega)$  and  $\bar{r}_b^l(\omega)$  were relative displacements for the nodes above the base and at the base, respectively,  $\underline{1}$  was directional unit vector,  $\bar{R}_h^l(\omega)$  was the hydrodynamic forces at the upstream face,  $\bar{Q}_h(\omega)$  was the hydrodynamic forces at the reservoir bottom.  $\underline{S}_{rq}$  and  $\underline{S}_{qq}$  were the sub-matrices in the force-displacement relation of the foundation rock substructure (Eq. 2.6). These terms are also shown in Figure 2.5.

$$\begin{bmatrix} \underline{S}_{rr}(\omega) & \underline{S}_{rq}(\omega) \\ \underline{S}_{rq}^T(\omega) & \underline{S}_{qq}(\omega) \end{bmatrix} \begin{Bmatrix} \bar{r}_f(\omega) \\ \bar{q}(\omega) \end{Bmatrix} = \begin{Bmatrix} \bar{R}_f(\omega) \\ \bar{Q}_h(\omega) \end{Bmatrix} \quad (2.6)$$

$$\underline{S}_f(\omega) = \underline{S}_{rr}(\omega) - \underline{S}_{rq}(\omega) \underline{S}_{qq}^{-1}(\omega) \underline{S}_{rq}^T(\omega) \quad (2.7)$$

and  $\underline{S}_f(\omega)$  was the condensed dynamic stiffness matrix of the foundation (Eq. 2.7). By the equilibrium and compatibility equations at the dam-foundation intersection ( $\bar{R}_b(\omega) + \bar{R}_f(\omega) = 0$ ,  $r_b(\omega) = r_f(\omega)$ ), Eq. 2.8 could be derived to substitute  $\bar{R}_f(\omega)$  in Eq. 2.5.

$$\bar{R}_b^l(\omega) = -\underline{S}_f(\omega) \bar{r}_b^l(\omega) - \underline{S}_{rq}(\omega) \underline{S}_{qq}^{-1}(\omega) \bar{Q}_h(\omega) \quad (2.8)$$

where,  $\bar{R}_b(\omega)$  was the forces on the bottom of dam at dam-foundation intersection,  $\bar{R}_f(\omega)$  was the forces on the surface of the foundation,  $\bar{r}_f(\omega)$  was the relative

displacements for nodes on the surface of foundation,  $\bar{q}(\omega)$  was the relative displacements at the reservoir bottom.

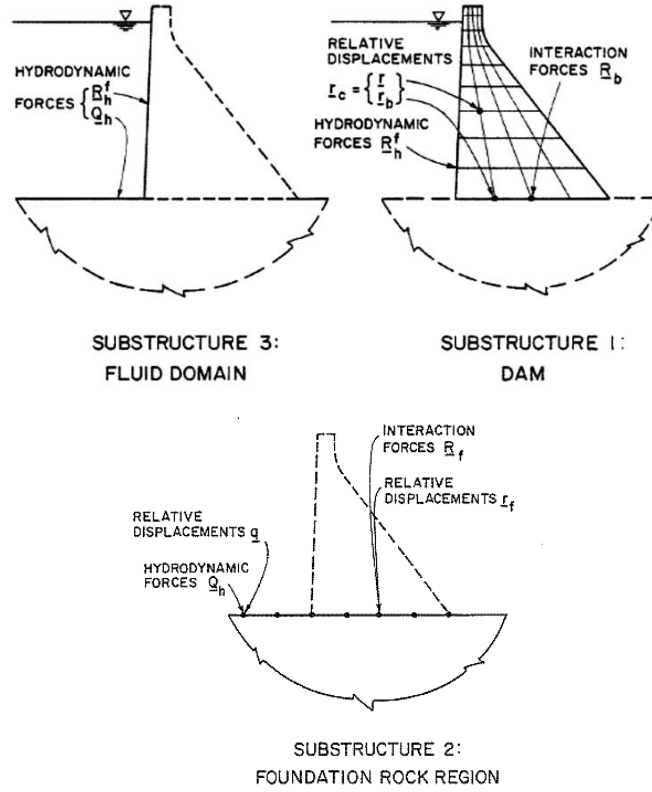


**Figure 2.5.** Substructures Representation of Dam-Reservoir-Foundation System  
[Chopra et al 1980]

The complex valued foundation stiffness matrix  $\underline{S}_f(\omega)$  was obtained by using the numerical method proposed by Dasgupta and Chopra (1979). The bottom absorption was modeled approximately by the modification of the boundary condition at the reservoir bottom. Its effect was included by a wave reflection coefficient ( $\alpha$ ) that represents the ratio of the amplitude of reflected hydrodynamic pressure wave to the amplitude of a vertically propagating pressure wave incident on the reservoir bottom, which depended on the damping coefficient of the reservoir materials, and the velocity of the pressure waves in water.

The hydrodynamic forces  $\bar{R}_h^l(\omega)$  were evaluated by solving the Poisson' problem for an infinite channel and coupled with the upstream face deformation. In the solution, the effect of the surface waves was neglected for the boundary condition of the free surface. The solution included the water compressibility so that the hydrodynamic



response was excitation frequency dependent. Further details of the method can be found in Fenves and Chopra (1984.a).

EAGD is appropriate for analyzing gravity dams with straight and keyed contraction joints, for which the plane stress and the plane strain assumptions are valid, respectively. In EAGD, the dam body is modeled by a finite number of planar four-node elements whose details are given in Taylor et al (1976). Both quadrilateral and triangular elements could be utilized while defining the dam section.

The reservoir water was described by a fluid domain. This domain is assumed to extend to infinity in the upstream direction and to have a constant depth. 2D wave equation is used in the solution phase with default unit mass ( $\gamma=1 \text{ ton/m}^3$ ) and default pressure wave velocity ( $C=1438.7 \text{ m/s}$ ). Consequently, the effect of water compressibility on the response of dam body is considered in the analysis. In addition, the bottom of reservoir should also be horizontal.

The energy absorption due to reservoir bottom materials (sediments) was also included in the analysis as described in Fenves and Chopra (1985.a). A reflection coefficient ( $\alpha$ ) was defined as given in Eq. 2.5. This coefficient provided the rate of reflection:  $\alpha=1$  for full reflection of the pressure waves at the reservoir bottom and  $\alpha=0$  for full absorption of the pressure waves at the reservoir bottom.

The effect of flexible foundation on the response of dam body was also considered by the dynamic stiffness matrix of the foundation rock (Fenves and Chopra 1984.c). For this reason, the frequency dependent compliance functions should be determined for each degree of freedom at the nodes on the flexible foundation boundary for a constant hysteretic damping value. The hysteretic damping for the foundation rock should be determined before the analytical model formation from site tests. The detail for the hysteretic damping determination is summarized in Fenves and Chopra (1984.a).

The energy dissipation was also included in the analysis by constant hysteretic damping ( $\eta_s$ ). For a dam body with empty reservoir lying on a rigid foundation, the

hysteretic damping was twice the viscous damping ratio, which is constant for all natural vibration modes ( $\eta_s=2\xi_s$ ). A constant viscous damping for all modes is possible as EAGD works in frequency domain.

Although EAGD's analytical capabilities are superior to other available general purpose finite element software, EAGD had no graphical user interface or auto mesh options. However, there have recently been some efforts to produce a user-friendly graphical user interface for EAGD (Yucel 2011, Arıcı 2016).

## **2.3 Pseudo Dynamic Testing of a Gravity Dam Monolith**

The rigorous solution presented in this section is assumed to be the exact elastic response for the dam-reservoir-foundation interaction problem. It is used in the next section to calibrate the simplified single-degree-of-freedom model to develop a pseudo-dynamic testing method.

### **2.3.1 Assumptions involved in Testing Procedure**

One of the important steps of this dissertation is to propose a new testing procedure for the seismic performance evaluation of concrete gravity dams by utilizing the pseudo dynamic testing method. For a distributed mass system, like gravity dams, the application of the pseudo dynamic testing procedure is a significant challenge. As explained in the previous subchapters, Fenves and Chopra (1984.b) had proposed two different techniques to analyze a 2D dam-reservoir-foundation system under seismic excitations:

- 1) A simplified single degree of freedom (SDFS) approach (Fenves and Chopra 1985.a and 1985.b) enabling the estimation of the seismic demands on the monolith approximately.
- 2) A rigorous frequency domain semi-analytical numerical procedure codified in the finite element program EAGD (Fenves and Chopra 1984.a),

The SDOF approach is sufficiently accurate in estimating the base shear and overturning moment demands at the dam base and can be used for preliminary design purposes, especially for checking the condition of the base of the dam as given in

Basili and Nuti (2011). Inspired from this idea, a pseudo dynamic testing scheme is formulated for the testing of a scaled dam model using the SDOF approach in this study. For this purpose, the scaled cross-section of a dam is idealized as a distributed stiffness system up to its critical height ( $h_p$ ) where a concentrated mass ( $m$ ) is located as shown in Figure 2.6. With a proper selection of  $m$  and  $h_p$ , earthquake induced stress demands at the base of the dam can match those obtained from a rigorous procedure (Fenves and Chopra 1984.a), hence a SDOF idealization can be shown to be a viable option for conducting pseudo dynamic tests of dam monoliths under seismic loading.

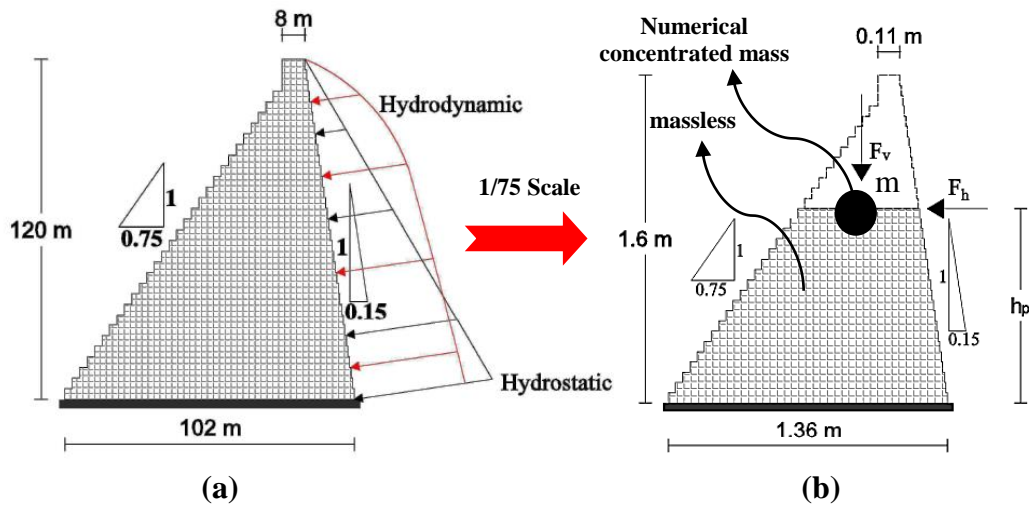


**Figure 2.6.** Models used in Validation of Pseudo Dynamic Tests : (a) Prototype Dam and (b) Scaled Dam Model/Specimen

A 1/75 scaled version of 120 meter-high Melen Dam, built for water supply and energy generation purposes in the North West of Turkey, is utilized for this validation study. This prototype dam is composed of monoliths of 15m width. The geometrical properties of the tallest section of the dam along with the scaled specimen are shown in Figure 2.6.

The spectrum compatible ground motions (Figure 2.7.a) for this project were developed based on the site specific design response spectrum used in the actual design of the dam body (Akkar 2010) for three different seismic hazard levels, namely the Operational Based Earthquake (OBE), the Maximum Design Earthquake (MDE) and the Maximum Characteristic Earthquake (MCE) levels. The peak ground

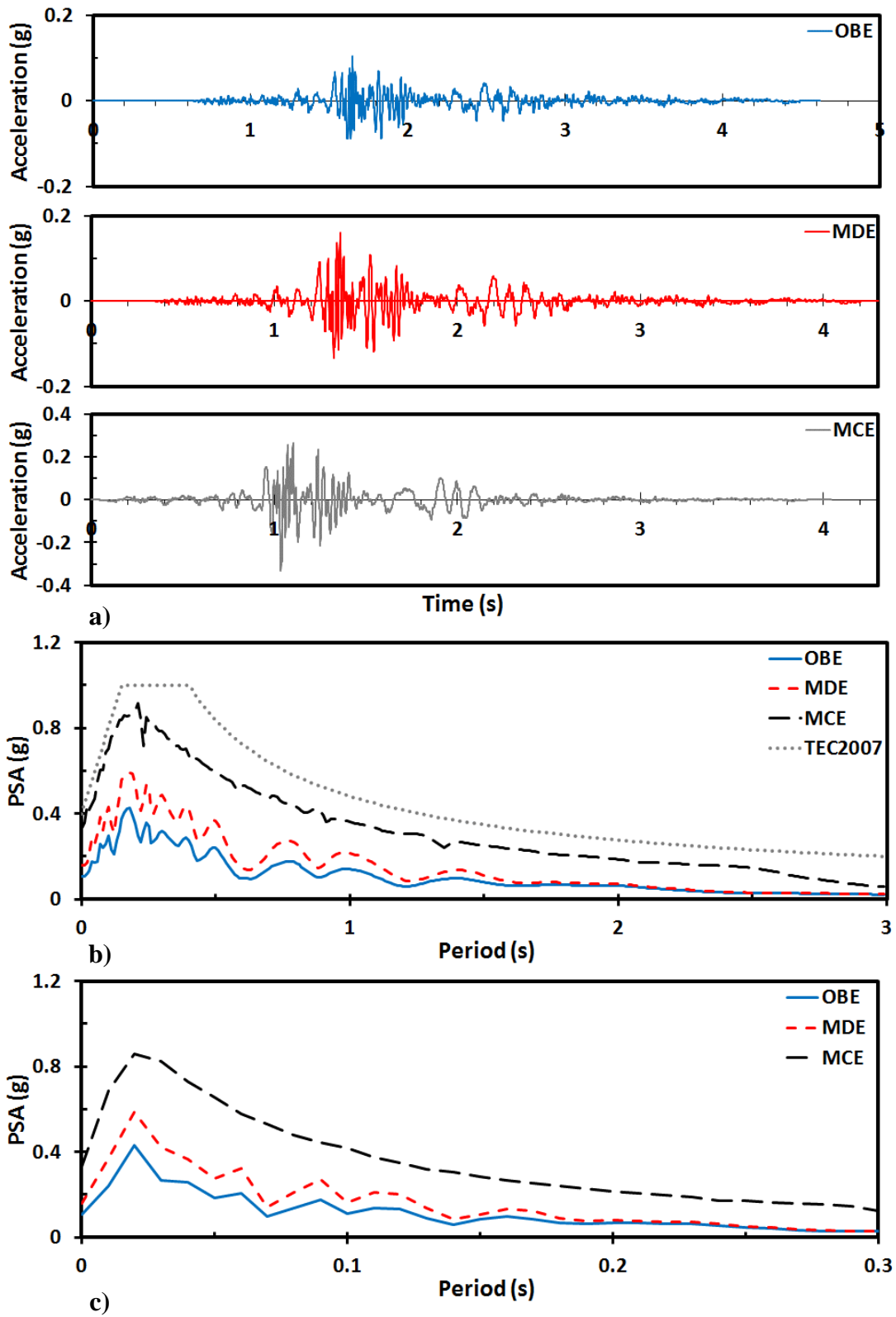


**Figure 2.7.** Seismicity of Prototype Dam : (a) Design Spectrum compatible Synthetic Ground Motions (scaled); (b) Spectra for OBE, MDE and MCE (not time-scaled) and (c) Spectra for OBE, MDE and MCE (time-scaled)

acceleration of the ground motions for the OBE, MDE and MCE levels were 0.11g, 0.16g and 0.33g, respectively. The original time histories were compressed in time by a factor of  $1/\sqrt{75}$  to account for the effects of scaling with respect to similitude law (Bertero et al 1984 and Elkhoraibi and Mosalam 2007). The response spectra of both the unscaled and scaled ground motions are presented in Figure 2.7.b and Figure 2.7.c.

The assumptions for the SDFS pseudo dynamic testing of the scaled dam section are given as follows :

**Assumption 1:** Hydrostatic and inertial forces act at a point located  $h_p$  away from the dam base and the magnitude of the inertial and hydrodynamic forces are dictated by the value of concentrated mass  $m$ .

In order to justify the validity of the first assumption, the value of concentrated (numerical) mass  $m$  and its location  $h_p$  (i.e. the height of the scaled dam) must be determined. To accomplish this task, base shear force ( $V$ ) and overturning moment ( $M$ ) time histories of the prototype dam are obtained from a seismic analysis including dam – reservoir interaction under the effect of different motions. Then, the effective height ( $e$ ) of the prototype dam is calculated from the slope of the  $M$ - $V$  time history (Figure 2.8.a). The height of the scaled dam,  $h_p$ , is calculated multiplying the effective height by the scale factor. It will be shown in Chapter 2.3 that the slope of  $M$ - $V$  diagram is nearly constant throughout the application of ground motion, which proves the applicability of a constant height assumption during an experiment. It should be reminded that the choice of the effective height directly affects the numerical mass value required to match the stress distribution over the dam base in both the scaled dam and prototype dam. In short, the effective height and numerical mass values are meaningful as a couple. Consequently, one could change the effective height and come up with a different numerical mass as long as the stress distributions at the base of both the scaled dam and prototype dam have a good agreement. The numerical mass required for each hazard level is also obtained by comparing  $M$ ,  $V$ , and  $\sigma$  demand histories from the scaled dam model with the ones from the prototype dam model. It is then proved that a SDFS system with a proper numerical mass (to match the fundamental period of the prototype dam) results in an

excellent match in  $M$ ,  $V$  and  $\sigma$  responses. The details for validations are presented in Chapter 2.3.1 – 2.3.3.

**Assumption 2:** The gravity induced vertical stresses at the base of the dam can be simulated by applying an axial force at a height sufficiently away from the dam base on the scaled dam.

The accuracy of the second assumption is investigated by comparing the results of two different static (linear elastic) analyses. Base stresses obtained from the elastic stress analysis of the prototype dam model (unscaled, Figure 2.6.a) subjected to gravity and hydrostatic loads are compared to their counterparts obtained from scaled dam model (Figure 2.6.b) loaded at a height of  $h_p$  from the base with a lateral ( $F_h$ ) and vertical force ( $F_v$ ). For the given hydrostatic force ( $F_h$ ), the vertical force ( $F_v$ ) was selected to match the base stress profile between the two models by using a trial and error procedure. The selected  $F_h$  and  $F_v$  are found as 174kN and 400kN. The agreement of the base stresses is excellent as shown in Figure 2.8.b, enabling the use of point loads for the simulation of the hydrostatic and gravity loads. Such a close match in the base stress estimations is parallel with the results of the SDFS approximation of the dam-reservoir system as given by Fenves and Chopra (1984.b). Their studies have shown that upon the representation of the fundamental frequency and the damping characteristics of a dam-reservoir system with a SDFS oscillator, one can have a tool capable of estimating the earthquake induced demands (base shear force, overturning moment and base vertical stresses even by employing Euler Bernoulli beam theory) with a reasonable accuracy.

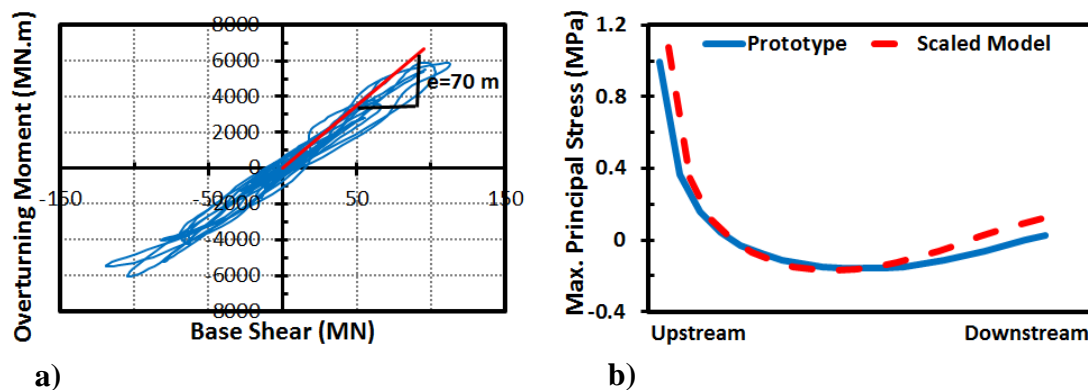


**Figure 2.8.** Analytical Results : (a) Determination of Effective Height from the Prototype Dam and (b) Comparison of Maximum Principal Stresses from Static Loading Effects

**Assumption 3:** Values of  $m$  and  $h_p$  do not change with earthquake induced damage during the period of the ground motion.

The third assumption can be validated by observing the change of the fundamental period of the system during each test. Hui (1992) claimed that the base cracks do not change the fundamental period of the system drastically. Given that the period change during seismic action is limited, the hydrodynamic and inertial forces can be estimated with SDFS model with fixed  $m$  and  $h_p$  as shown in Figure 2.14. In addition, this assumption is also be validated with the identified periods during each experiment presented in Chapter 5.

**Assumption 4:** Dynamic strength enhancement of concrete is indirectly considered.

The fourth assumption is related to the material properties of the specimen and the dynamic nature of the loading. The strength increase of concrete as a result of rapid loading cannot be obtained during the pseudo dynamic test due to the slow nature of this testing procedure. However, the concrete strength was adjusted such that the static tensile strength of the scaled model matches the dynamic tensile strength of the actual dam section under high loading rates. In the scaling process of the test specimen, the stress and strain values are scale independent whereas the fracture energy of the concrete was scaled by the reciprocal of the scale, i.e.  $1/75$  (Uchita et al 2005). Therefore, the fracture process zone of the concrete should be reduced to decrease the fracture energy (Saouma et al 1991 and Uchita et al 2005). To accomplish this, the aggregate sizing was also reduced by the scale factor during the concrete manufacturing process as discussed in Chapter 3.

**Assumption 5:** Uplift pressures are not considered before, during and after seismic excitations.

As explained in Chapter 1, Javanmardi et al (2005) showed that the effect of uplift pressures during dynamic loading could be neglected due to the small saturation lengths during crack opening period. The other argument might be the fact that the

foundation soil of the dam body usually jet-grouted before construction, preventing the minor crack formations in the foundation rock. In addition, the application of drainage systems beneath the dam body would apparently reduce the uplift forces.

**Assumption 6:** The presence of water penetrating into the cracks and the influence of water in the cracks reducing the friction coefficient is neglected.

This assumption was also verified by Javanmardi et al (2005) by conducting water flow and water penetration experiments on concrete specimens. They determined the saturation length of cracks and concluded that only a small portion of a crack zone was saturated during dynamic loading. Therefore, this amount of penetrated water has negligible influence on the behavior of the crack zone, including the reduction in friction.

**Assumption 7:** Cracking is assumed to take place within the lower 6/10<sup>th</sup> of the dam model. Cracking above this region is assumed to be negligible.

The last assumption could be justified by investigating the work by Soysal et al (2016). Soysal et al (2016) presented estimated crack propagations on a dam body by performing incremental dynamic analysis by utilizing a fix-based finite element model. In the models, the hydrodynamic effects were also considered by utilizing compressible fluid elements and absorptive boundary elements. They showed that PGA levels of around 0.35g, which corresponds to PGA level of MCE scenario, caused cracks, mostly, at the base of the dam sections or some body cracks within 60% of the dam height.

### **2.3.2 The Outline of the Testing Procedure**

The procedure used in determining the necessary parameters, i.e.  $m$ ,  $h_p$ ,  $F_v$  and  $F_h$  (Figure 2.9) is outlined as follows:

- 1) Conduct rigorous seismic elastic stress analysis of prototype dam model including dam reservoir interaction, as presented in Section 2.2, and obtain



the fundamental frequency ( $T_1^s$ ), base shear force ( $V$ ) and the overturning moment ( $M$ ) time histories (Figure 2.8.b),

- 2) Determine the effective height ( $e$ ) from the slope of overturning moment-shear force response. This height is then multiplied by the scale factor to obtain the height of the scaled dam,  $h_p$ .
- 3) Build the laboratory specimen with the scaled dimensions and effective height and conduct an initial loading test (vertical load that simulates gravity loads and a small lateral force) to obtain the actual stiffness of the specimen (considering any unintended base flexibility of the setup),
- 4) Calibrate the finite element scaled dam model (SDFS) to match the stiffness of the test specimen by selecting the appropriate modulus of elasticity,
- 5) Determine the numerical mass  $m$  such that the fundamental period of the prototype dam with reservoir (from EAGD in this study) matches the fundamental period of the scaled dam model times the square root of the scale factor with a certain tolerance ( $\pm 5\%$  in this study),
- 6) Conduct dynamic analysis on the scaled model from Step 4 with concentrated mass from Step 5. Compare the demand parameters (overturning moment, base shear force and toe vertical stress time histories) with the results from Step 1 (prototype dam) considering appropriate scale factors. Check the errors on the maximum and minimum of these quantities,
- 7) If the errors of the maximum demand parameters are more than a specified tolerance ( $\pm 20\%$  in this study), adjust  $m$  and go to Step 5.
- 8) Determine the vertical force  $F_v$  acting on the scaled model that results in similar base stresses to the hydrostatic plus gravity induced base stresses of the prototype model. Apply the static lateral force as the hydrostatic force.
- 9) Conduct the ground motion test with the selected mass  $m$ . Identify the dynamic properties of the tested dam. Determine the effective elongated fundamental period of the specimen due to possible cracking.
- 10) Go to step 1 and redo all steps for the next ground motion.

The procedure outlined above mainly relies on two key calibrations:

- i. Matching the overturning moment and base shear from the action of a single piston located at an effective height with the base moment on the prototype model,
- ii. Matching the fundamental period of the prototype dam with the fundamental period of the scaled dam model.

Hence, it is very similar to the simplified single degree of freedom approach of Fenves and Chopra (1984.b). The main difference from that approach is the use of EAGD instead of simplified formulas for the determination of effective mass and height so that ground motion dependency on stresses, moment or shear force are better considered. For the benefit of a better match of the stresses (or moments and shear forces), the procedure allows for a fine tuning of the numerical mass if needed, sacrificing from the exact match of the fundamental period.

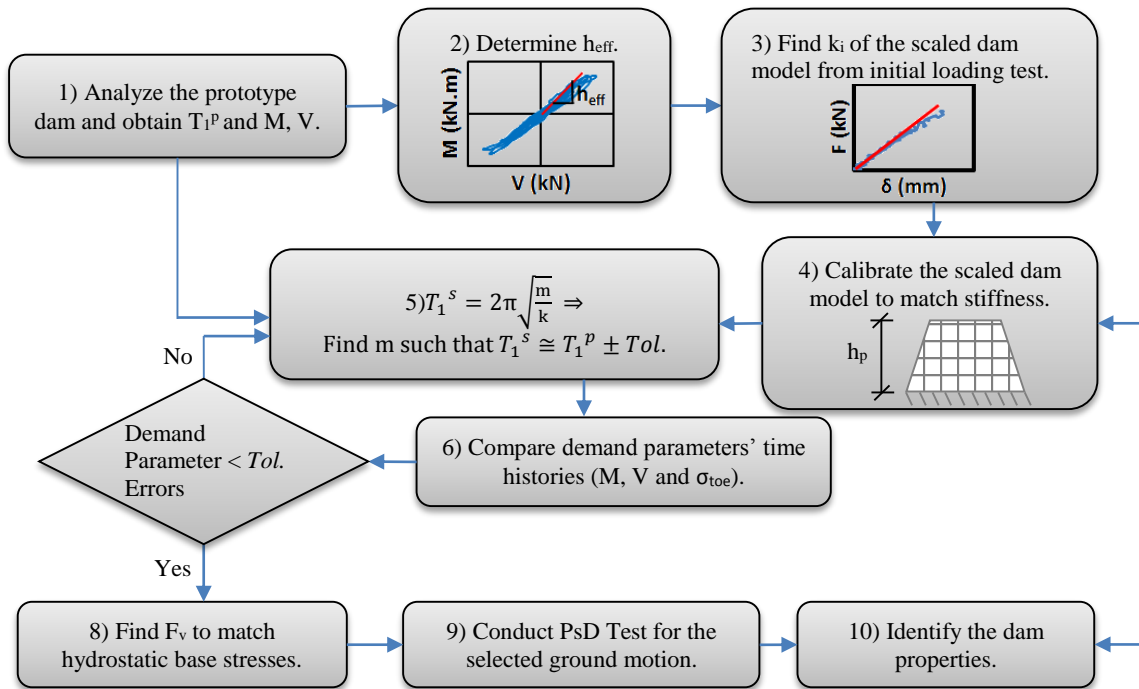


**Figure 2.9.** Flowchart Explaining the Testing Procedure

In the following sections, the above procedure is implemented for the three different test specimens, whose details are explained in Chapter 4:

- Specimen 1: Conventionally vibrated concrete (CVC) with uniaxial compressive strength of 25 MPa on the day of testing.

- Specimen 2: Roller compacted concrete (RCC) with uniaxial compressive strength of 15 MPa on the day of testing.
- Specimen 3: Roller compacted concrete (RCC) with uniaxial compressive strength of 25 MPa on the day of testing.

### 2.3.2.1 Specimen 1: CVC Gravity Dam

The summary of the parameters given in the above procedure (Figure 2.9) for the CVC gravity dam specimen with 25 MPa are presented in this section for the OBE, MDE and MCE motions are summarized herein. In the following figures, the terms “Prototype” and “Scaled” are used to refer the analysis performed in EAGD (numerical model for unscaled dam) and ANSYS (numerical model for the scaled single mass distributed stiffness model presented in Figure 2.6).

**Step 1-2:** First, the effective height of the prototype dam was found as 70 m from the slope of  $M - V$  response of the prototype dam (Figure 2.11). Therefore, the height of the specimen ( $h_p$ ) was calculated as 0.95 m.

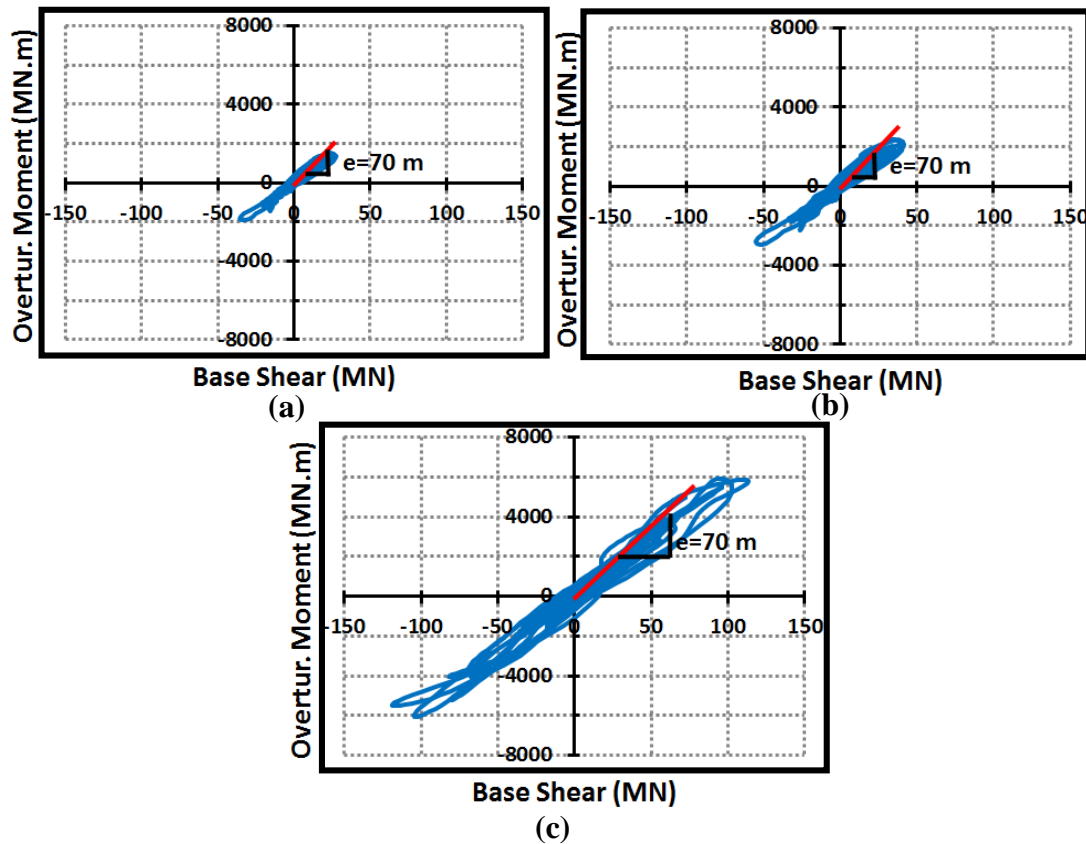


**Figure 2.10.** Determination of Effective Height for Specimen 1 : (a) OBE, (b) MDE and (c) MCE motions

**Step 3:** The initial loading test on the scaled CVC dam specimen gave a lateral stiffness of 595 kN/mm (Figure 2.11).

**Step 4-5:** The modulus of elasticity of the scaled dam model was selected as 13,850 MPa to obtain the same stiffness as the scaled dam specimen (Figure 2.11). The fundamental period of the prototype dam with full reservoir ( $T_1^P$ ) was calculated as 0.43 sec. For the scaled dam, this corresponded to a fundamental period ( $T_1^S$ ) of about 0.05 sec found by dividing  $T_1^P$  by the square root of the scale factor. Therefore, the first trial on the numerical mass was calculated as 37.5 ton.

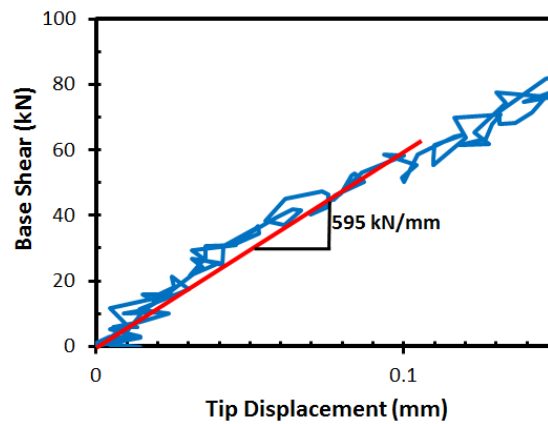


**Figure 2.11.** Preliminary Test for Lateral Stiffness Determination of Specimen 1

**Step 6:** The numerical mass ( $m$ ) calculated at Step 5 may not guarantee that  $M$ ,  $V$  and the stress time histories of the specimen are estimated perfectly. There may be a numerical mass that produces better internal force and base stress history estimations. At this stage, SDFS models with different masses were analyzed to investigate the best match for each hazard level. The analysis results for different numerical masses can be found in Appendix B. Comparisons of analysis results for the base shear, overturning moment and toe vertical stress time series between the full scale dam (prototype dam) and the scaled dam model for OBE, MDE and MCE motions are presented in Figure 2.12 - Figure 2.14. Those figures correspond to the best match cases for each hazard level. In those figures, SDFS system results are named as “Scaled” and the scaled EAGD overturning and base shear and unscaled EAGD stress results are represented as “Prototype”. It could be concluded from Figure 2.12 - Figure 2.14 that the agreement between the analysis results with rigorous consideration of dam reservoir interaction (prototype dam) and the scaled dam model with concentrated mass was excellent. The errors in the fundamental period, the maximum and the minimum base shear force, the overturning moment

and the vertical stresses at the toe were presented in Table 2.2 – Table 2.4 for varying values of numerical masses. The numerical mass that provided the best match for the fundamental period turned out to be a reasonable match for the other demand parameters for OBE and MDE motions (errors being less than 20% for vertical stress). For the MCE motion, the numerical mass was selected such that none of the considered maximum demand parameters had an error larger than 20% with a 3% error in the fundamental frequency. In all of the analysis, the damping was assumed to be 5%.

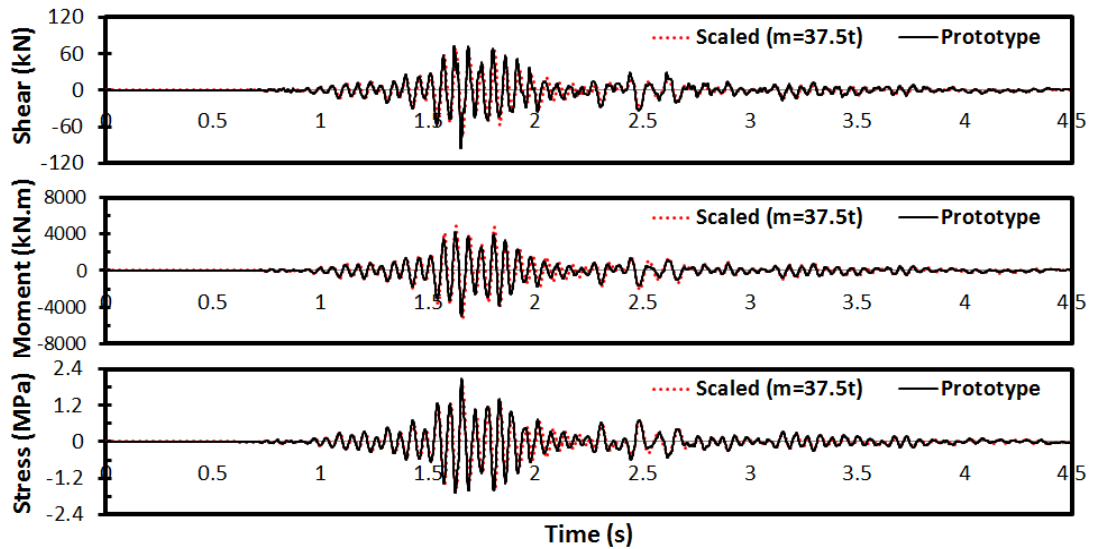


**Figure 2.12.** Comparison of the Analysis Results of Specimen 1 for the OBE ground motion: (a) Base Shear, (b) Overturning Moment and (c) Vertical Stress

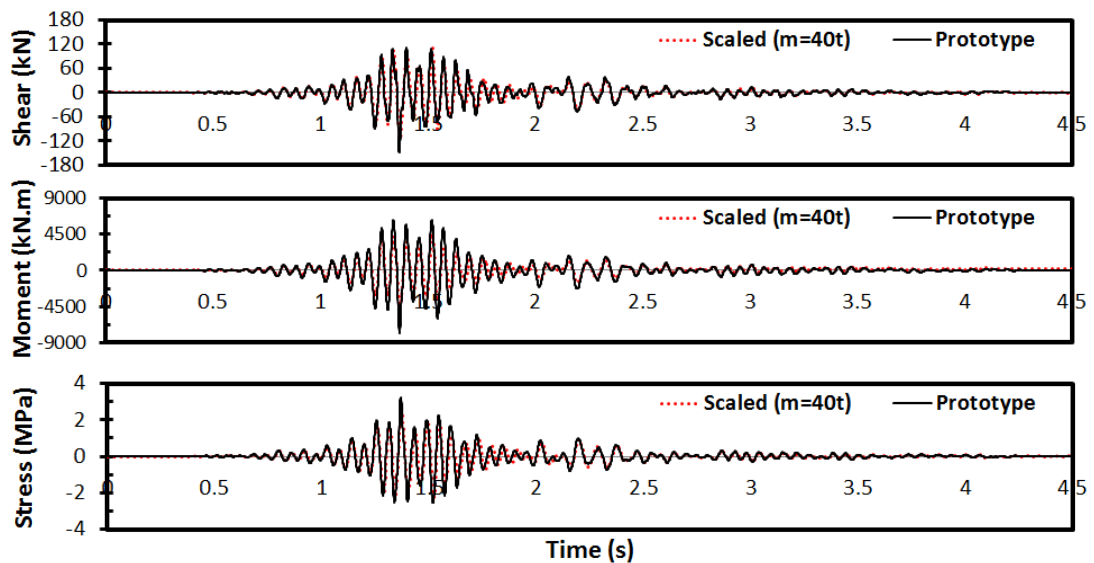


**Figure 2.13.** Comparison of the Analysis Results of Specimen 1 for the MDE ground motion: (a) Base Shear, (b) Overturning Moment and (c) Vertical Stress

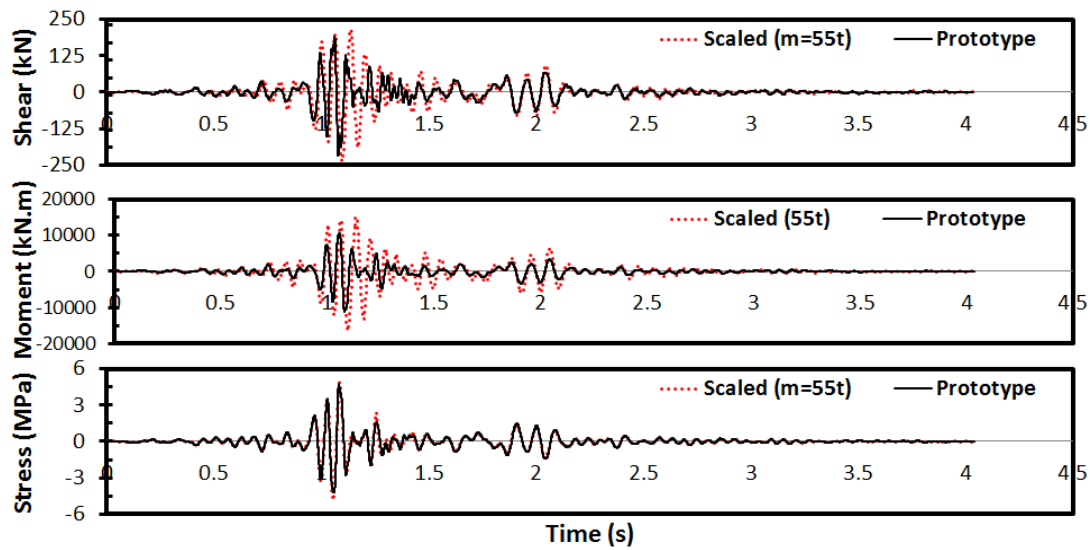


**Figure 2.14.** Comparison of the Analysis Results of Specimen 1 for the MCE ground motion: (a) Base Shear, (b) Overturning Moment and (c) Vertical Stress

**Table 2.2.** Comparisons of the Errors in the Response Quantities for Scaled Dam Models of Specimen 1 with Different Mass  $m$  for OBE motion

	<i>Percentage Errors Values with respect to Prototype Dam (%)</i>						
<b>m (ton)</b>	<b>f</b>	<b>V<sub>max</sub></b>	<b>V<sub>min</sub></b>	<b>M<sub>max</sub></b>	<b>M<sub>min</sub></b>	<b>σ<sub>y,max</sub></b>	<b>σ<sub>y,min</sub></b>
<b>20</b>	37.7	-23.8	-44.3	-6.0	-25.5	-39.1	-20.4
<b>30</b>	12.5	-16.8	-34.0	2.7	-11.8	-28.1	-13.0
<b>35</b>	4.2	<b>3.5</b>	<b>-14.9</b>	27.9	14.1	<b>-7.0</b>	8.7
<b>37.5</b>	<b>0.6*</b>	-5.7	-21.2	16.5	<b>5.6</b>	-14.0	<b>-1.1</b>
<b>40</b>	-2.6	-18.5	-30.8	<b>0.7</b>	-7.3	-24.4	-14.5
<b>45</b>	-8.1	-31.5	-47.2	-15.3	-29.6	-42.5	-28.1
<b>55</b>	-16.9	-30.8	-47.2	-14.6	-30.8	-43.5	-27.5

\*The minimum error within a column is shown in ***bold italics***.

**Table 2.3.** Comparisons of the Errors in the Response Quantities for Scaled Dam Models of Specimen 1 with Different Mass  $m$  for MDE motion

	<i>Percentage Errors Values with respect to Prototype Dam (%)</i>						
<b>m (ton)</b>	<b>f</b>	<b>V<sub>max</sub></b>	<b>V<sub>min</sub></b>	<b>M<sub>max</sub></b>	<b>M<sub>min</sub></b>	<b>σ<sub>y,max</sub></b>	<b>σ<sub>y,min</sub></b>
<b>30</b>	9.1	-18.7	-34.3	-40.3	-50.9	-32.7	-20.0
<b>37.5</b>	<b>-2.6*</b>	-16.0	-30.2	-38.1	-47.6	-28.3	-17.3
<b>40</b>	-5.6	<b>-1.8</b>	<b>-21.2</b>	<b>-27.8</b>	<b>-40.7</b>	<b>-19.1</b>	<b>-3.3</b>
<b>50</b>	-15.8	-36.7	-56.8	-53.2	-68.0	-55.6	-37.5

\*The minimum error within a column is shown in ***bold italics***.

**Table 2.4.** Comparisons of the Errors in the Response Quantities for Scaled Dam Models of Specimen 1 with Different Mass  $m$  for MCE motion

	<i>Percentage Errors Values with respect to Prototype Dam (%)</i>						
<b>m (ton)</b>	<b>f</b>	<b>V<sub>max</sub></b>	<b>V<sub>min</sub></b>	<b>M<sub>max</sub></b>	<b>M<sub>min</sub></b>	<b><math>\sigma_{y,max}</math></b>	<b><math>\sigma_{y,min}</math></b>
<b>45</b>	5.4	-13.2	-22.1	<b>6.2</b>	<b>6.9</b>	17.5	23.3
<b>55</b>	<b>-1.5*</b>	<b>-6.7</b>	-11.6	14.1	21.1	<b>3.7</b>	<b>14.7</b>
<b>65</b>	-3.0	20.8	<b>-6.8</b>	48.0	27.9	24.1	59.9
<b>75</b>	-4.6	41.3	-223.2	-99.6	-99.6	71.3	87.1

\*The minimum error within a column is shown in **bold italics**.

**Step 7:** The numerical masses that result in minimum percentage error in  $M$ ,  $V$  and  $\sigma_{toe}$  for OBE, MDE and MCE motions were found to be 37.5 t, 40 t and 55 t, respectively.

**Step 8:** The vertical external force ( $F_v$ ) to produce base stress distribution equal to the one in the prototype is readily calculated in a trial and error procedure as 400 kN (Figure 2.8).

**Step 9-10:** The pseudo dynamic test of this specimen was performed and its detailed results are presented in Chapter 5.

### 2.3.2.2 Specimen 2: RCC Gravity Dam 1

The parameters given in the testing procedure (Figure 2.9) for the RCC gravity dam specimen with  $f_c=15$  MPa are summarized in this section. The prototype dam for Specimen 2 had a uniaxial compressive strength of 15 MPa.

**Step 1-2:** The effective height of the prototype dam was also found as 70 m from the slope of  $M - V$  response of the prototype dam (Figure 2.15). Therefore, the height of the specimen ( $h_p$ ) was calculated as 0.95 m.

**Step 3:** The initial loading test on the scaled dam specimen gave a lateral stiffness of 438 kN/mm (Figure 2.16).

**Step 4-5:** The fundamental period of the prototype dam with full reservoir ( $T_1^P$ ) was calculated as 0.49 sec, corresponding to a fundamental period ( $T_1^S$ ) of about 0.06sec for the scaled dam. Consequently, the required numerical mass of the scaled specimen was calculated as 37.5 tons. This mass was considered as an initial guess in the trial and error process.

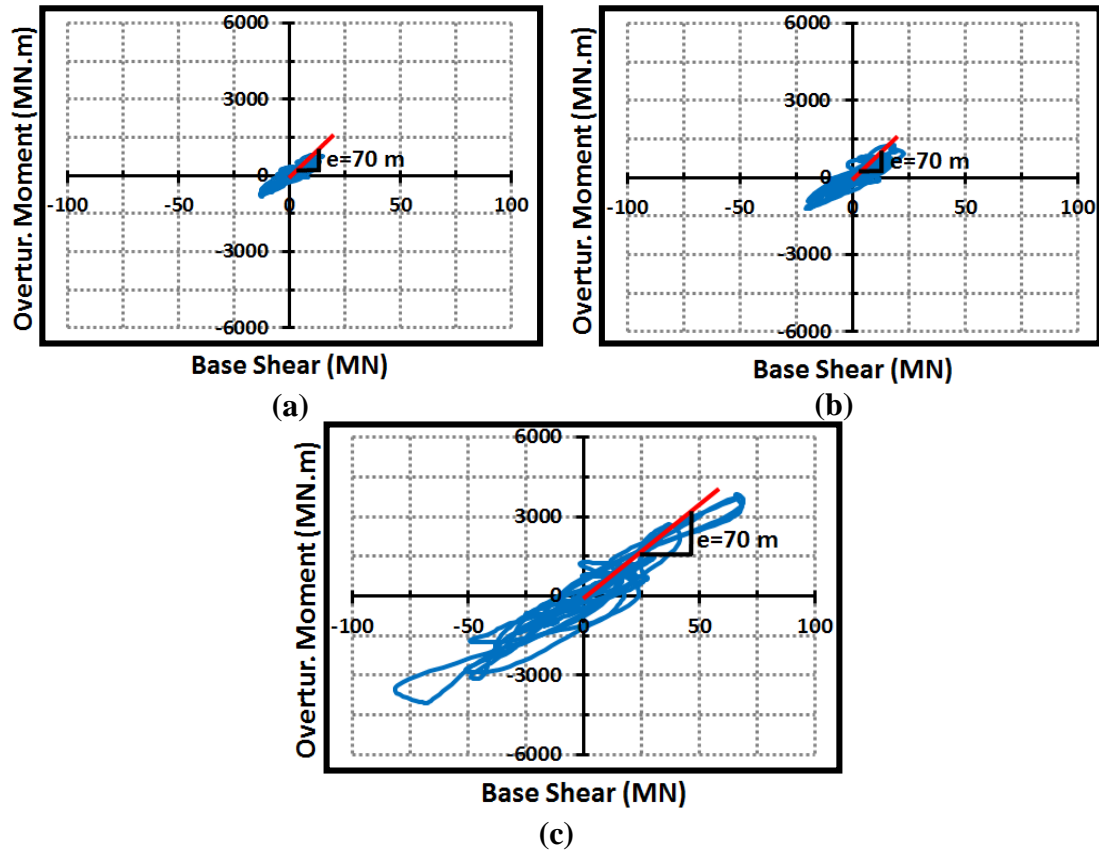


**Figure 2.15.** Determination of Effective Height for Specimen 2: (a) OBE, (b) MDE and (c) MCE motions

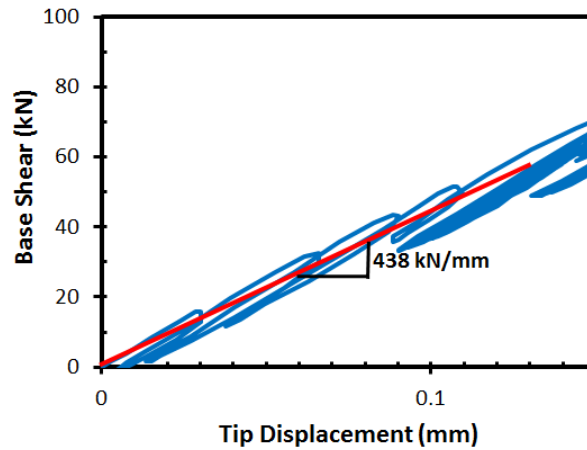


**Figure 2.16.** Preliminary Test for Lateral Stiffness Determination of Specimen 2

**Step 6:** For Specimen 2, the comparison of base shear, overturning moment and toe vertical stress time series between the full scale dam (prototype dam) and the scaled dam model (SDFS) for OBE, MDE and MCE motions are presented in Figure 2.17- Figure 2.19. Comparisons of analysis results for those figures corresponded to the best match cases for each hazard level. The estimations for different numerical mass



values can be found in Appendix C. It can be concluded from Figure 2.17 – Figure 2.19 that the agreement between the analysis results with rigorous consideration of dam reservoir interaction (prototype dam) and the scaled dam model with concentrated mass was promising. The errors in the fundamental period, the maximum and the minimum base shear force, the overturning moment and the vertical stresses at the toe are presented in Table 2.5 – Table 2.7 for varying values of numerical masses. For Specimen 2, the numerical masses causing the best fundamental period estimate for all hazard levels (at most 2%) also resulted in an error less than 30% on the vertical stress histories.

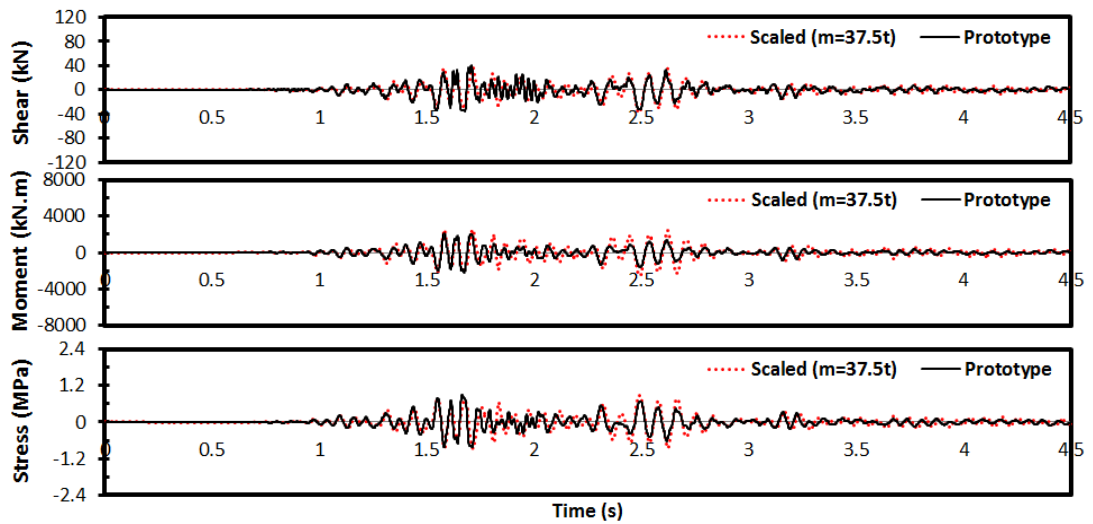


**Figure 2.17.** Comparison of the Analysis Results of Specimen 2 for the OBE ground motion: (a) Base Shear, (b) Overturning Moment and (c) Vertical Stress

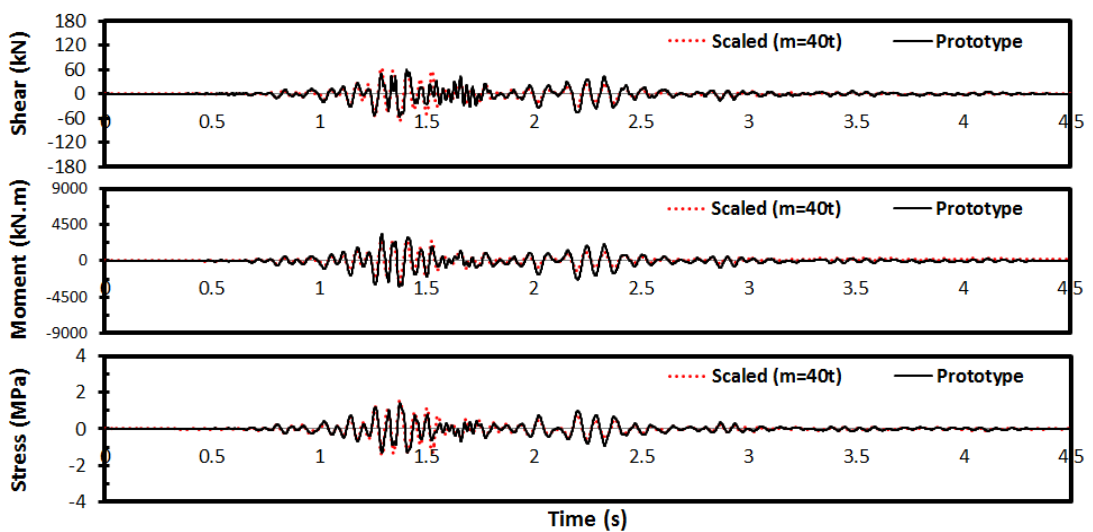


**Figure 2.18.** Comparison of the Analysis Results of Specimen 2 for the MDE ground motion: (a) Base Shear, (b) Overturning Moment and (c) Vertical Stress

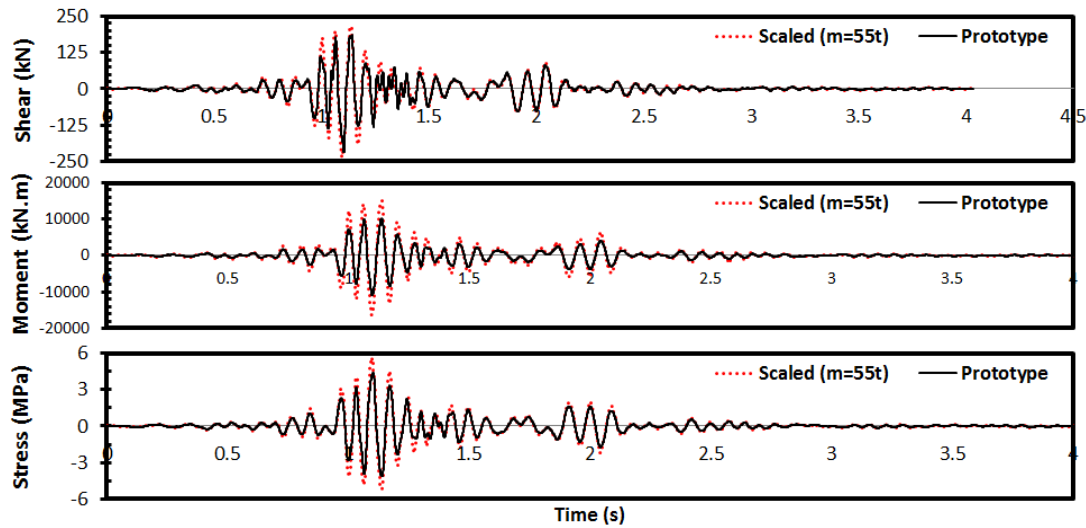


**Figure 2.19.** Comparison of the Analysis Results of Specimen 2 for the MCE ground motion: (a) Base Shear, (b) Overturning Moment and (c) Vertical Stress

**Table 2.5.** Comparisons of the Errors in the Response Quantities for Scaled Dam Models of Specimen 2 with Different Mass  $m$  for OBE motion

	<i>Percentage Errors Values with respect to Prototype Dam (%)</i>						
<b>m (ton)</b>	<b>f</b>	<b>V<sub>max</sub></b>	<b>V<sub>min</sub></b>	<b>M<sub>max</sub></b>	<b>M<sub>min</sub></b>	<b>σ<sub>y,max</sub></b>	<b>σ<sub>y,min</sub></b>
<b>20</b>	36.9	-8.2	8.3	22.9	17.7	17.4	14.7
<b>30</b>	11.7	<b>-2.7</b>	25.5	30.7	37.0	17.4	14.7
<b>35</b>	3.5	-17.2	-5.7	<b>10.7</b>	2.8	-11.8	-2.9
<b>37.5</b>	<b>0.0*</b>	-12.3	-8.1	17.6	<b>0.4</b>	<b>-1.6</b>	<b>5.8</b>
<b>40</b>	-3.2	-10.2	<b>5.2</b>	20.6	14.7	-13.9	3.2
<b>45</b>	-8.7	29.9	45.6	74.1	58.9	36.4	52.7
<b>50</b>	-13.4	78.2	113.4	138.8	133.1	99.9	109.3

\*The minimum error within a column is shown in **bold italics**.

**Table 2.6.** Comparisons of the Errors in the Response Quantities for Scaled Dam Models of Specimen 2 with Different Mass  $m$  for MDE motion

	<i>Percentage Errors Values with respect to Prototype Dam (%)</i>						
<b>m (ton)</b>	<b>f</b>	<b>V<sub>max</sub></b>	<b>V<sub>min</sub></b>	<b>M<sub>max</sub></b>	<b>M<sub>min</sub></b>	<b>σ<sub>y,max</sub></b>	<b>σ<sub>y,min</sub></b>
<b>30</b>	9.5	1.6	21.8	<b>-24.0</b>	<b>-18.0</b>	-15.8	-7.6
<b>37.5</b>	<b>-2.1*</b>	-16.4	-19.8	-37.0	-47.0	-28.8	-12.9
<b>40</b>	-5.2	<b>-11.2</b>	<b>-5.3</b>	-31.9	-38.3	<b>8.5</b>	<b>5.8</b>
<b>50</b>	-15.2	81.6	107.1	35.6	39.0	84.1	89.0

\*The minimum error within a column is shown in **bold italics**.

**Table 2.7.** Comparisons of the Errors in the Response Quantities for Scaled Dam Models of Specimen 2 with Different Mass  $m$  for MCE motion

	<i>Percentage Errors Values with respect to Prototype Dam (%)</i>						
<b>m (ton)</b>	<b>f</b>	<b>V<sub>max</sub></b>	<b>V<sub>min</sub></b>	<b>M<sub>max</sub></b>	<b>M<sub>min</sub></b>	<b><math>\sigma_{y,max}</math></b>	<b><math>\sigma_{y,min}</math></b>
<b>45</b>	9.1	27.8	14.4	60.6	60.2	36.7	36.1
<b>55</b>	<b>-1.3*</b>	<b>16.9</b>	<b>7.4</b>	<b>46.8</b>	<b>50.4</b>	<b>28.3</b>	<b>24.4</b>
<b>65</b>	-9.2	45.4	24.2	82.8	73.9	48.4	54.8
<b>75</b>	-15.5	65.6	42.7	108.1	99.9	70.6	76.3

\*The minimum error within a column is shown in **bold italics**.

**Step 7:** The numerical masses that result in minimum percentage error in  $M$ ,  $V$  and  $\sigma_{toe}$  for OBE, MDE and MCE motions are found to be  $m=37.5$  t, 40 t and 55 t, respectively.

**Step 8:** The vertical external force ( $F_v$ ) to produce base stress distribution equal to the one in the prototype is readily calculated in a trial and error procedure as 400kN (Figure 2.8).

**Step 9-10:** The pseudo dynamic test of this specimen is performed and its detailed results are presented in Chapter 5.

### 2.3.2.3 Specimen 3: RCC Gravity Dam 2

The parameters for the RCC gravity dam with  $f_c=25$  MPa are presented in this part. The prototype dam for Specimen 3 is also assumed to have the same compressive strength. Therefore, the analyses of the prototype dam are exactly the same as the CVC gravity dam. The application of the aforementioned procedure for the OBE, MDE and MCE motions are summarized herein.

**Step 1-2:** The effective height of the prototype dam was found as 70 m, being analogous to Specimen 1. Thus, the height of the specimen ( $h_p$ ) is calculated as 0.95 m.

**Step 3:** The initial loading test on the scaled CVC dam specimen gave a lateral stiffness of 615 kN/mm (Figure 2.20). This initial stiffness is also very close to the one obtained for Specimen 1 (595 kN/mm). Accordingly, the stiffness of Specimen 3 is very similar to the stiffness of Specimen 1 (CVC gravity dam specimen), along with the same prototype properties. Consequently, the following steps (Step 4 – 10) will not be performed again for RCC gravity dam 2. Therefore, the numerical masses

of 37.5 t, 40 t and 55 t for OBE, MDE and MCE motions, respectively, are assumed to bring about minimum percentage errors in  $M$ ,  $V$  and  $\sigma_{toe}$  for the specimen in concern.

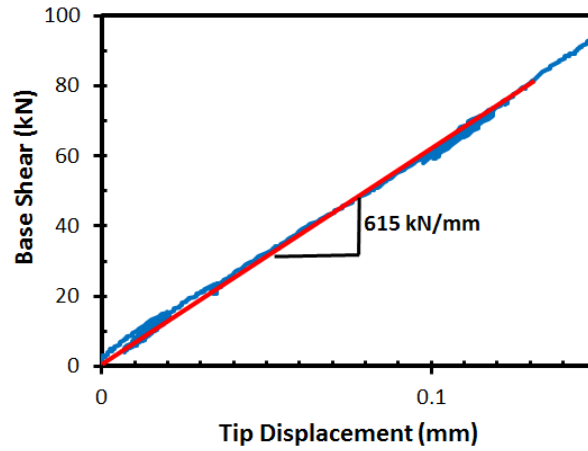


**Figure 2.20.** Preliminary Test for Lateral Stiffness Determination

It can be observed that due to the difference in the initial stiffness of specimens similar numerical mass values were found to be valid for testing. It should be noted that this situation may not be valid for different test campaigns.

### 2.3.3 Concluding Remarks

The capability of a distributed stiffness and concentrated mass system (SDFS) to capture the behavior of a distributed mass and stiffness system (EAGD or prototype) was investigated in this section. The demand parameters like stresses at the base of the dam, the overturning moments, the base shears as well as the fundamental periods were compared. The results were promising as both the magnitude and frequency contents of each demand parameter could be captured well for each hazard level. It should be noted that these results are valid for elastic analysis. The validity of the method should be re-investigated during the experiment by analyzing the change in the fundamental period during the experiment. In Chapter 5, this issue will be discussed by referring to the identification results of each specimen. It will be presented that the fundamental period changes of each specimen under the effect of earthquakes of different hazard levels were very limited, which implies that the stiffness of the system remains nearly unchanged.

## **CHAPTER 3**

### **MATERIALS**

This chapter describes the materials utilized throughout the experimental program and the effect of scaling on the material response. The results of this chapter demonstrate the applicability of using scaled aggregate materials to represent the unscaled properties.

#### **3.1 Aggregates and Sieve Analysis Results**

Five different batches of aggregates commonly used in practice were supplied (Figure 3.1) and the mixture ratios for different concrete types (i.e. conventionally vibrated concrete (CVC) and roller compacted concrete (RCC)) were determined. First, the maximum aggregate sizes (MAS) were selected for each concrete type. For convenience as well as representing the current business practice, MAS were selected as 30 mm and 50 mm for full-scale CVC and RCC, respectively. On the other hand, for the 1/75 scaled concrete mixture, MAS was scaled by selecting it as 3 mm to reduce the fracture process zone as suggested by Saouma et al (1991). Specimens with scaled and unscaled aggregate sizes were prepared and tested to investigate the effect of scaling on the mechanical properties.

The physical tests, namely sieve analysis, unit weights and water absorption capacity, for the coarse and fine aggregates were carried out by following the recommendations of ASTM C 127-12 and 128-12, respectively. The aforementioned properties of each aggregate batch are presented in the following subsections.

##### **3.1.1 Sieve Analysis Results**

For each aggregate batch, sieve analyses were performed at Materials of Construction Laboratory of Middle East Technical University. The gradation curves of each aggregate batch are presented in Figure 3.2. By utilizing the obtained gradation curves, the ratios of aggregate batches in each concrete type were calculated in order to maximize the density of the mixture. In other words, the

available batches were mixed so that the void amounts between the particles were reduced. To accomplish this goal, the gradation curve of aggregate mixture was arranged to approach the Fuller's Curve given in Eq. 3.1 (Fuller and Thompson 1907). In Eq. 3.1,  $d_i$  represents opening size of  $i^{\text{th}}$  sieve,  $D_{\text{max}}$  is MAS and  $p_i$  is the percentage passing  $i^{\text{th}}$  sieve.

$$p_i = \left( \frac{d_i}{D_{\text{max}}} \right)^{0.5} \quad (3.1)$$

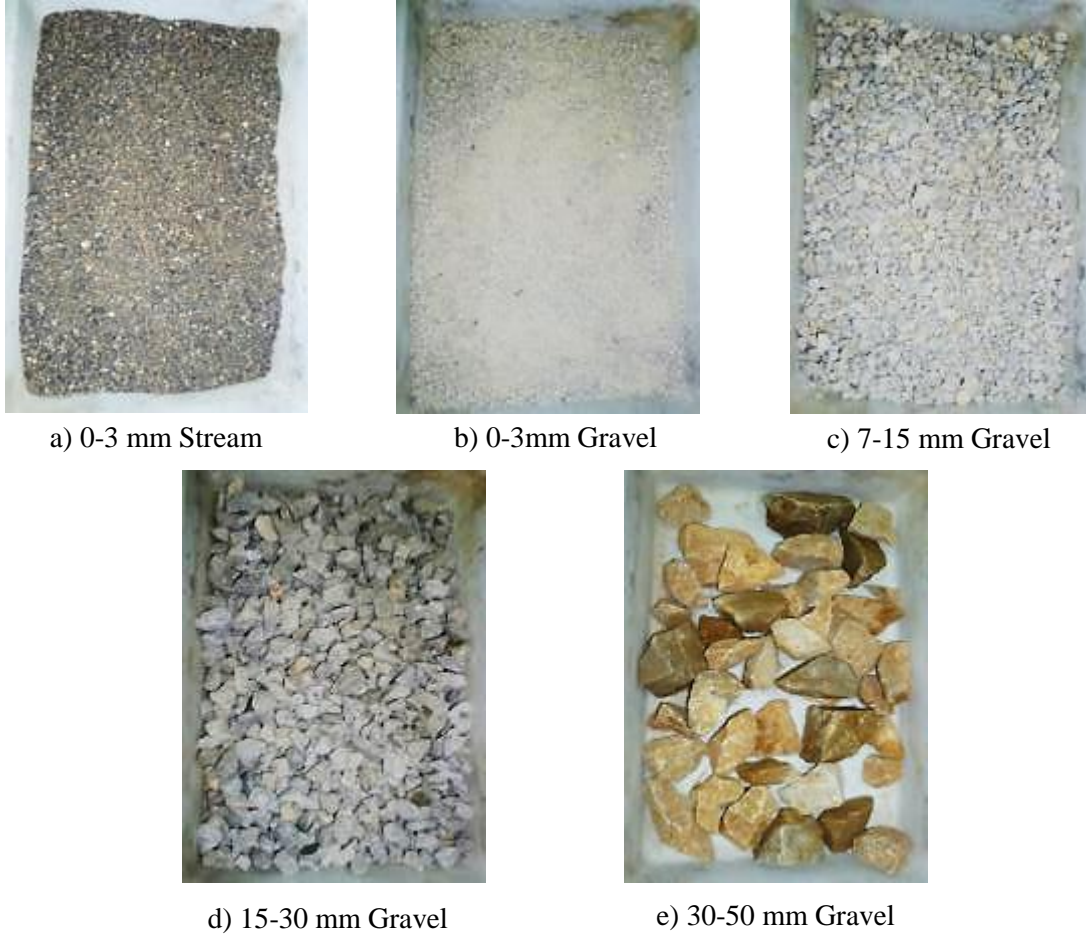


**Figure 3.1.** Different Batches of Aggregates

The mixture ratios for both scaled and unscaled CVC and RCC concrete types are given in Table 3.1 and Table 3.2. It should be emphasized that two different aggregate mixtures were prepared by using stream sand or crushed stone as the choice of aggregate was not clear at this stage. Furthermore, the comparisons of gradation curves of aggregate mixtures with the Fuller's Curve are presented in Figures 3.3 and 3.4. From those figures, it could easily be inferred that there was an acceptable match between each mixture gradation curve and its corresponding

Fuller's Curve, implying a satisfactory mixture density with a minimum compaction effort.

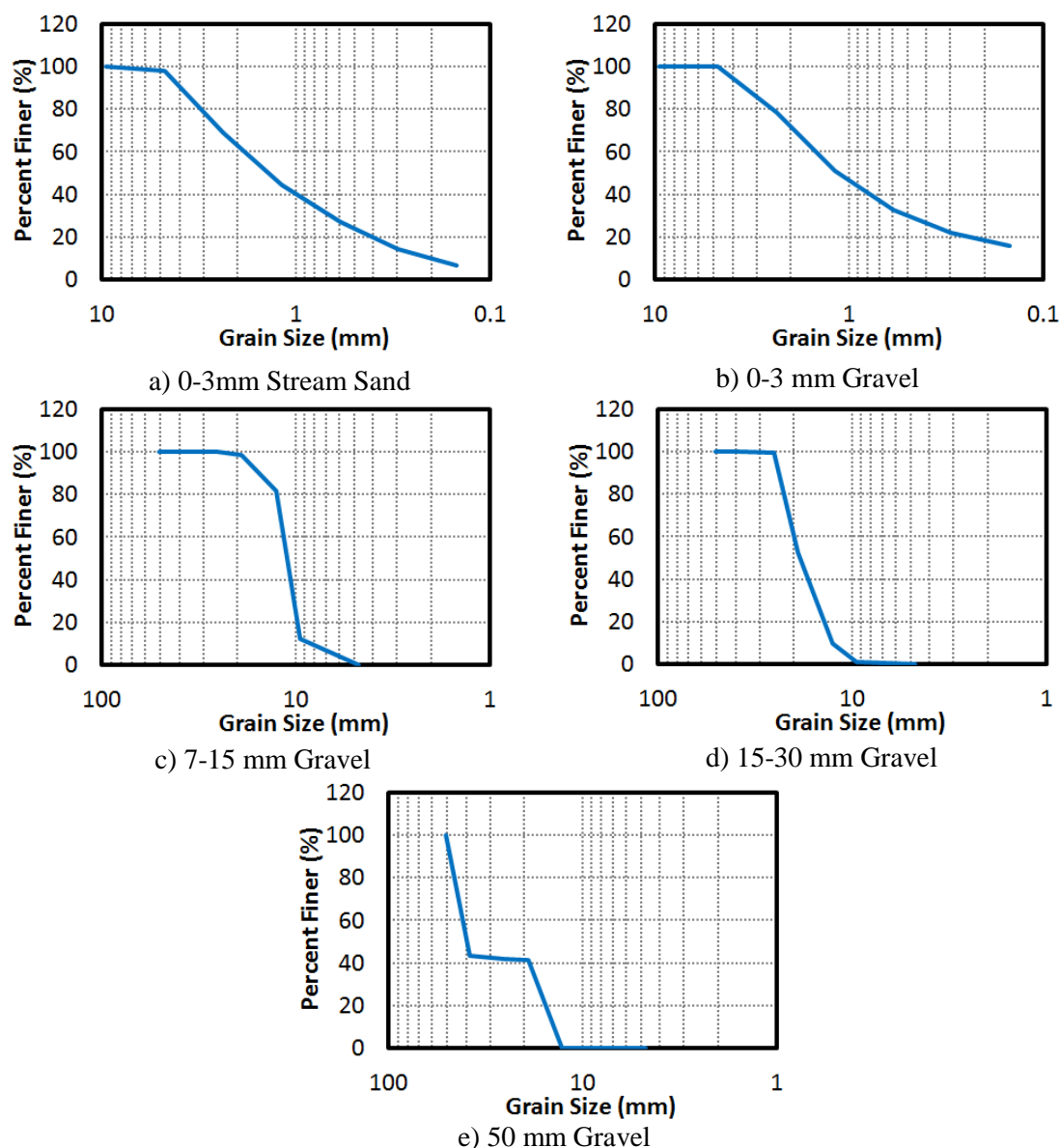


**Figure 3.2.** Gradation Curves for the Different Batches of Aggregates

**Table 3.1.** Aggregate Mixtures with 0-3 mm Stream Sand

	Scaled CVC	Scaled RCC	Unscaled CVC	Unscaled RCC
0-3mm Stream Sand	100 %	100 %	45 %	25 %
0-3mm Gravel	-	-	-	-
3-15mm Gravel	-	-	25 %	22.5 %
15-30mm Gravel	-	-	30 %	32.5 %
30-50mm Gravel	-	-	-	20 %

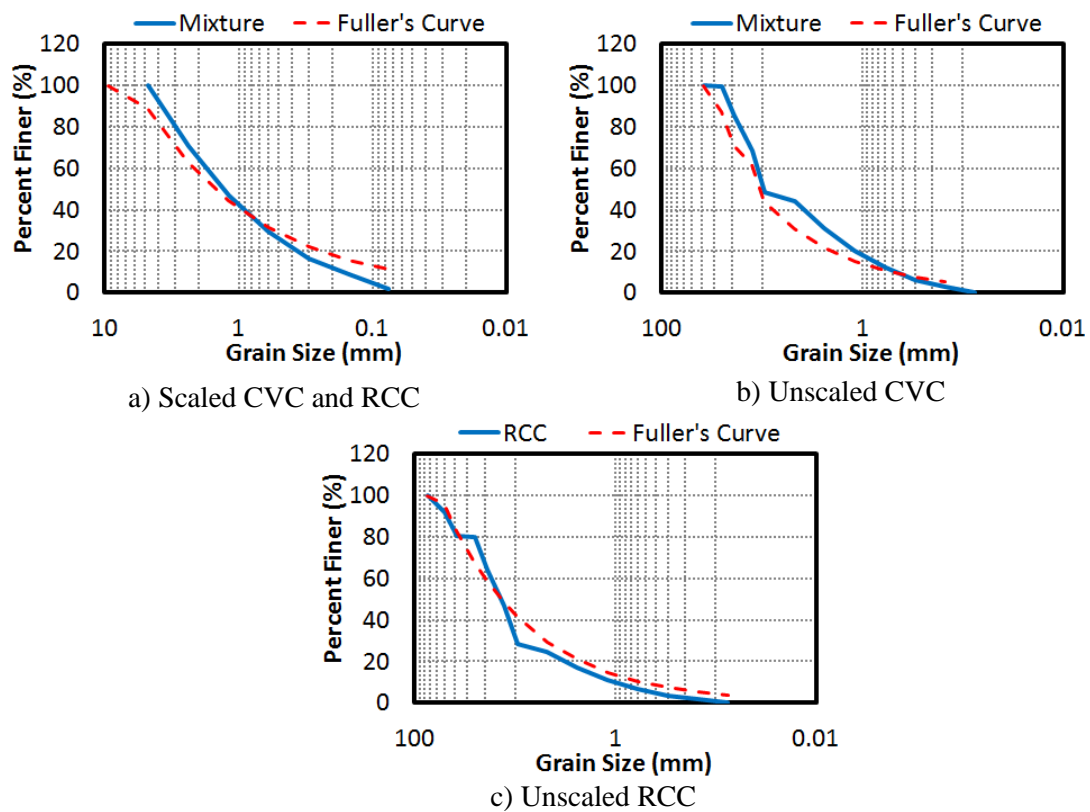


**Figure 3.3.** Gradation Curves for Concrete Mixtures  
(Fine Aggregate from 0-3mm Stream Sand Batch)

**Table 3.2.** Aggregate Mixtures with 0-3 mm Gravel

	Scaled CVC	Scaled RCC	Unscaled CVC	Unscaled RCC
<b>0-3mm Stream Sand</b>	-	-	-	-
<b>0-3mm Gravel</b>	100 %	100 %	45 %	25 %
<b>3-15mm Gravel</b>	-	-	25 %	22.5 %
<b>15-30mm Gravel</b>	-	-	30 %	32.5 %
<b>30-50mm Gravel</b>	-	-	-	20 %



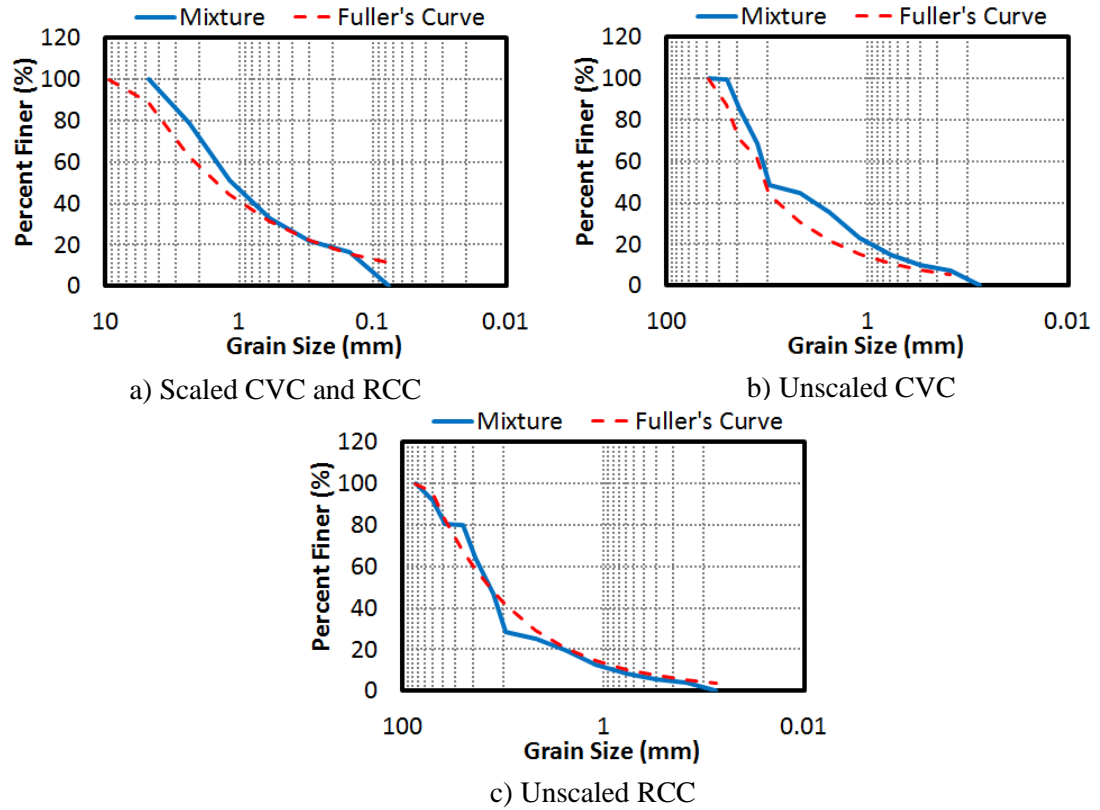


**Figure 3.4.** Gradation Curves for Concrete Mixtures  
(Fine Aggregate from 0-3mm Gravel Batch)

### 3.1.2 Specific Gravity and Water Absorption Capacity Experiments

The unit weights and water absorption capacities of each batch were determined by utilizing ASTM C 127-12 and 128-12 at Materials of Construction Laboratory of Middle East Technical University. The results for fine and coarse aggregates are presented in Table 3.3 and Table 3.4, respectively. These densities are utilized while determining the weights of each aggregate batch in a  $1\text{m}^3$  of concrete mixture. The water absorption capacities are also important as they directly affect the water content that will take action in the hydration process. The water amount during concrete mixture preparations are arranged according to the water absorption and the water content of each aggregate batch.

**Table 3.3.** Unit Weights and Water Absorption Capacities for Fine Aggregates

	<b>0-3 mm Stream Sand</b>	<b>0-3 mm Gravel</b>
<b>Specific Gravity (SSD)</b>	1.681 ton/m <sup>3</sup>	1.628 ton/m <sup>3</sup>
<b>Specific Gravity (Dry)</b>	1.613 ton/m <sup>3</sup>	1.584 ton/m <sup>3</sup>
<b>Water Absorption</b>	4.201 %	2.796 %

**Table 3.4.** Unit Weights and Water Absorption Capacities for Coarse Aggregates

	<b>7-15mm and 15-30mm Gravel</b>	<b>30-50mm Gravel</b>
<b>Specific Gravity (SSD)</b>	2.713 ton/m <sup>3</sup>	2.556 ton/m <sup>3</sup>
<b>Specific Gravity (Dry)</b>	2.705 ton/m <sup>3</sup>	2.547 ton/m <sup>3</sup>
<b>Water Absorption</b>	0.294 %	0.475 %

### 3.2 Chemical Properties of Cement and Pozzolan

The cement type CEM I (Portland Cement) was used throughout the experimental program as this type contains no pozzolan or other additional chemicals. While producing the RCC, some pozzolan should also be added to the mixture in order to reduce the heat of hydration. For this purpose, the readily available fly ash from Iskenderun Iron and Steel Enterprises was used. The chemical properties of both the cement and fly ash should comply with the limits recommended by the corresponding standards. The chemical compositions of those binding materials were determined in Turkish Cement Manufacturers' Association (TCMA) and the results are given in Table 3.5 and Table 3.6. It could be concluded from those tables that both cement and fly ash are compatible with ASTM C150-12 and ASTM C618-12, respectively.

**Table 3.5.** Chemical Composition of Cement

Oxides and Other Properties	% by Weight	ASTM C150 Limit
<b>SiO<sub>2</sub></b>	18.30	-
<b>Al<sub>2</sub>O<sub>3</sub></b>	4.27	-
<b>Fe<sub>2</sub>O<sub>3</sub></b>	4.10	-
<b>CaO</b>	62.20	-
<b>MgO</b>	1.29	Max. 6.0
<b>SO<sub>3</sub></b>	2.78	Max. 3.0
<b>Na<sub>2</sub>O</b>	0.18	-
<b>K<sub>2</sub>O</b>	0.60	-
<b>Equivalent Tot. Alkali (Na<sub>2</sub>O+0.658K<sub>2</sub>O)</b>	0.57	Max 0.60
<b>Cl<sup>-</sup></b>	0.0102	Max. 0.1
<b>2-Day Comp. Strength</b>	19.2 MPa	Min. 12.0
<b>7-Day Comp. Strength</b>	36.1 MPa	Min. 19.0
<b>28-Day Comp. Strength</b>	48.7 MPa	Min. 28.0
<b>Initial Setting Time</b>	235 min	Min. 60.0
<b>Final Setting Time</b>	445 min	Max. 600.0

### 3.3 Water-Cement Ratio

In this part, the water – cementitious material ratios for an average target compressive strength of 25 MPa CVC (both scaled and unscaled), 15 MPa and 25 MPa RCC (both scaled and unscaled) were determined. Concrete batches were mixed by using different water – cementitious material ratios and the 7<sup>th</sup>, 28<sup>th</sup> and 90<sup>th</sup> day strengths of 150x300 mm cylindrical specimens were determined.

For unscaled CVC mixture, the water – cement ratio was assumed to be 0.55 as this ratio was determined not to cause workability problems during initial trials. In addition, for the scaled CVC, this ratio was increased in order to compensate the increased amount of water absorption stemming from using no coarse aggregates in the mixture, which increased the surface area of aggregate batch. Thus, the amount of cement should also be larger than the unscaled CVC since the required Calcium-Silicate-Hydrate (C-S-H) gel (concrete paste) to bind the aggregates together was

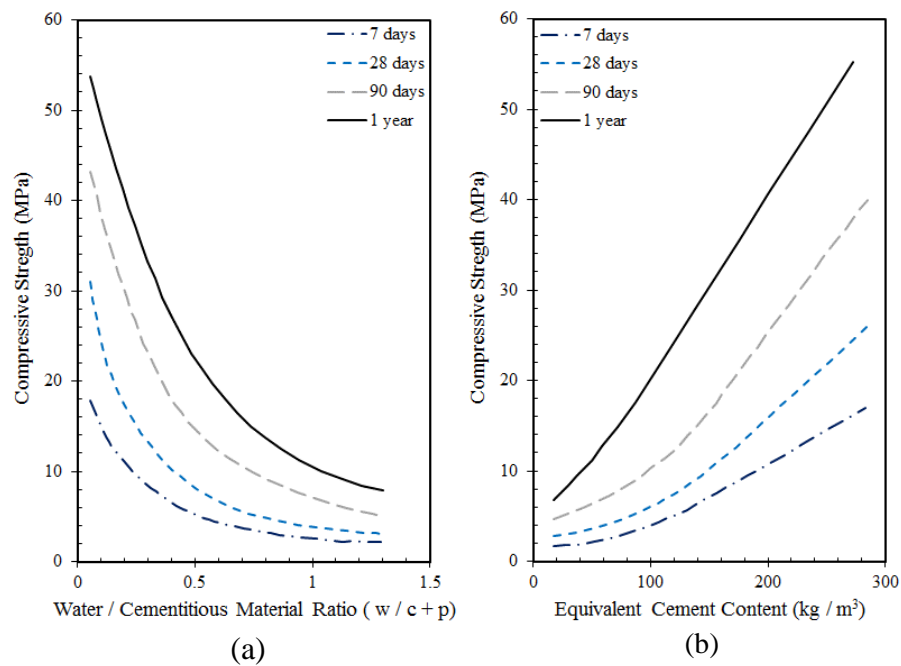
more due to this increased surface area of aggregates. In the trial and error process to determine the cement amount for gaining the target compressive strength, the water – cement ratios were taken as constant but the cement amount was varied for different concrete batches. Consequently, the cement amount versus compressive strength curves were obtained for CVC.

**Table 3.6.** Chemical Composition of Fly Ash

<b>Oxides and Other Properties</b>	<b>% by Weight</b>	<b>ASTM C618 Limit For Class F</b>
<b>SiO<sub>2</sub></b>	63.79	-
<b>Al<sub>2</sub>O<sub>3</sub></b>	19.04	-
<b>Fe<sub>2</sub>O<sub>3</sub></b>	6.76	-
<b>CaO</b>	1.68	-
<b>MgO</b>	1.65	Max. 6.0
<b>SO<sub>3</sub></b>	0.30	Max. 3.0
<b>Na<sub>2</sub>O</b>	1.11	-
<b>K<sub>2</sub>O</b>	2.18	-
<b>Equivalent Tot. Alkali (Na<sub>2</sub>O+0.658K<sub>2</sub>O)</b>	2.54	-
<b>Free CaO</b>	0.14	-
<b>Cl<sup>-</sup></b>	0.0067	-
<b>Reactive CaO</b>	0.31	-
<b>Density</b>	2.340 ton/m <sup>3</sup>	-
<b>Retained 45 µm seive</b>	20.6	Max. 34.0
<b>28 Day Strength Activity Index</b>	78.0	Min. 75
<b>90 Day Strength Activity Index</b>	90.2	Min. 75

In the preliminary trials, the scaled CVC samples prepared from 0-3mm stream sand were found to have less strength compared to the unscaled ones composed of gravel (55% of total aggregate mass). The other problem with the stream sand batch was the probable difference in the modulus of elasticity between the scaled and unscaled concrete mixtures. In order to eliminate those drawbacks, gravel batch was decided to be used as fine aggregates.

The RCC mixture design was performed with the aid of ACI 207 (1999). In ACI 207 (1999), the curves to determine both the water – cementitious material ratios and the cementitious material amounts for a target compressive strength value at a desired age of concrete including 7<sup>th</sup>, 28<sup>th</sup>, 90<sup>th</sup>-day and 1-year are presented (Figure 3.5). Those curves are derived from the database of field core tests of RCC dams built in the USA. In this dissertation, the fly ash amount is taken as 40% of cementitious material in order to be compatible with ACI 207 (1999) curves. In addition, the water – cement ratio is assumed as 0.40 for the unscaled RCC mixture.



*Note: These curves based on use of 75mm MAS with 30 to 40 percent fly ash per volume of cementitious material*

**Figure 3.5.** Curves Used in RCC Mixture Design (ACI 207) : (a) Water – Cementitious Material Ratio and (b) Cementitious Material Amount

The compaction necessary for the placement of RCC was simulated by a pneumatic hand compactor in the laboratory environment (Figure 3.6.a). The uniform compaction of specimens was ensured by 50-mm-thick plates for both 100x200mm (Figure 3.6.b) and 150x300mm (Figure 3.6.c) cylindrical specimens. The concrete was placed in layers of 70mm and 100mm in the 100x200mm and 150x300mm molds, respectively. Each layer was compacted by using a pneumatic hand compactor (Figure 3.6.a). While compacting the specimens, the aim was to generate

the same compaction energy per second as the one given by vibrating rollers in practice. The calculations on this phenomenon are presented in Chapter 4.

The water – cementitious material ratios and fly ash ratio in cementitious material in RCC mixture were taken as constant similar to the CVC mix design. On the other hand, the cementitious material amount was varied for different concrete batches. Consequently, the cementitious material amount versus compressive strength curves were obtained.



**Figure 3.6.** Apparatus Used in RCC Placement : (a) Pneumatic Hand Compactor; (b) 100x200mm Cylindrical Mold; (c) 100x200mm Cylindrical Mold and (d) Steel Apparatus for Uniform Compaction

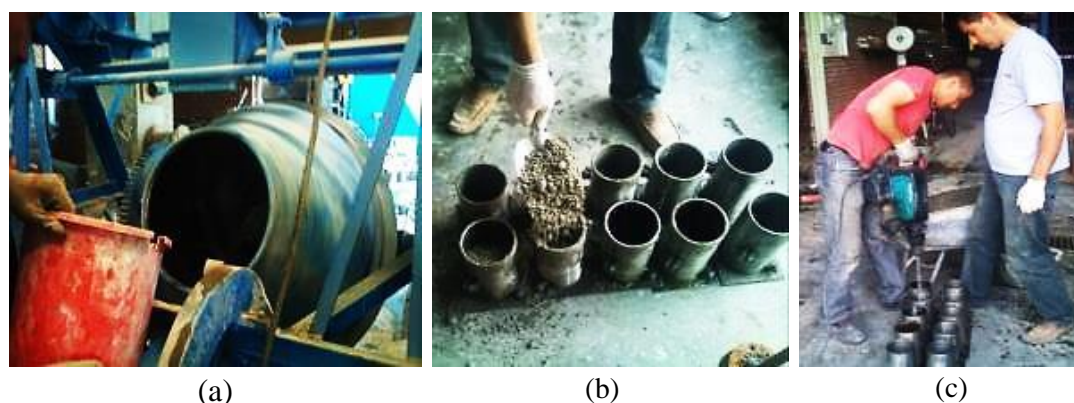


**Figure 3.7.** Stages in RCC Placement : (a) Mixture in Mixer; (b) Placement of Concrete in Molds and (c) Compaction

### 3.4 Concrete Mixture Results

In this part, the concrete mixtures for unscaled and scaled CVC and RCC's are presented. The 3<sup>rd</sup>, 7<sup>th</sup>, 28<sup>th</sup> and 90<sup>th</sup>-day compressive and split tensile strength values for each type of concrete are also tabulated for the final mixtures. In addition, the

size effect on the strength was examined by comparing the 7<sup>th</sup> and 28<sup>th</sup>-day results of 100x200mm and 150x300mm cylindrical specimens. Finally, the stress-strain curves at the age of 7 and 28 days were obtained and presented for each concrete types excluding unscaled RCC specimens. This is because; the capacity of the available testing machine at Materials of Construction Laboratory of Middle East Technical University, MTS (Figure 3.8), is 20t. This limit nearly corresponds a pressure value of 11 MPa on a specimen having a diameter of 150mm and a height of 300mm.



**Figure 3.8.** MTS Testing Machine

#### **3.4.1 Unscaled CVC Results**

After trial and error procedure outlined above, the cement amount was determined as 250 kg/m<sup>3</sup> and the water-cement ratio was selected as 55% for unscaled CVC. The compressive strength values obtained by utilizing above mixture ratios are presented in Table 3.7. From Table 3.7, it could be stated that the compressive strength values of 100x200mm specimens were approximately 10% larger than 150x300mm specimens. This difference was compatible with the literature values (Day 1994, Vandegrift and Schindler 2006 and Hamad 2015). In addition, this mixture was capable of producing the target average compressive strength value of 25 MPa at the 28<sup>th</sup>-day with an acceptable tolerance.

**Table 3.7.** Compressive Strength Values of Unscaled CVC Specimens

Day	100x200 mm			150x300 mm		
	Specimen 1	Specimen 2	Average	Specimen 1	Specimen 2	Average
3	22.2 MPa	20.3 MPa	21.3 MPa	-	-	-
7	23.9 MPa	23.8 MPa	23.8 MPa	22.3 MPa	22.4 MPa	22.3 MPa
28	31.4 MPa	29.9 MPa	30.7 MPa	24.3 MPa	27.7 MPa	26.0 MPa
90	31.9 MPa	33.3 MPa	32.6 MPa	-	-	-

At the age of 7 and 28 days, the stress-strain curves were also obtained from the testing of 100x200mm specimens. These curves are shown in Figure 3.9. By examining Figure 3.9.c, an increase in the compressive strength can be detected. From that figure, it can clearly be inferred that the increase in the modulus of elasticity was nearly 20% from 7<sup>th</sup> day to 28<sup>th</sup> day. Besides, there is a leftward shift in the strain at the ultimate strength value in accordance with the observations in literature. Furthermore, the split tensile strengths are summarized in Table 3.8.

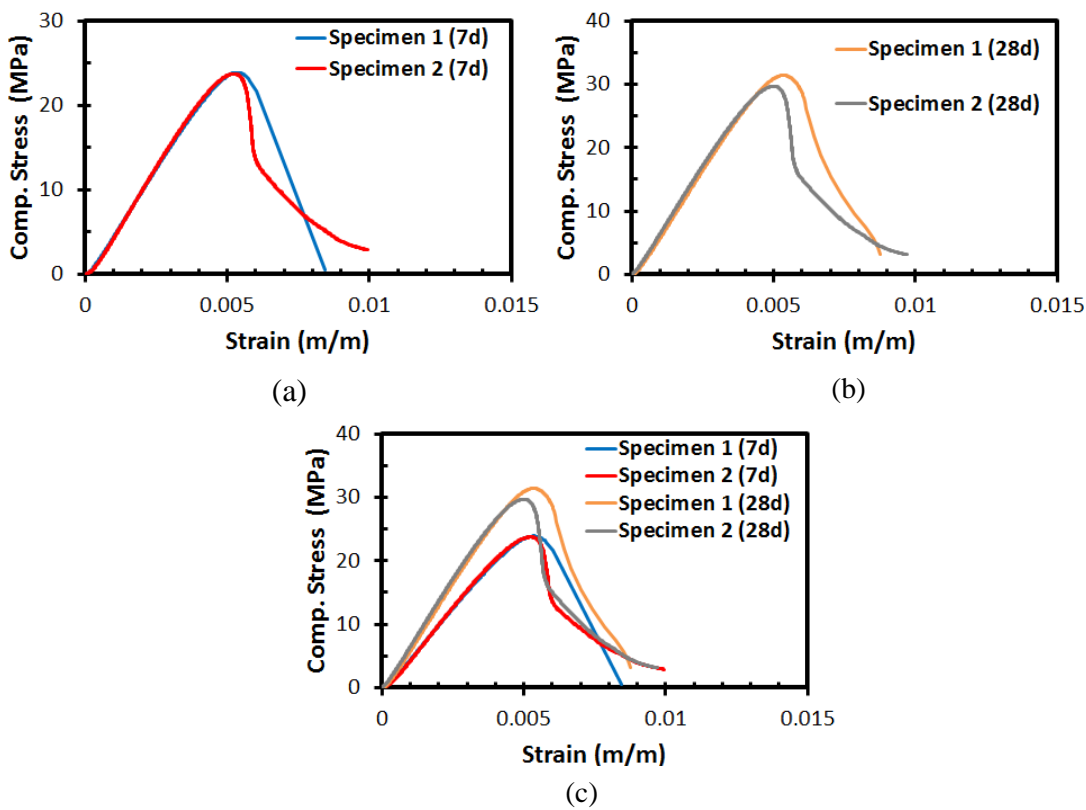


**Figure 3.9.** Stress-Strain Curves of the Unscaled 100x200mm CVC Specimens:  
 (a) 7<sup>th</sup> Day Results; (b) 28<sup>th</sup> Day Results and (c) All Results



**Table 3.8.** Split Tensile Strength Values of Unscaled CVC Specimens

Day	100x200 mm			150x300 mm		
	Specimen 1	Specimen 2	Average	Specimen 1	Specimen 2	Average
3	2.4 MPa	2.2 MPa	2.3 MPa	-	-	-
7	3.3 MPa	3.1 MPa	3.2 MPa	2.6 MPa	1.7 MPa	2.2 MPa
28	4.0 MPa	2.7 MPa	3.3 MPa	1.8 MPa	2.3 MPa	2.1 MPa
90	4.0 MPa	3.4 MPa	3.7 MPa	-	-	-

### 3.4.2 Scaled CVC Results

The cement amount was determined as 300 kg/m<sup>3</sup> and the water-cement ratio was selected as 60% for scaled CVC after several trials. The compressive strength values obtained by utilizing the mixture ratios given above are presented in Table 3.9. From Table 3.7, it can be stated that the compressive strength values of 100x200mm specimens are approximately 10% larger than the 150x300mm specimens. This difference was compatible with the values reported in literature. In addition, this mixture was capable of producing the target average compressive strength value of 25 MPa at 28<sup>th</sup>-day with an acceptable tolerance.

**Table 3.9.** Compressive Strength Values of Scaled CVC Specimens

Day	100x200 mm			150x300 mm		
	Specimen 1	Specimen 2	Average	Specimen 1	Specimen 2	Average
3	20.5 MPa	19.1 MPa	19.8 MPa	-	-	-
7	22.4 MPa	24.8 MPa	23.60MPa	22.8 MPa	23.3 MPa	23.0 MPa
28	31.0 MPa	31.1 MPa	31.0 MPa	27.5 MPa	28.1 MPa	27.8 MPa
90	31.9 MPa	31.3 MPa	31.6 MPa	-	-	-

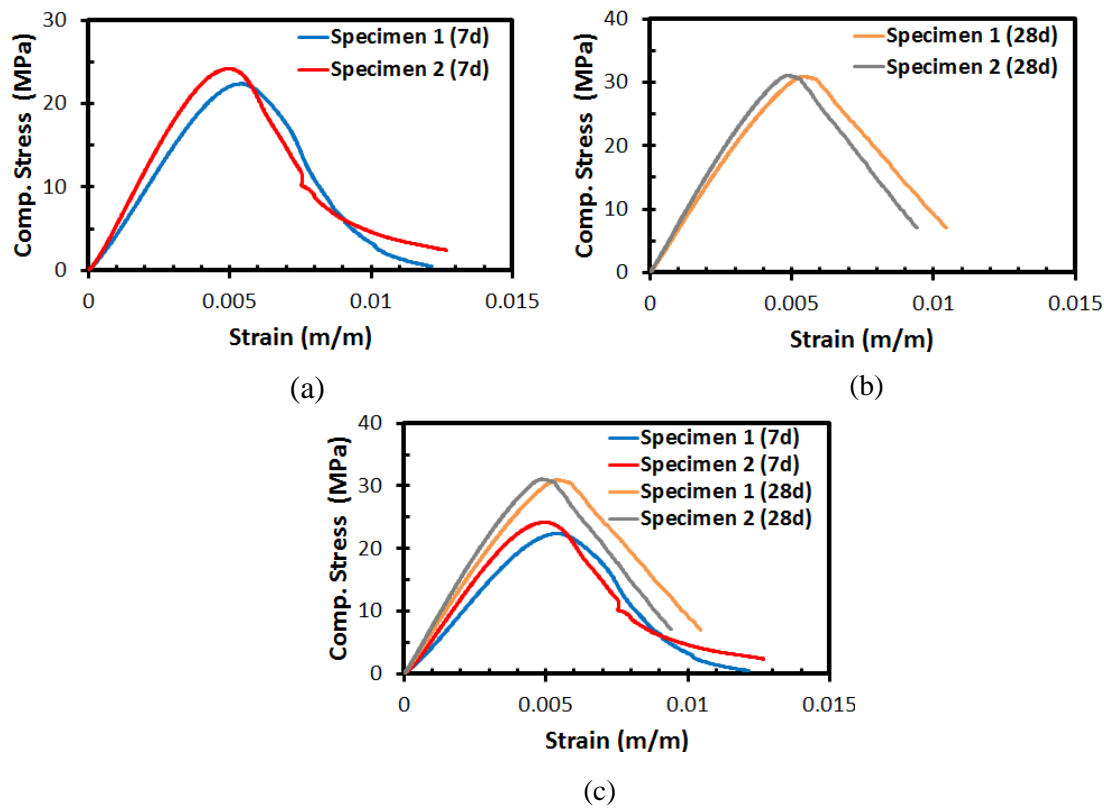


**Figure 3.10.** Stress-Strain Curves of Scaled 100x200mm CVC Specimens:  
(a) 7<sup>th</sup> Day Results; (b) 28<sup>th</sup> Day Results and (c) All Results

At the age of 7 and 28 days, the stress-strain curves were also obtained from the 100x200mm specimens. These curves are shown in Figure 3.10. By examining Figure 3.10.c, the compressive strength increase from 7 and 28 days can be observed. From that figure, it can clearly be inferred that the increase in the modulus of elasticity was nearly 10% from 7<sup>th</sup> day to 28<sup>th</sup> day. Besides, there is a leftward shift in the strain at the ultimate strength value in accordance with the observations in literature. The split tensile strengths are summarized in Table 3.10.

**Table 3.10.** Split Tensile Strength Values of Scaled CVC Specimens

Day	100x200 mm			150x300 mm		
	Specimen 1	Specimen 2	Average	Specimen 1	Specimen 2	Average
3	1.7 MPa	2.6 MPa	2.2 MPa	-	-	-
7	2.9 MPa	3.0 MPa	3.0 MPa	2.3 MPa	2.5 MPa	2.4 MPa
28	3.6 MPa	3.3 MPa	3.4 MPa	3.1 MPa	2.9 MPa	3.0 MPa
90	3.9 MPa	4.1 MPa	4.0 MPa	-	-	-

### 3.4.3 Scaled RCC15 Results

The cement and fly ash amounts were determined as 140 kg/m<sup>3</sup> and 95 kg/m<sup>3</sup>, respectively. The water – cementitious material ratio was selected as 40% for scaled RCC. The compressive strength values obtained by utilizing above mixture ratios are presented in Table 3.11. From Table 3.11, it can be stated that the compressive strength values of the 100x200mm specimens are approximately 15% larger than the 150x300mm specimens. This difference was more than CVC as a result of the better compaction in the smaller specimen. In addition, this mixture is capable of producing the target average compressive strength value of 15 MPa at 28<sup>th</sup>-day.

**Table 3.11.** Compressive Strength Values of Scaled RCC15 Specimens

Day	100x200 mm			150x300 mm		
	Specimen 1	Specimen 2	Average	Specimen 1	Specimen 2	Average
3	5.66 MPa	4.20 MPa	4.93 MPa	-	-	-
7	12.27 MPa	9.83 MPa	11.05 MPa	9.91 MPa	11.79 MPa	10.85 MPa
28	16.38 MPa	19.12 MPa	17.75 MPa	13.23 MPa	17.10 MPa	15.16 MPa
90	19.85 MPa	23.95 MPa	21.90 MPa	-	-	-

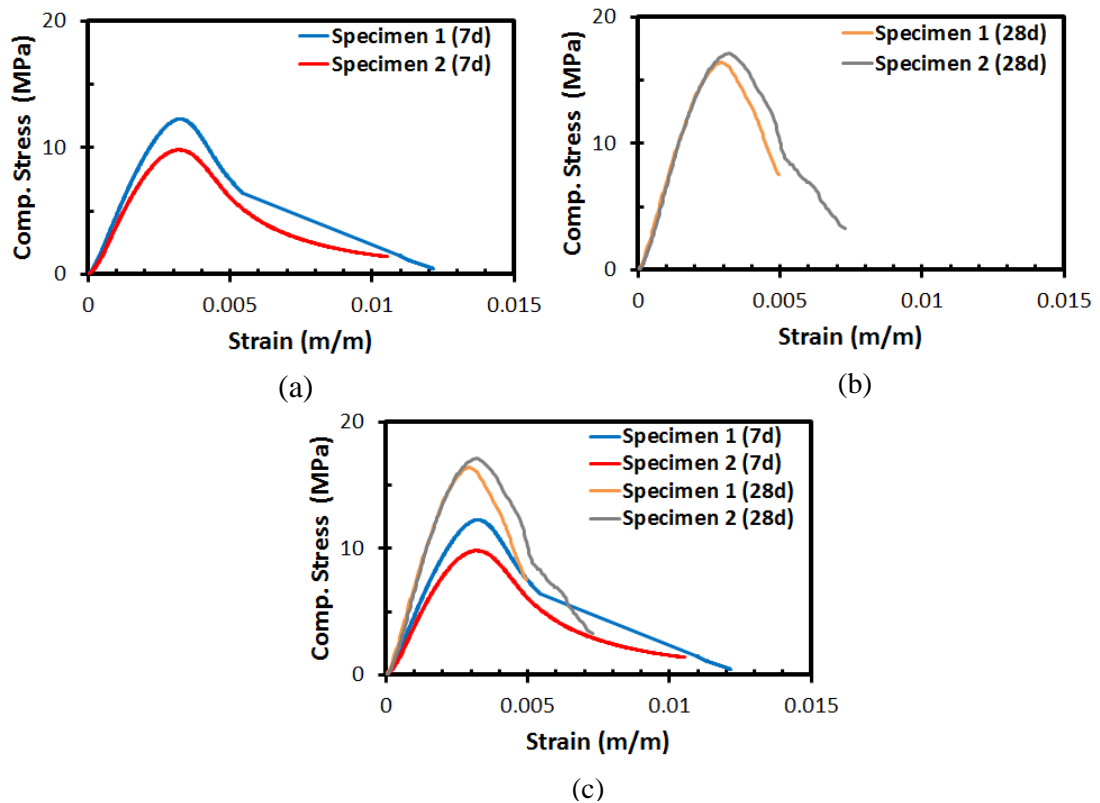


**Figure 3.11.** Stress-Strain Curves of 100x200mm Scaled RCC15 Specimens: (a) 7<sup>th</sup> Day Results; (b) 28<sup>th</sup> Day Results and (c) All Results

At the age of 7 and 28, the stress-strain curves were also obtained from 100x200mm specimens. These curves are shown in Figure 3.11. From that figure, it can clearly be inferred that the increases in the modulus of elasticity and the compressive strength are nearly 20% and 75% from 7<sup>th</sup> to 28<sup>th</sup> day, respectively. The split tensile strengths are summarized in Table 3.10.

**Table 3.12.** Split Tensile Strength Values of Scaled RCC15 Specimens

Day	100x200 mm			150x300 mm		
	Specimen 1	Specimen 2	Average	Specimen 1	Specimen 2	Average
3	0.36 MPa	0.52 MPa	0.44 MPa	-	-	-
7	0.99 MPa	0.71 MPa	0.85 MPa	0.89 MPa	0.91 MPa	0.90 MPa
28	2.73 MPa	0.79 MPa	1.76 MPa	1.39 MPa	1.24 MPa	1.31 MPa
90	1.42 MPa	2.25 MPa	1.83 MPa	-	-	-

#### 3.4.4 Scaled RCC25 Results

The cement and fly ash amounts were determined as 195 kg/m<sup>3</sup> and 130 kg/m<sup>3</sup>, respectively. The water – cementitious material ratio was selected as 40% for scaled RCC. The compressive strength values obtained by utilizing above mixture ratios are presented in Table 3.13. From Table 3.13, it can be stated that the compressive strength values of the 100x200mm specimens were approximately 30% larger than the 150x300mm specimens. This difference was more than the corresponding CVC, due to the better compaction in the smaller specimens. In addition, this mixture was capable of producing the target average compressive strength value of 25 MPa at 28<sup>th</sup>-day in an acceptable error range.

**Table 3.13.** Compressive Strength Values of Scaled RCC25 Specimens

Day	100x200 mm			150x300 mm		
	Specimen 1	Specimen 2	Average	Specimen 1	Specimen 2	Average
3	9.59 MPa	10.47 MPa	10.03 MPa	-	-	-
7	24.81 MPa	26.86 MPa	25.84 MPa	17.98 MPa	20.82 MPa	19.40 MPa
28	31.41 MPa	33.75 MPa	32.58 MPa	24.86 MPa	25.95 MPa	25.41 MPa
90	37.19 MPa	35.15 MPa	36.17 MPa	-	-	-

At the age of 7 and 28, the stress-strain curves are also obtained from the 100x200mm specimens. These curves are shown in Figure 3.12. By examining Figure 3.12.c, the compressive strength increase can be observed from 7<sup>th</sup> to 28<sup>th</sup> day.

From that figure, it can clearly be inferred that the increase in the modulus of elasticity was nearly 10% from 7<sup>th</sup> day to 28<sup>th</sup> day. Furthermore, the split tensile strengths are summarized in Table 3.14.

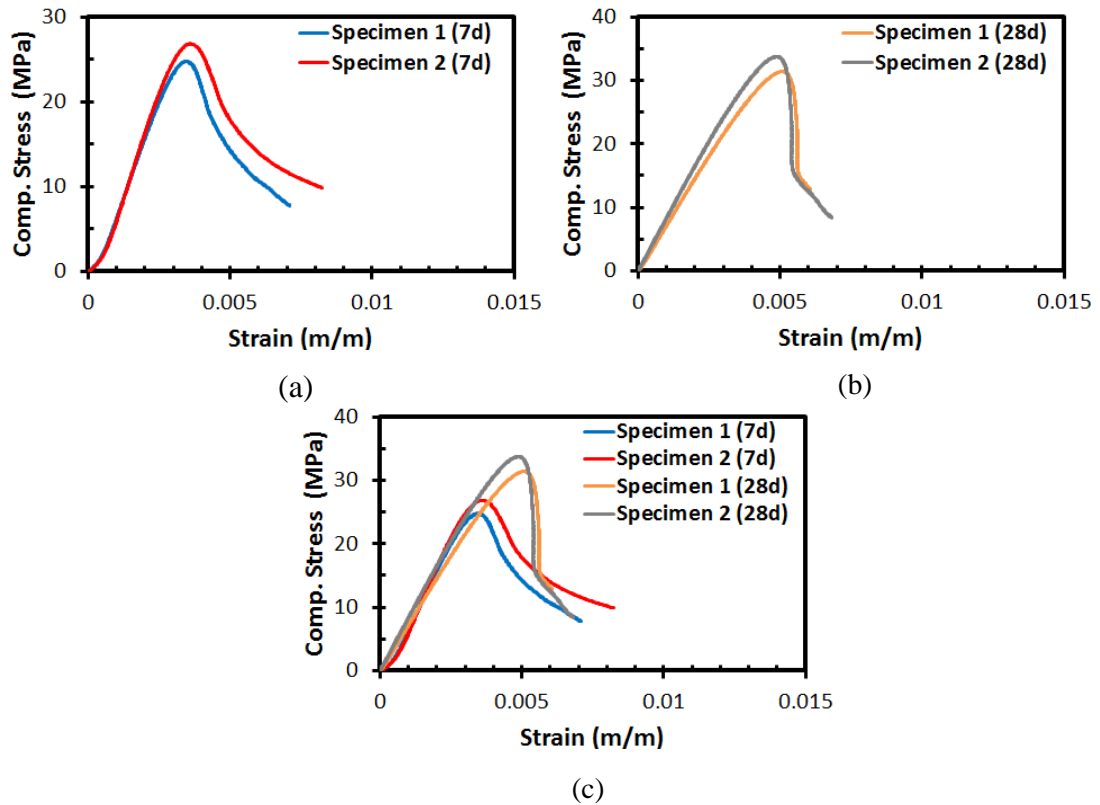


**Figure 3.12.** Stress-Strain Curves of 100x200mm Scaled RCC25 Specimens:  
(a) 7<sup>th</sup> Day Results; (b) 28<sup>th</sup> Day Results and (c) All Results

**Table 3.14.** Split Tensile Strength Values of Scaled RCC25 Specimens

	100x200 mm			150x300 mm		
Day	Specimen 1	Specimen 2	Average	Specimen 1	Specimen 2	Average
3	0.95 MPa	0.85 MPa	0.90 MPa	-	-	-
7	2.28 MPa	3.42 MPa	2.85 MPa	1.09 MPa	1.39 MPa	1.24 MPa
28	3.36 MPa	3.03 MPa	3.20 MPa	1.43 MPa	1.93 MPa	1.68 MPa
90	3.09 MPa	3.73 MPa	3.41 MPa	-	-	-

### 3.4.5 Unscaled RCC15 Results

After many trial and error steps, the cement and fly ash amounts were determined as 130 kg/m<sup>3</sup> and 85 kg/m<sup>3</sup>, respectively. The water – cementitious material ratio was selected as 40% for scaled RCC. The compressive strength values obtained by

utilizing above mixture ratios are presented in Table 3.15. For this type of concrete, only 150x300mm specimens are prepared. This is because of the ASTM C42 (1994) limitation of the minimum diameter of cylindrical specimens to 3 times the maximum aggregate size, which is 50mm for this case. In addition, this mixture is capable of producing the target average compressive strength value of 15 MPa at 28<sup>th</sup>-day in an acceptable error range. The split tensile strengths are summarized in Table 3.16.

The stress-strain curves could not be obtained for this type of concrete for the 150mm diameter specimens due to insufficient capacity of the testing machine.

**Table 3.15.** Compressive Strength Values of the Unscaled RCC15 Specimens

Day	100x200 mm			150x300 mm		
	Specimen 1	Specimen 2	Average	Specimen 1	Specimen 2	Average
3	-	-	-	6.54 MPa	4.90 MPa	5.72 MPa
7	-	-	-	11.77 MPa	13.62 MPa	12.70 MPa
28	-	-	-	14.99 MPa	19.94 MPa	17.46 MPa
90	-	-	-	22.71 MPa	27.14 MPa	24.92 MPa

**Table 3.16.** Split Tensile Strength Values of the Unscaled RCC15 Specimens

Day	100x200 mm			150x300 mm		
	Specimen 1	Specimen 2	Average	Specimen 1	Specimen 2	Average
3	-	-	-	0.42 MPa	0.59 MPa	0.50 MPa
7	-	-	-	0.94 MPa	0.98 MPa	0.96 MPa
28	-	-	-	1.43 MPa	1.31 MPa	1.37 MPa
90	-	-	-	1.64 MPa	2.62 MPa	2.13 MPa

### 3.4.6 Unscaled RCC25 Results

The cement and fly ash amounts were determined as 185 kg/m<sup>3</sup> and 120 kg/m<sup>3</sup>, respectively. The water – cementitious material ratio was selected as 40% for scaled RCC. The compressive strength values obtained by utilizing above mixture ratios are presented in Table 3.17. Again, for this type of concrete, only the 150x300mm specimens were prepared. In addition, this mixture was capable of producing the target average compressive strength value of 25 MPa at 28<sup>th</sup>-day in an acceptable error range. Furthermore, the split tensile strengths are summarized in Table 3.18.

The stress-strain curves could not be obtained for this type of concrete due to the lack of testing apparatus for the 150mm diameter specimens and due to insufficient capacity of the testing machine.

**Table 3.17.** Compressive Strength Values of Unscaled RCC25 Specimens

Day	100x200 mm			150x300 mm		
	Specimen 1	Specimen 2	Average	Specimen 1	Specimen 2	Average
3	-	-	-	10.87 MPa	12.21 MPa	11.54 MPa
7	-	-	-	9.48 MPa	12.50 MPa	10.99 MPa
28	-	-	-	28.71 MPa	29.40 MPa	29.06 MPa
90	-	-	-	44.18 MPa	40.98 MPa	42.58 MPa

**Table 3.18.** Split Tensile Strength Values of Unscaled RCC25 Specimens

Day	100x200 mm			150x300 mm		
	Specimen 1	Specimen 2	Average	Specimen 1	Specimen 2	Average
3	-	-	-	1.12 MPa	1.01 MPa	1.07 MPa
7	-	-	-	1.17 MPa	1.46 MPa	1.32 MPa
28	-	-	-	1.47 MPa	2.05 MPa	1.76 MPa
90	-	-	-	3.60 MPa	4.31 MPa	3.95 MPa

### 3.5 Discussion of Results

The summary of test results and the mixture details of each batch are presented in Table 3.19. From Table 3.19, it is apparent that the target compressive strengths required for the generation of different dam specimens in the laboratory environment could be attained by utilizing these mixtures. In addition, the compressive and split tensile strength of specimens with fly ash continued to increase after 28 days from the concrete placement. In contrast, CVC specimens had nearly gained their target strength at the 28<sup>th</sup> day.

The effect of aggregate scaling on the evolution of the mechanical properties was negligible for CVC specimens as shown in Figure 3.14 and Table 3.19. However, this observation was not true for the RCC specimens. Although the scaled RCC specimens gained their compressive strengths nearly as fast as their unscaled counterparts, the scaled RCC specimens attained their split tensile strengths faster than unscaled ones. At first glance, this situation could be thought as a problem.

However, the design strength of real RCC dams are selected at 90<sup>th</sup> day due to the slow rates of hydration process stemming from the inclusion of pozzolans in the mixture (UBK 2012). For the dam tests, the design strengths of the scaled RCC were selected at 28<sup>th</sup> day in order to reduce the test preparation duration and to make the test program feasible. This choice helped to represent the material behavior of real dams at their 90<sup>th</sup> day in a reasonable manner.

**Table 3.19.** Summary of Test Specimens and Test Results

	CVC		RCC25		RCC15		
	Day	Scaled	Unscaled	Scaled	Unscaled	Scaled	Unscaled
Cement (kg/m <sup>3</sup> )		300	250	195	185	140	130
Fly Ash (kg/m <sup>3</sup> )		-	-	130	120	95	85
W/C		60%	55%	40%	40%	40%	40%
MAS (mm)		3	30	3	50	3	50
Compressive Strength (MPa)*	7	23.60	23.80	25.84	10.99	11.05	12.70
	28	31.00	30.70	32.58	29.06	17.75	17.46
	90	31.60	32.60	36.17	42.58	21.90	24.92
Split Tensile Strength (MPa)*	7	3.00	3.20	2.85	1.32	0.85	0.96
	28	3.40	3.30	3.20	1.76	1.76	1.37
	90	4.00	3.70	3.41	3.95	1.83	2.13
Strain Energy of Compressive Tests (N.m)*	7	216.19	173.92	173.41	-	73.93	-
	28	289.71	222.69	186.97	-	99.11	-
Fracture Energy of Compressive Tests (N/mm)*	7	16.00	12.51	12.83	-	5.25	-
	28	21.44	16.48	13.84	-	7.33	-

\*: Average values are tabulated.

The difference of CVC and RCC behavior on the stress-strain scale was also investigated by the stress-strain curves of CVC and RCC25 specimens on the same plot for both the 7<sup>th</sup> day and 28<sup>th</sup> day. In those comparisons, only the scaled specimens were utilized as the unscaled stress-strain curves of RCC specimens were not available. From Figure 3.13, it could be inferred that the stress-strain curves of CVC specimens have more strain capacity and their strain values at the ultimate strength are larger than the ones for RCC25 at 7<sup>th</sup> day. However, the stress-strain curves of CVC and RCC25 specimens are similar at 28<sup>th</sup> day as far as the ascending portions of the curves are concerned. However, the softening region of RCC25 specimens are steeper than the CVC ones. This may be due to the layered nature of RCC specimens as there are at least three horizontal layers in a cylindrical specimen.



These layers were not perfectly aligned in the horizontal direction, which could have led to the faster reduction in capacity during loading.

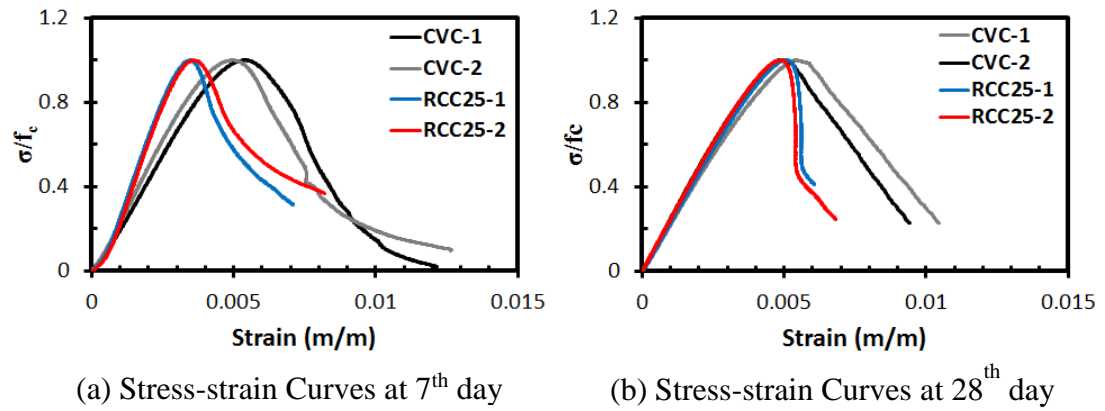


**Figure 3.13.** Comparisons of Strength Normalized Stress-Strain Curves of Scaled CVC and Scaled RCC25

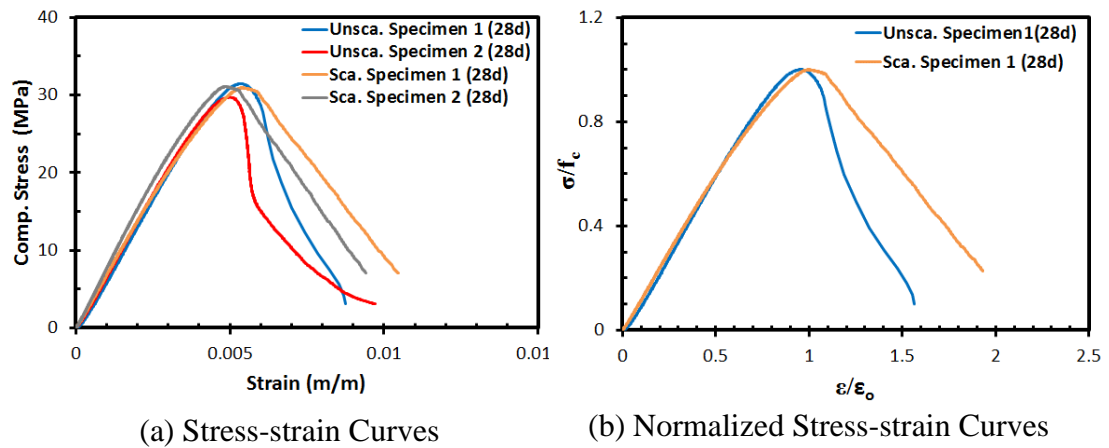


**Figure 3.14.** The Effect of Scaling on Stress-Strain Curve of CVC

The effect of aggregate scaling on the stress-strain curve characteristics was examined by drawing the stress-strain curves of the unscaled and scaled CVC specimens. From Figure 3.14 and Table 3.19, it is apparent that the scaled CVC specimens had more strain energy capacity (nearly 25% larger on average) due to their softer descending regions. This observation was probably due to the relatively more cement paste inside the scaled CVC specimens and more aggregate surface area as a result of not using coarse aggregates in the scaled CVC mixture.

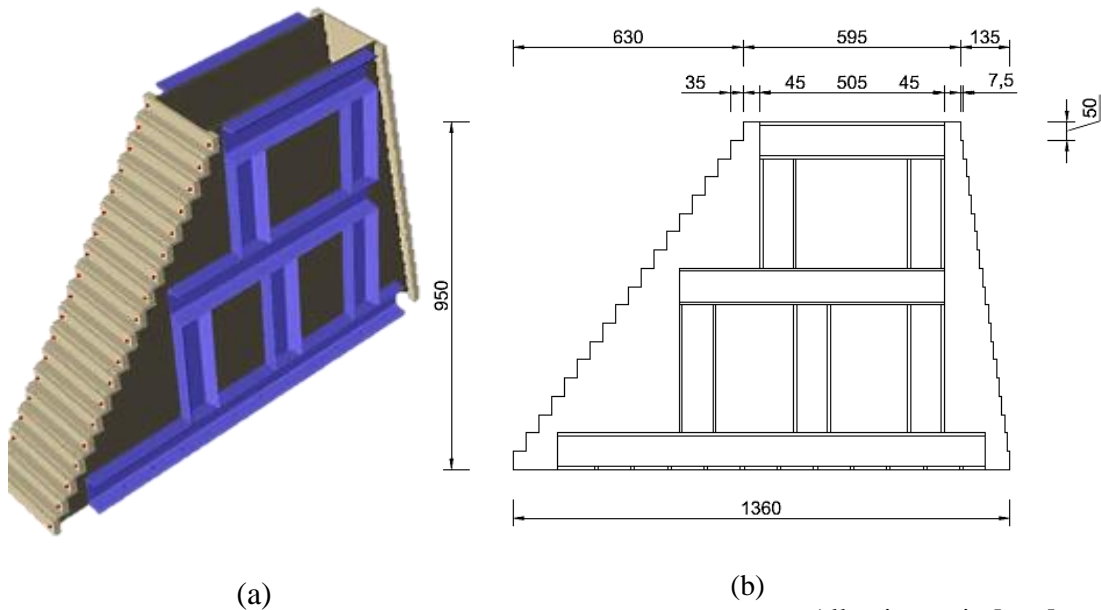
In summary, the concrete mixtures capable of producing the target compressive strengths without significantly changing the stress – strain curves were obtained (Figure 3.14). Consequently, both the scaled CVC and RCC (both RCC15 and RCC25) concretes will be utilized while building the test specimens. Results demonstrate that upon scaling of the aggregates, the target compressive and split tensile strengths of the unscaled concrete could be matched. In addition, the percentage difference in the ultimate strain (strain at 85% capacity drop) was determined as only 15% between the scaled and the unscaled CVC specimens. Furthermore, the error in the fracture energy due to scaling process was found to be in the order of about 25%.

## CHAPTER 4

### TEST SETUP AND INSTRUMENTATION OF SPECIMENS

#### 4.1 Test Setup

The formwork for the specimens was prepared by considering the stepped nature of the RCC dams and the pressure induced due to compaction during the RCC placement. The formwork consisted of 2 main steel sheets reinforced with UPN profiles to prevent excessive deformations and plate buckling. Those steel sheets were connected to each other at every 50mm by utilizing bolted steel components (Figure 4.1). This formwork was also used for the CVC placement provided that all of the bolted steel components are connected to the main plates before concrete placement as shown in Figure 4.1.a.



All units are in [mm].

**Figure 4.1.** Formwork Drawings : (a) 3D View and (b) 2D View

After manufacturing of the formwork, the test setup was prepared. At this stage, the most critical step was the design of the vertical loading system. As the vertical load to mimic the gravitational effects on the prototype dam section was determined as

400kN (detailed explanations were presented in Section 2). Such a high load precludes the use of steel gravity blocks for mimicking the vertical loading. Consequently, a loading system with tie rods and hydraulic cylinders was built for this purpose (Figure 4.2-Figure 4.4). The vertical loading system is shown in Figure 4.2. The prestressing forces on the tie rods were transferred to the dam as compressive forces through a built-up steel section. The expected change in the load for a target lateral displacement of 2mm was calculated as approximately 20kN, which corresponds to a 5-percent change (Figure 4.5). This change is due to the additional elongation demand on the tie rods.

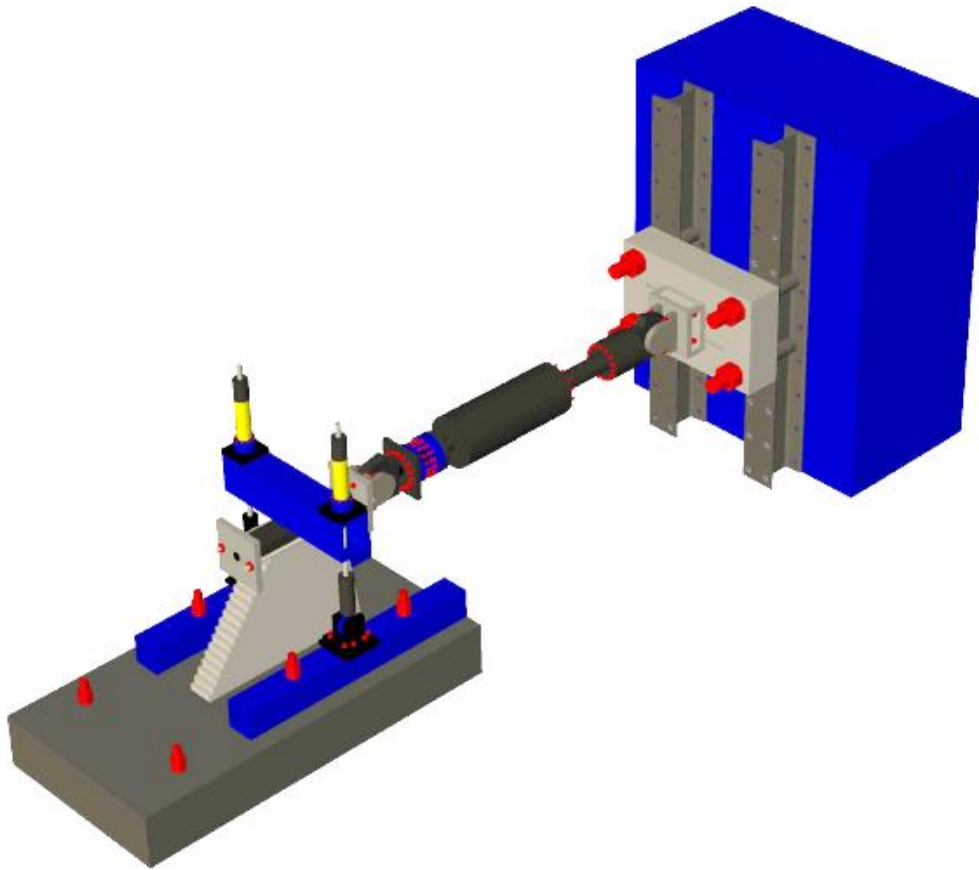


**Figure 4.2.** Test Setup (Isometric View)

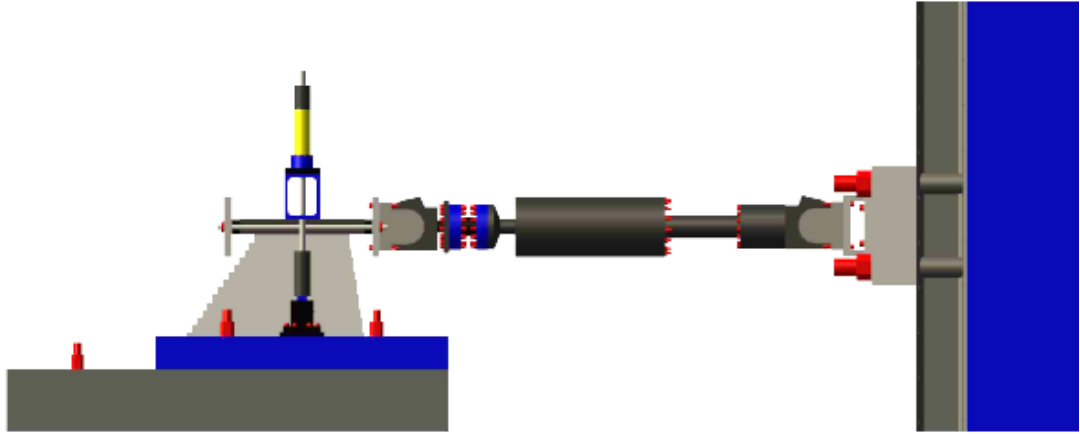


**Figure 4.3.** Test Setup (Side View)

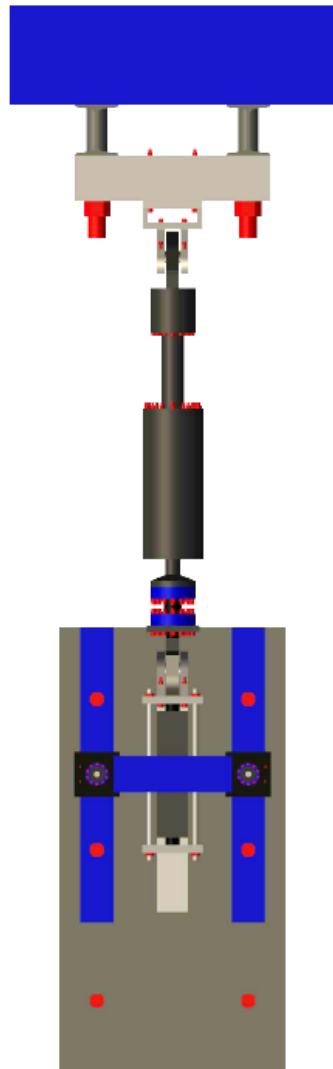
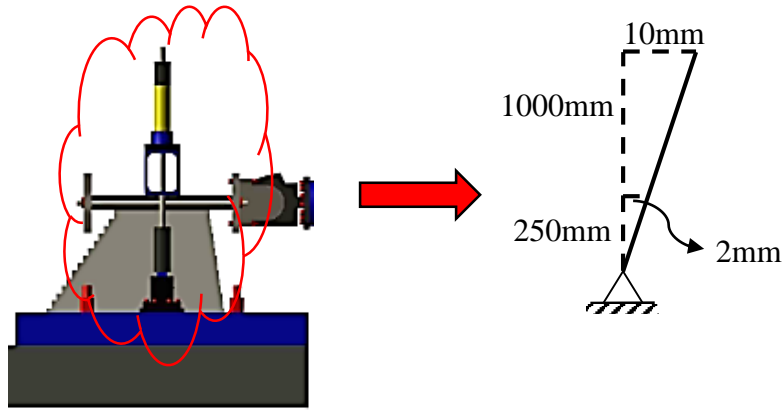


**Figure 4.4.** Test Setup (Top View)



$$\Delta P = \frac{EA}{L} * \Delta = \frac{200000 * \pi * 20^2}{1250} * 3.9994 * 10^{-2} = 8 \text{ kN for one tie rod}$$

**Figure 4.5.** Change in Axial Load

The lateral load transfer to the scaled dam specimen was also a challenging problem since the top area of specimen was a 200x595mm rectangular region. This concrete area was insufficient to transfer the estimated lateral load capacity of dam specimens, i.e. nearly 450 kN, using anchorage rods. Therefore, a specially designed threaded steel plate of 10mm thickness was used to enable the proper transferring of this lateral load to the specimen in order to prevent local damaging due to stress concentrations (Figure 4.6). The design of transfer plate was conducted based on the bearing capacity of concrete coupled with threaded steel plate.

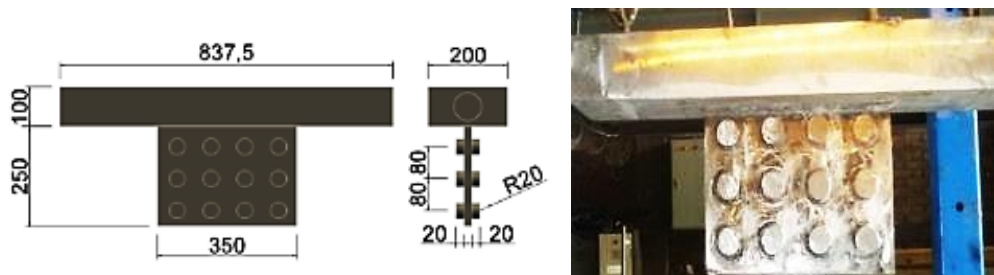


**Figure 4.6.** Transfer Plate : (a) Drawings and (b) Photo

ACI318 (2011) requires a 6mm roughness amplitude in order to classify a surface as a “rough surface”. The connection between the strong-floor and the specimen was made by roughening the foundation concrete in accordance with the ACI 318 (2011)

provisions (Figure 4.7). All specimens were cast on this rough surface by placing concrete within the formwork.

#### 4.2 Validation of the PSD System

The experimental test program in this dissertation was carried out by utilizing the pseudo dynamic testing technique proposed by Molina et al (1999). In this method, tests are conducted by solving the following equation of motion:

$$M * a^i + C * v^i + R^i = -M * a_g^i \quad (4.1)$$

where  $M$  is the mass,  $C$  is the viscous damping,  $R^i$  is the restoring force vector,  $a^i$ ,  $v^i$  are the acceleration and velocity of the associated degree of freedom, respectively, and  $a_g^i$  is the ground acceleration at time  $i$ . Numerical mass values, which will be discussed later, are utilized during the pseudo dynamic testing for each ground motion. The hysteretic damping of the structure is accounted by the physical testing of the specimens. Therefore, the viscous damping is assumed to be zero, consistent with the approach proposed in the literature (Bertero et al 1984 and Elkhoraibi and Mosalam 2007). The equation of motion is solved by explicit Newmark time integration. In this procedure, the time step integration of equation of motion is carried out by directly determining the displacements and velocities at time step  $n+1$  from the displacements ( $D_n$ ) and velocities ( $V_n$ ) at time step  $n$  by utilizing Eq. 4.2.

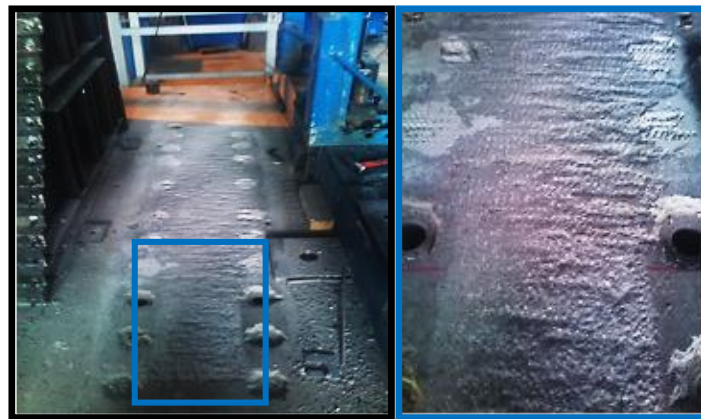


**Figure 4.7.** Intentionally Roughened Foundation Concrete

$$\begin{aligned}
d_{n+1} &= d_n + v_n \Delta t + \frac{a_n \Delta t^2}{2} \\
a_{n+1} &= (M + C \Delta t)^{-1} \left[ F_{n+1} - R_{n+1} - C v_n + \frac{\Delta t C a_n}{2} \right] \\
v_{n+1} &= v_n + \frac{\Delta t (a_n + a_{n+1})}{2}
\end{aligned} \tag{4.2}$$

where  $F$  is the external applied force and  $\Delta t$  is the time step size.

The steps in the integration scheme, the detailed explanations for which could be found in Molina et al (1999) are as follows:

- 1) Determine the displacements at time step  $n+1$  (Eq. 4.2).
- 2) Impose these displacements to the structure and measure the restoring force ( $R_{n+1}$ ).
- 3) Compute the acceleration at time  $n+1$  (Eq. 4.2).
- 4) Calculate the velocities at time step  $n+1$  (Eq. 4.2).
- 5) Repeat all steps for the remaining time steps.

In this testing system, similar to the European Laboratory for Structural Assessment (ELSA) system, Proportional-Integral-Derivative (PID) control algorithm is utilized to apply the target displacement to the test specimen continuously by the actuators. In this control method, the difference between the target and the measured variable, i.e. tip displacement, is determined. The purpose of the PID controller is to minimize this difference. In other words, PID control algorithm has three parameters: the proportional (P), the integral (I) and the derivative (D) values (Eq. 4.3). Those parameters are also called as present error (P), sum of past errors (I) and predicted future errors (D). The error in the target displacement is calculated by the weighted sum of these parameters (Eq. 4.3) and the measured displacement is adjusted by this error. Then, the controller forces the measured displacement to approach the target counterpart in a few iterations via a control valve.

$$E(t) = K_p e(t) + K_i \int_0^t e(\tau) d\tau + K_d \frac{d}{dt} (e(t)) \tag{4.3}$$



where  $K_p$  is proportional gain constant,  $K_i$  is integral gain constant,  $K_d$  is derivative gain constant,  $e(t) = \text{Target Displacement} - \text{Measured Displacement}$ ,  $t$  is present time,  $\tau$  is time integration variable used in iterations.

At this stage, it should be stated that the feedback information in the testing system is obtained from the high precision displacement transducer (Heidenhain) as this controlling strategy is claimed as accurate and stable due to being a displacement control strategy by Molina et al (1999).

The gain constants ( $K_p$ ,  $K_i$  and  $K_d$ ) should be determined from preliminary experiments after selecting the feedback variable and type. The optimum values for these constants for a stiff (and flexible) system is selected by conducting preliminary tests on a steel frame (Figure 4.8). The fundamental period of this frame was adjusted to test both stiff and flexible structures under the effect of El Centro and MCE ground motions (Figure 4.9). While selecting the ground motions, the frequency contents of motions were taken into account. El Centro motion, which is rich in low-frequency waves (Figure 4.10.a), was used to test a frame with a fundamental period of 1.01 sec. The MCE motion, which is rich in high-frequency waves (Figure 4.10.b), was utilized to examine the behaviour of a frame with a fundamental period of 0.07 sec, very close to the fundamental period of scaled dam specimens. Two different systems from a single frame were tested by changing the numerical mass on the pseudo dynamic system, i.e. numerical mass of 200t for El Centro and 0.4t for MCE, resulting in periods of 1.01sec and 0.07sec, respectively.

For the preliminary tests, an L-shaped frame was mounted to the base by using two pins. For the sake of examining the SDFS performance of the testing system, the force was applied to L-shaped steel frame at its top by utilizing single piston (Figure 4.11). The feedback information was selected as the tip displacement of L-shaped frame (Figure 4.12) and the feedback was obtained by utilizing Heidenhain. The low frequency system was obtained by selecting a large mass whereas the high frequency system was generated by utilizing a small mass.

The tip displacement and base shear histories from both the pseudo dynamic test and analytical simulation (elastic SDFS analysis) are presented in Figure 4.13 and Figure 4.14. From those figures, it can easily be inferred that the values obtained by solving an elastic SDFS system for these two different systems match the ones obtained from pseudo dynamic tests. Consequently, the pseudo dynamic test system was validated to work properly with the selected gain constants of  $K_p=1.0$ ,  $K_i=1/250$  and  $K_d=0.0$  both for the long and the short-period structures.

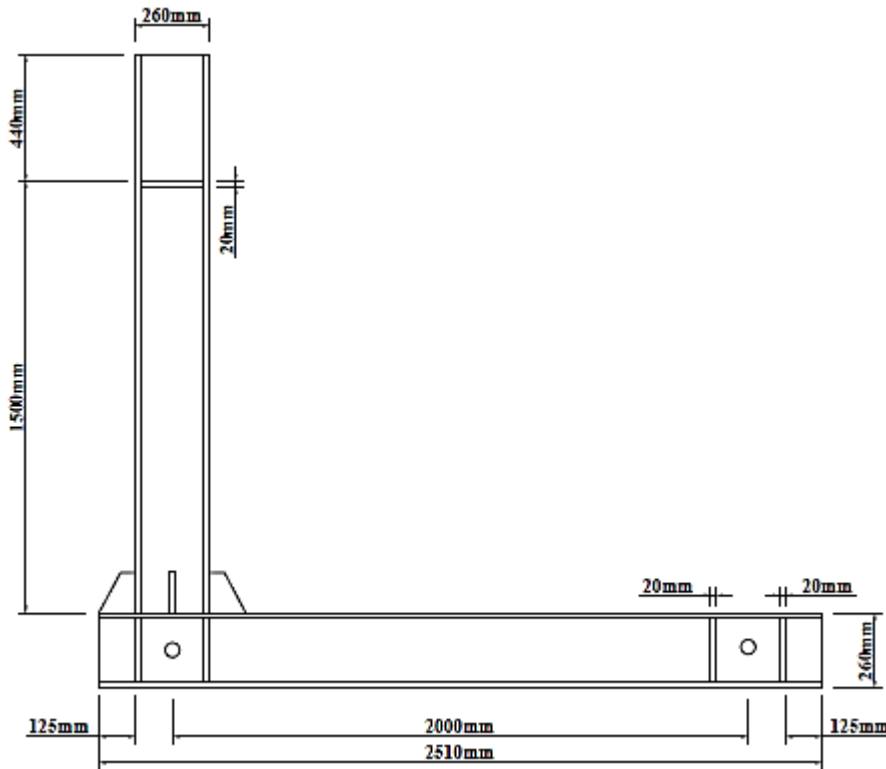


**Figure 4.8.** Verification Frame

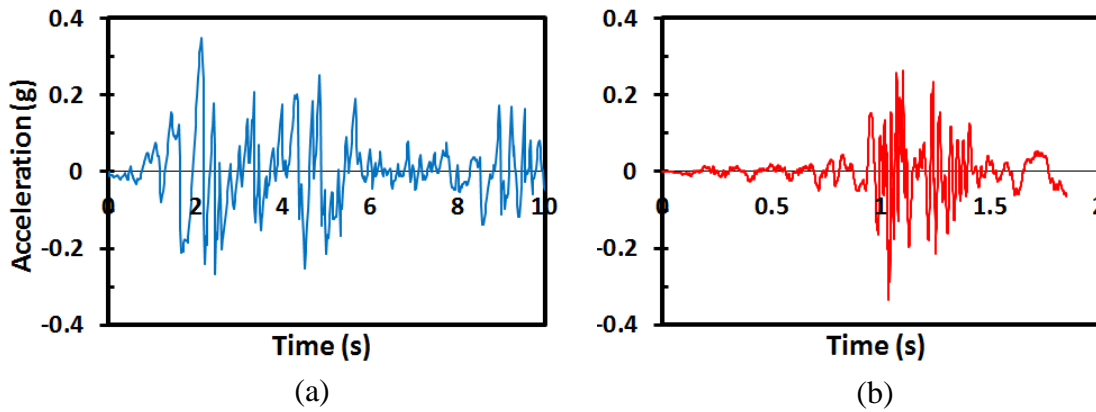


**Figure 4.9.** Ground Motions : (a) El Centro and (b) MCE

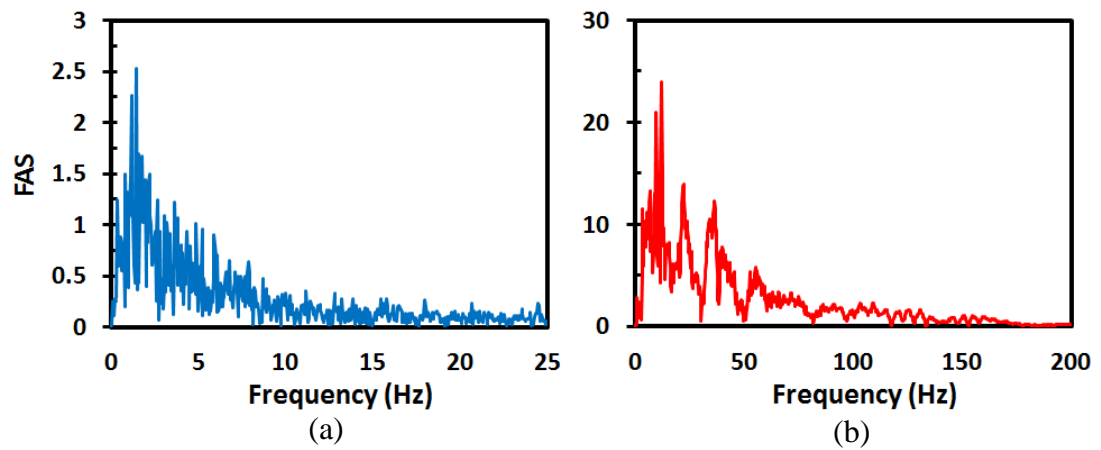


**Figure 4.10.** Fourier Amplitude Spectrums : (a) El Centro and (b) MCE

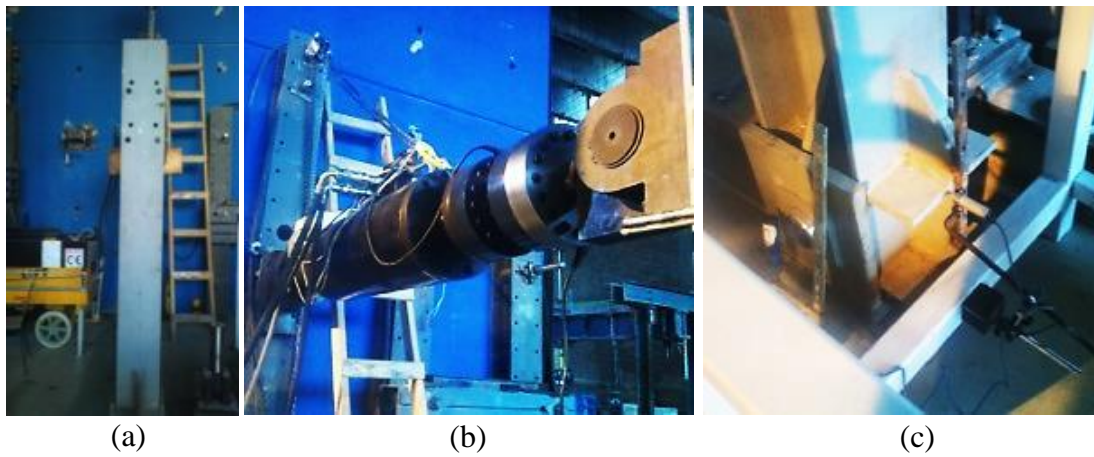


**Figure 4.11.** Verification Frame Photos: (a) L-shaped Steel Frame; (b) Pin-ended Piston and (c) LVDT to Measure Base Sliding

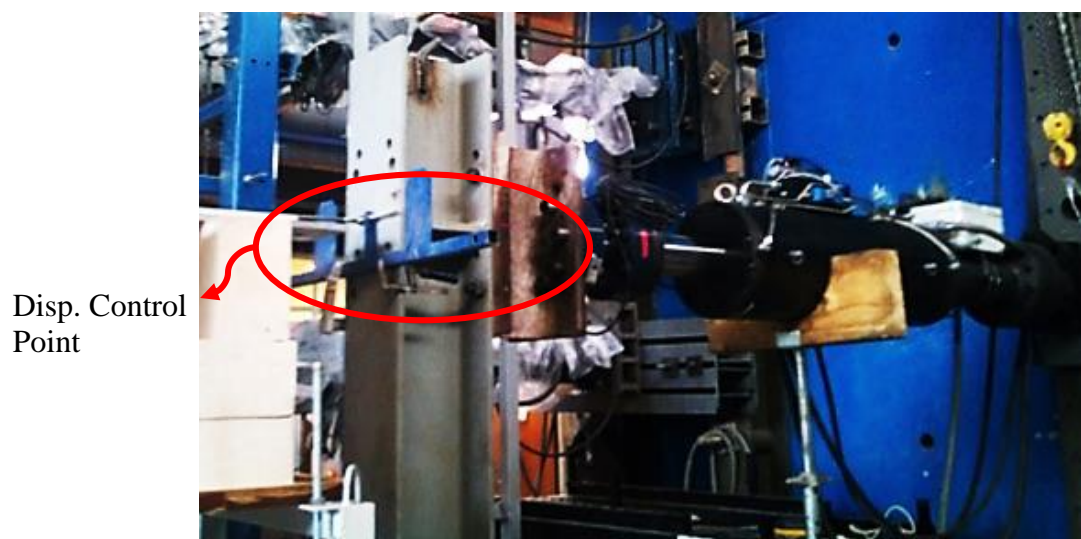


**Figure 4.12.** Feedback Point

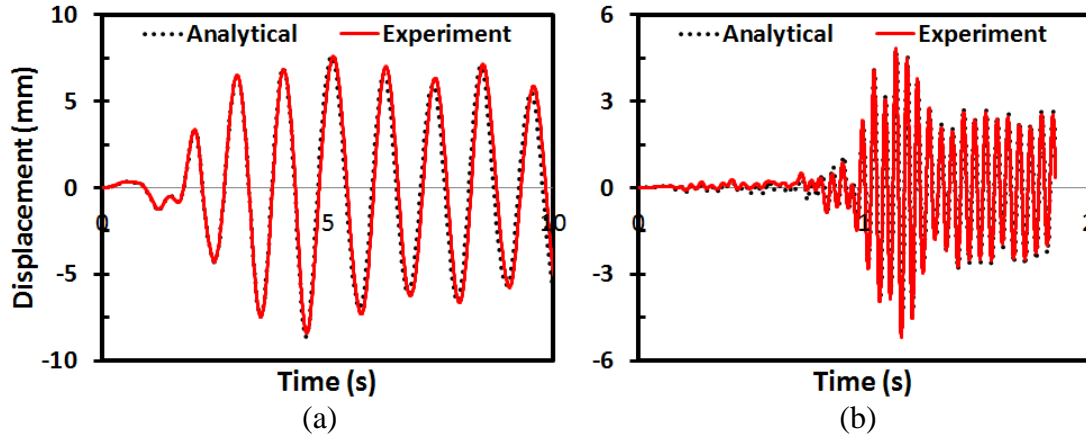


**Figure 4.13.** Comparison of Tip Displacements : (a) El Centro and (b) MCE

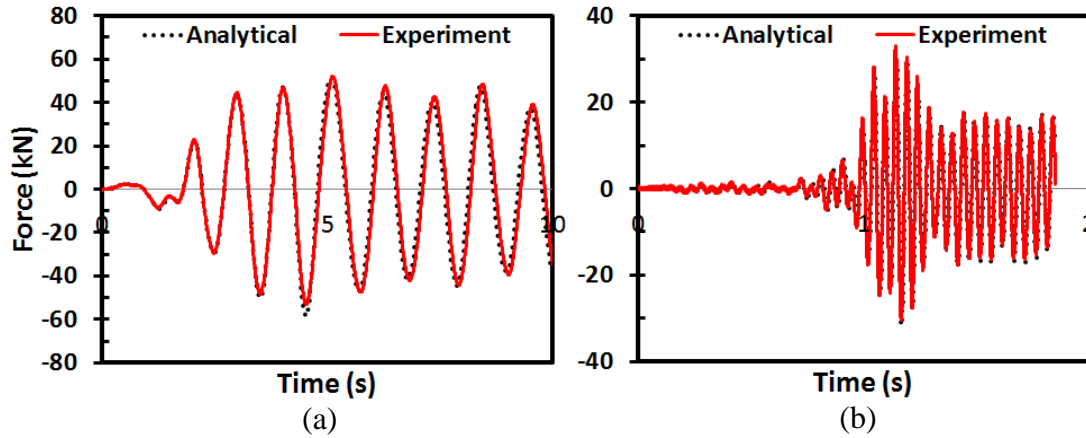


**Figure 4.14.** Comparison of Base Shears : (a) El Centro and (b) MCE

### 4.3 Instrumentation

Linear variable differential transducers (LVDTs) were installed to record the lateral and vertical movements of dam base in both upstream and downstream directions (Figure 4.15.a and 4.14.b). In addition, three different LVDTs were installed at the top of the specimen. One of the LVDTs was used to check the feedback information supplied by a high precision displacement transducer (Heidenhain with accuracy of  $\pm 10 \mu\text{m}$ ) to the pseudo dynamic system (Figure 4.15.c). This high precision displacement transducer was used to provide the displacement feedback of the specimen at the top while executing the pseudo dynamic test. The other one was placed to measure the relative displacement of the top of test specimen with respect to its base (Figure 4.15.d). The third one was set up on directly concrete just below

the transfer plate in order to detect the slip at the interface of transfer plate and concrete portion (Figure 4.15.d).

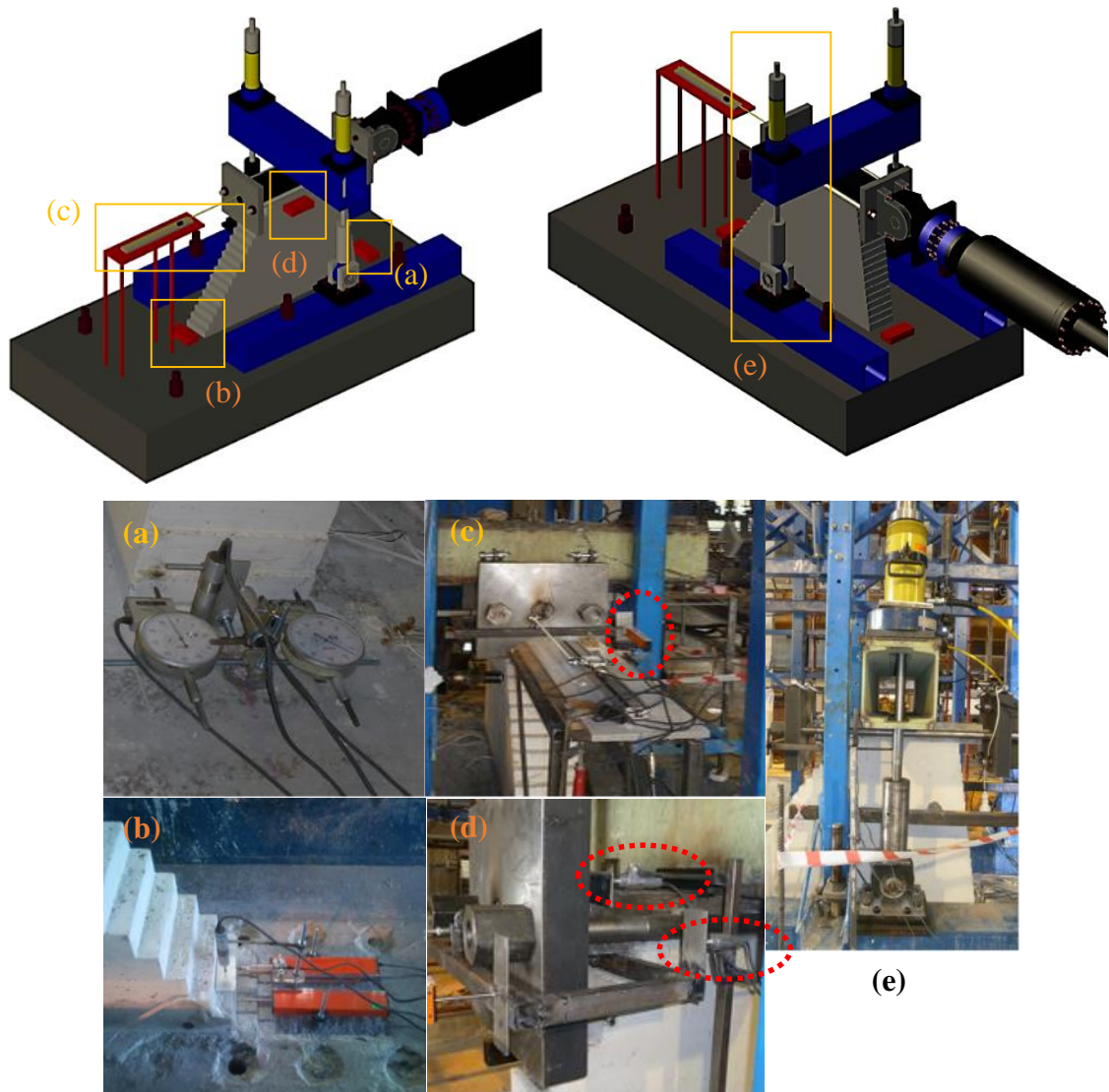


**Figure 4.15.** Test Setup and Instrumentation : (a) LVDT's at Upstream Dam Base, (b) LVDT's at Downstream Dam Base, (c) High Precision Displacement Transducer, (d) LVDT's at the Dam Tip and (e) Static Axial Load Application Setup

As given in the Section 4.1, first a vertical load was applied to the specimen in order to simulate the gravity induced effects. The loading system was built with tie rods and hydraulic cylinders (Figure 4.15.e) for this purpose. The prestressing forces on the tie rods were transferred to the dam as compressive forces through a built-up steel section (The change in the prestressing force, varying by less than 10% during the experiments, did not significantly affect the results as shown in Chapter 5.). Keeping this vertical load constant, the hydrostatic load (174 kN) was applied to the



specimen using an hydraulic jack. The execution of the pseudo dynamic testing was initiated by assuming at rest conditions with zero lateral force.

After the installation of the LVDTs, strain rosettes were placed at the base of the dam to record the strains and to determine the direction of principal strains. Rosettes having 1cm capacity were bonded directly to the concrete specimen in every 20 cm except for the first one in the upstream direction that was placed 10 cm away from the next rosette (Figure 4.16). This decision was mainly due to the expected crack formation on the upstream face of the specimen.

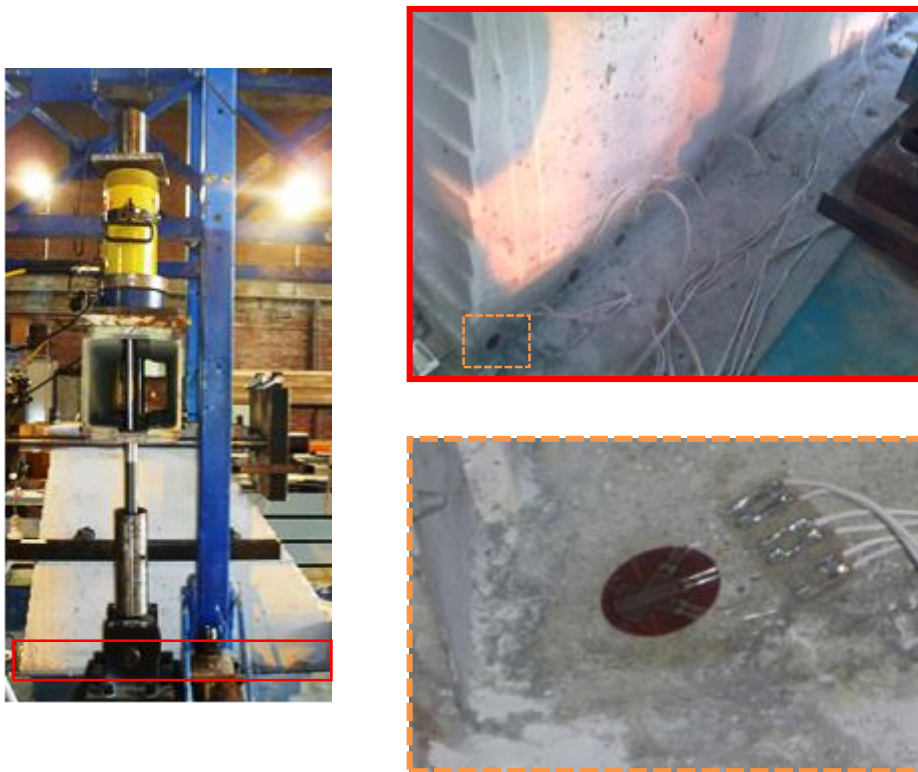


**Figure 4.16.** Strain Rosettes at the Dam Base

The only change in the instrumentation among the three specimens was the location of high precision displacement transducer in Specimen 3 (RCC25). In this specimen, the high precision displacement transducer was directly attached to the dam specimen instead of connecting it to the lateral load transfer system (steel plates around the dam specimen). For this specimen, the initial stiffness of the specimen was found to be affected by the load transfer plate. To remedy this situation, such a change in the location of Heidenhain was conducted. The attachment was conducted

by eliminating extra elements between the dam specimen and the high precision displacement transducer by drilling the steel plate at the back side of the dam (Figure 4.17).



**Figure 4.17.** Test Setup and LVDT's for Tip Displacement Recording in Specimen 3

#### 4.4 Specimens

All the specimens were built and tested in Structural Mechanics Laboratory of Middle East Technical University. The details of specimen preparation are presented in the following pages.

#### 4.4.1 Specimen 1: CVC Gravity Dam

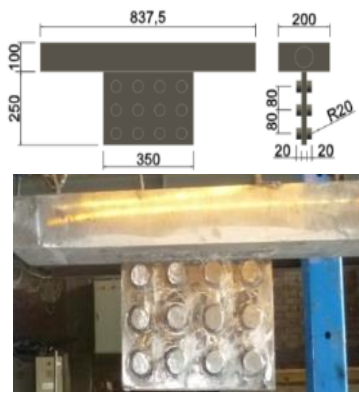
The first scaled dam specimen was made up of CVC concrete. The target compressive strength of concrete was selected as 25 MPa. The concrete mixture was prepared by utilizing the mixture design ratios given in Chapter 3. The specimen was directly cast on rough surface as described in Chapter 4.1. Therefore, the formwork was placed on the available concrete foundation. Then, silicone based adhesives were applied to prevent leakage of concrete grout from the voids (Figure 4.18). While placing the concrete inside the formwork. The concrete was vibrated from both inside and outside to ease the settling.



**Figure 4.18.** Preparation of Specimen : (a) Formwork, (b) Concrete Placement and (c) Vibration for Concrete Settling

The specially designed threaded steel plate was used to enable the proper transferring of lateral load to the specimen in order to prevent local damaging due to stress concentrations. This plate was placed inside the fresh concrete by the aid of vibration and hammering (Figure 4.19). After concrete placement, the formwork was removed and the concrete was cured to prevent the water loss by using absorptive covers, i.e. wet canvas. These covers were watered once a day for seven days (Figure 4.20). The average compressive and split tensile strengths and the modulus of elasticity of the specimen were obtained as 24.95 MPa, 2.60 MPa and 20,500 MPa, respectively, using cylinder tests at the testing day.





(a)



(b)



(c)



(d)

**Figure 4.19.** Transfer Plate: (a) Details, (b) Transportation of Plate, (c) Alignment of Plate and (d) Placement inside Fresh Concrete



(a)

(b)

**Figure 4.20.** Curing : (a) Wet Covers and (b) Specimen after Curing

#### 4.4.2 Specimen 2: RCC Gravity Dam 1

The second scaled dam specimen was produced from RCC. The target compressive strength of concrete was selected as 15 MPa. The formwork was placed and fixed on the available concrete foundation. Then, the concrete was placed into the formwork in layers of nearly 2.5cm thickness (Figure 4.21). After that, 0.20x0.20x0.02m steel plate (Figure 4.21.a) was placed to compact the concrete layer. The compaction process was performed starting from the downstream face to the upstream face of the dam specimen in portions of 20 cm length by using the pneumatic compactor (Figure 4.21.d). After completing the concrete placement of a 5cm-high layer, the side plates of the formwork were mounted (Figure 4.21.e). During RCC placement, the time period between two lift joints was 5 – 10 min so there was no cold joint formation inside the dam body.

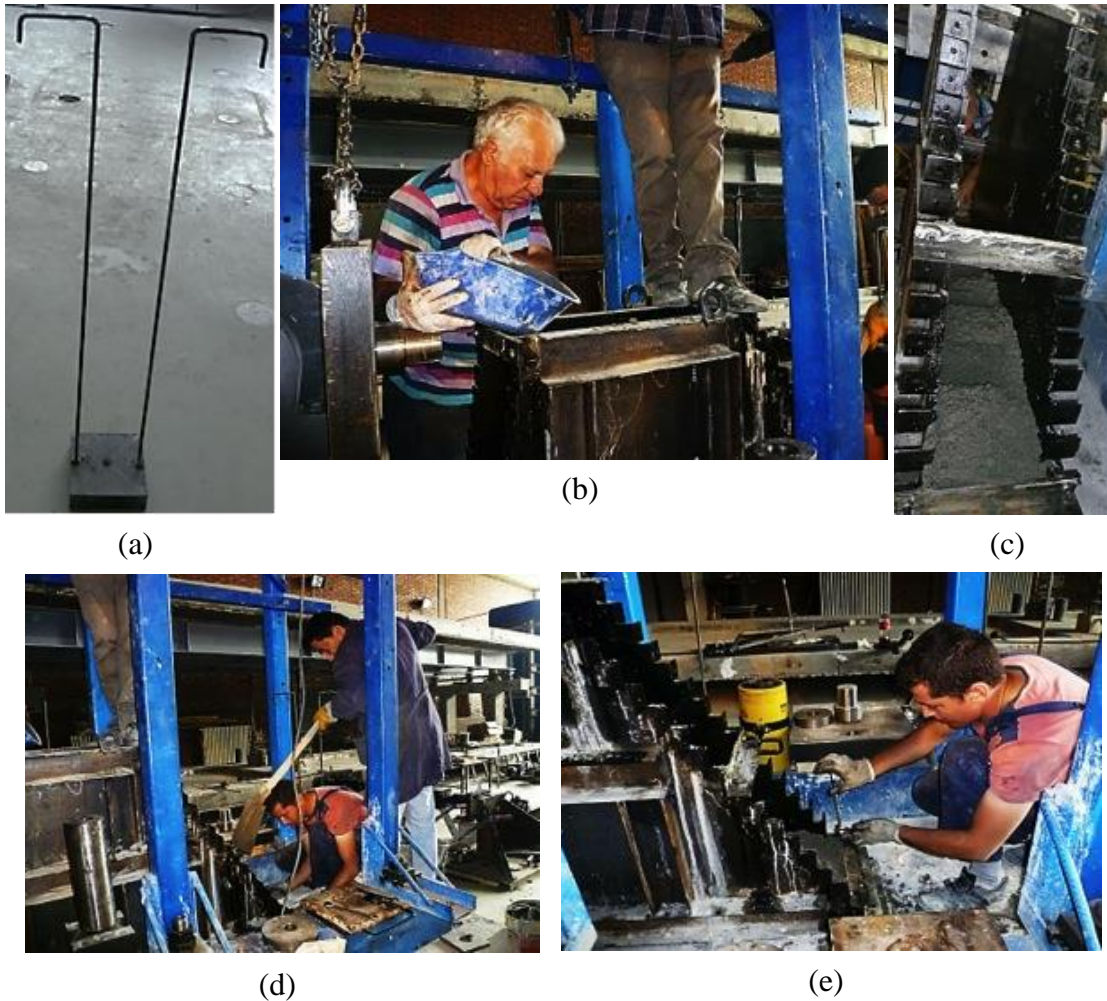


**Figure 4.21.** Preparation of Specimen : (a) Compaction Plate, (b)-(d) Concrete Placement and (e) Montage of Formwork Side Plates

As the compaction effort has a positive effect on the concrete strength, the compaction energy transferred at the site should be simulated properly in the laboratory environment. To this end, the compaction energy on a unit concrete area was targeted to be the same for both the prototype and the scaled dam specimens. In the calculations, the technical properties of the compacting cylinder Caterpillar CS563E and the pneumatic compactor Makita 5201C (Hilti) were utilized (Table 4.1).

**Table 4.1.** Specifications of Compaction Machines

	<b>Velocity (v)</b>	<b>Force (F)</b>	<b>Frequency (f)</b>	<b>Displacement Amplitude (<math>u_{max}</math>)</b>
<b>Caterpillar Cylinder</b>	1.39 m/s	266 kN	30 Hz	1.7 mm
<b>Makita Hilti</b>	-	0.74 kN	25 Hz	1 mm

The dimension of contact surface of Caterpillar Cylinder was determined as 2.13mx0.2m. Therefore, the time to travel 0.2m was calculated as

$$t = \frac{u}{v} = \frac{0.2}{1.39} = 0.144 \text{ s}$$

The total number of strokes ( $N_s$ ) on the contact surface was

$$N_s = f_s * t = 30 * 0.144 = 4.32$$

The total energy ( $E_s$ ) transferred to the contact surface was

$$E_s = F * u_{max} * N_s = 266000 * 1.7 * 10^{-3} * 4.32 = 1953.5 \text{ N.m}$$

The compaction energy on a unit concrete area ( $EoUCA$ ) was

$$EoUCA = \frac{E_s}{A_s} = \frac{1953.5}{2.13*0.2} = 4577.1 \text{ N/m}$$

The time sufficient to transfer the same compaction energy on a unit concrete area by Makita Hilti could be calculated as follows:

$$EoUCA = \frac{E_h}{A_p} = \frac{E_h}{0.2*0.2} = 4577.1 \text{ N/m} \Rightarrow E_h = 183.1 \text{ N.m}$$

$$E_h = F * A * N_s = 740 * 1 * 10^{-3} * N_h = 183.1 \text{ N.m} \Rightarrow N_h = 247.4$$

$$N_h = f_h * t = 25 * t = 247.9 \Rightarrow t = 9.9 \text{ s}$$

In the light of the above calculations, 10-second compaction could generate the same compaction energy on a unit concrete area if a 0.20x0.20m plate area was used. However, the compaction time should be reduced while placing standard cylindrical specimens (h=0.30m and d=0.15m). The corresponding compaction time for those specimens was approximately 5s.

The placement of the transfer plate inside RCC was impossible due to the lack of fluidity. Therefore, the top 30cm of the dam specimen was built by placing CVC having a target compressive strength of about 20 MPa. Concrete for the top part was designed to have a high fluidity provided by relatively high water – cement ratio (75%) and by adding some plasticizers. This CVC was placed immediately after completing RCC placement so that the cold joint formation between the RCC and CVC was eliminated. Thus, the transfer plate was placed inside the fresh concrete by aid of vibration and hammering (Figure 4.22). After concrete placement, the formwork was removed and the concrete was cured to prevent the water loss by using absorptive covers. These covers were watered once a day for seven days. The average compressive and split tensile strengths and the modulus of elasticity of the specimen were obtained as 15.6 MPa, 1.12 MPa and 14,905 MPa, respectively, using cylinder tests at the testing day.

#### **4.4.3 Specimen 3: RCC Gravity Dam 2**

The preparation of Specimen 3 was similar to that of Specimen 2, the only change being the employed materials (Figure 4.23).

The compaction procedure explained in Chapter 4.4.2 was also utilized for this specimen. Similar to the second specimen, the top 30 cm of the dam specimen was built by CVC having a compressive strength of 40 MPa. Thus, the transfer plate was placed inside the fresh concrete by aid of vibration and hammering. After concrete placement, the formwork was removed and the concrete was cured to prevent the water loss by using absorptive covers. These covers were watered once a day for



seven days. The average compressive and split tensile strengths and the modulus of elasticity of the specimen were obtained as 23.10 MPa, 1.95 MPa and 21,305 MPa, respectively, using cylinder tests at the testing day.

#### 4.5 Testing

The pseudo-dynamic test procedure was initiated with the application of the vertical load ( $F_v$ ) of 400 kN to mimic the gravitational actions on the prototype dam. Then, the specimen was pushed by a lateral force ( $F_h$ ) of 174 kN in order to simulate the hydrostatic effects.

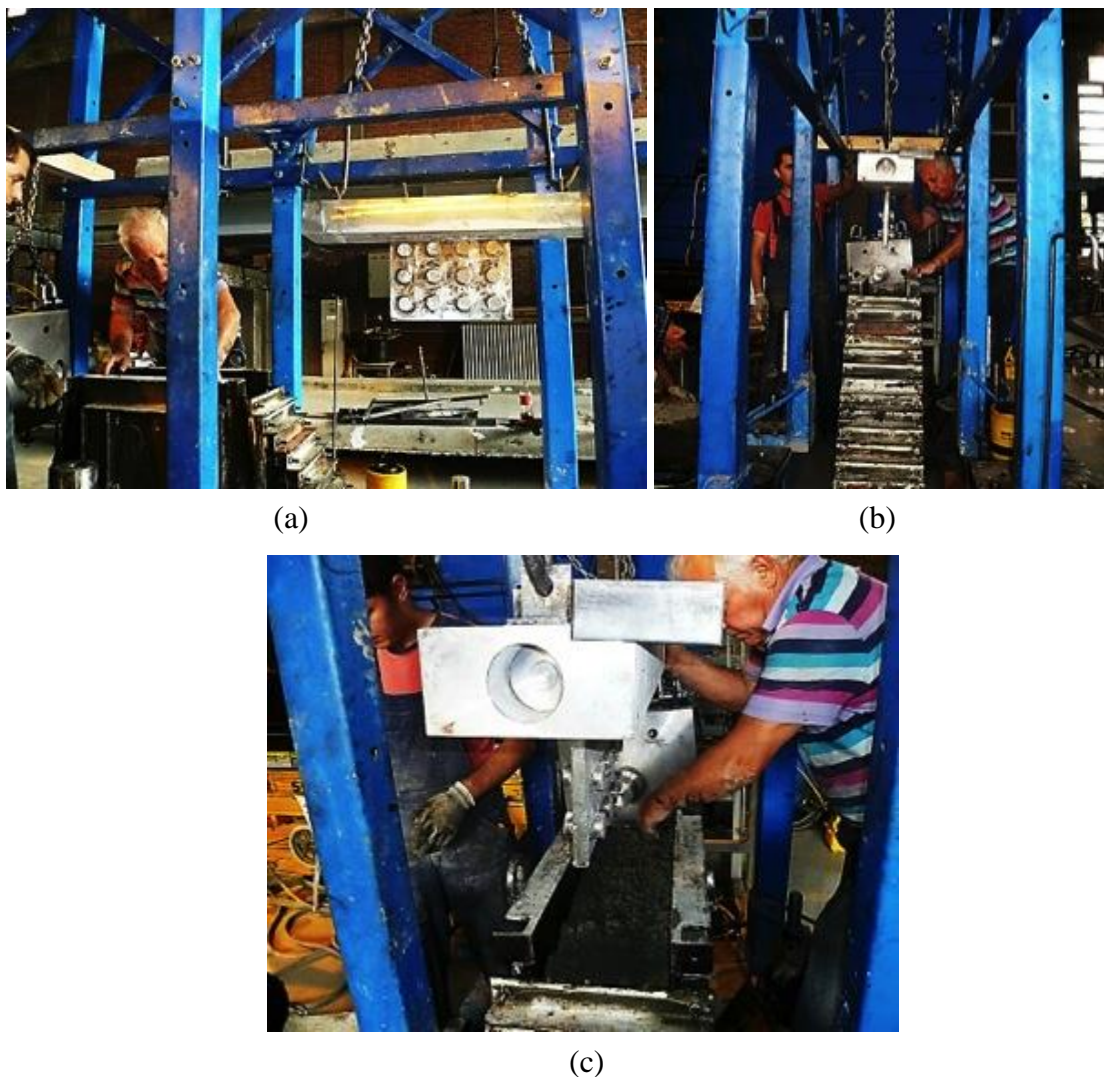


**Figure 4.22.** Transfer Plate: (a) Details, (b) Transportation of Plate, (c) Alignment of Plate and (d) Placement inside Fresh Concrete



**Figure 4.23.** Preparation of Specimen : (a) Placement of Concrete, (b) Compaction, (c) Compacted Concrete Layer, (d)-(e)

The PSD algorithm was executed by assuming at rest conditions, zero force and displacement. Another data acquisition system was used to record the experimental data without resetting the vertical and lateral load effects. Three ground motions, namely the OBE, MDE and MCE time histories presented in the Chapter 2, were applied to the test specimen. Between the ground motions, the test was stopped, the vertical force was removed and the system was checked. Then, an initial test was conducted to determine the new lateral stiffness of the specimen, which was required to determine the necessary numerical mass for the next ground motion. All the initial conditions were set to zero, the numerical mass was input to its relevant value and

the consecutive testing was initiated. For each earthquake scenario, the recorded tip and sliding displacements along with the observed crack patterns are presented in the following sections. It should be reminded that the horizontal and lateral force values were determined with the calibration procedure presented in detail in this chapter. After completing all the ground motion scenarios, a lateral load pushover test was conducted in order to estimate the load-deformation capacity and the ultimate conditions of each specimen.





## CHAPTER 5

### EXPERIMENTAL RESULTS

This chapter presents the results from the testing of three scaled dam models by using the PSD method. Results are given in terms of measured engineering demand parameters such as the forces, displacements and the strains along with the observed cracking patterns. The chapter is concluded with a detailed discussion of results towards a better understanding of seismic dam response.

#### 5.1 Specimen 1: CVC Gravity Dam

##### 5.1.1 Hydrostatic Loading

The base shear force versus tip displacement (measured 950mm from base by using Heindenhain) and base shear force versus base displacement (measured 25mm from base by using 10-mm LVDT as shown in Figure 4.15) curves during hydrostatic loading are presented in Figure 5.1.

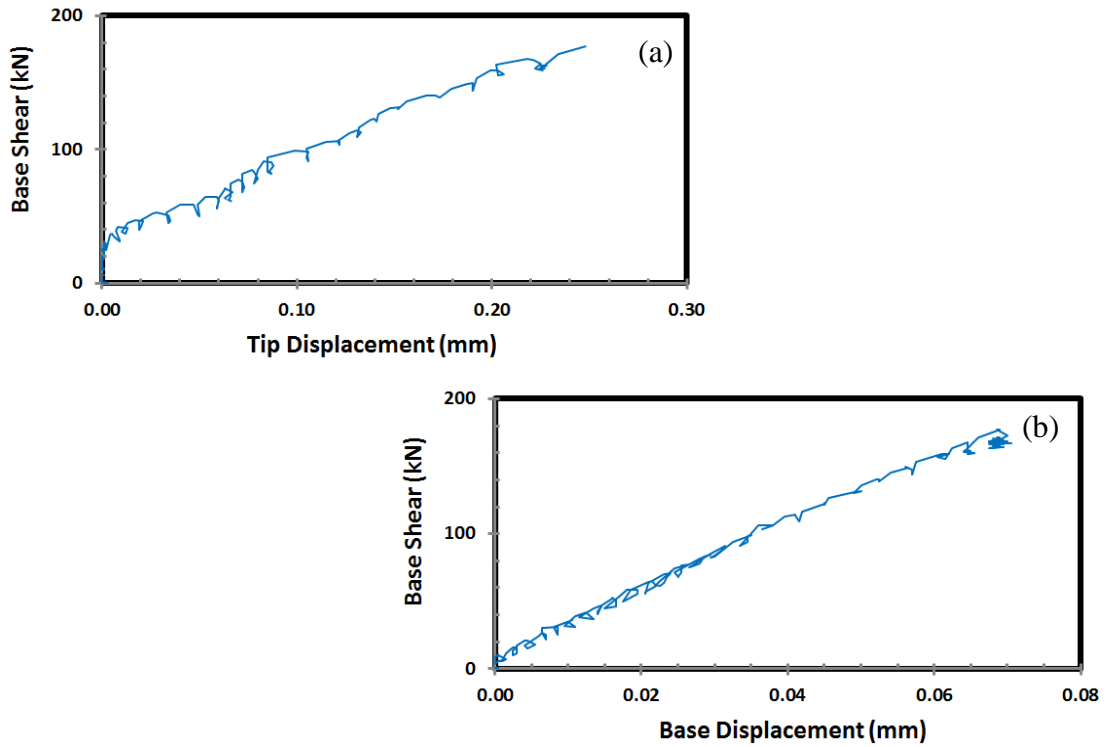


**Figure 5.1.** (a) Base Shear – Tip Displacement and (b) Base Shear – Base Displacement Curves during Hydrostatic Loading for Specimen 1

From this figure, it is apparent that the specimen remained in the linear elastic range, i.e. without any change in the slope of the load deformation curve, although some micro-cracking having widths remaining below 0.1 mm was observed at the base of the upstream face (Figure 5.2). The observed cracks had negligible effect on the lateral stiffness of the specimen as both their widths and lengths were very small.

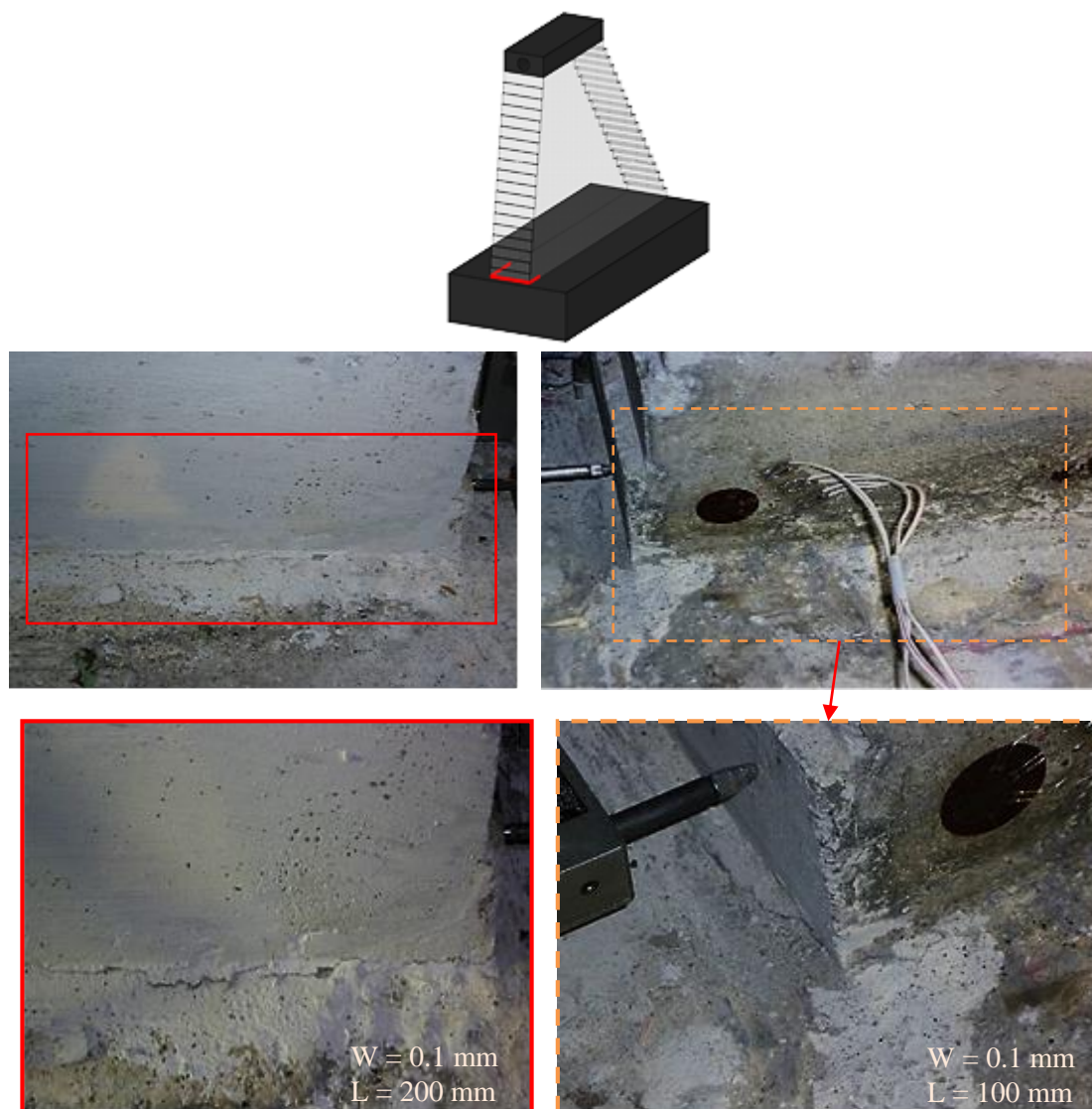


**Figure 5.2.** Cracks Formed during Hydrostatic Loading for Specimen 1

## 5.1.2 PSD Testing

### 5.1.2.1 OBE

The recorded base shear, tip displacements, base displacement and axial force histories during the first level of earthquake, OBE, are presented in Figure 5.3. The base shear-tip displacement response of the test specimen is also given in Figure 5.3.

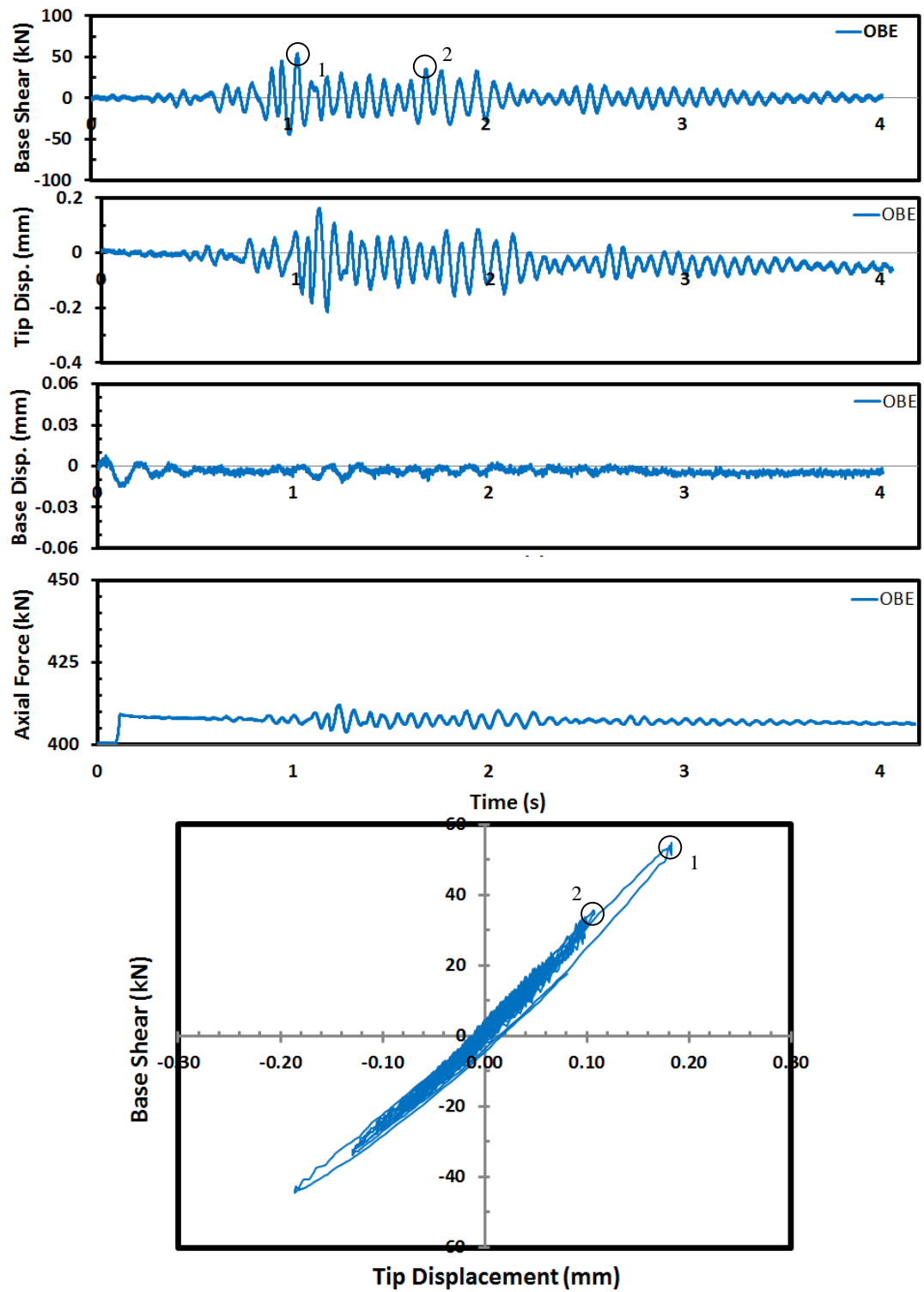


**Figure 5.3.** Force and Displacement Demands during OBE Experiment for Specimen 1

The recorded base uplift and rotation demands are shown in Figure 5.4. The locations of significant damage on the system for the OBE motion are presented in Figure 5.5.

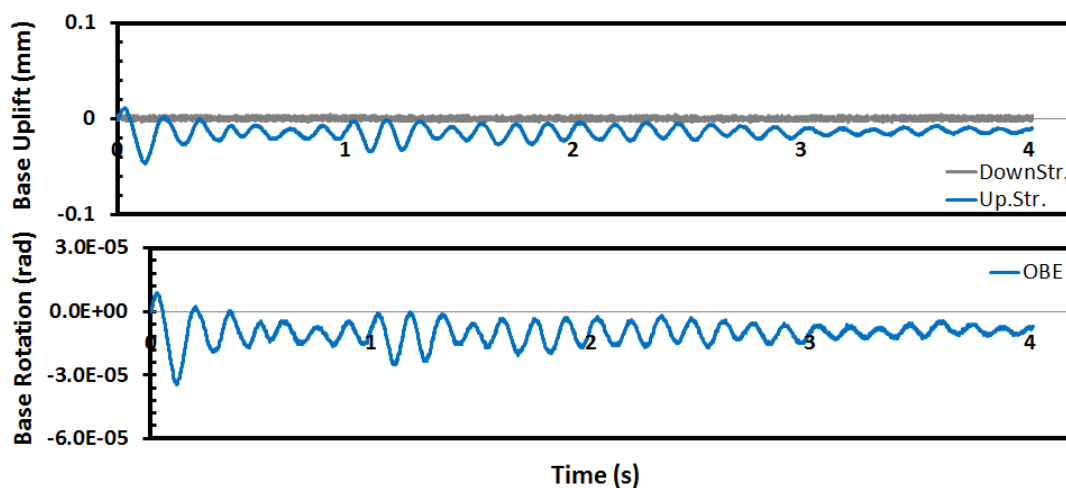


**Figure 5.4.** Base Uplift and Rotation Demands during OBE Experiment for Specimen 1

There were two peak demands that caused cracks. At the first peak, i.e. at 1.10sec, the base crack propagated 150 mm towards the downstream side with the maximum crack width reaching 0.2 mm (Figure 5.5). Then, this crack propagated 50 mm more reaching a total length of 400 mm and a crack width of 0.3 mm at the second peak, i.e. at 1.75sec. In addition, no crack formation at the downstream face of the dam was detected. The maximum base shear and the tip displacement demands were measured as 55 kN and 0.20 mm, respectively (Figure 5.3). From the recorded force-deformation curve, it was clear that the lateral stiffness of the specimen did not exhibit any significant reduction despite the observed cracking. The maximum deformation at the base was less than 0.05mm and the applied axial load did not change more than 5%, showing the success of the axial loading system in maintaining the axial force.

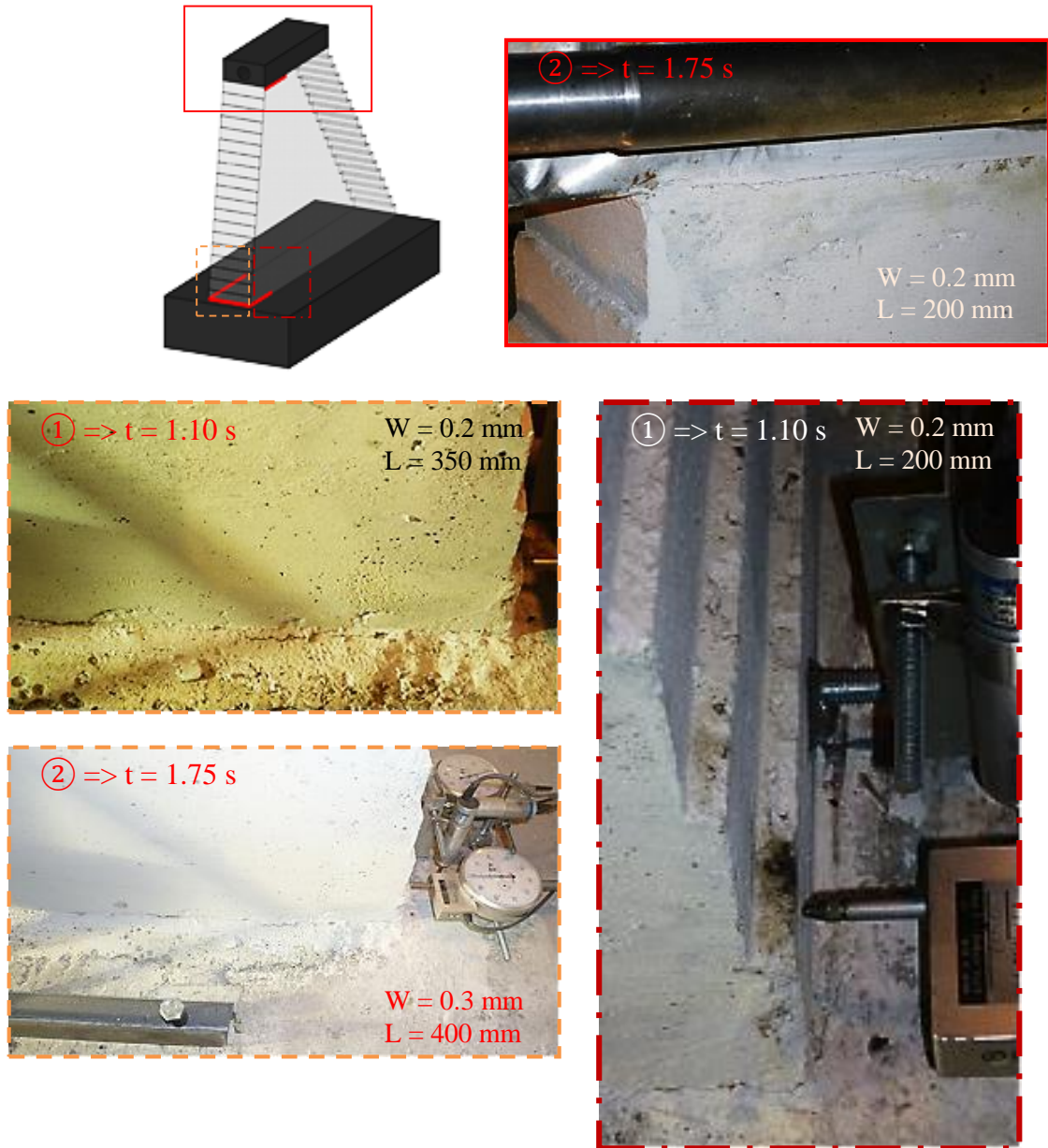


**Figure 5.5.** Cracks Formed during the OBE motion for Specimen 1

#### 5.1.2.2 MDE

The obtained base uplift and rotation demands are shown in Figure 5.6. The recorded base shear, tip displacements, base displacement and the axial force histories during the second hazard level, MDE, are presented in Figure 5.7. The base shear-tip displacement response of the test specimen is given in Figure 5.7. The locations of significant damage on the system for the MDE motion are presented in Figure 5.8.

The maximum tip displacement was obtained as 0.31 mm, corresponding to a maximum base shear demand of 69 kN (Figure 5.7). The increase in the displacement and force demands with respect to the OBE level were about 15% and 25%, respectively. Consequently, MDE level testing resulted in an increased crack (550mm) and width (0.4mm) (Figure 5.8). In addition to the cracking at the base, another crack at the body in the upstream face was initiated at 2.10 sec, which was the second peak demand during MDE motion (Figure 5.7 and Figure 5.8). In addition, no crack formation at the downstream face of the dam was detected. Similar to the first level of earthquake, the lateral stiffness of the specimen was nearly unchanged. The base deformation was also less than 0.05mm during this level as well (Figure 5.7). Although a permanent base deformation of 0.02mm were observed, this deformation was not interpreted as a sliding deformation because there were no sudden jumping throughout the base deformation history. Like the OBE motion, the difference in the axial load level was not more than 5%.

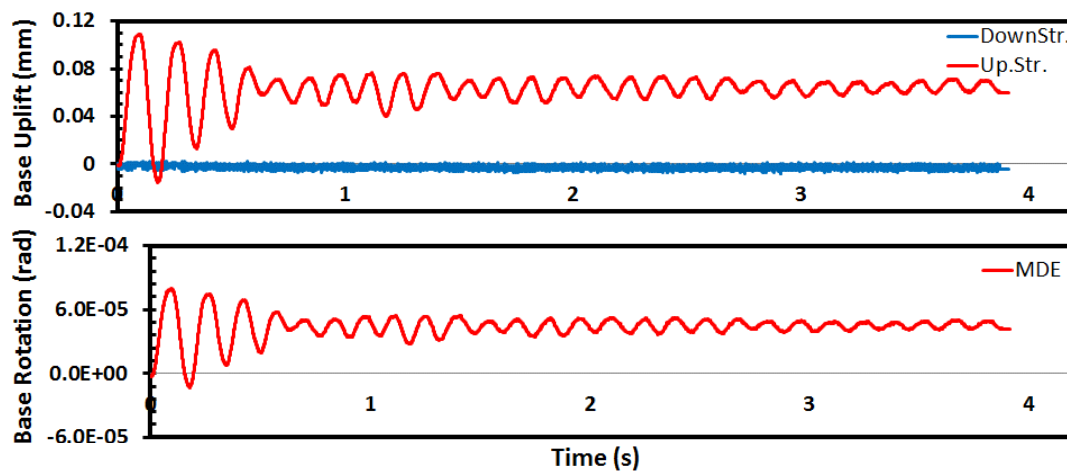


**Figure 5.6.** Base Uplift and Rotation Demands during MDE Experiment for Specimen 1

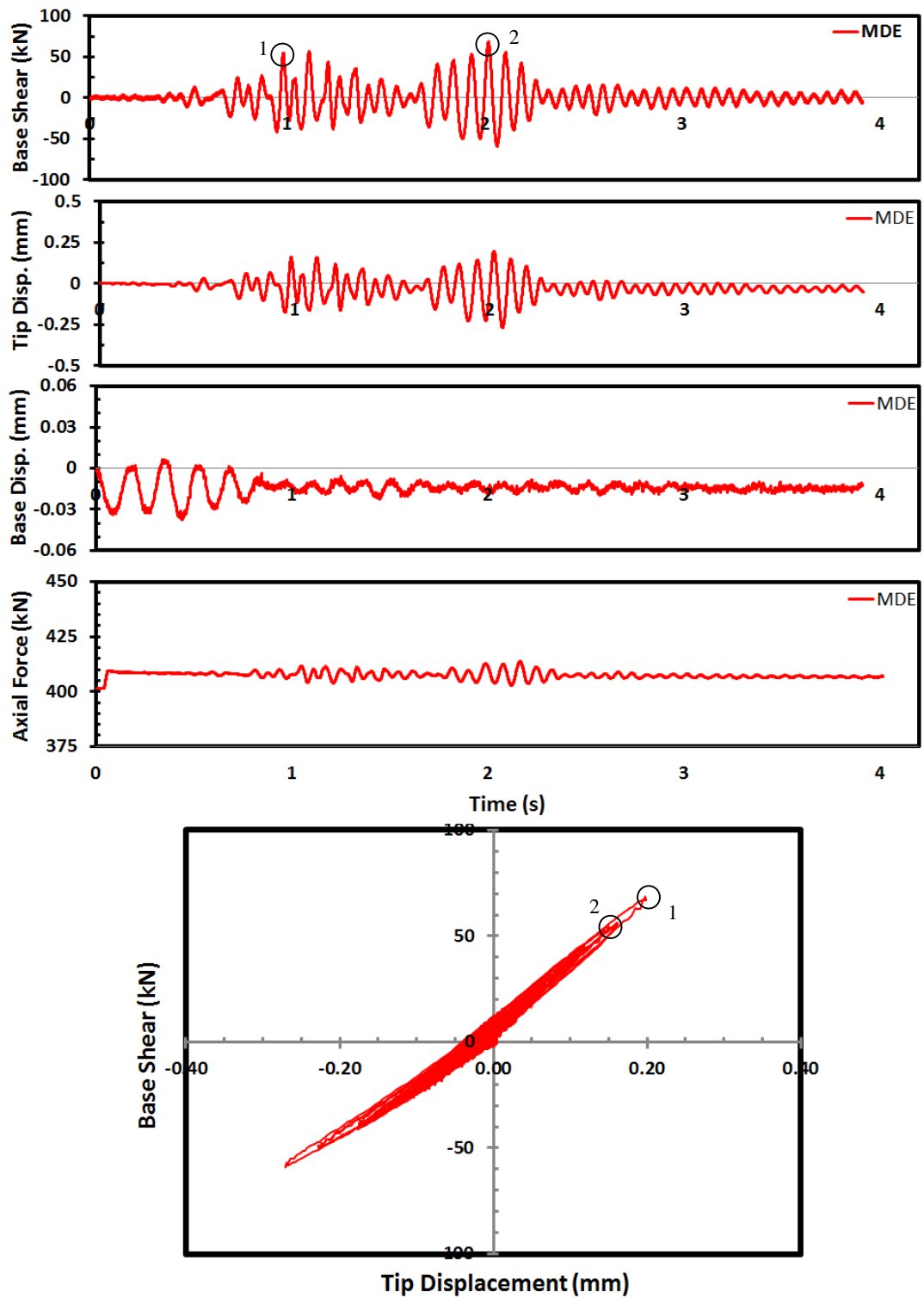


**Figure 5.7.** Force and Displacement Demands during MDE Experiment for Specimen 1



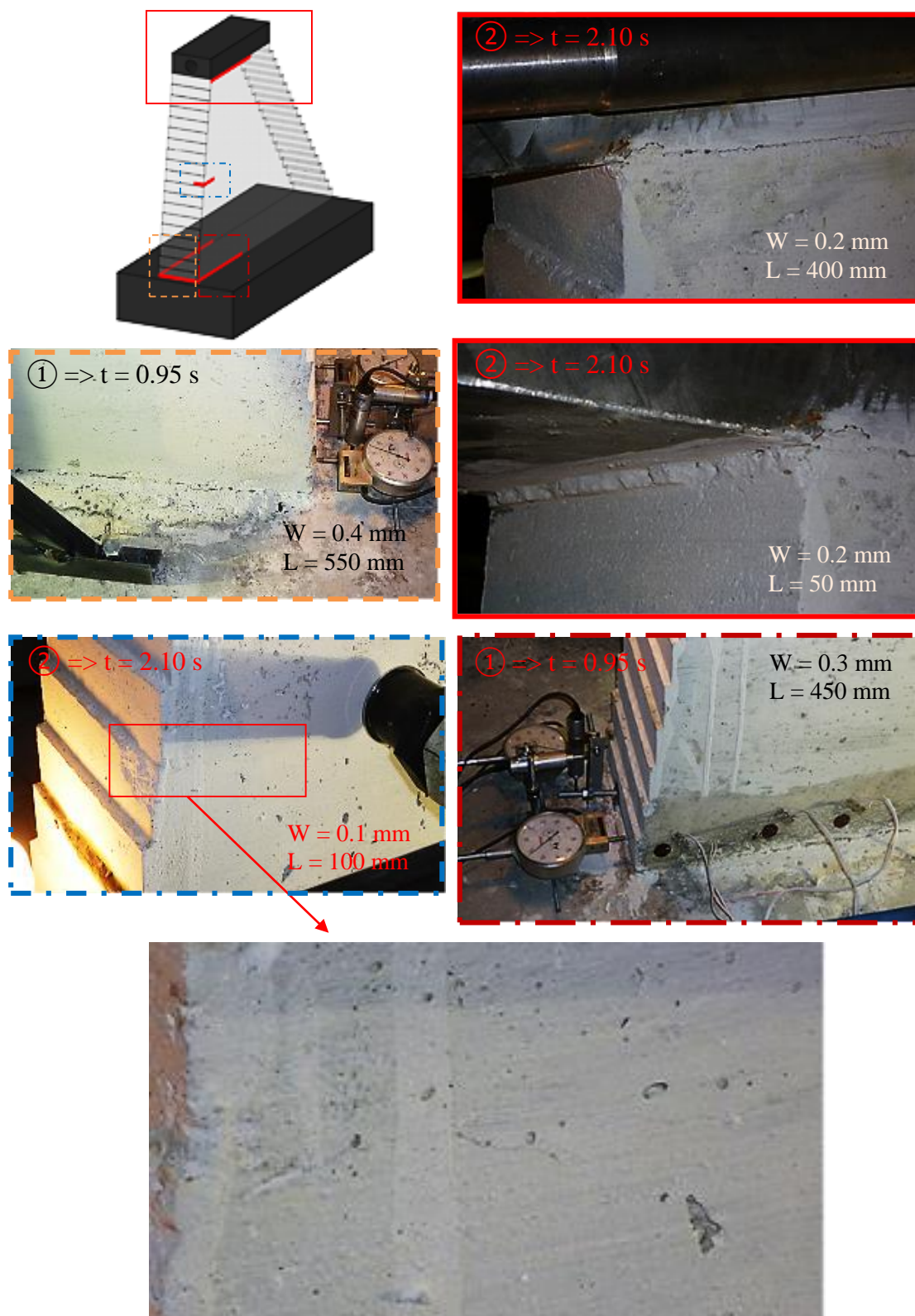


**Figure 5.8.** Cracks Formed during the MDE motion for Specimen 1



### 5.1.2.3 MCE

The recorded base shear, tip displacements, base displacement and the axial force histories during the last level of earthquake, MCE, are presented in Figure 5.9.

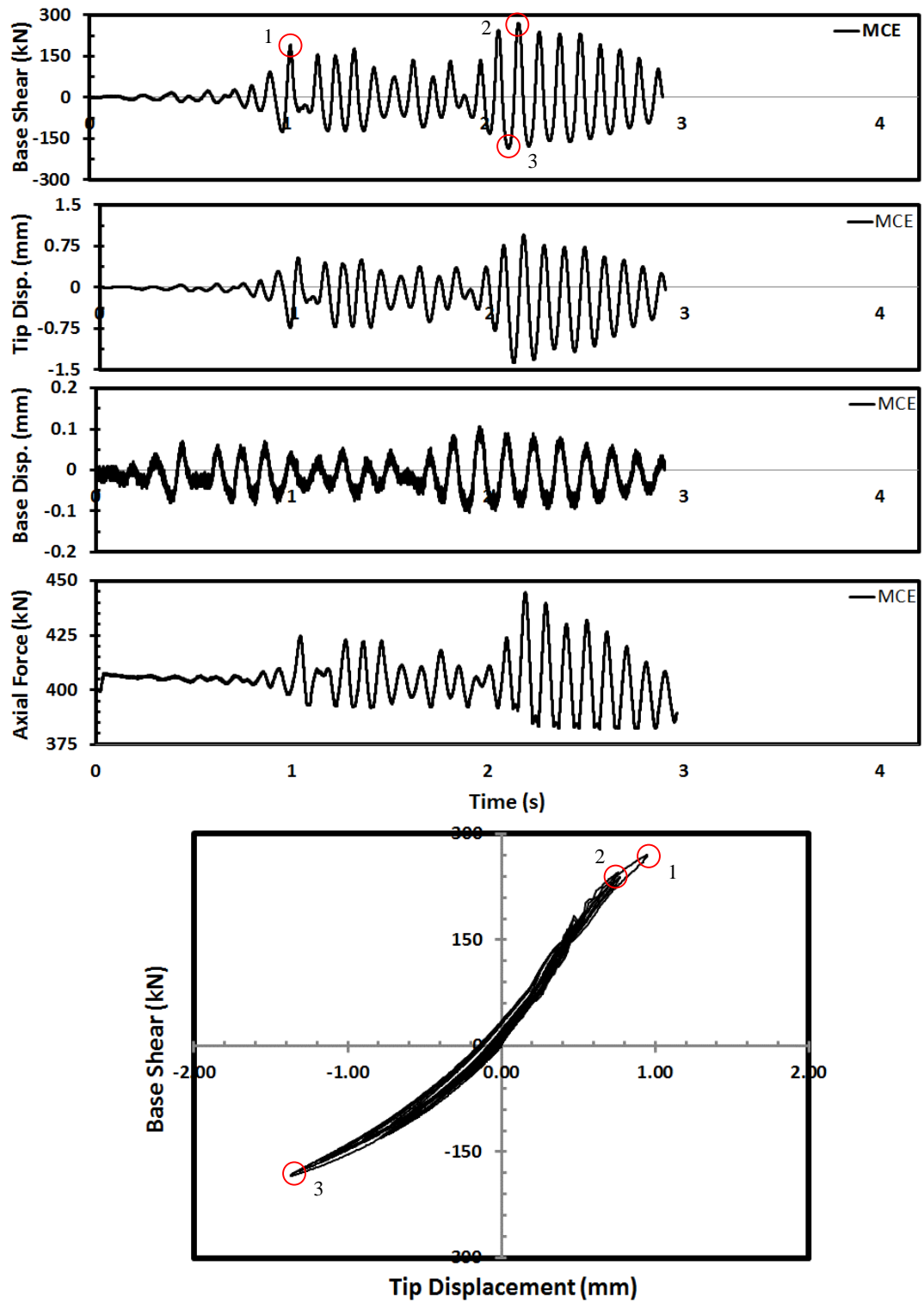


**Figure 5.9.** Force and Displacement Demands during MCE Experiment for Specimen 1

The base shear-tip displacement response of the test specimen is also given in Figure 5.9. The recorded base uplift and rotation demands are shown in Figure 5.10. The locations of significant damage on the system for the MCE motion are presented in Figure 5.11 and Figure 5.12.

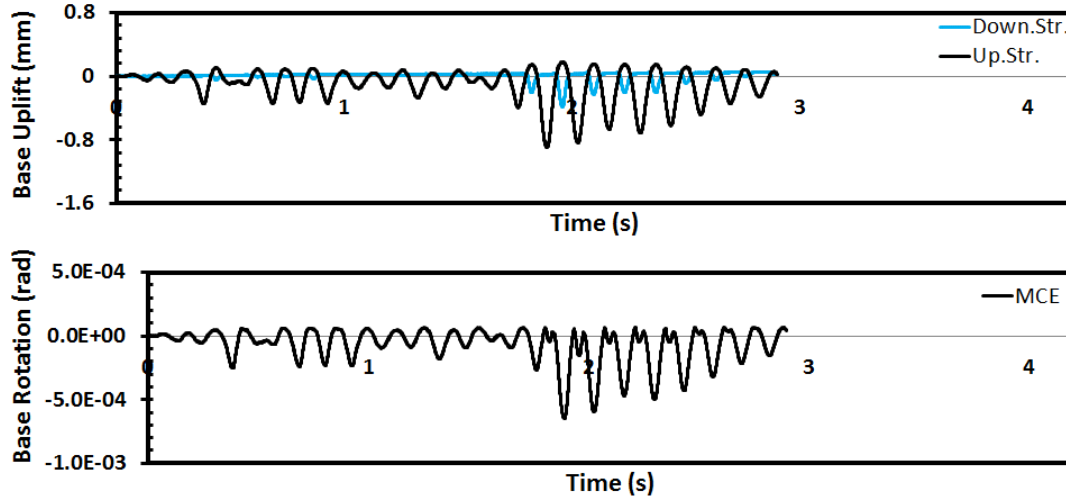


**Figure 5.10.** Base Uplift and Rotation Demands during MCE Experiment for Specimen 1

During the MCE level testing, the top displacement reached a maximum of 1.37 mm, which was approximately 5 times the displacement demand observed in the MDE level (Figure 5.9). Similarly, the base shear demand was obtained as 270kN, nearly 3 times the maximum demand measured during the MDE level testing. The length of the crack that formed on the upstream face of the dam body in the previous level of earthquake increased to 200mm at 2.20sec (Figure 5.11 and Figure 5.12). During this earthquake motion, a 200-mm-long base crack at the downstream face was also observed at 2.15 sec (Figure 5.12). However, the cracks observed on the downstream and upstream sides of the dam specimen did not join each other (Figure 5.12). Also, the maximum base deformation demand remained below 0.10 mm and no sign of base sliding was observed, evidenced by the oscillatory-type base deformations. The change in axial force was larger during MCE motion as expected but the maximum change was less than 10%, which was in acceptable limits. Based on the large base shear demand, the specimen began to behave in the nonlinear range (Figure 5.9). However, the level of nonlinearity was not excessive to exhibit signs of distress that could lead to a near-collapse situation.

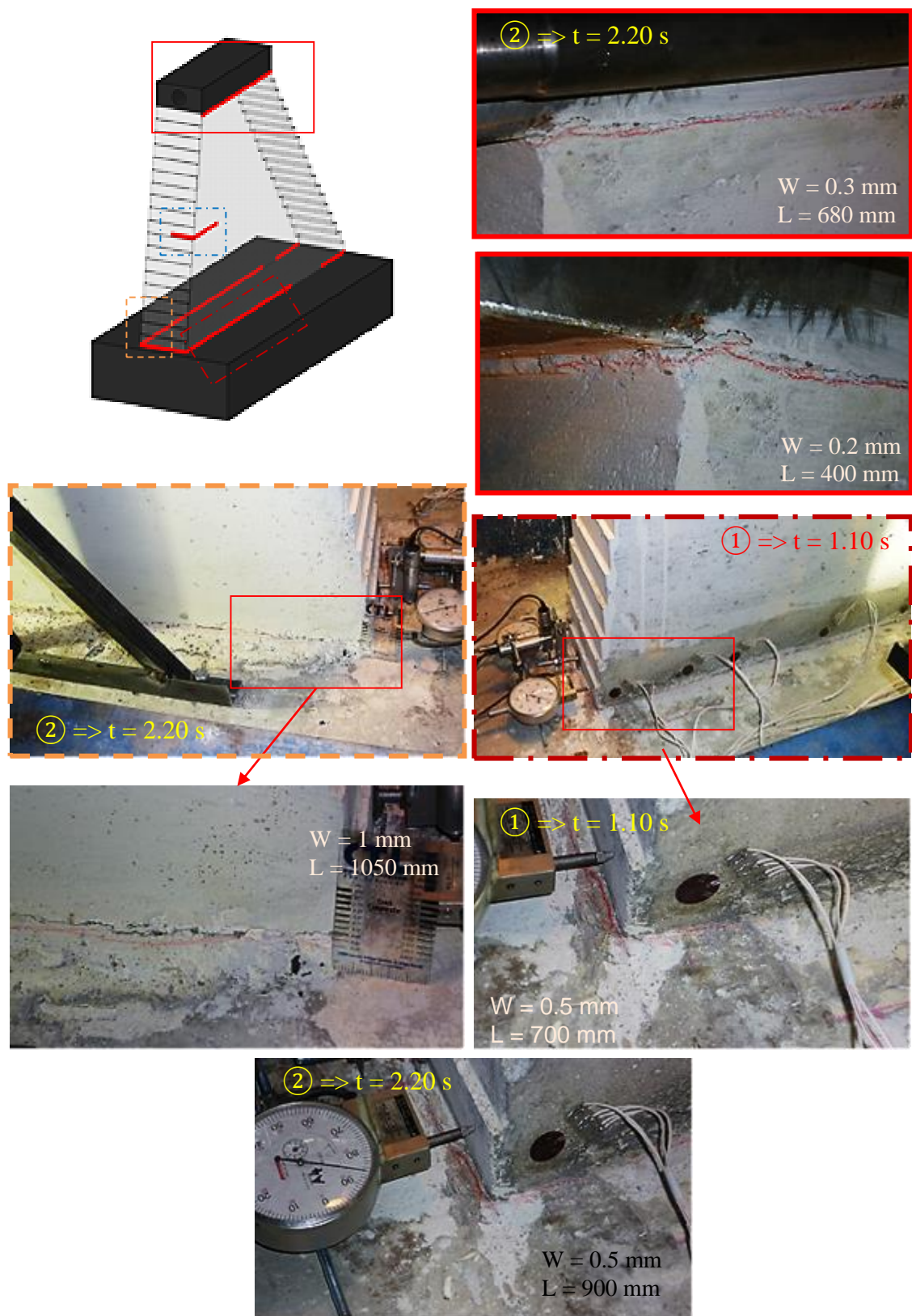


**Figure 5.11.** Cracks Formed in Specimen 1 during the MCE motion 1

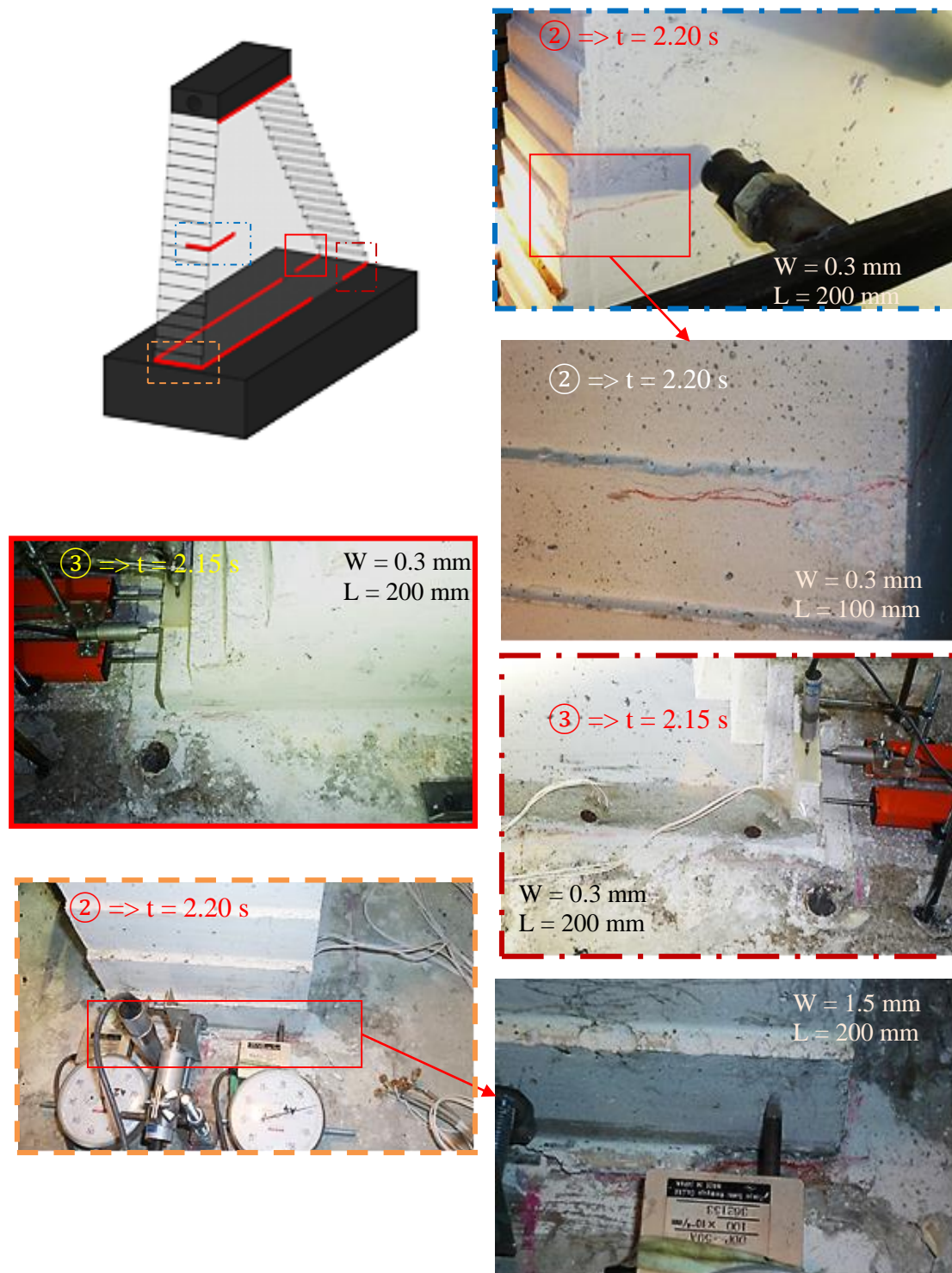


**Figure 5.12.** Cracks Formed in Specimen 1 during the MCE motion 2

#### 5.1.2.4 Pushover Experiment

After the end of the MCE testing, the specimen was brought to the zero lateral load position. A static pushover test was conducted in order to determine the reserve capacity of the specimen. The specimen was loaded in a displacement-controlled manner by loading the specimen to a specified axial force level to prevent the excessive axial forces over the dam base as the additional axial load could cause misleading results as far as base sliding was concerned. The details of the pushover loading is shown in Appendix D whereas the envelope curve is shown in Figure 5.13.

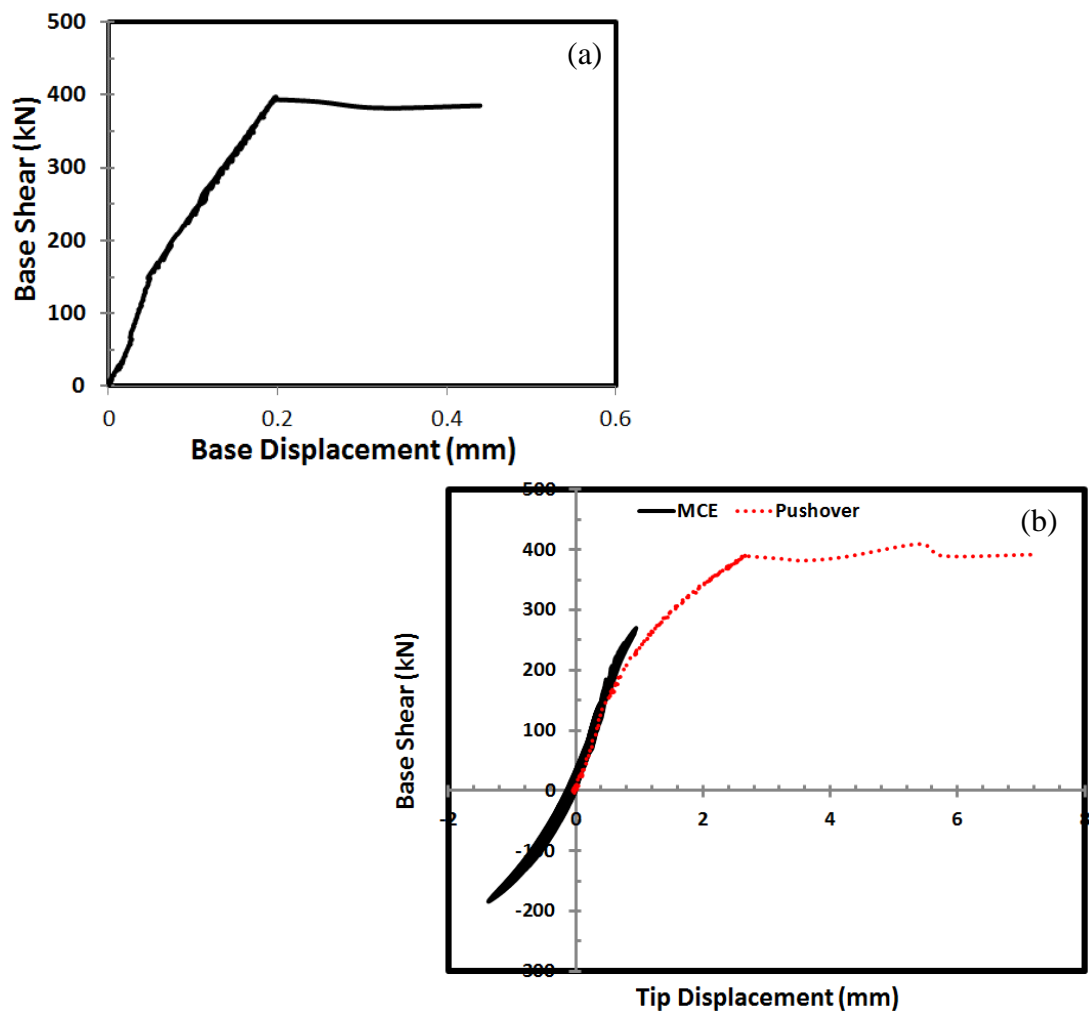


**Figure 5.13.** (a) Base Deformations and (b) Pushover Curve for Specimen 1

During the pushover loading, the specimen reached its maximum capacity at a base shear value of around 400 kN corresponding to a tip displacement of 3 mm (Figure 5.13). A yield plateau was obtained after this point: the specimen was taken to a



displacement of more than 7 mm and the test was stopped without obtaining a failure or degradation in the strength of the specimen. The capacity of the specimen was determined to be nearly 1.5 times the maximum demand in the MCE motion. At the final stage of the pushover test, the crack widths nearly reached 1.5 mm while the crack lengths remained nearly unchanged (Figure 5.14). In addition, no base sliding was detected, which is clear from the base shear-base deformation curve given in Figure 5.13. From that figure, it is apparent that due to excessive base cracks the stiffness was degraded but some plastic deformation took place at the base level. No visual deformation caused by sudden sliding of base was observed. The dam stability was maintained until the end of pushover testing.



**Figure 5.14.** Cracks Formed during Pushover Experiment for Specimen 1

### 5.1.3 Identification of the Dynamic Parameters

The natural period and the equivalent viscous damping of the specimen were obtained for each of the three pseudo-dynamic tests using the procedure proposed by Molina et al (1999). In this method, the equation of motion was modeled at discrete time intervals as given in Eq. 5.1:

$$m a(n) + r(n) = f(n) \quad (5.1)$$

where  $m$  is the mass matrix of the structure,  $a(n)$  and  $f(n)$  are the acceleration and external force for  $n^{\text{th}}$  time interval and  $r(n)$  is the restoring force that represents the structure's response for the corresponding displacement value. For a dynamic system modeled by equivalent viscous damping approach, the restoring force at any time step can be thus expressed as:

$$\begin{bmatrix} u^T(n) & v^T(n) & 1 \end{bmatrix} \cdot \begin{bmatrix} k^T \\ c^T \\ o^T \end{bmatrix} = r^T(n) \quad (5.2)$$

where  $k$  and  $c$  are the secant stiffness and damping matrices,  $u$  and  $v$  are the displacement and velocities at the corresponding degrees of freedom and  $o$  is an equilibrium constant.

Eq. 5.2 can be solved for  $k$  and  $c$  using the data obtained at  $N$  time intervals as long as  $N > 2 \times \text{ndof} + 1$ . By selecting a time window containing steps not less than  $N$ , least square solution is obtained for  $k$  and  $c$ . Following, Maia and Silva (1997), one can then extract the frequency and damping coefficient from:

$$s \begin{bmatrix} C & M \\ M & 0 \end{bmatrix} v + \begin{bmatrix} K & 0 \\ 0 & -M \end{bmatrix} v = 0 \quad (5.3)$$

$$s_1, s_1^* = w_1 \left( \zeta_1 \pm i \sqrt{1 - \zeta_1^2} \right) \text{ where } i^2 = -1 \quad (5.4)$$

In Eq. 5.4,  $w_1$  is the natural frequency and  $\zeta_1$  is the equivalent viscous damping ratio (or simply damping ratio) at the first mode. The equation of motion, as discretized in

the pseudo-dynamic solution (Eq. 5.1), was utilized to obtain the damping ratios and natural frequencies at the  $i^{\text{th}}$  mode of the system (Maia and Silva 1997). A window of 1000 data points with 20 data point increments were used to acquire smoother curves in the calculations. The data for the first 0.5 seconds was not considered because of having very small displacement increments (in the order of 0.01 mm for the MCE earthquake). In addition, the secant stiffness matrix was utilized for the calculation of the fundamental periods in accordance with Kurt et al (2011), who showed the change in the fundamental period calculated using the secant stiffness had better correlations with the observed damage. The hydrostatic force and corresponding displacement were ignored during the calculations. The fundamental period of the undamaged test specimen was obtained at 0.07 sec which was nearly constant during the OBE and MDE level earthquakes (Figure 5.15.a). However, the period elongated to nearly 0.12 sec during the MCE level due to the enlarged cracks formed during the previous earthquakes and the newly formed base cracking (Figure 5.8 and Figure 5.12). The identified damping ratios were about 2 to 5% for the three consecutive earthquakes.

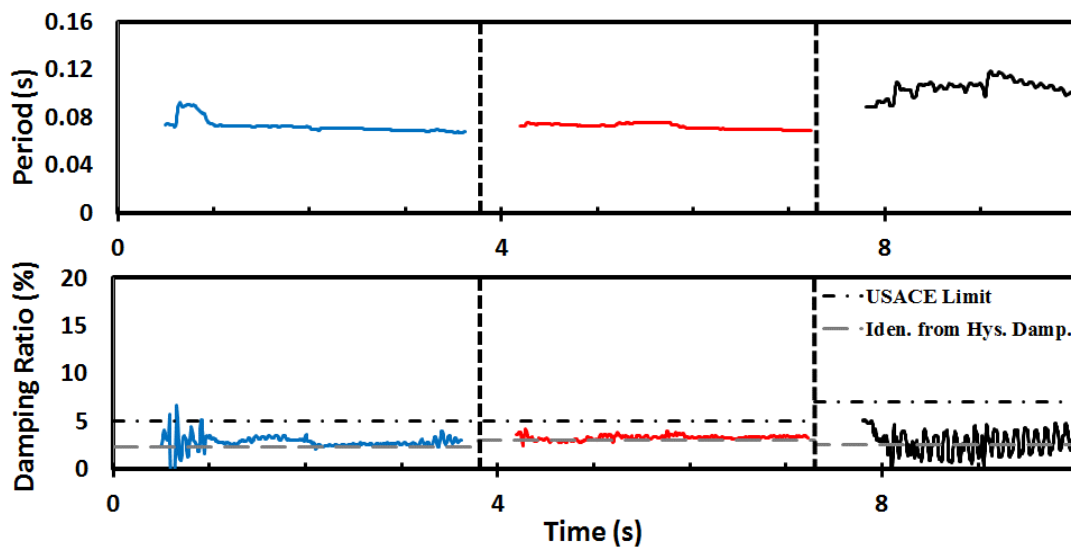


**Figure 5.15.** Variation of the Fundamental Period and Damping Ratio during the Experiment for Specimen 1



## 5.2 Specimen 2: RCC Gravity Dam 1

### 5.2.1 Hydrostatic Loading

The base shear versus tip displacement and base shear – base displacement curves during hydrostatic loading are presented in Figure 5.16. From this figure, it is apparent that this specimen also remained in its linear range similar to the first specimen. In contrast to the first specimen, no visual cracking was observed during the hydrostatic loading process.

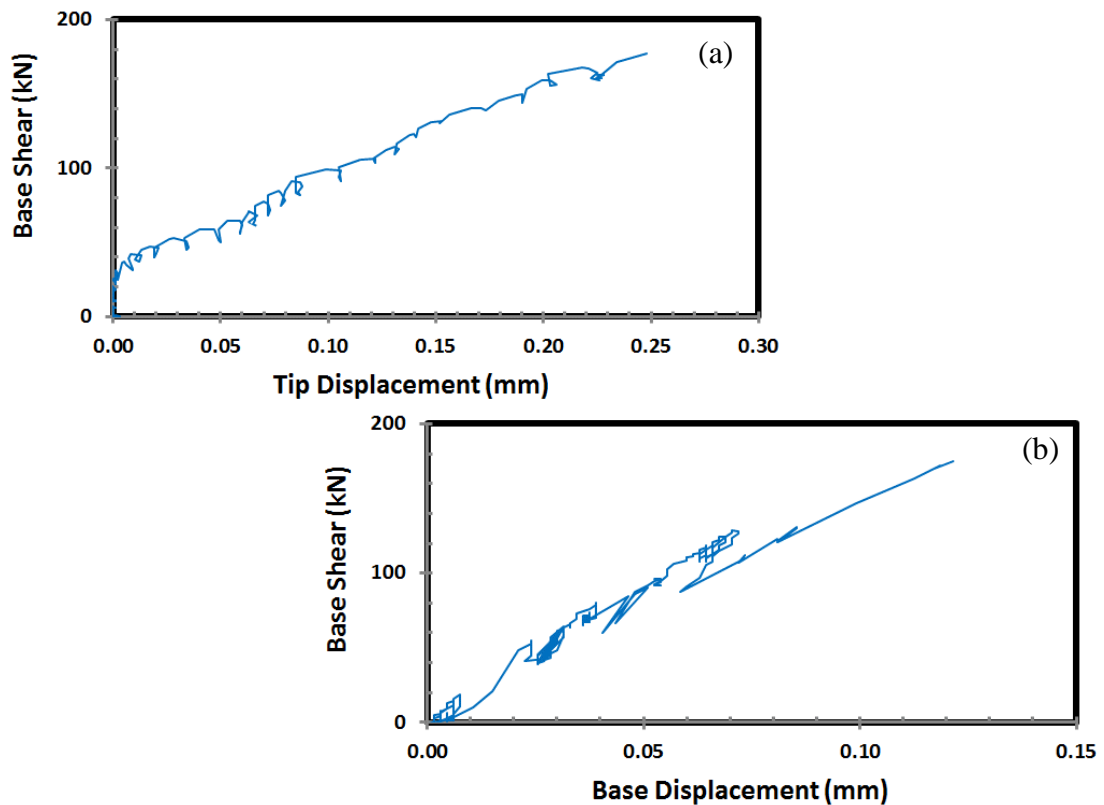


**Figure 5.16.** (a) Base Shear – Tip Displacement and (b) Base Shear – Base Displacement Curves during Hydrostatic Loading for Specimen 2

### 5.2.2 PSD Testing

#### 5.2.2.1 OBE

During the OBE motion, the base shear, tip displacements, base displacement and the axial force were monitored (Figure 5.17). The base shear-tip displacement response of the test specimen is also presented in Figure 5.17. The locations of the significant

damage for the OBE motion are depicted in Figure 5.18. The recorded base uplift and rotation demands are shown in Figure 5.19.

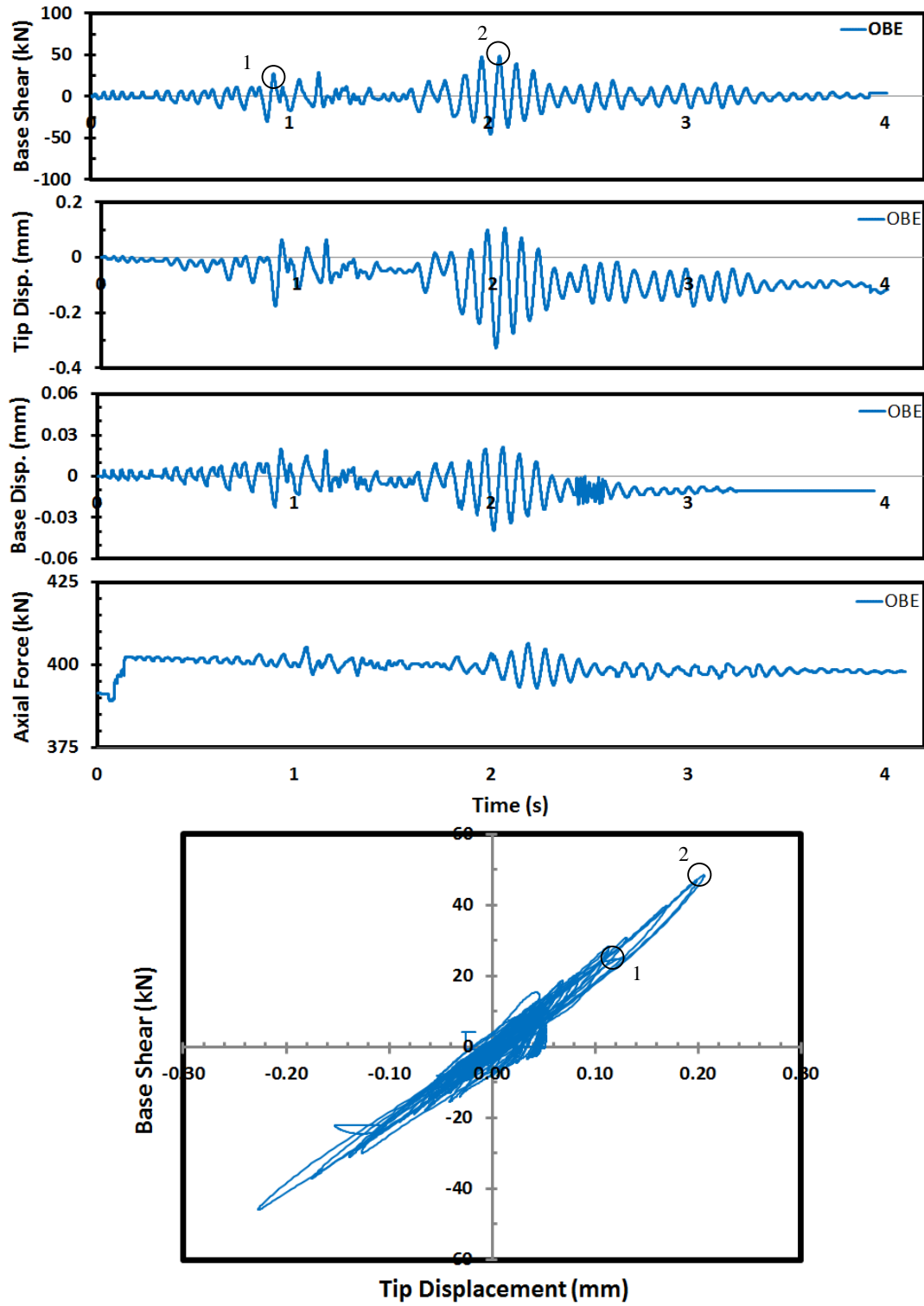


**Figure 5.17.** Force and Displacement Demands during OBE Experiment for Specimen 2

After the hydrostatic loading, the first level of earthquake, the OBE ground motion, was applied to the specimen. During the OBE motion, some minor cracks at the base were observed. Unlike the first specimen, there were only one time period during which the base shear demand caused significant base cracks. The maximum crack length was recorded as 200 mm with the maximum crack width reaching 0.2 mm at 2.10 sec (Figure 5.18). The maximum base shear and the tip displacement demands were measured as 48 kN and 0.33 mm, respectively.

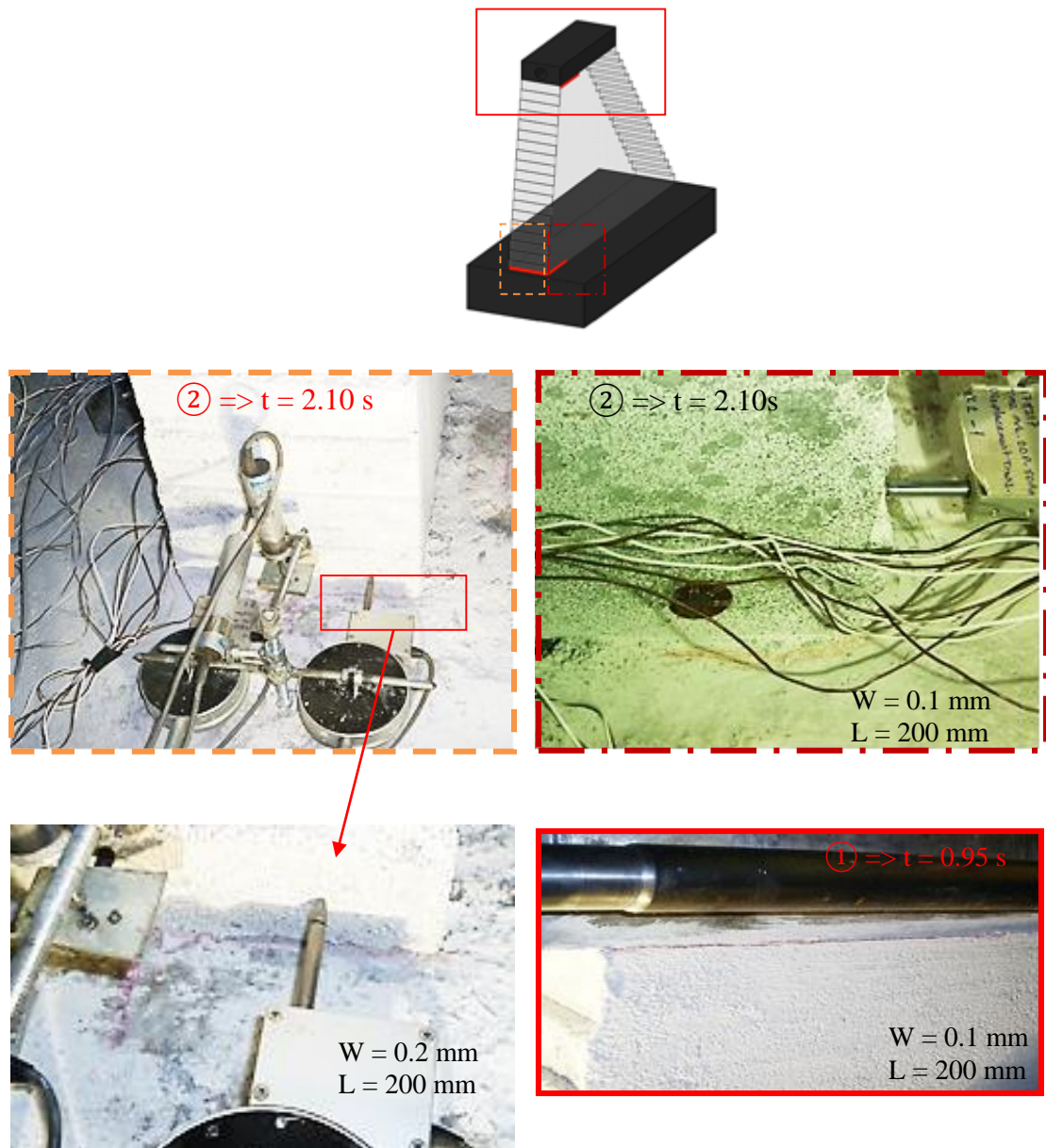


**Figure 5.18.** Cracks Formed during the OBE motion for Specimen 2

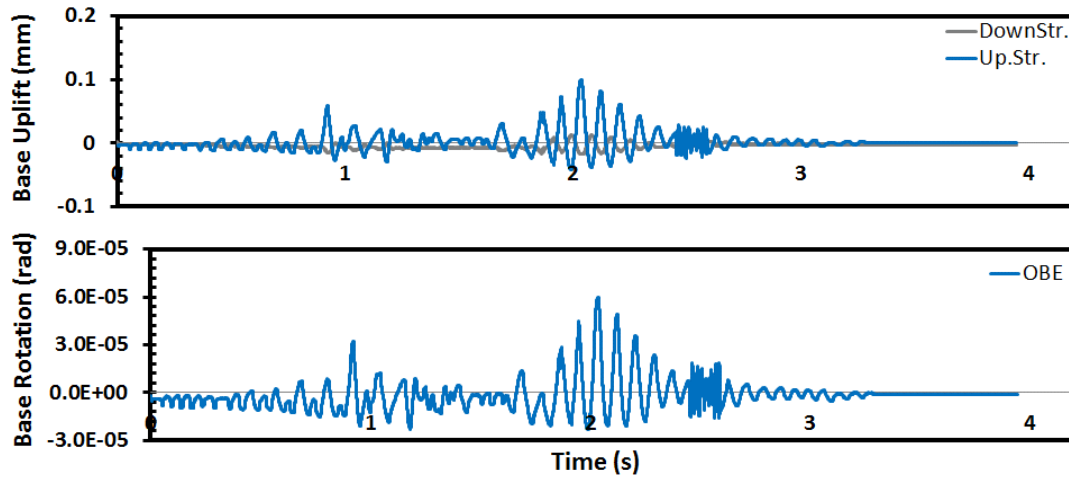


**Figure 5.19.** Base Uplift and Rotation Demands during OBE Experiment for Specimen 2

The deformation at the base was less than 0.05 mm during the full duration of the test (Figure 5.17). The axial load on the specimen did not change significantly, deviating from the target value by only 2.5%. Although there were some minor base cracks, the lateral stiffness of the specimen did not change significantly, evidenced by the nearly linear force-displacement curve given in Figure 5.17.

#### 5.2.2.2 MDE

The recorded base uplift and rotation demands are shown in Figure 5.20. The base shear, tip displacements, base displacement and axial force were monitored in time and they are shown in Figure 5.21. The base shear-tip displacement response of the test specimen is also presented in Figure 5.21.

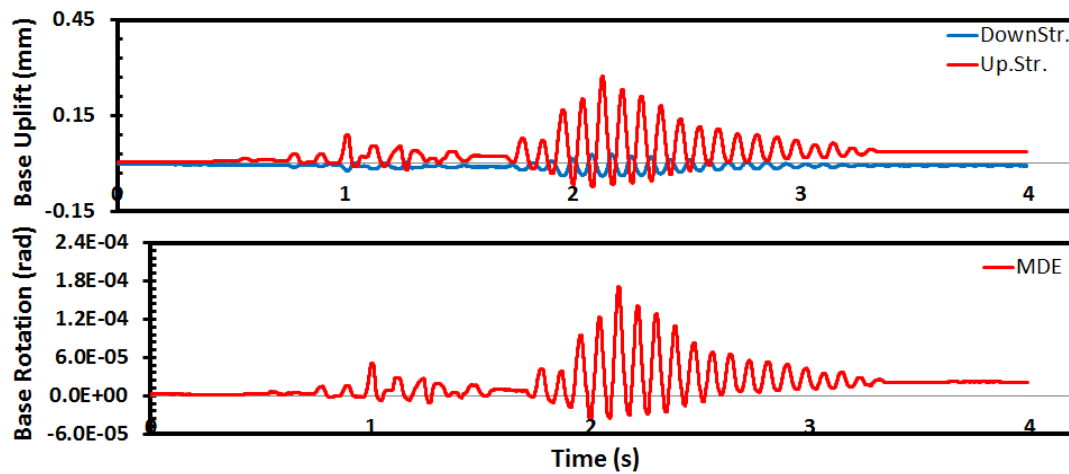


**Figure 5.20.** Base Uplift and Rotation Demands during MDE Experiment for Specimen 2

The locations of significant cracking on the system for the MDE motion are summarized in Figure 5.22.

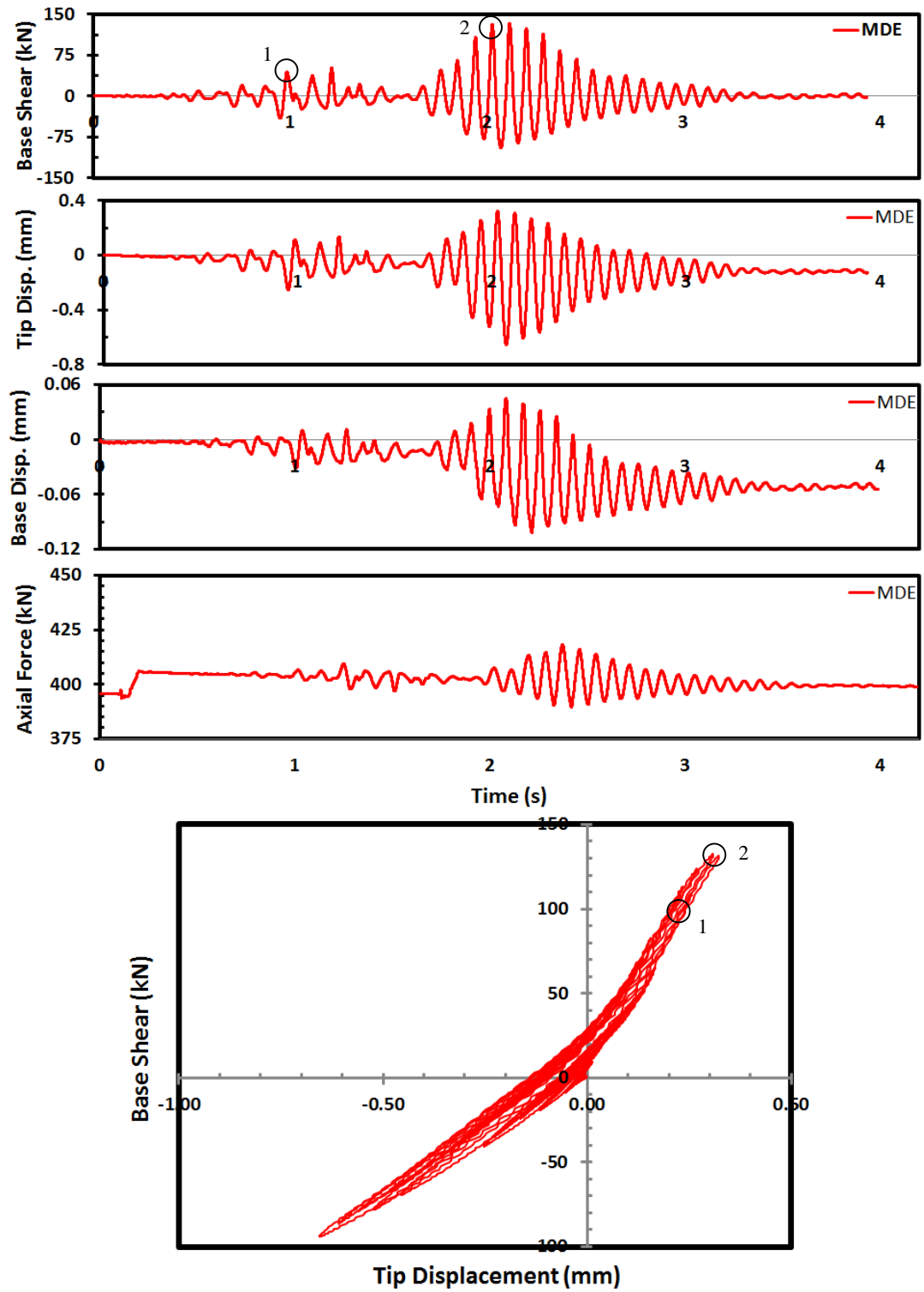


**Figure 5.21.** Force and Displacement Demands during MDE Experiment for Specimen 2



**Figure 5.22.** Cracks Formed during the MDE motion for Specimen 2



During this stage of the testing, the maximum tip displacement was obtained as 0.66 mm, corresponding to a maximum base shear demand of 132 kN. The additional demand in the displacement and base shear force with respect to the OBE level were calculated as 100.7% and 173.1%, respectively. Consequently, MDE level testing resulted in increased crack lengths and widths at 2.10 sec. The maximum crack width and length reached 0.5 mm and 450 mm, respectively (Figure 5.22). Unlike the first specimen, no body crack was observed at the upstream face during this level. The base deformation was detected to be less than 0.10 mm during this level as well (Figure 5.21). Although a permanent base deformation of 0.06 mm were observed, this deformation was not interpreted as a sliding deformation because there were no stick-slip type jumps throughout the base deformation history. The permanent base deformation was purely due to plastic deformations at the base level (Figure 5.23). In addition, there were no axial load problem.

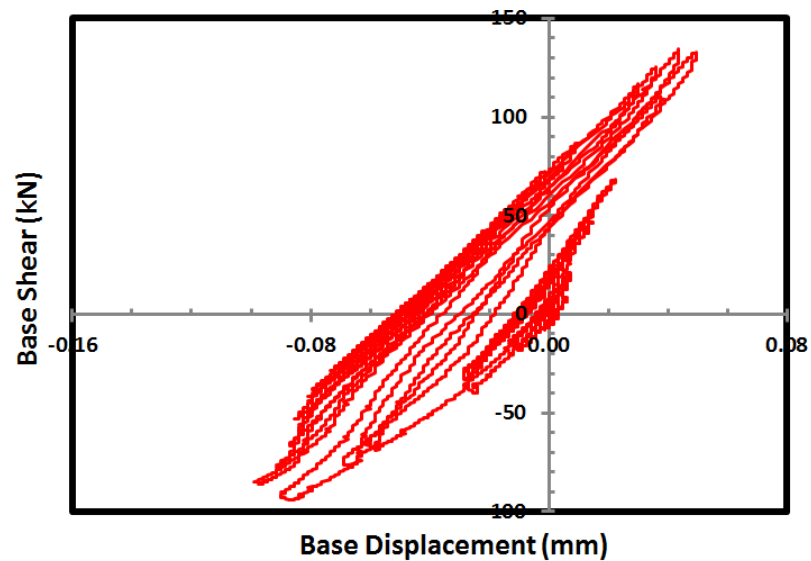


**Figure 5.23.** Base Shear versus Base Displacement Curve during the MDE motion for Specimen 2

#### 5.2.2.3 MCE

During the MCE experiment, the base shear force, tip and base displacements and the axial force were monitored (Figure 5.24). The base shear-tip displacement response of the test specimen is also presented in Figure 5.24. The locations of the cracks during the MCE motion are shown in Figure 5.25 and Figure 5.26. The recorded base uplift and rotation demands are shown in Figure 5.27.

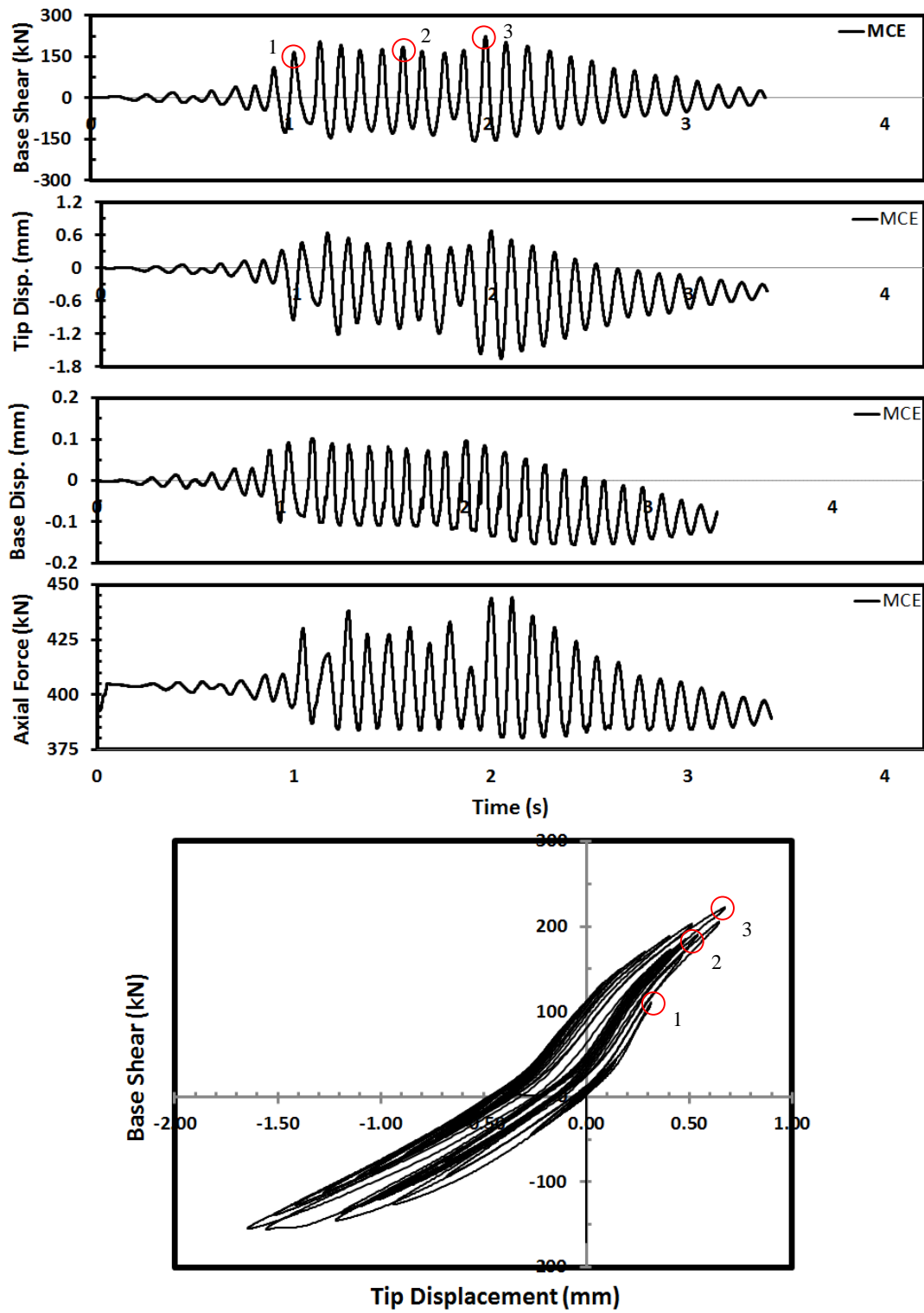


**Figure 5.24.** Force and Displacement Demands during MCE Experiment for Specimen 2



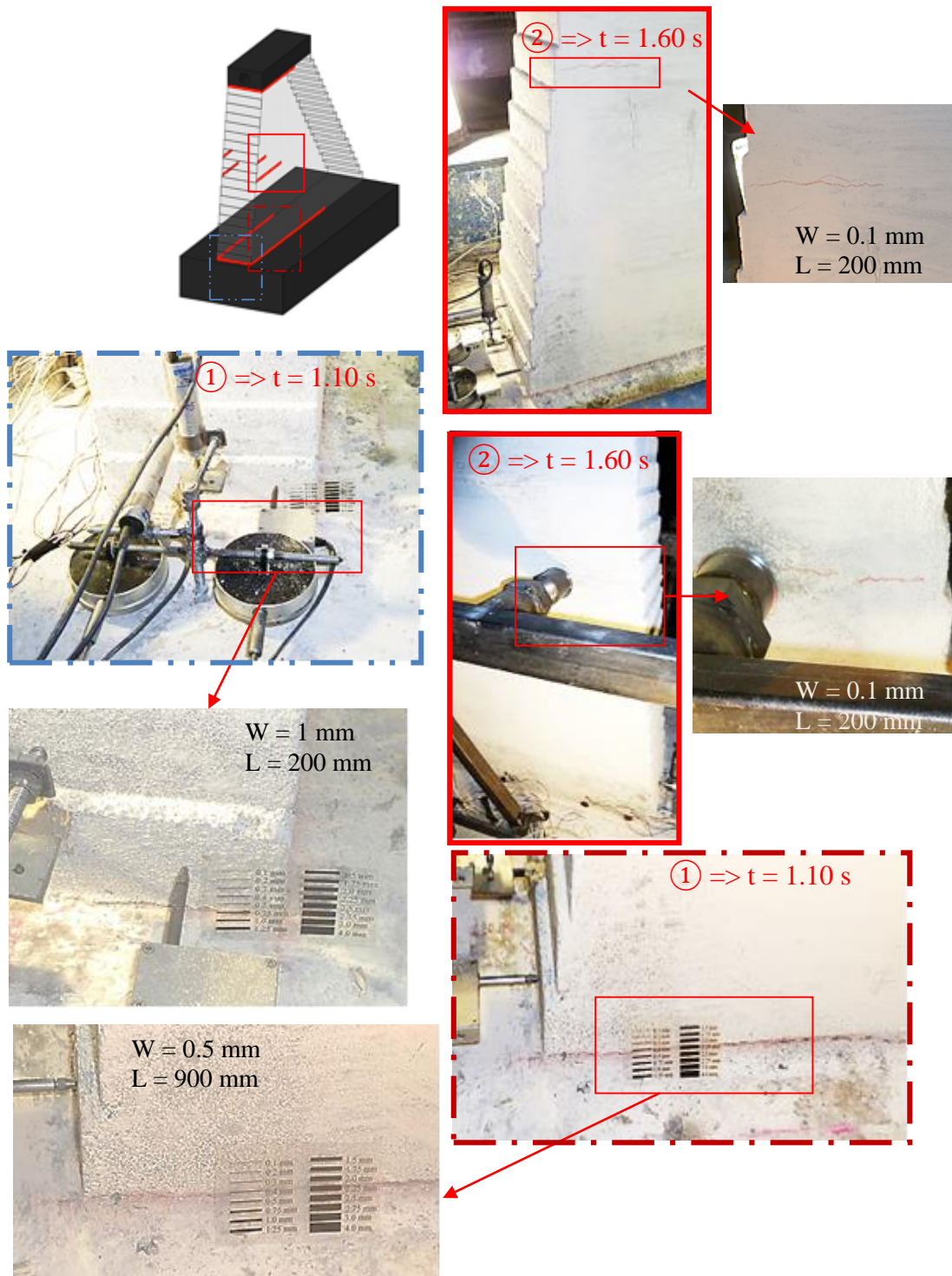


**Figure 5.25.** Cracks Formed in Specimen 2 during the MCE motion 1

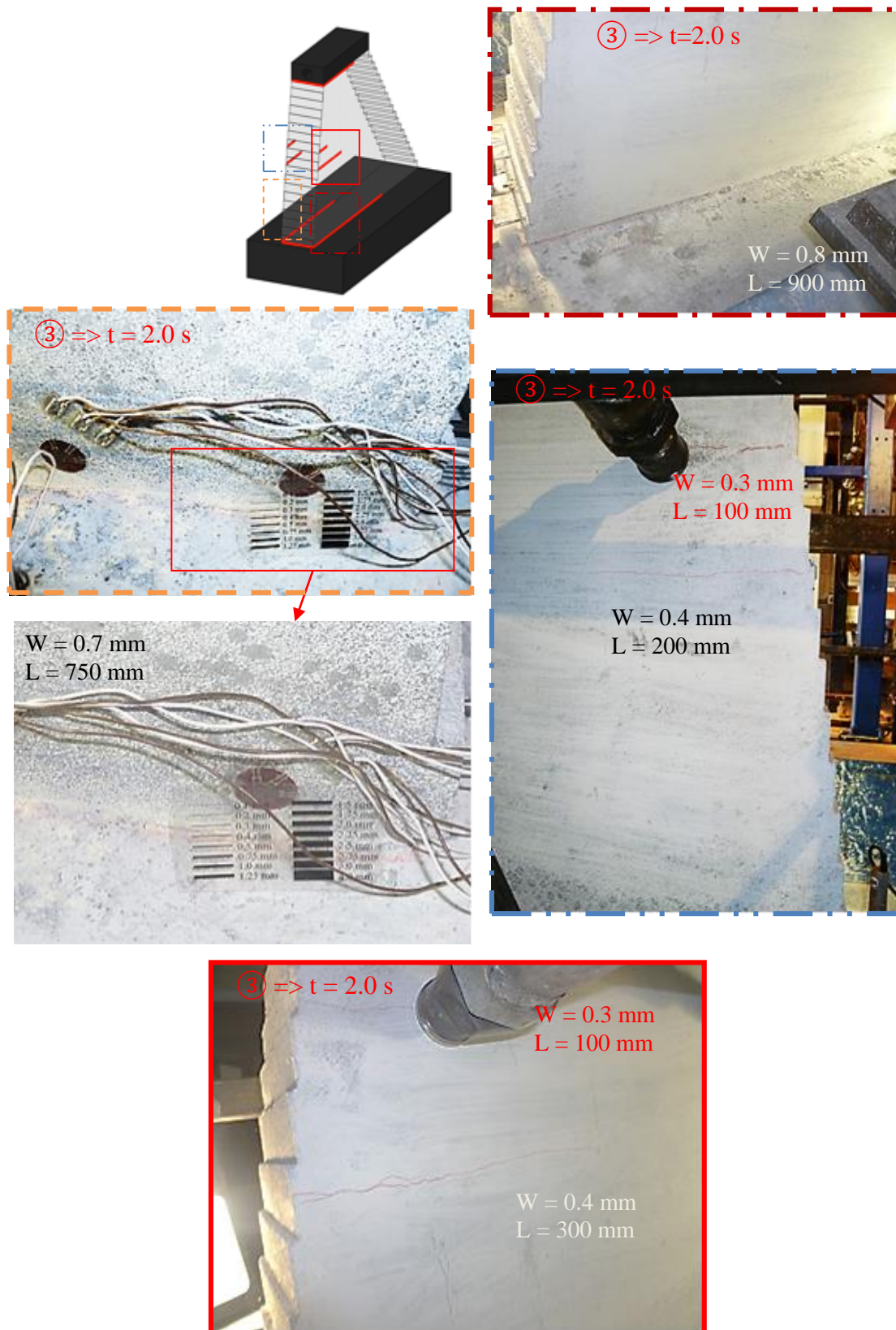


**Figure 5.26.** Cracks Formed in Specimen 2 during the MCE motion 2

The tip displacement reached a maximum of 1.65mm, which was approximately 2.5 times the displacement demand observed in the MDE level (Figure 5.24). Similarly, the base shear demand was obtained as 222 kN, nearly 1.7 times the maximum demand measured during the MDE level testing. Two parallel body cracks in the upstream face formed on the dam body reaching to a length of 300mm. During this earthquake motion, cracking of the base at the downstream face was not observed in contrast to the first specimen.

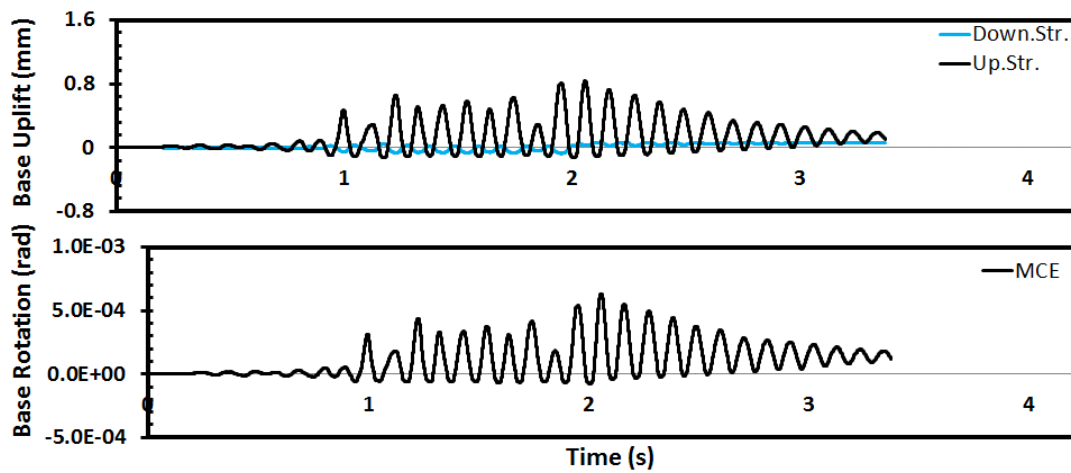


**Figure 5.27.** Base Uplift and Rotation Demands during MCE Experiment for Specimen 2

Also, the maximum base deformation demand remained below 0.15 mm. The permanent base deformation reached to a value of 0.10 mm (Figure 5.28). Similar to the MDE motion, the permanent base deformation was due to the plastic deformations formed during cyclic motions (Figure 5.28). The change in the axial force on the specimen was larger during MCE motion but the maximum change was less than 10%, which was within the acceptable limits. Based on the large base shear demand, the specimen began to behave in its nonlinear range (Figure 5.24). However, the level of nonlinearity was not excessive.

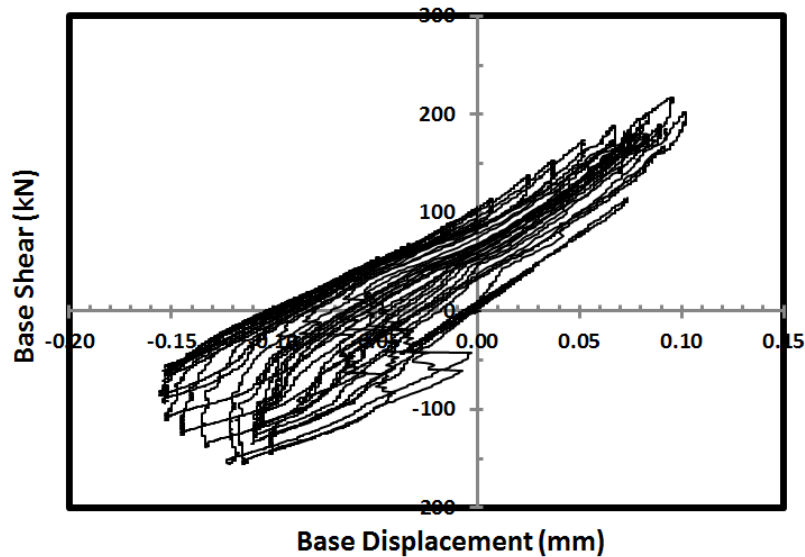


**Figure 5.28.** Base Shear versus Base Displacement Curve during MCE motion for Specimen 2

#### 5.2.2.4 Pushover Experiment

After the end of the MCE testing, a static pushover test was also conducted in order to determine the reserve capacity in the specimen as no stability problems were observed during the ground motion tests. The pushover experiment was conducted by utilizing the procedure explained in Appendix D. During the pushover loading, the specimen reached its maximum capacity at a base shear value of around 330 kN, which was nearly 1.5 times the maximum demand in the MCE motion. The maximum tip displacement corresponded to a tip displacement of 2.5 mm. A yield plateau was obtained until a tip displacement of nearly 4.3 mm was reached. After that point, the capacity of the specimen suddenly dropped to 260 kN due to the body cracks and their propagations through the dam body (Figure 5.29).

The collapse mechanism observed in the pushover test is presented in Figure 5.30- Figure 5.32. The specimen lost its load carrying capacity immediately after the inclined cracks converged to the downstream toe of the dam specimen. The failure was caused by shear – compression mechanism (Figure 5.32). In addition, no base sliding was detected (Figure 5.29).

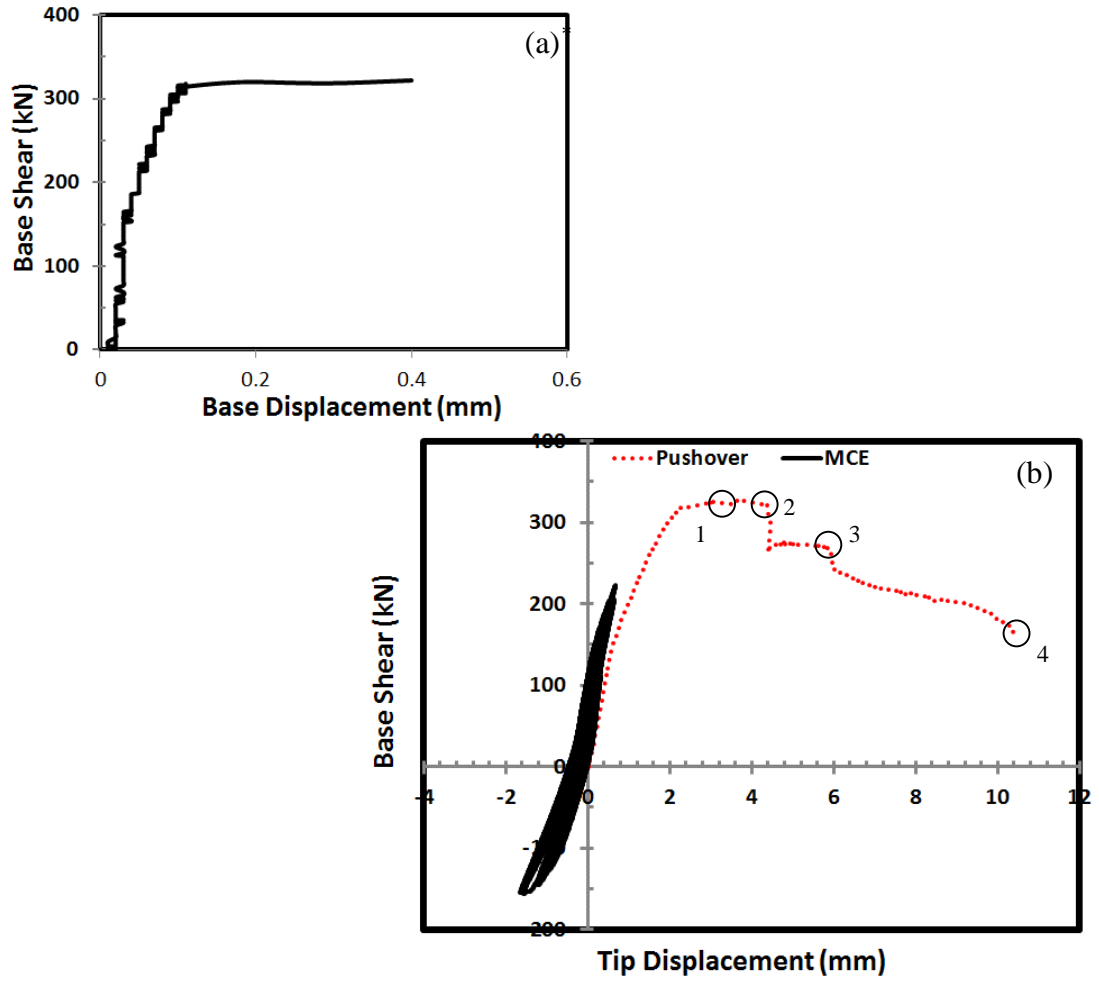


**Figure 5.29.** (a) Base Sliding and (b) Pushover Curve for Specimen 2

*\*: The reason for low resolution was that 10mm LVDT's were not collected data properly during this test, so the results recorded by 50mm LVDT was presented.*

### 5.2.3 Strain Gage Recordings

The principal strain distributions over the dam base for the second specimen were determined by processing the data recorded by the rosettes (Figure 5.33). In Figure 5.33, the magnitudes of the first principal strains and their orientations are also depicted by vectors. It is clear that the compressive strains (strain gages 5-7) tended to get larger starting from the OBE motion to the MCE motion. Also, their orientation slightly changed. The tensile strains increased as expected till the MDE motion. However, the tensile strains in the outermost position (strain gage 1) tended to decrease during the MCE motion due to the formation of a body crack, which modified the shape of the load flow. The measured principal strains at the downstream face confirm the visually observed situation of no cracking during



hydrostatic loading and presence of the cracks verified by the exceedance of crack strain limit during ground motions.

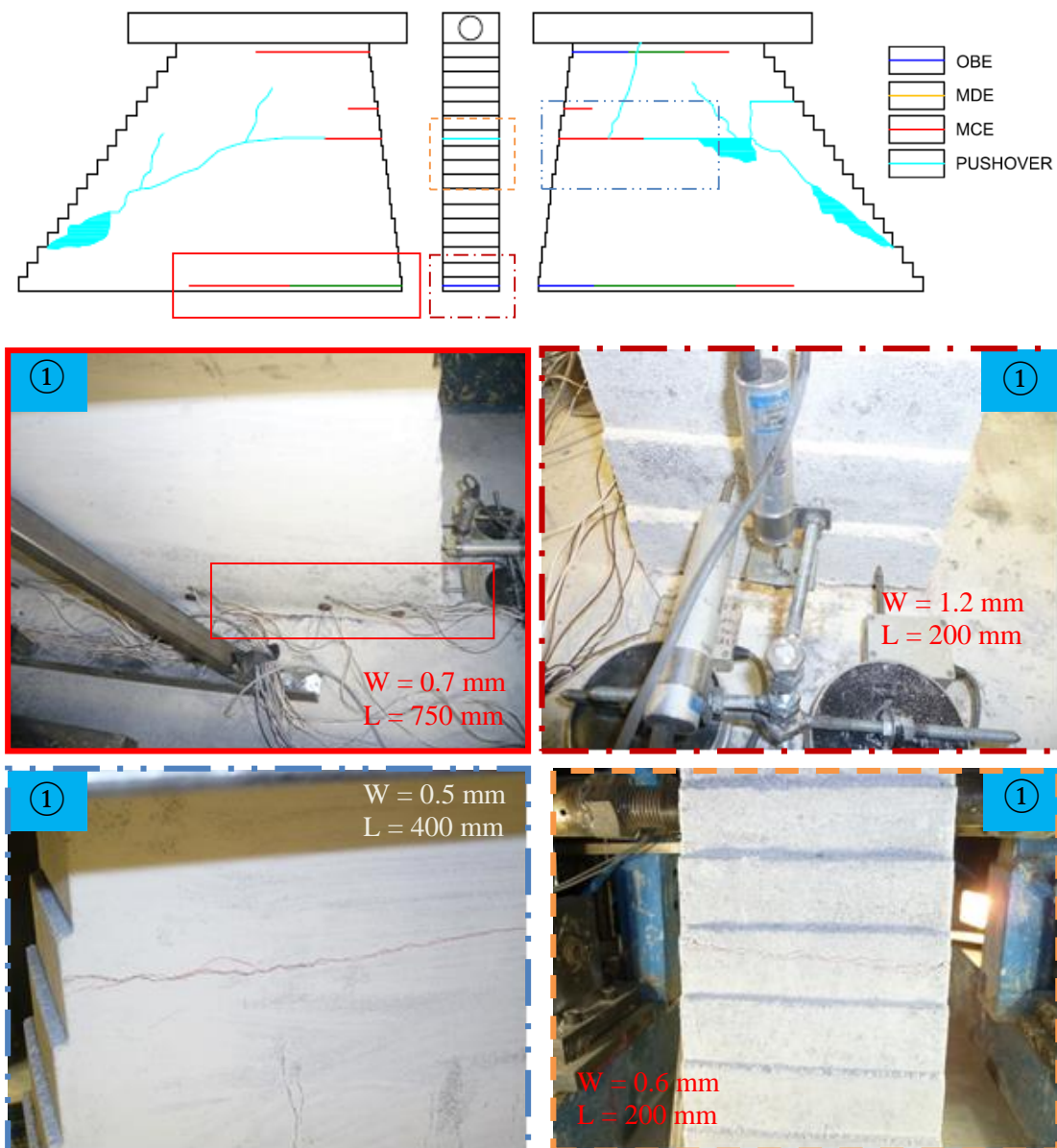


**Figure 5.30.** Cracks Formed in Specimen 2 during Pushover Experiment 1

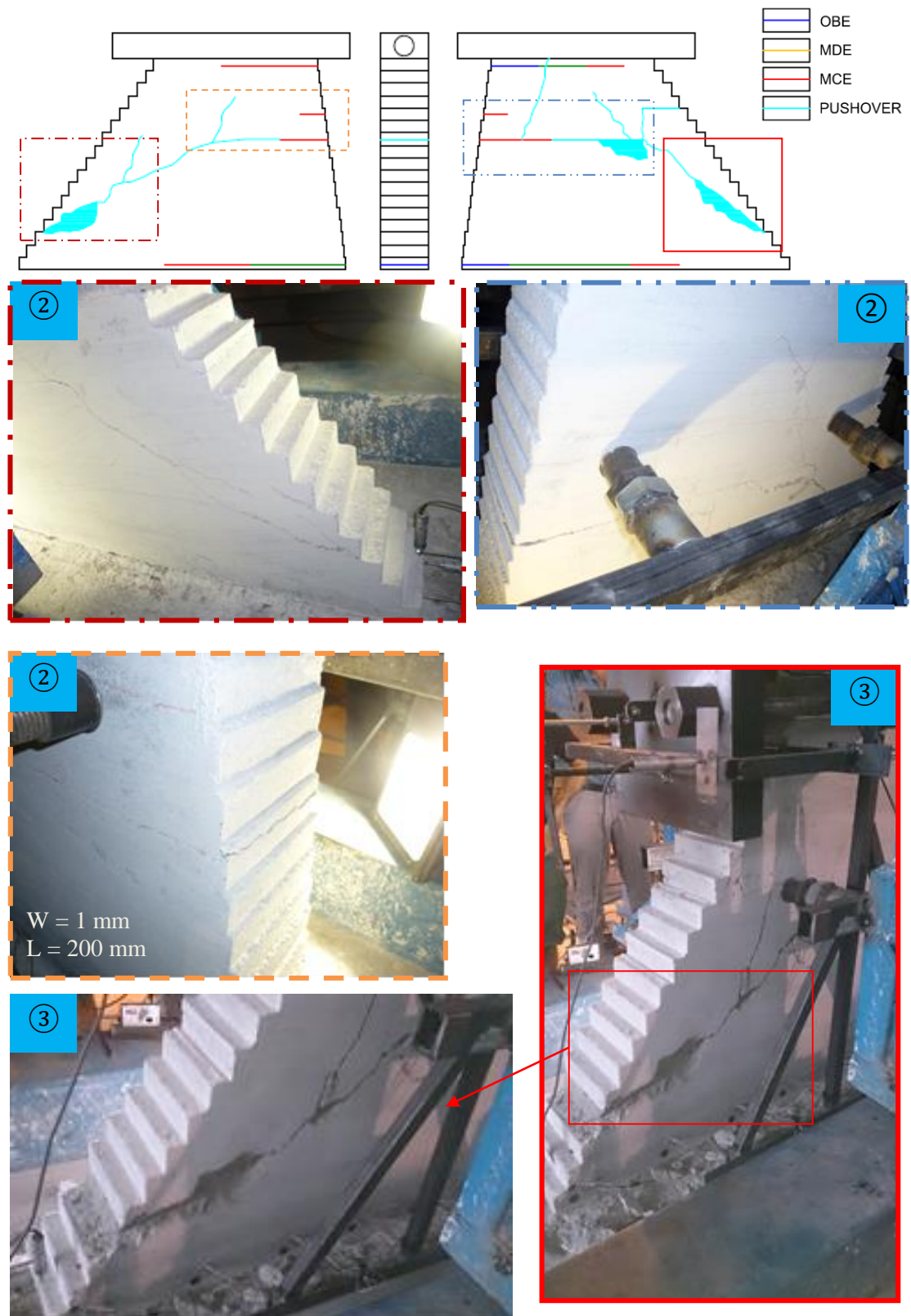


**Figure 5.31.** Cracks Formed in Specimen 2 during Pushover Experiment 2

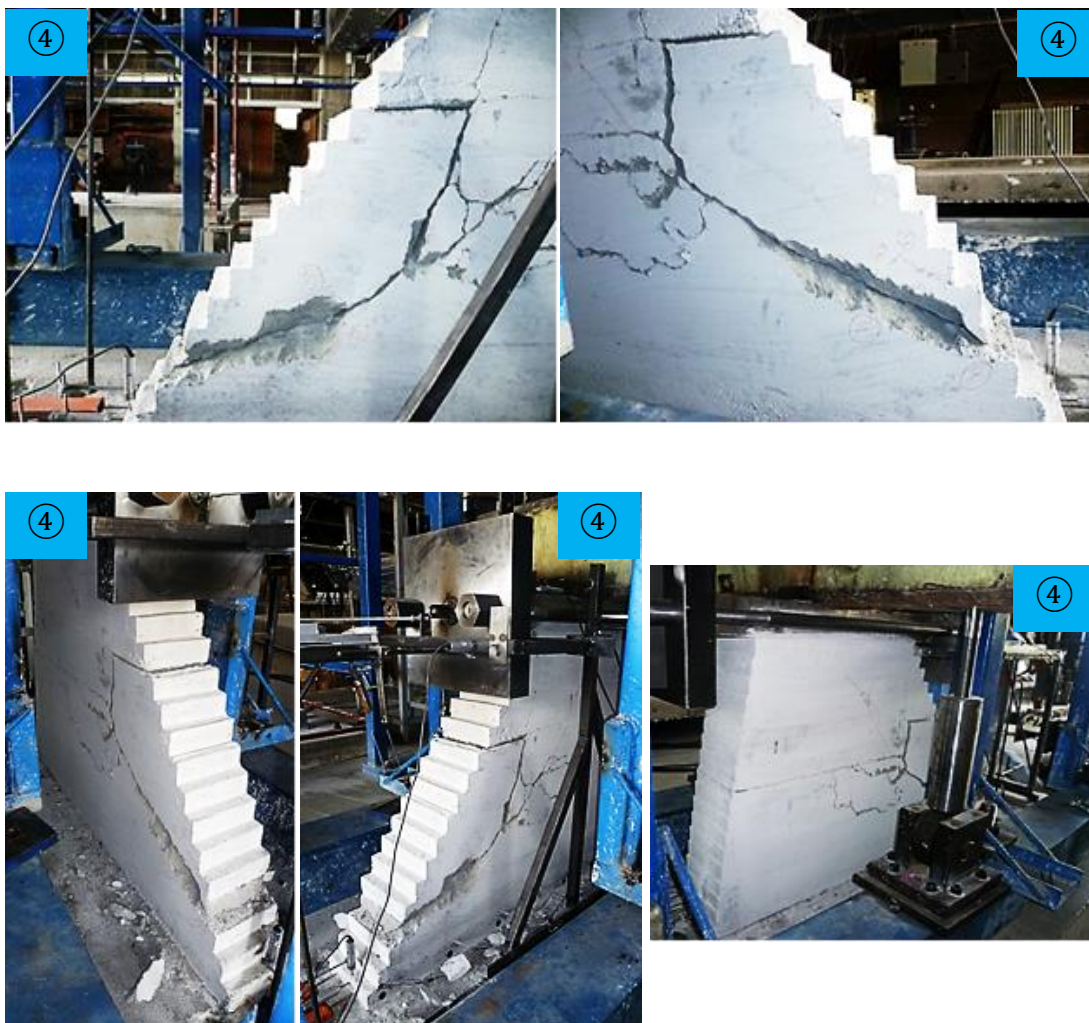
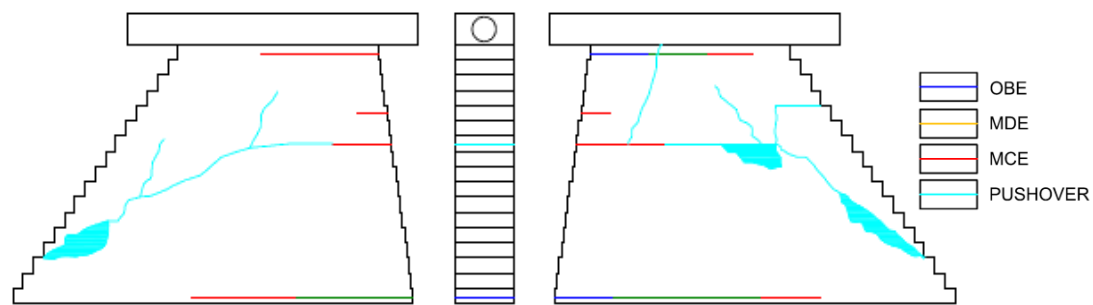


**Figure 5.32.** Cracks Formed in Specimen 2 during Pushover Experiment 3



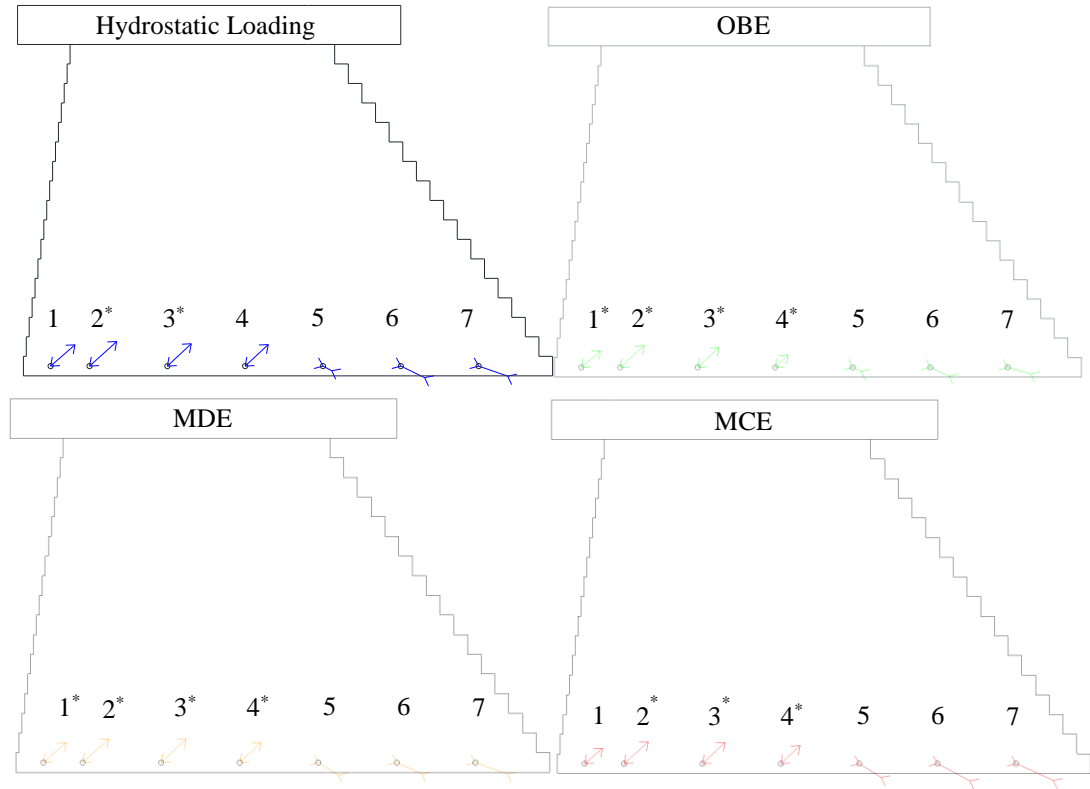


**Figure 5.33.** Principal Strain Distributions over the Base of Dam Specimen for Specimen 2

*Inward arrows indicate compressive strains and outward arrows indicate tensile strains.*

*\* : These values indicate that the recorded principal strain has exceeded the cracking strain limit.*

#### 5.2.4 Identification of Dynamic Parameters of the Specimen

The fundamental period and the equivalent viscous damping of the second specimen were obtained for each hazard level by using the procedure described in Chapter 5.1.3.

The natural period of the undamaged test specimen was determined as 0.08s. This calculated period was detected remaining nearly constant (Figure 5.34.a). However, the period elongated to nearly 0.12 sec during the MCE level due to the enlarged cracks formed during the previous earthquakes (Figure 5.18 and Figure 5.26).

Unlike the first specimen, the identified damping ratio did show a change between 2% and 20% for OBE motion. During the strong shaking (between 1s and 2s), the damping ratio was identified up to 15%, which was much larger than the 5% value suggested by USACE (2003). This behavior could be explained by the fact that, before cracking (damage accumulation), the energy was damped out by the relative

motion between the RCC layers. But, due to the opening of major cracks, the energy was dissipated by crack openings and closing as in Specimen 1. The explained energy dissipation mechanism was also validated by identified damping ratios for MDE and MCE motions. The damping ratio tended to decrease with increased base crack lengths. Consequently, the damping ratios were identified as 5 and 3% for MDE and MCE motions, respectively (Figure 5.34.b).

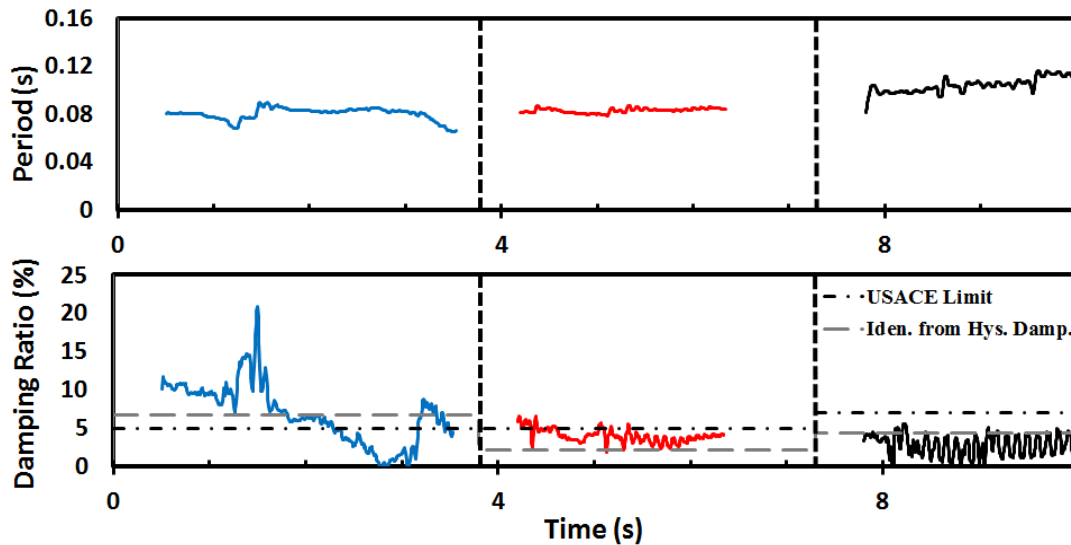


**Figure 5.34.** Variation of the Fundamental Period and Damping Ratio during the Experiment for Specimen 2

### 5.3 Specimen 3: RCC Gravity Dam

#### 5.3.1 Hydrostatic Loading

The base shear versus tip displacement and base shear – base displacement curves during hydrostatic loading are presented in Figure 5.35.

From this figure, it is apparent that this specimen also remained in its linear range. Similar to the second specimen, no cracking was observed during the application of hydrostatic load.

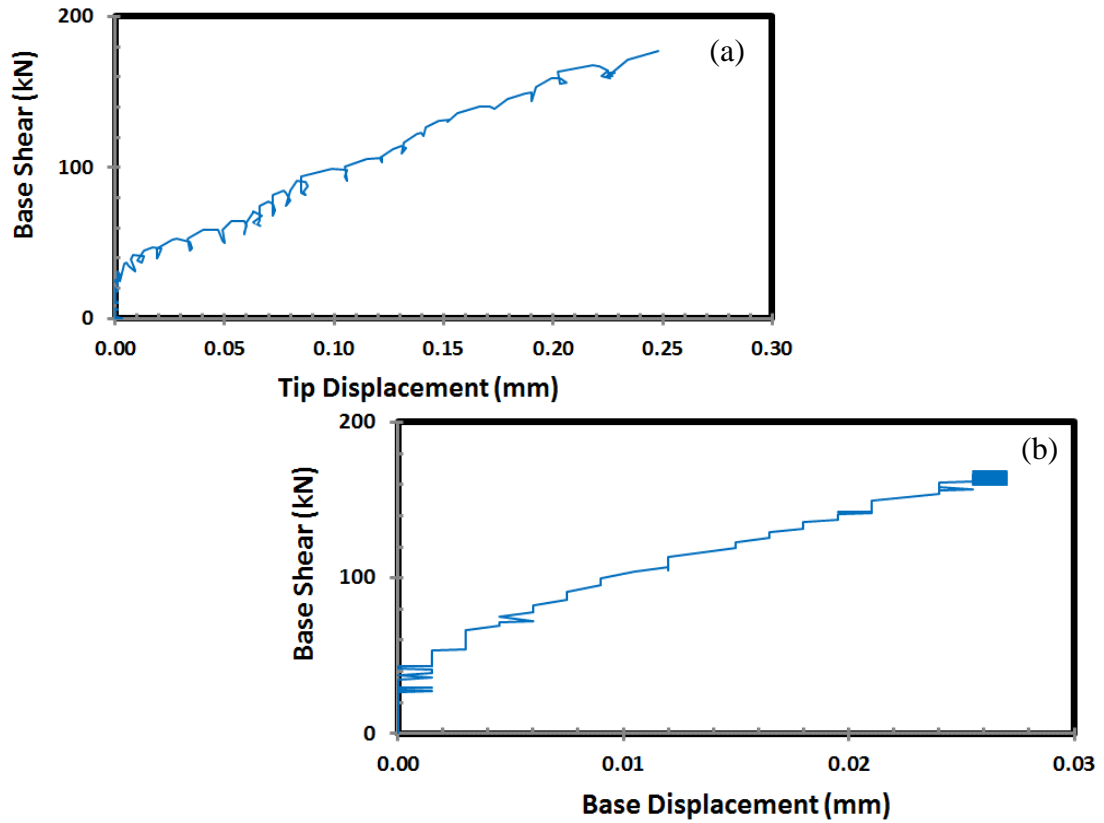


**Figure 5.35.** (a) Base Shear – Tip Displacement and (b) Base Shear – Base Displacement Curves during Hydrostatic Loading for Specimen 3

### 5.3.2 PSD Testing

#### 5.3.2.1 OBE

The base shear, tip and base displacements and the axial force were monitored and the change of these parameters and the base shear-tip displacement response of the test specimen are shown in Figure 5.36. The locations of significant damage on the system for the OBE motion are depicted in Figure 5.37. The recorded base uplift and rotation demands are shown in Figure 5.38.

During the OBE motion, some minor cracks at the upstream side of the dam base were observed. The maximum crack length was recorded as 200 mm with the maximum crack width reaching 0.2 mm (Figure 5.37). The maximum base shear and the tip displacement demands were measured as 146 kN and 0.29 mm, respectively. Furthermore, the deformation at the base was less than 0.03 mm during the full duration of the test (Figure 5.36). In addition, the stiffnesses in upstream and

downstream directions were different for this specimen as this specimen had some minor damage at the upstream face.

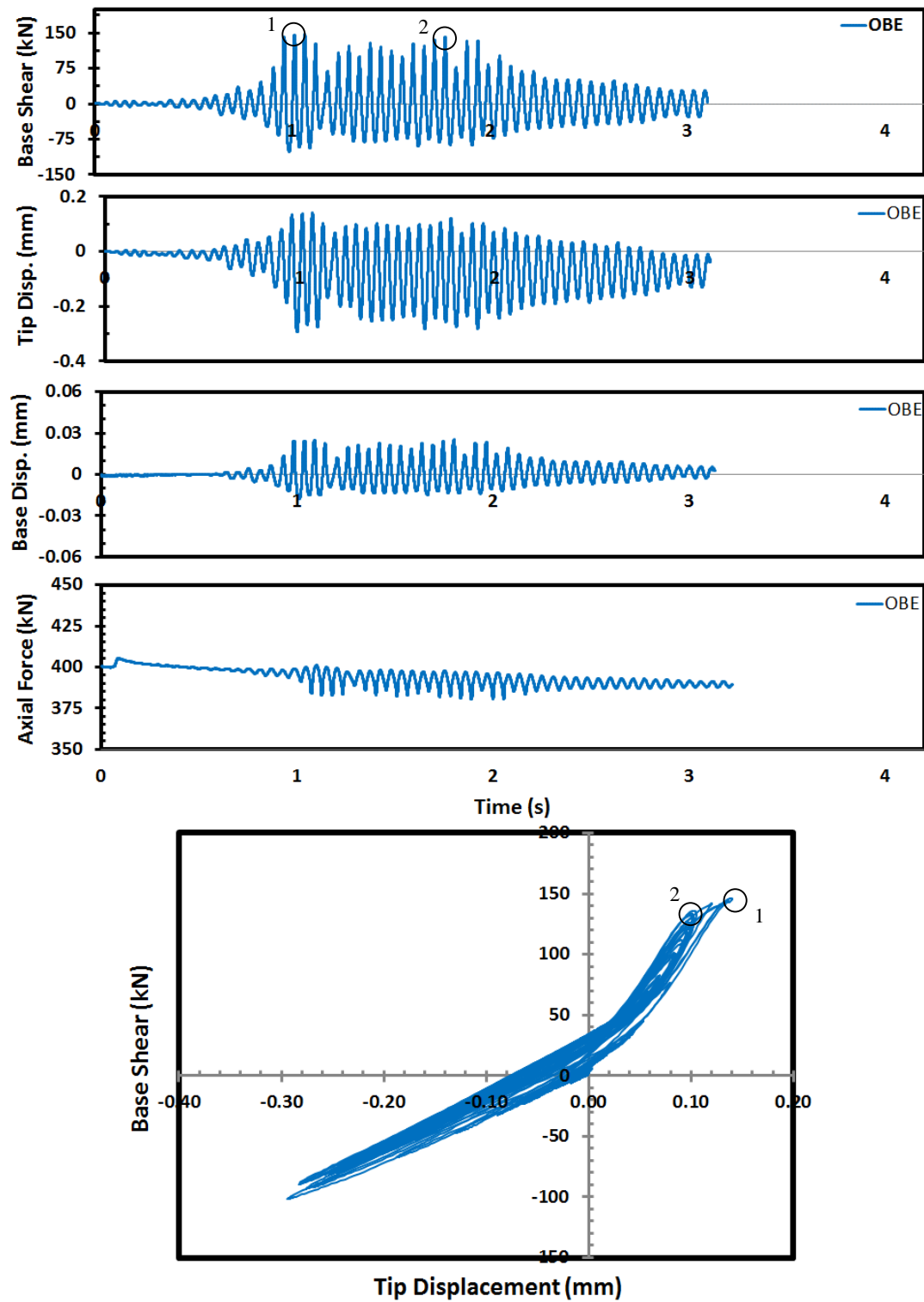


**Figure 5.36.** Force and Displacement Demands during OBE Experiment for Specimen 3

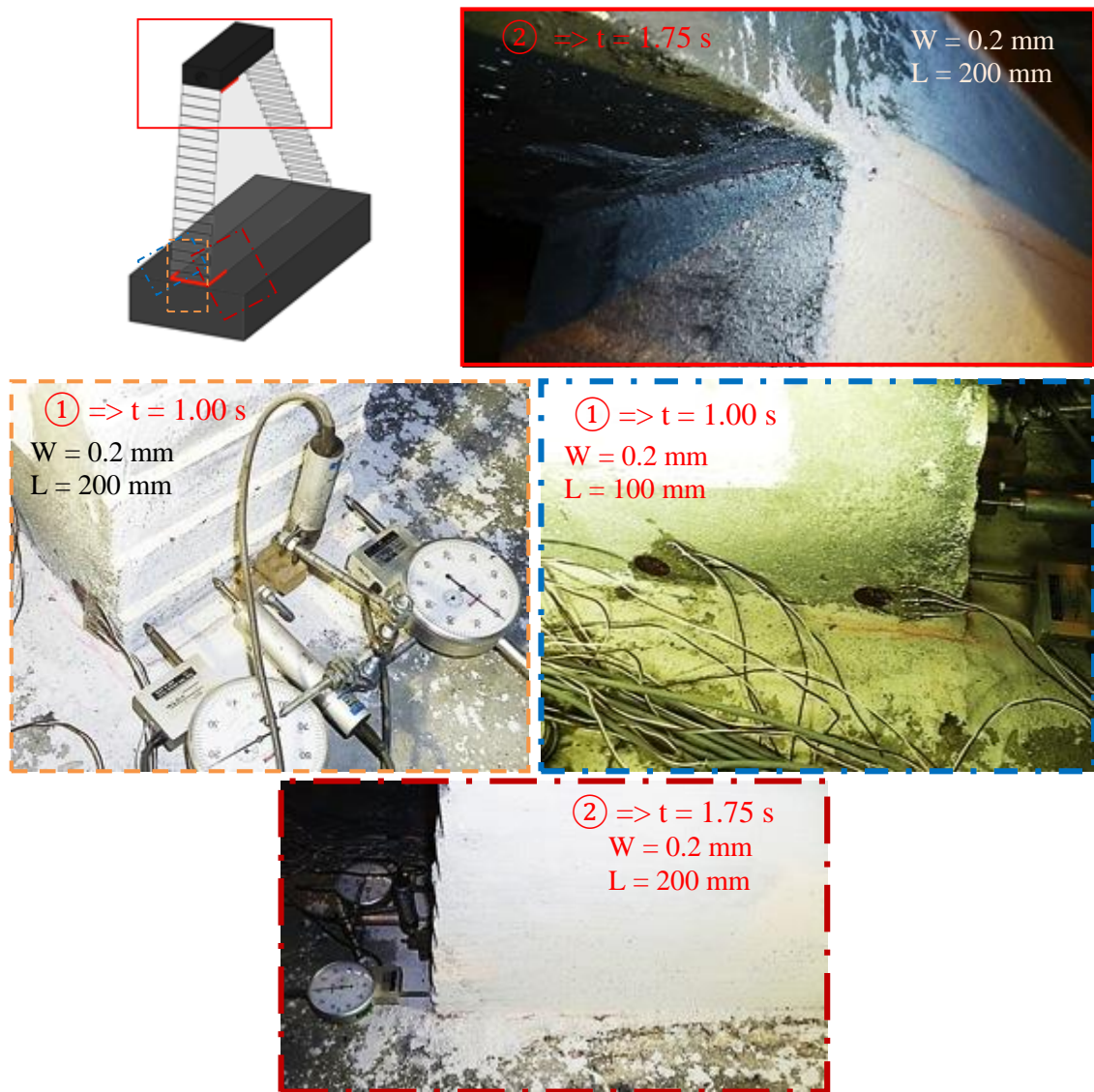


**Figure 5.37.** Cracks Formed during OBE motion for Specimen 3

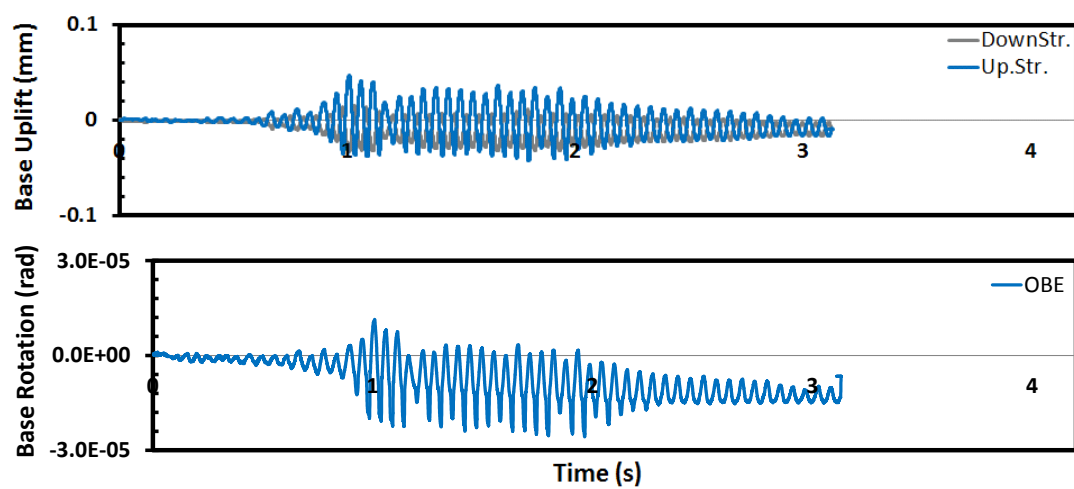


**Figure 5.38.** Base Uplift and Rotation Demands during OBE Experiment for Specimen 3

### 5.3.2.2 MDE

The recorded base shear, tip displacements, base displacement and axial force during MDE motion are presented in Figure 5.39.

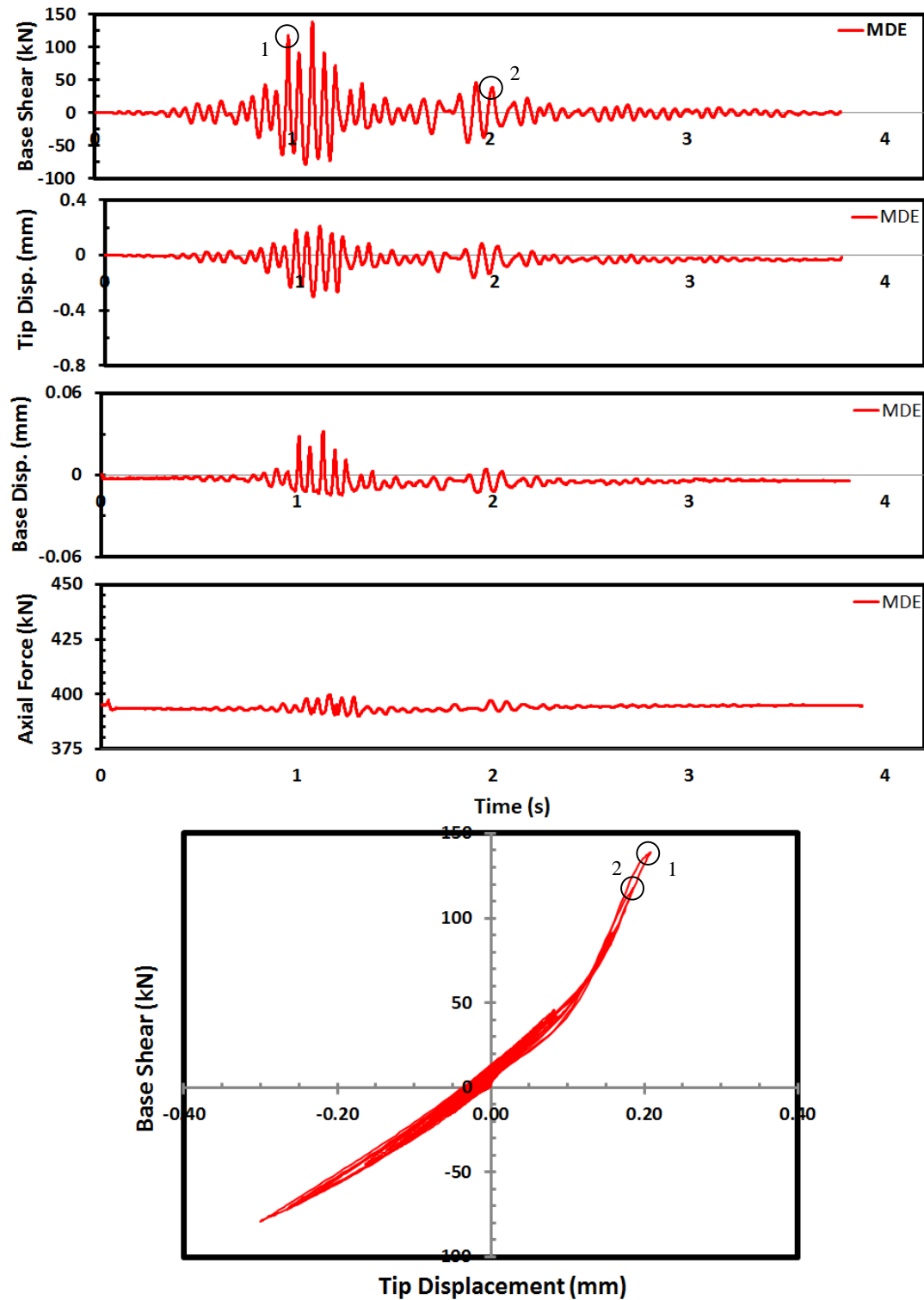


**Figure 5.39.** Force and Displacement Demands during MDE Experiment for Specimen 3

The base shear-tip displacement response of the test specimen is also shown in Figure 5.39. The recorded base uplift and rotation demands are shown in Figure 5.40. The locations of significant damage on the system for the MDE motion are depicted in Figure 5.41.

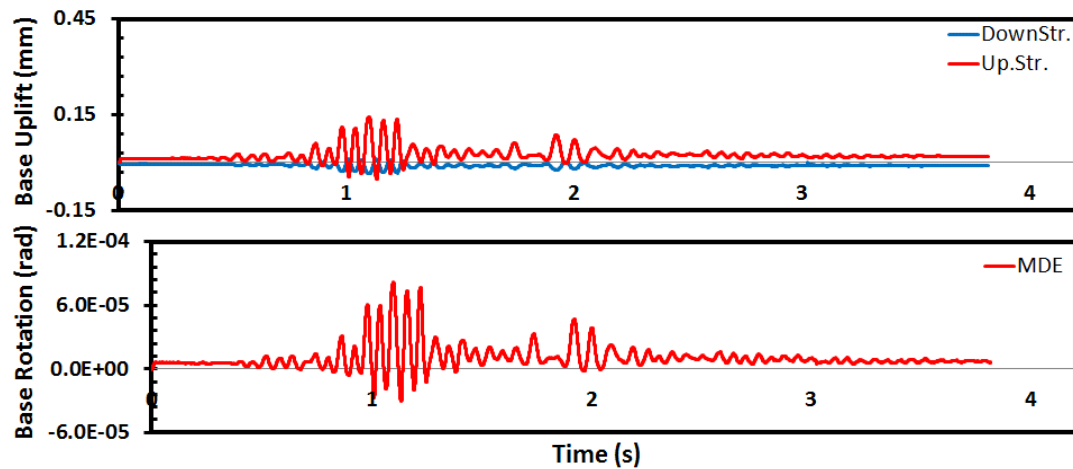


**Figure 5.40.** Base Uplift and Rotation Demands during MDE Experiment for Specimen 3

For the second ground motion, MDE, the maximum tip displacement was obtained as 0.43 mm, corresponding to a maximum base shear demand of 176 kN. The increase in the displacement and force demands with respect to the OBE level were calculated as 47.7% and 20.7%, respectively. Consequently, the MDE level testing resulted in increased crack lengths and widths at 2.10sec. The maximum crack width and length reached 0.3mm and 300mm, respectively (Figure 5.41). Similar to the second specimen, no body crack was observed at the upstream face during this level. The base deformation was less than 0.05mm during this level as well (Figure 5.39). In addition, there were no axial load problem, evidenced by the axial load change of 5%.



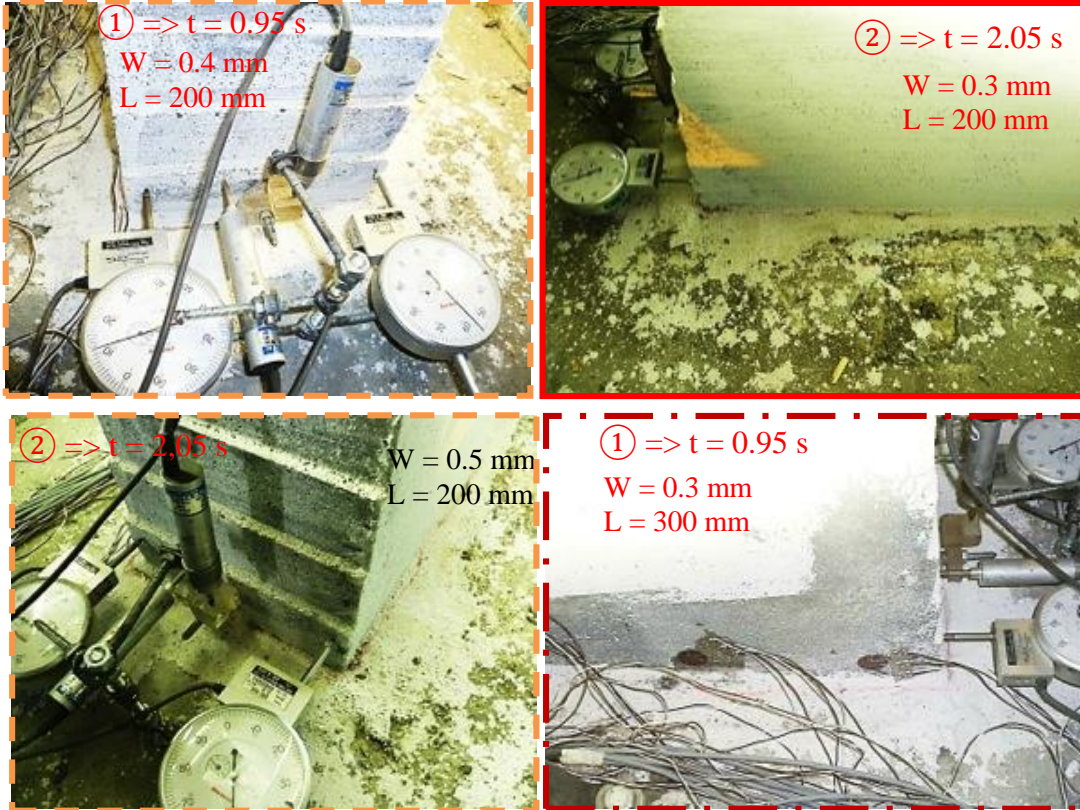
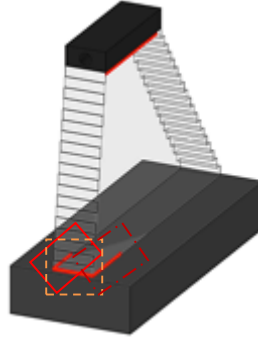


**Figure 5.41.** Cracks Formed during MDE motion for Specimen 3

### 5.3.2.3 MCE

The base shear, tip displacements, base displacement and axial force along with the base shear-tip displacement response of the test specimen are shown in Figure 5.42. The locations of significant damage on the system for the MCE motion are depicted in Figure 5.43 and Figure 5.44. The recorded base uplift and rotation demands are shown in Figure 5.45.



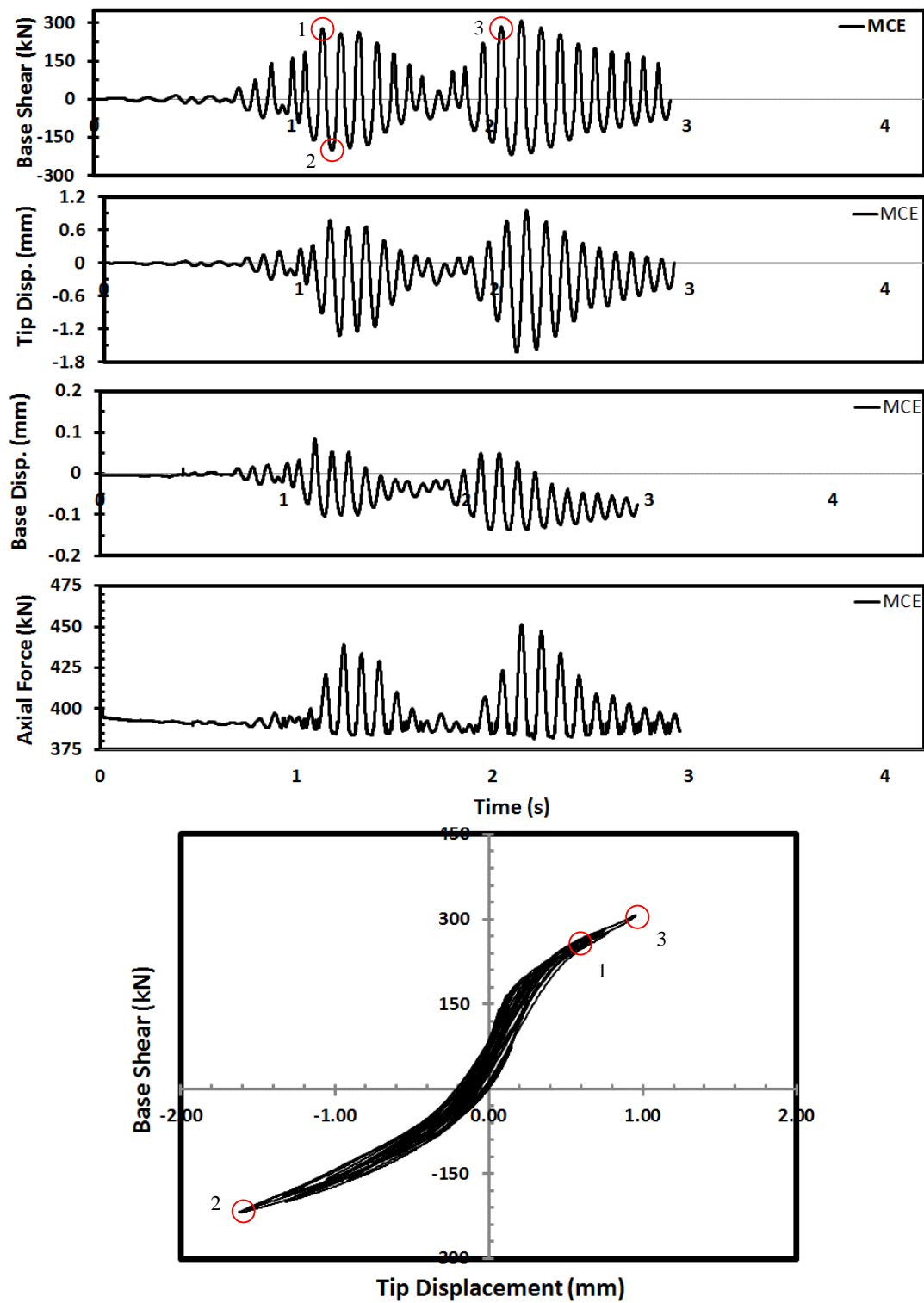


**Figure 5.42.** Force and Displacement Demands during MCE Experiment for Specimen 3

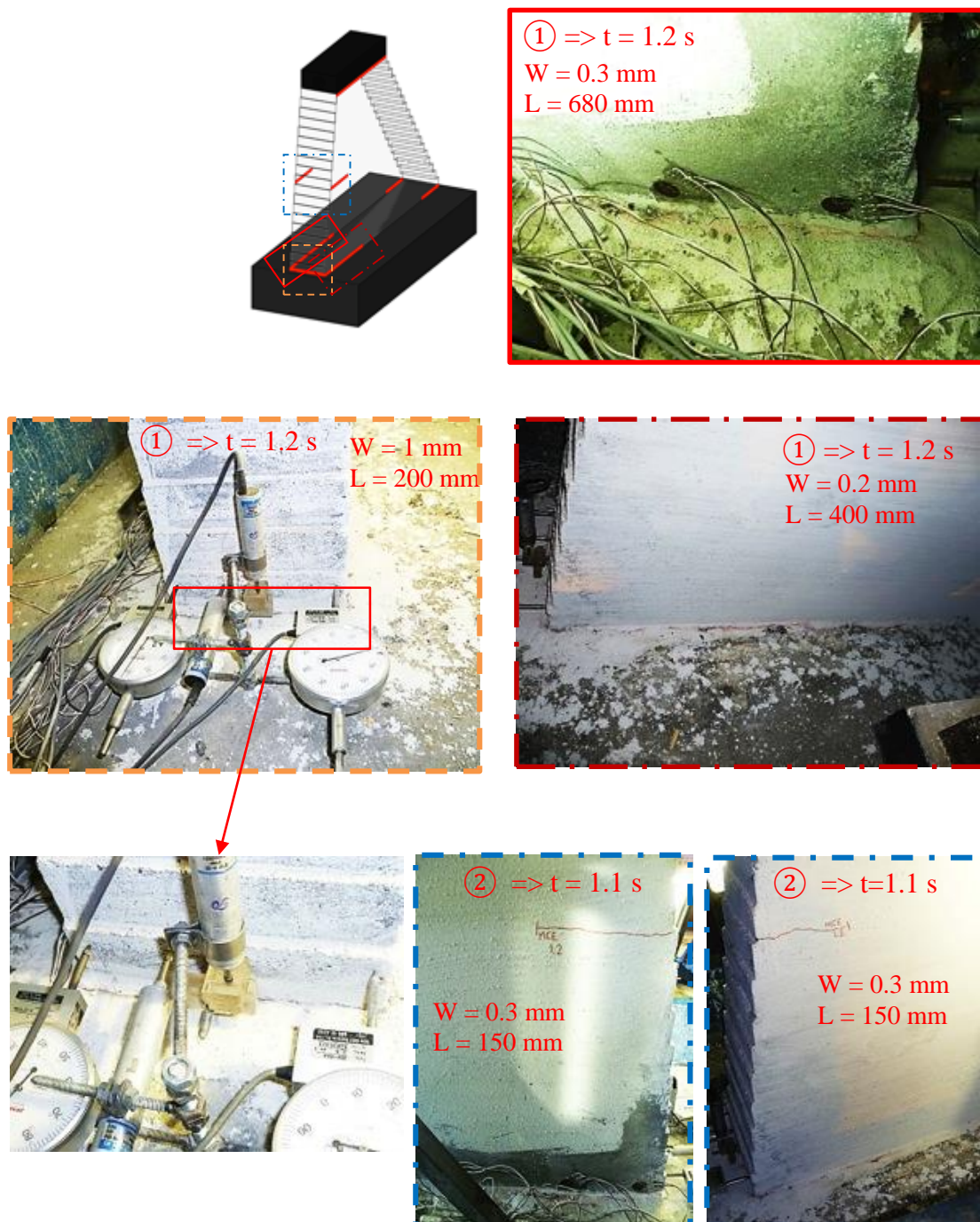


**Figure 5.43.** Cracks Formed in Specimen 3 during the MCE motion 1

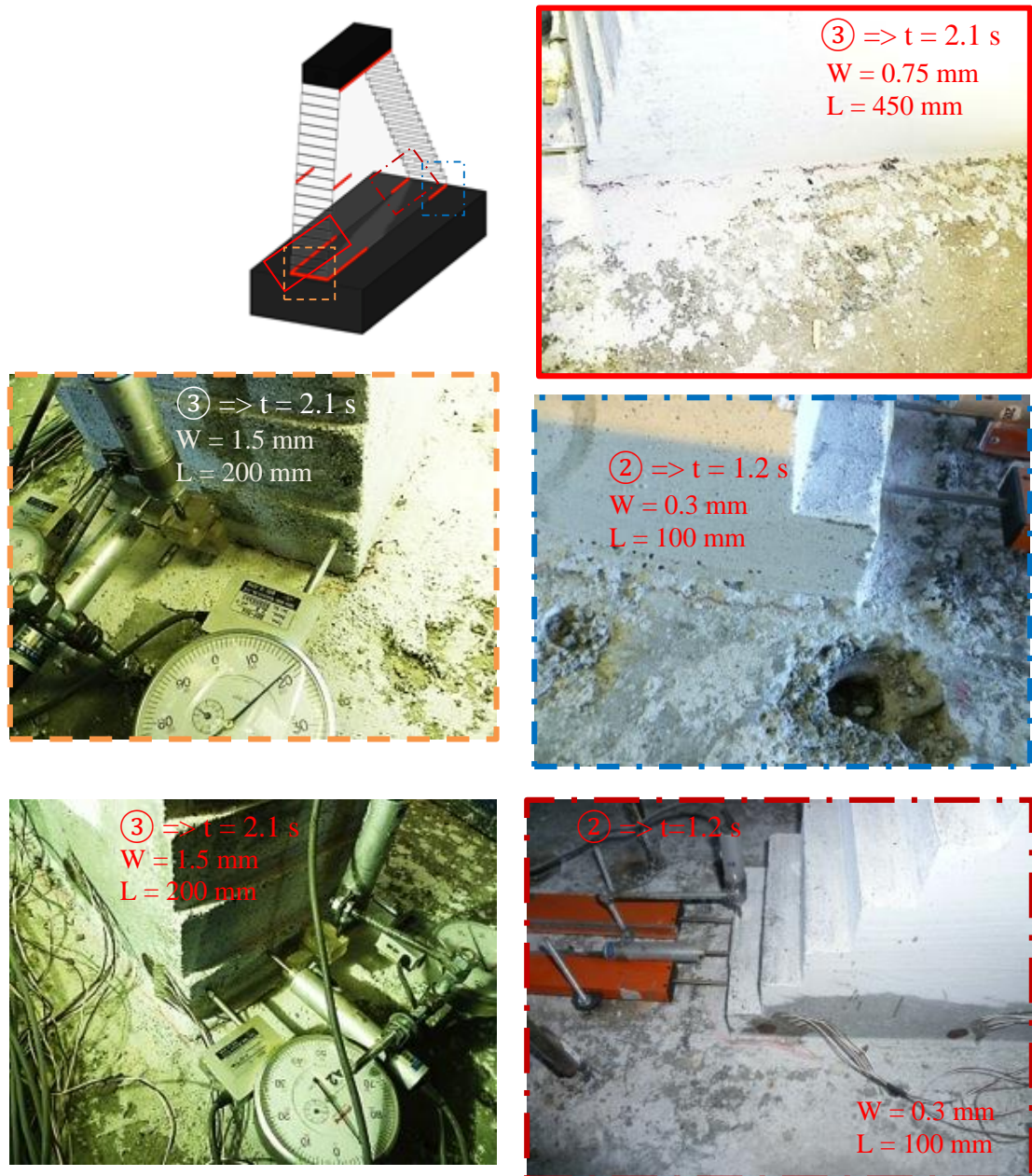


**Figure 5.44.** Cracks Formed in Specimen 3 during the MCE motion 2

During the MCE hazard level, the maximum top displacement demand was recorded as 1.62 mm. The increase in the displacement demand was approximately 4 times the displacement demand observed in the MDE level. Similarly, the base shear demand was obtained as 307 kN, nearly 1.7 times the maximum demand measured during the MDE level testing. In addition to the cracking at the base, another crack reaching to a length of 150 mm was initiated at the upstream face during this level (Figure 5.43 and Figure 5.44). During this hazard level, base cracking at the downstream face was also detected (Figure 5.42).

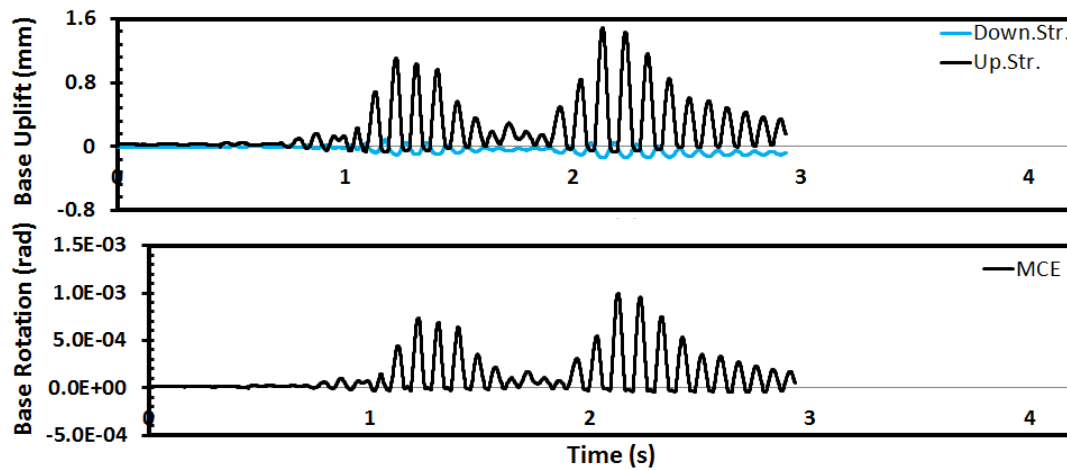


**Figure 5.45.** Base Uplift and Rotation Demands during MCE Experiment for Specimen 3

The maximum base deformation demand remained below 0.15 mm. The permanent base displacement was reached a value of 0.08 mm, which was not caused by sliding (Figure 5.46). The main reason for this permanent deformation was the residual deformations during inelastic concentrated deformation cycles. The change in axial force was larger during MCE motion but the maximum change was less than 10%, which was in acceptable limits. Based on the large base shear demand, the specimen began to behave in its nonlinear range (Figure 5.42). However, the level of nonlinearity was not excessive.

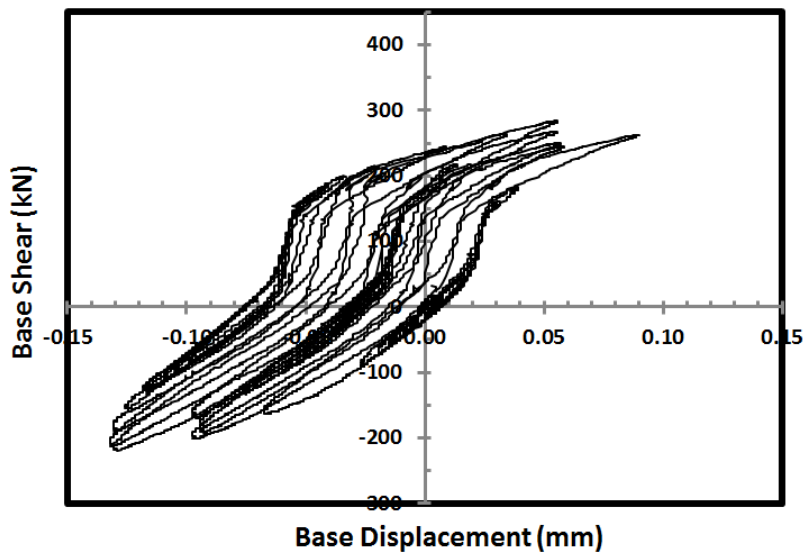


**Figure 5.46.** Base Shear versus Base Displacement Curve during MCE motion for Specimen 3



#### 5.3.2.4 Pushover Experiment

The specimen had reached its lateral load carrying capacity (nearly 400 kN) at a tip displacement of approximately 3 mm (Figure 5.47). After this tip displacement, a yield plateau was observed till the end of the test, which corresponded to a tip displacement of about 11 mm. During the pushover test, the previously formed cracks widened (reaching nearly 1.5-mm width) and the crack lengths remained nearly constant (Figure 5.48). In addition, there was some residual base deformation that was very small compared to the tip displacement (Figure 5.47). From Figure 5.47, it can also be inferred that the base stiffness was reduced at high levels of tip displacement due to the large cracks without losing its stiffness completely. Some concentrated plastic deformations took place at the base level but that deformation was not caused by a sudden sliding of the base.

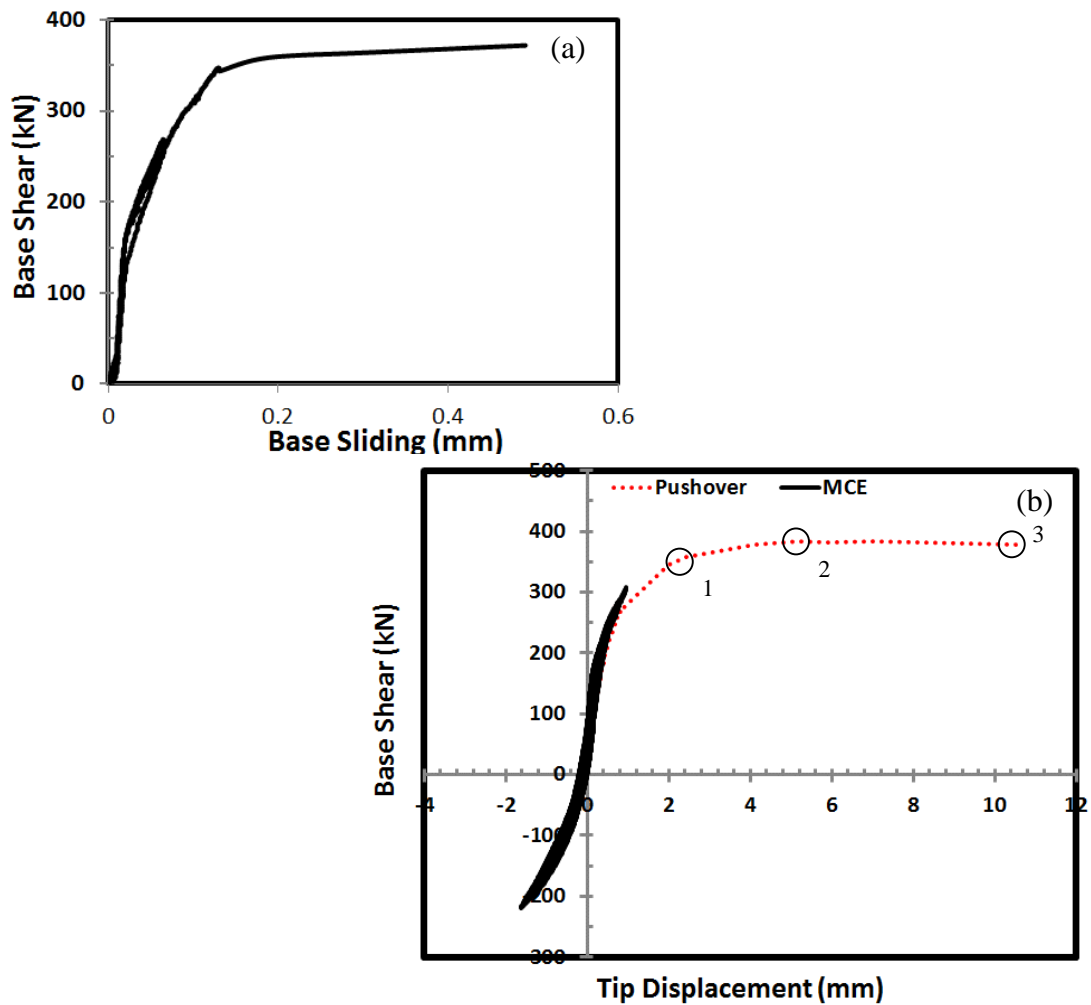
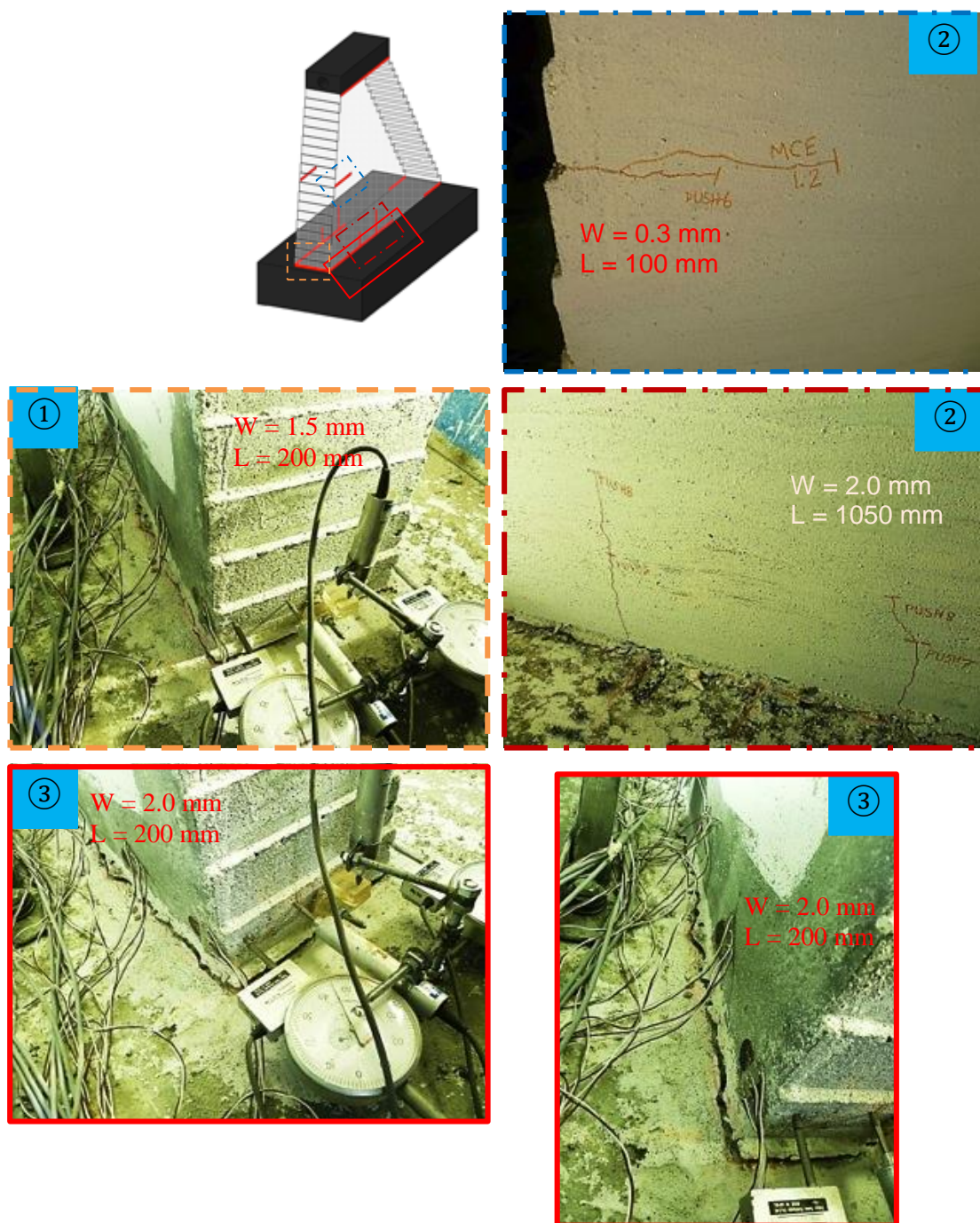


Figure 5.47. Pushover Curve for Specimen 3



**Figure 5.48.** Cracks Formed During Pushover Experiment for Specimen 3

### 5.3.3 Identification of the Dynamic Parameters of the Specimen

The fundamental period and the equivalent viscous damping of the second specimen were obtained for each ground motion by using the procedure described in Chapter 5.1.3.

The natural vibration period of the undamaged test specimen was determined as 0.06s. This calculated period was nearly constant during the ground motions OBE and MDE (Figure 5.49.a). However, the period elongated to nearly 0.10s during the MCE level due to the enlarged cracks formed during the previous earthquakes (Figure 5.43 and Figure 5.44).

The identified damping ratio changed between 1% to 3% for the OBE motion. The damping ratio was identified as less than 5%, which was recommended by USACE (2003). This low damping ratio was, most probably, because of the fact that this specimen was tested under the effect of OBE motion, twice. Similar to the second specimen, the damping ratio tended to decrease with increased base cracking. Consequently, the damping ratios were identified as 5 and 3% for MDE and MCE motions, respectively (Figure 5.49.b).

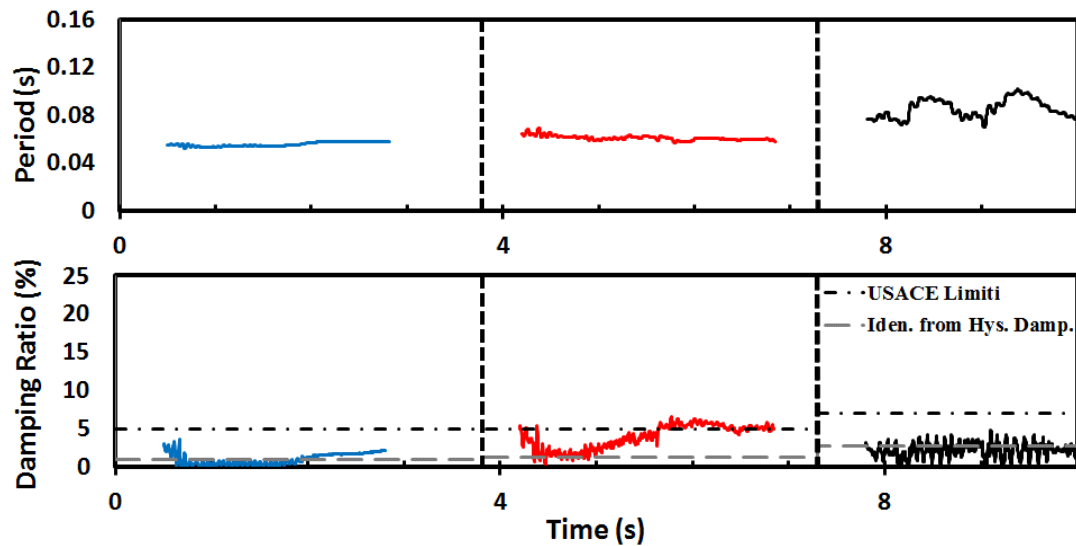


**Figure 5.49.** Variation of the Fundamental Period and Damping Ratio during the Experiment for Specimen 3

#### 5.4 Discussion of Test Results

In this part, the results for the three different specimens will be discussed based on the monitored capacity curves and the observed crack patterns. The key points of discussion will be the effect of the compressive strength and the material type (CVC or RCC) on the behavior of the dam specimens. The experimental results are

summarized in Table 5.1. Following important remarks can be made based on the observations from the tests:

- The type of material (CVC vs RCC) was detected to have negligible effect on the behavior and the base shear capacity of the specimens as long as the compressive strength values were similar. This conclusion was apparent from the obtained capacity curves of Specimen 1 and 3 (Figure 5.50). It is apparent that the lateral load carrying capacities of Specimen 1 and 3 are very close to each other. Although there was a difference in the maximum displacements, one should remind that the pushover experiments of these two specimens were stopped before the failure mechanism was formed. Therefore, those maximum displacements did not necessarily imply the displacement capacities of specimens.

**Table 5.1.** Summary of All Tests

		Maximum Upstream Crack Length (mm)	Maximum Downstream Crack Length (mm)	Percentage of Uncracked Region	Ave. Period (s)	$\Delta_{max}$ (mm)	$F_{max}$ (kN)	$\xi$ (%)
Specimen 1	<i>OBE</i>	400	0	29	0.07	0.20	55	2
	<i>MDE</i>	550	0	40	0.08	0.31	69	3
	<i>MCE</i>	1050	200	92	0.12	1.37	270	4
	<i>Pushover</i>	1050	200	92	-	7.6	400	-
Specimen 2	<i>OBE</i>	200	0	15	0.08	0.33	48	5
	<i>MDE</i>	700	0	51	0.09	0.66	132	5
	<i>MCE</i>	900	0	66	0.12	1.65	222	3
	<i>Pushover</i>	900	0	66	-	10.4	330	-
Specimen 3	<i>OBE</i>	200	0	15	0.06	0.29	146	1
	<i>MDE</i>	300	0	22	0.06	0.43	176	3
	<i>MCE</i>	680	100	57	0.10	1.62	307	2
	<i>Pushover</i>	1050	100	85	-	10.8	395	-

- The type of concrete also did not influence the crack propagation and length significantly. To compare the crack propagations, the pushover experiment results of Specimen 1 and Specimen 3 were utilized as the demands during OBE, MDE and MCE motions were different for Specimen 1 and Specimen 3 depending on the distinct periods of these specimens. From Figure 5.14 and



Figure 5.48, it is clear that the observed base cracks had similar lengths and geometries for the two specimens. Although there were some additional vertically oriented base cracks in Specimen 3 contrary to Specimen 1, general appearance of the cracks and their lengths were similar.

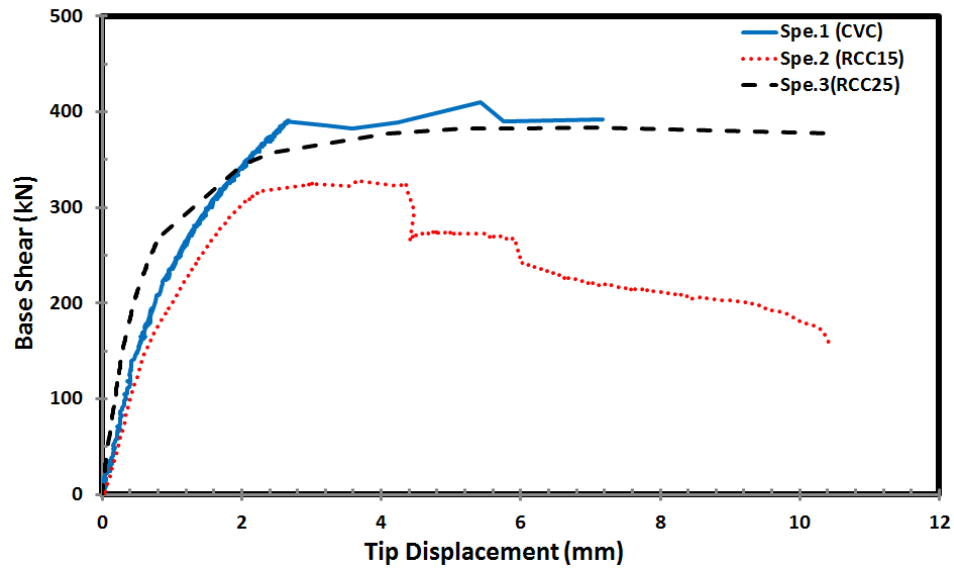


**Figure 5.50.** Comparison of Capacity Curves of All Specimens

- The effect of compressive/tensile strength on the behavior of dam specimens could be investigated by comparing the results of Specimen 2 and Specimen 3 as these specimens had the same material type (RCC) with different compressive strengths. A 20% difference in the lateral load capacity could be identified between these two specimens. Furthermore, lateral displacement capacities of these two specimens differed more than two times. More importantly, the failure mechanism observed in Specimen 2 was not detected in Specimen 3 due to additional lateral displacement capacity of this specimen. This observation was attributed to the comparable low tensile strength of Specimen 2, which resulted in more severe body cracks.
- The normalized dissipated energies during each hazard level for all specimens were also calculated. It can be inferred from Figure 5.51 that there are some discrepancies between the normalized dissipated energies for all specimens. This could stem from the different demands dependent on the fundamental periods of each specimen. The normalized dissipated energies

during each scenario was comparable to each other. In addition, the damping ratio for the most demanding cycles was also determined by using the proposed method by Megally (1998) (Eq.5.5) and summarized in Table 5.2. It is clear from Table 5.2 that the calculated damping ratios were similar to the ones obtained from the identifications. This result double checks the identified damping ratios.

$$\xi = \frac{1}{4\pi} * \frac{\text{Dissipated Energy in Cycle}}{\text{Elastic Energy}} \quad (5.5)$$

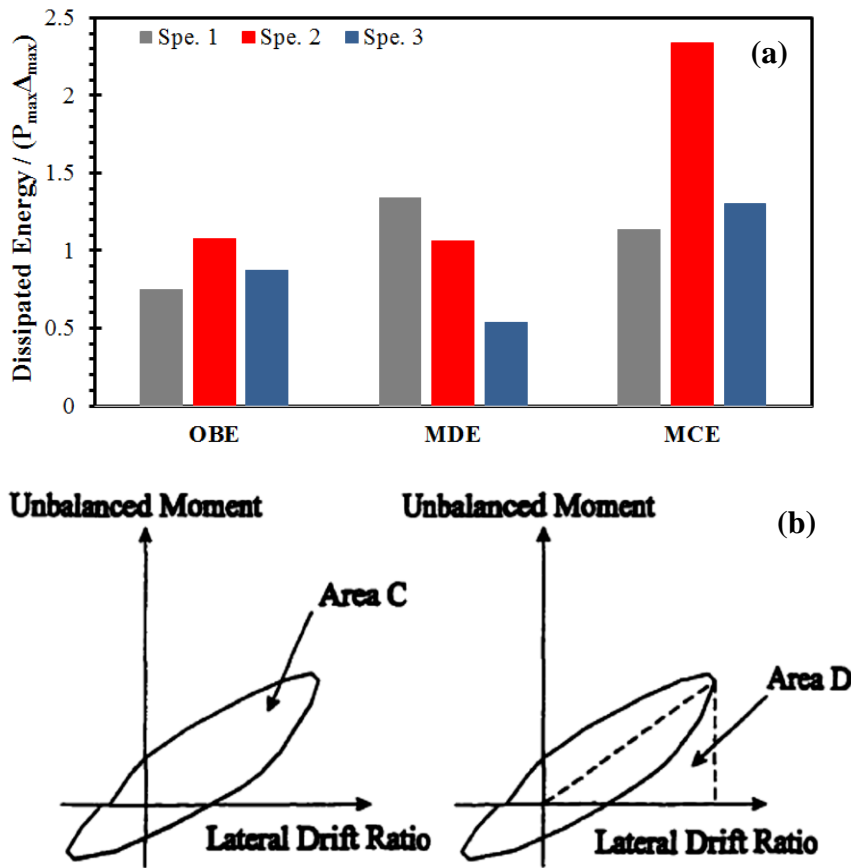


**Figure 5.51.** (a) Total Dissipated Energies for All Specimens and (b) Hysteretic Damping Plot from Megally (1998)

- The stiffness of the base of each dam specimen was reduced due to major base cracks especially at the upstream face. However, none of the specimens had showed pure sliding motion, i.e. a time period in which zero stiffness was detected (spike-type motions in base deformation records). Therefore, it could be concluded that the base application (surface roughening) would prevent

base sliding type failure modes. In fact, there was another on-going research that reveals the importance of base treatment (Binici et al 2016). In that research, it was shown that very limited base and body cracks were observed in the specimens with untreated base (smooth base). However, some base sliding was detected even during MCE level (Figure 5.52). Base sliding during pushover experiment was measured as about 12 mm, which resulted in stability loss of the dam body (Figure 5.53). The danger of this base sliding was also the fact that the base sliding would tear the waterstoppers at the foundation interface and would cause leakage. Therefore, the base application has an important effect on the seismic behaviour of concrete gravity dams. Consequently, the type of base treatment would affect the failure mechanism of the dam specimens.

**Table 5.2.** Damping Ratios calculated by the Method proposed by Chopra (2012)

<b>Damping Ratio (%)</b>						
<b>Specimen</b>	<b>OBE</b>		<b>MDE</b>		<b>MCE</b>	
	<b>Eq. 5.5</b>	<b>Ave. Iden.</b>	<b>Eq. 5.5</b>	<b>Ave. Iden.</b>	<b>Eq. 5.5</b>	<b>Ave. Iden.</b>
<b>1</b>	2.34	3.00	3.03	3.50	2.50	4.00
<b>2</b>	6.76	8.00	2.08	4.00	4.79	3.50
<b>3</b>	1.00	1.00	1.18	3.00	2.72	2.50

- The identified damping ratios of all specimens were similar to each other. When these identified damping ratios were compared with those utilized while performing time history analysis of concrete gravity dams recommended by USACE (2003) (Figure 5.15, Figure 5.34 and Figure 5.49), it could be observed that USACE damping values were in reasonable agreement with the identified values during OBE and MDE motions. Conversely, the USACE (2003) recommended 7% material damping seemed to be higher than the identified value for the MCE motion. The visual inspection of the load-deformation response of the dam also exhibited that in the absence of any significant sliding the hysteresis loops are narrow and crack opening-closing could only produce 2 to 4% damping. It should be

mentioned that the identified damping discussed herein only referred to the material damping for a single monolith excluding any interaction between monoliths. For dam monoliths that could interact with each other and built on flexible foundation, the damping could be much higher due to radiation damping and bottom absorption (Fenves and Chopra 1984.b).

- Due to the successive application of ground motions, it should be reminded that the identified damping ratios included the effects of previous damages. Therefore, contrary to the expected behavior for damping, the trend in damping ratio did not accrued due to the accumulated damage. In other words, the damping ratio during the MCE motion was not determined as the maximum one as the cracks during previous motions had dissipated energy and they tended to open and close during the MCE motion. Therefore, the previously opened cracks could not cause a significant loss of energy. Consequently, the damping values would be different than the identified ones if the MCE motion was applied to an undamaged specimen.

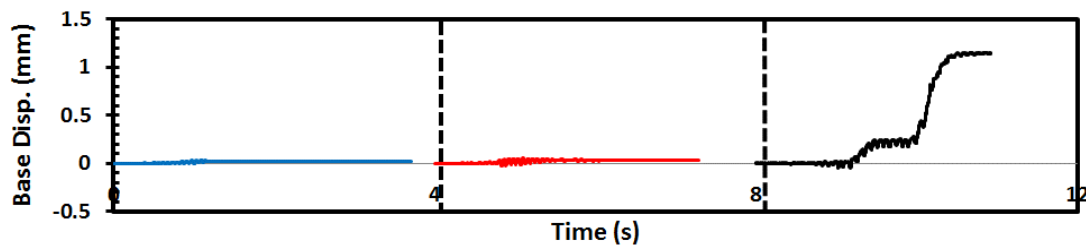


**Figure 5.52.** Base Displacement recorded in the Research conducted by Binici et al 2016

- The period of each specimen had a tendency to increase during consecutive earthquake load applications. The initial period of each specimen increased nearly 1.6 times during the last motion, MCE. This observation was valid for each specimen. More importantly, the deviations in periods during the same motion was not more than 20%. This observation was vital as the verification of the test method was totally dependent on the performed linear analysis. Therefore, the period change during any motion should not be too much not to lose the control of test results. The degree of effect of the period change was investigated by comparing numerical results of the Specimen 1 (linear

time history analysis results performed in ANSYS) with the recorded base shear response during OBE and MCE motions (Figure 5.54). While conducting the numerical analysis, the modulus of elasticity for concrete was selected such that the fundamental period matched the identified initial periods of 0.07 sec and 0.10 sec for OBE and MCE motions, respectively. It could be observed that agreement between the base shear time series are acceptable, indicating the validity of the pretest assumptions.

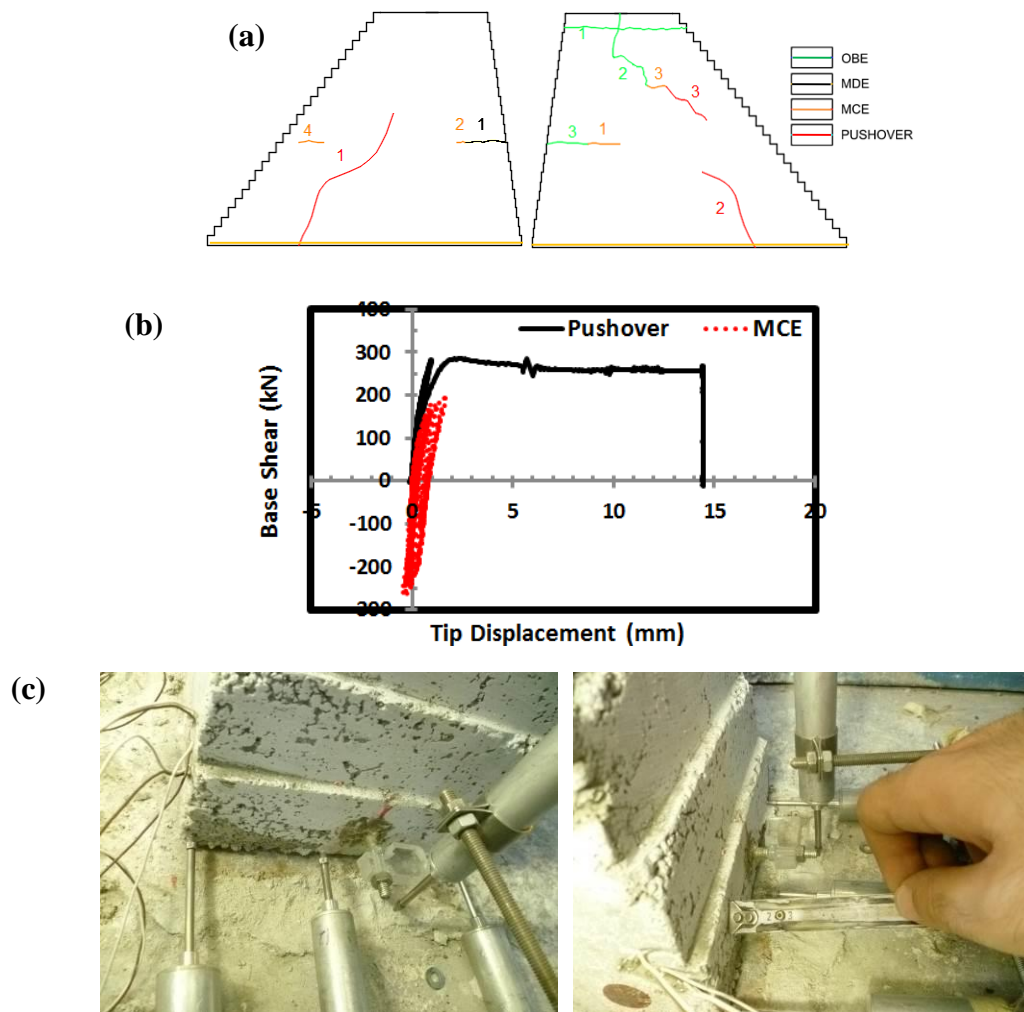
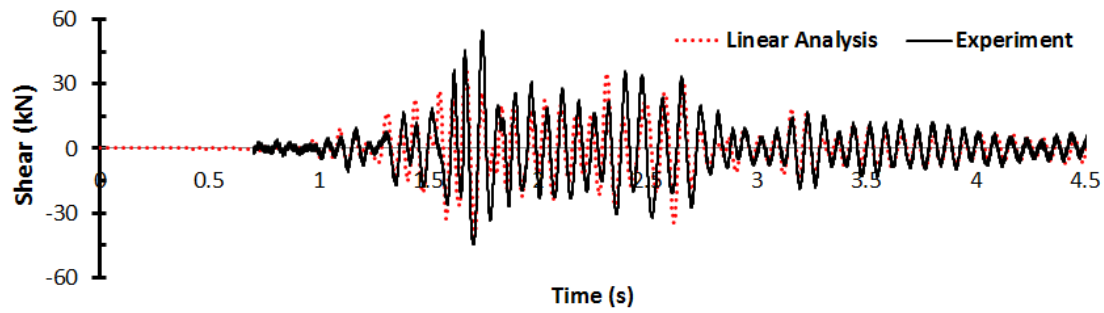
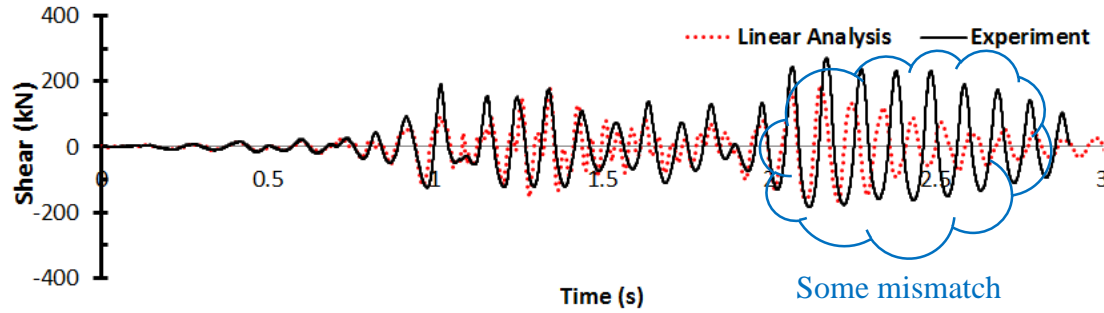


**Figure 5.53.** Results of Pushover Experiment from the Research conducted by Binici et al 2016



(a) OBE Motion



(b) MCE Motion

**Figure 5.54.** Comparison of the Base Shear Values obtained from EAGD and Experiments

- The test results for the Specimen 1, which resembles closely the properties of the actual Melen Dam reveal that the dam is not expected to sustain any significant damage (i.e. sliding, overturning, shear failure) under the expected hazard level. This conclusion is obviously limited with the assumptions of the testing and the production scheme for the specimens.

## CHAPTER 6

### NUMERICAL SIMULATIONS

The use of appropriate numerical tools for the seismic performance estimation of dams is extremely important due to the following reasons:

- There is a very limited number of concrete dams subjected to strong ground motions to quantify actual performance and make a judgement based solely on observed behavior,
- The number of experimental studies on dams is quite limited to reach a decisive conclusion on their performance by using an experimental database.

Consequently, numerical simulations play a crucial role in seismic design of dams. Design engineers, when employing nonlinear models for dam analysis are usually unaware of the accuracy of their models in predicting displacements, strains, crack lengths, etc. Recently, Soysal et al (2016) employed some of the test results presented in this dissertation to validate the ability of DIANA (2008) in estimating the cracking and capacity. Her findings suggested that the dam strength can be estimated with a reasonable accuracy, however crack locations and widths are found with a greater margin of error.

In this chapter, the goal is to verify the role of analytical modeling in the prediction of the behavior of the concrete monoliths using the data from the well documented and controlled experiment as a case study.

The employed platform in this dissertation, ANSYS, offers a fixed smeared crack model that is also utilized in other platforms such as ATENA (Červenka 2016), DIANA (2008), ABAQUS (2012), etc. with some differences. The results from these simulations obviously cannot be extrapolated to every tool, however, general conclusions are believed to represent the ability of the smeared crack models in estimating dam response during seismic events.

## 6.1 Brief Information on the Concrete Constitutive Model in ANSYS

Solid65 is the special element of ANSYS (2010.a) dedicated to model both reinforced and unreinforced concrete members. It is a three-dimensional eight-node solid element, which has three translational degrees of freedom at its nodes ( $u_x$ ,  $u_y$  and  $u_z$ ). This element can simulate cracking (in three orthogonal directions), crushing, creep deformations, etc. Although it is out-of-scope of this study, reinforcements can also be embedded inside this element by assuming smeared reinforcement within the element. It is important to note that these embedded reinforcements only contribute to axial stresses for both axial and bending loadings.

### 6.1.1 Modeling the Cracking and Crushing of Concrete

Detection of a crack at an integration point requires a modification of the stress-strain relation of the element (Eq. 6.1). Upon cracking, a plane of weakness along the perpendicular direction to the crack plane is defined by reducing the stiffness term for the direction perpendicular to the crack plane (ANSYS 2010.d). In all calculations, the principal directions are utilized as denoted by superscript “ck” in Eq. 6.2. In general, the cracking factor,  $R^t$ , is zero but the calculations are performed by assuming a value of  $1 \times 10^{-6}$  for numerical stability as the stress relaxation after cracking is ignored. If stress relaxation is taken into account to facilitate the convergence,  $R^t$  is determined from the slope of the secant line (Figure 6.1) drawn to the stress-strain relation (ANSYS 2010.d).

$$D = \frac{E}{(1+\nu)(1-2\nu)} \begin{bmatrix} 1-\nu & \nu & \nu & 0 & 0 & 0 \\ \nu & 1-\nu & \nu & 0 & 0 & 0 \\ \nu & \nu & 1-\nu & 0 & 0 & 0 \\ 0 & 0 & 0 & \frac{1-2\nu}{2} & 0 & 0 \\ 0 & 0 & 0 & 0 & \frac{1-2\nu}{2} & 0 \\ 0 & 0 & 0 & 0 & 0 & \frac{1-2\nu}{2} \end{bmatrix} \quad (6.1)$$



$$D^{ck} = \frac{E}{(1+\nu)} \begin{bmatrix} R^t \frac{1+\nu}{E} & 0 & 0 & 0 & 0 & 0 \\ 0 & \frac{1}{1-\nu} & \frac{\nu}{1-\nu} & 0 & 0 & 0 \\ 0 & \frac{\nu}{1-\nu} & \frac{1}{1-\nu} & 0 & 0 & 0 \\ 0 & 0 & 0 & \frac{\beta_t}{2} & 0 & 0 \\ 0 & 0 & 0 & 0 & \frac{1}{2} & 0 \\ 0 & 0 & 0 & 0 & 0 & \frac{\beta_t}{2} \end{bmatrix} \quad (6.2)$$

At a crack location, a parameter that measures the proportion of the transmitted shear is employed. This parameter could be different for i- open crack ( $\beta_t$ ) and ii- closed crack ( $\beta_c$ ) cases, as implemented in ANSYS (ANSYS 2010.d). In other words, the shear transfer coefficients directly determine the amount of sliding across the crack plane. For a perfectly smooth crack, the shear transfer is assumed to diminish corresponding to a shear transfer coefficient of 0 whereas this coefficient takes a value of 1 for a perfectly rough crack plane. For instance, the stress-strain relation for an element with a crack along its one principal direction is presented in Eq. 6.2 (ANSYS 2010.d).

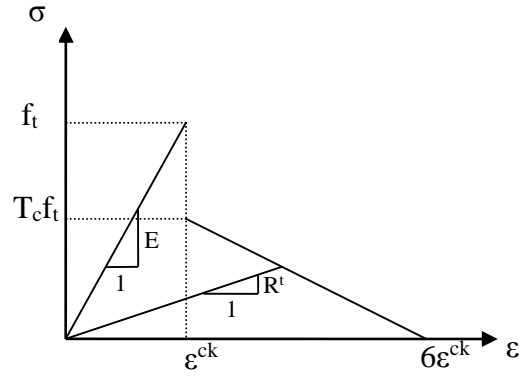


**Figure 6.1.** Description for Stress Relaxation after Cracking [ANSYS 2010.d]  
( $f_t$  is the uniaxial tensile strength and  $T_c$  is the multiplier for amount of tensile stress relaxation.)

For a closed crack case, axial stresses normal to the crack face returns back to their uncracked states and a coefficient ( $\beta_c$ ) is introduced in front of the shear terms to reflect the shear transmission capability of the crack plane (Eq. 6.3).

$$D^{ck} = \frac{E}{(1+v)(1-2v)} \begin{bmatrix} 1-v & v & v & 0 & 0 & 0 \\ v & 1-v & v & 0 & 0 & 0 \\ v & v & 1-v & 0 & 0 & 0 \\ 0 & 0 & 0 & \beta_c \frac{1-2v}{2} & 0 & 0 \\ 0 & 0 & 0 & 0 & \frac{1-2v}{2} & 0 \\ 0 & 0 & 0 & 0 & 0 & \beta_c \frac{1-2v}{2} \end{bmatrix} \quad (6.3)$$

The elements are able to crack in any three principal direction at any quadrature points. The stress-strain relationships corresponding to an element with two and three directional cracks are presented in Eq. 6.4 and 6.5.

$$D^{ck} = E \begin{bmatrix} \frac{R^t}{E} & 0 & 0 & 0 & 0 & 0 \\ 0 & \frac{R^t}{E} & 0 & 0 & 0 & 0 \\ 0 & 0 & 1 & 0 & 0 & 0 \\ 0 & 0 & 0 & \frac{\beta_t}{2(1+v)} & 0 & 0 \\ 0 & 0 & 0 & 0 & \frac{\beta_t}{2(1+v)} & 0 \\ 0 & 0 & 0 & 0 & 0 & \frac{\beta_t}{2(1+v)} \end{bmatrix} \quad (6.4)$$

$$D^{ck} = E \begin{bmatrix} \frac{R^t}{E} & 0 & 0 & 0 & 0 & 0 \\ 0 & \frac{R^t}{E} & 0 & 0 & 0 & 0 \\ 0 & 0 & \frac{R^t}{E} & 0 & 0 & 0 \\ 0 & 0 & 0 & \frac{\beta_t}{2(1+v)} & 0 & 0 \\ 0 & 0 & 0 & 0 & \frac{\beta_t}{2(1+v)} & 0 \\ 0 & 0 & 0 & 0 & 0 & \frac{\beta_t}{2(1+v)} \end{bmatrix} \quad (6.5)$$

The stress-strain relations given in Eq. 6.4 and 6.5 become Eq. 6.6 if the cracks in all directions are detected to be closed.

$$D^{ck} = \frac{E}{(1+v)(1-2v)} \begin{bmatrix} 1-v & v & v & 0 & 0 & 0 \\ v & 1-v & v & 0 & 0 & 0 \\ v & v & 1-v & 0 & 0 & 0 \\ 0 & 0 & 0 & \beta_c \frac{1-2v}{2} & 0 & 0 \\ 0 & 0 & 0 & 0 & \beta_c \frac{1-2v}{2} & 0 \\ 0 & 0 & 0 & 0 & 0 & \beta_c \frac{1-2v}{2} \end{bmatrix} \quad (6.6)$$

If, at a quadrature point, the compressive stress is determined to exceed the compressive strength, the material is assumed to be crushed. Just like the cracking

(no stress relaxation after cracking), the stiffness term for a crushed element vanishes to zero but is assumed to be  $1 \times 10^{-6}$  for numerical stability purposes.

### 6.1.2 Concrete Material

Willam-Warnke (1975) failure criterion is used to model the behavior of plain concrete. It is an isotropic material model that is able to simulate the cracking/crushing under multi-directional stress state dictated by Eq. 6.7.

$$\frac{F}{f_c} - S \geq 0 \quad (6.7)$$

In the above equation,  $F$  is defined as a function dependent on the principal stress state ( $\sigma_{xp}$ ,  $\sigma_{yp}$  and  $\sigma_{zp}$ ).  $S$  is the failure surface and  $f_c$  is the uniaxial compressive strength (ANSYS 2010.d). The details on  $F$  and  $S$  are summarized in Appendix E. If this equation is satisfied, the element is assumed to sustain cracking or crushing. Five strength parameters are required to define the failure surface,  $S$ . (Table 6.1)

**Table 6.1.** Parameters to define Willam-Warnke Failure Surface [ANSYS 2010.d]

Parameter	Definition
$f_t$	Ultimate uniaxial tensile strength
$f_c$	Ultimate uniaxial compressive strength
$f_{cb}$	Ultimate biaxial compressive strength
$f_1$	Ultimate compressive strength for a state of biaxial compression superimposed on hydrostatic stress state ( $\sigma_h$ )
$f_2$	Ultimate compressive strength for a state of uniaxial compression superimposed on hydrostatic stress state ( $\sigma_h$ )

There also exist some default values for parameters  $f_{cb}$ ,  $f_1$  and  $f_2$  in case the necessary laboratory data are not available (Eq. 6.8). Note that these default values are valid only for a hydrostatic stress state less than  $\sqrt{3}f_c$  (Eq. 6.9).

$$f_{cb} = 1.2f_c \quad (6.8.a)$$

$$f_1 = 1.45f_c \quad (6.8.b)$$

$$f_2 = 1.725f_c \quad (6.8.c)$$

$$\text{Hydrostatic Stress State} = |\sigma_h| = \left| \frac{1}{3}(\sigma_{xp} + \sigma_{yp} + \sigma_{zp}) \right| \leq \sqrt{3}f_c \quad (6.9)$$

If the principal stresses are sorted from maximum to minimum, there are only four possible failure domains (Eq. 6.10).

$$\sigma_1 = \max(\sigma_{xp}, \sigma_{yp}, \sigma_{zp}) \quad (6.10.a)$$

$$\sigma_3 = \min(\sigma_{xp}, \sigma_{yp}, \sigma_{zp}) \quad (6.10.b)$$

- I.  $0 > \sigma_1 > \sigma_2 > \sigma_3 \Rightarrow$  CCC Domain
- II.  $\sigma_1 > 0 > \sigma_2 > \sigma_3 \Rightarrow$  CCT Domain
- III.  $\sigma_1 > \sigma_2 > 0 > \sigma_3 \Rightarrow$  CTT Domain
- IV.  $\sigma_1 > \sigma_2 > \sigma_3 > 0 \Rightarrow$  TTT Domain

For each domain, different principal stress states (F) and failure surfaces (S) are defined. Therefore, there exist four different combinations of F and S pairs. In Willam-Warnke (1975) failure surface, S describes a continuous surface but the gradients are not continuous at any point where the principal stresses changes sign (Figure 6.2-Figure 6.3). Therefore, S is not differentiable at the intersection with the coordinate axes.

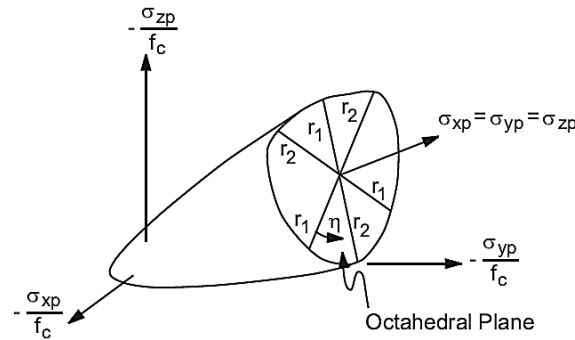


**Figure 6.2.** 3D Failure Surface in Dimensionless Principal Stress Axes  
[ANSYS 2010.d]

The failure surface for biaxial stress state is depicted in Figure 6.3. If the absolute values of  $\sigma_{xp}$  and  $\sigma_{yp}$  are two largest principal stresses,  $\sigma_{zp}$  could be i- zero, ii- little positive or iii- little negative values. For the aforementioned cases, if the projections of failure surfaces are investigated, they exhibit very close results. On the other hand, the failure mode is not the same for all of the different  $\sigma_{zp}$  options, which is utterly dependent on the sign of  $\sigma_{zp}$ . If  $\sigma_{zp}$  has taken little positive values, the failure mode will be cracking or crushing determined by the other stress states whereas the failure

mode is always crushing for other  $\sigma_{zp}$  values. Further details about the failure surface are given in Appendix E.

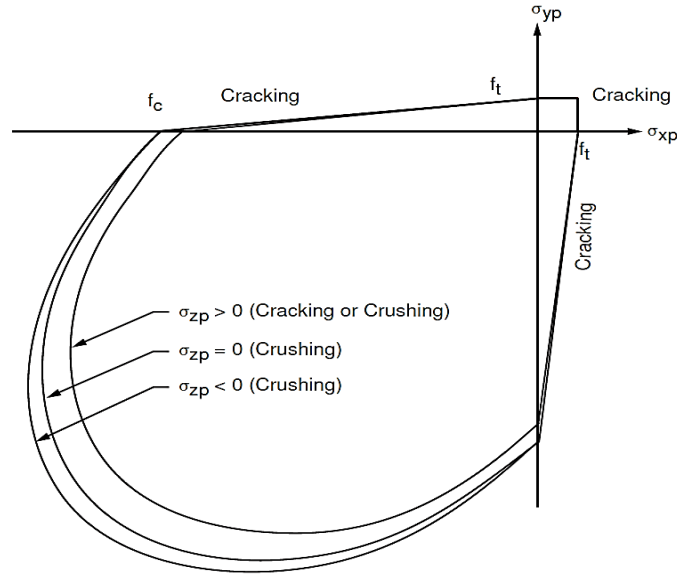


**Figure 6.3.** 2D Failure Surface in Principal Stress Space for Biaxial Stress State [ANSYS 2010.d]

## 6.2 Modeling Techniques used to Simulate Experimental Behavior

The test procedure presented in detail in Chapter 2 show that due to the unintended foundation (slight) flexibility, the actual stiffness of the dam specimen estimated by using the measured material properties (i.e. Modulus of Elasticity) is different than the actual specimen stiffness measured by the load cell and the LVDTs located at the tip. This base flexibility must be modeled appropriately in order to match the wave form of the measured response as discussed by Tinawi et al (2000). For this purpose two different modeling strategies were mainly utilized throughout this dissertation to simulate the experimentally observed behavior.

In the first modeling technique, i.e. Model 1 shown in Figure 6.4.a and Figure 6.5, the dam base was assumed to be fixed and the increased flexibility due to base and foundation rotations observed during experiments was incorporated by reducing the modulus of elasticities of each specimen. While performing this adjustment, the target was to match the first fundamental period of the numerical model with the experimentally determined one at the beginning of OBE test. The utilized reduced modulus of elasticity values were 10,500MPa, 8,750MPa and 13,500MPa whereas

the measured modulus of elasticities were 20,500MPa, 14,905MPa and 21,305MPa for specimens 1, 2 and 3, respectively. In addition, the uniaxial tensile strength of all specimens was used as 80% of their determined split tensile strength suggested by Raphael (1984) along with the measured cylindrical compressive strengths.

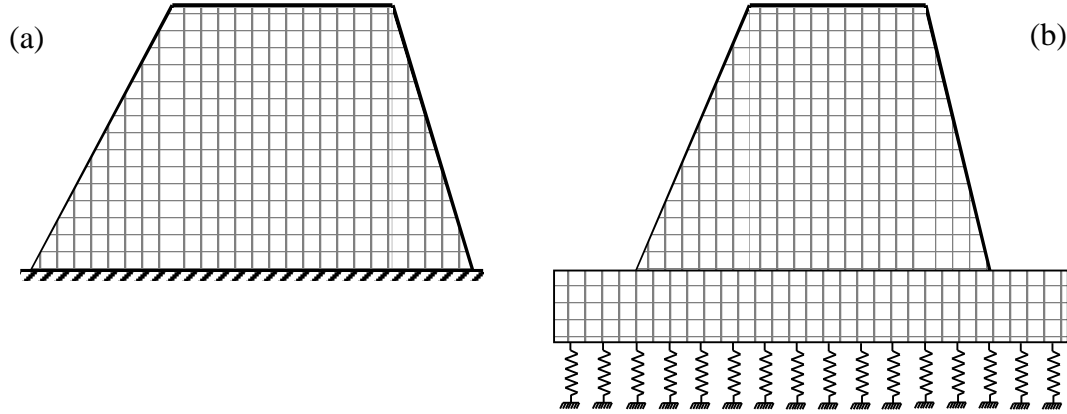


**Figure 6.4.** Different Numerical Models : a) Model 1 and b) Model 2

In the other modeling technique, i.e. Model 2 as shown in Figure 6.4.b and Figure 6.6, the dam and its RC foundation were modelled and connected to the vertical springs. The spring constants for compressive and tensile actions were selected to be different in order to reflect the uplift observed at the foundation base. The spring constants for each specimen were obtained by matching the lateral stiffness of the numerical model with the experimentally determined one during the application of lateral load ( $F_h$ ) before OBE experiment. Spring constants and the stress-strain curve in tension were similar to Model 1 the only difference being the use of actual  $E$  values.

In the course of material tests presented in Chapter 3, direct tensile strength tests were not conducted; hence tensile fracture energy ( $G_f$ ) values were not obtained. In order to use the appropriate tensile fracture energy in the numerical simulation, a literature survey was conducted. It was found that tests presented by Xu and Zhu (2009) cover the strength and MAS range employed in this study. In their work, the tensile fracture energy for compressive strength of 23.4 MPa was reported between 12.7N/m and 14.1N/m whereas  $G_f$  values for compressive strength of 33.8 MPa were

presented between 52.1N/m and 70.5N/m. Based on these values and performing linear interpolation, a  $G_f$  value of 20N/m was utilized for concrete strength of 25MPa. For the specimen with lower compressive strength, i.e. 15MPa,  $G_f$  value was selected as 5N/m. This value was selected based on engineering judgment as no value was found in the literature for such a low concrete compressive strength.

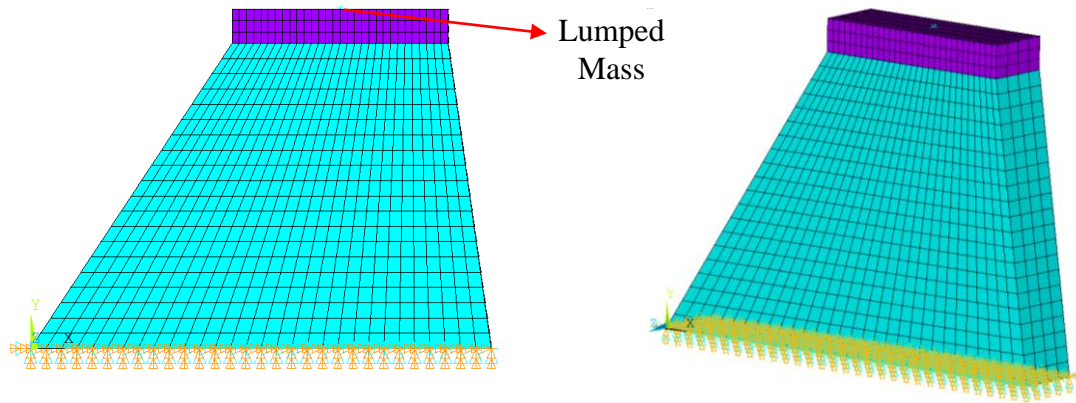


**Figure 6.5.** Numerical Model 1

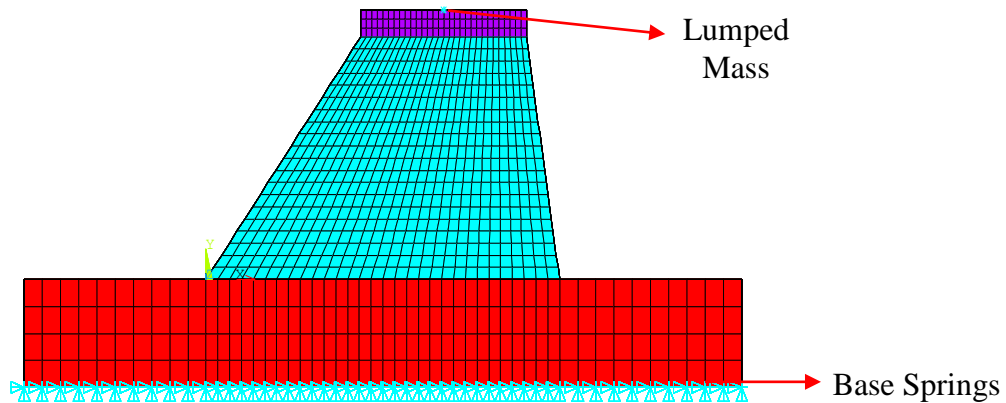


**Figure 6.6.** Numerical Model 2

During the time-history analysis, the damping ratios of all specimens were taken to be equal to the values determined during experiment for each hazard level. Finally, it was assumed that 45% (40%) and 100% (90%) of the applied shear forces could be transmitted through crack planes for open and closed crack cases for Model 1 (Model 2), respectively. This assumption is utterly dependent on some preliminary analysis of the specimens.

In the rest of this section, the numerical simulation results for both Model 1 and Model 2 are summarized. In the analysis, the same loading protocol was utilized as the experiment. For instance, the same model was subjected to successive application of earthquake scenarios OBE, MDE and MCE and then the capacity curve was estimated by simply performing a pushover analysis similar to the one conducted in the laboratory.

### **6.3 Numerical Simulation Results for Model 1**

#### **6.3.1 CVC Gravity Dam : Specimen 1**

The numerical predictions of the base shear force and the tip displacement demands are presented in Figure 6.7 and Figure 6.8. The base shear versus tip displacement curves from numerical model are also compared with the experimental ones (Figure 6.9). In addition, the ability of the numerical model to estimate the crack patterns is also shown in Figure 6.10. The static capacity curve of the dam specimen is presented in Figure 6.11. The percentage errors in the base shear and tip displacement demands from analytical model are summarized in Table 6.2 and Table 6.3, respectively. From these tables, it can be inferred that the maximum base shear could be estimated with an error of less than 10% in positive direction. However, the percentage error in the maximum tip displacement predictions reached to 30%. The frequency contents of both base shear and tip displacement demands were compatible with the experimental ones, especially under the effect of most demanding earthquake scenario MCE, but the magnitudes of the selected demand parameters were predicted generally less than the observed ones. This result can be attributed to the constant damping ratio employed during the numerical analysis and the inability of the crack model to impose hysteretic damping.

The comparisons of the estimated capacity curve with the experimentally obtained one show that the numerical estimations are promising as both the base shear and tip displacement capacities could be predicted very well. This result implied that the numerical model had difficulties under the effect of cyclic loading but this deficiency was not so pronounced when a monotonic loading protocol was utilized. This observation was mainly the fact that the cyclic model required realistic hysteretic



models, damping ratio estimations, failure criteria being capable of representing a reasonable stiffness degradation due to crack propagation, etc. In addition, the percentage errors in base shear and tip displacement capacities were detected to be less than 10% (Figure 6.11).

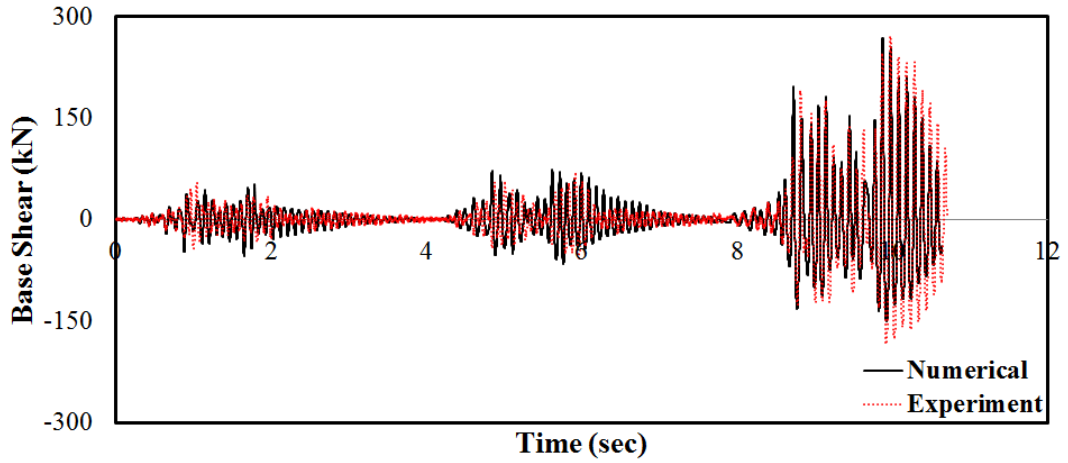


**Figure 6.7.** Comparison of Base Shear Demand Histories for Specimen 1 under the Effect of OBE, MDE and MCE Scenarios for Model 1

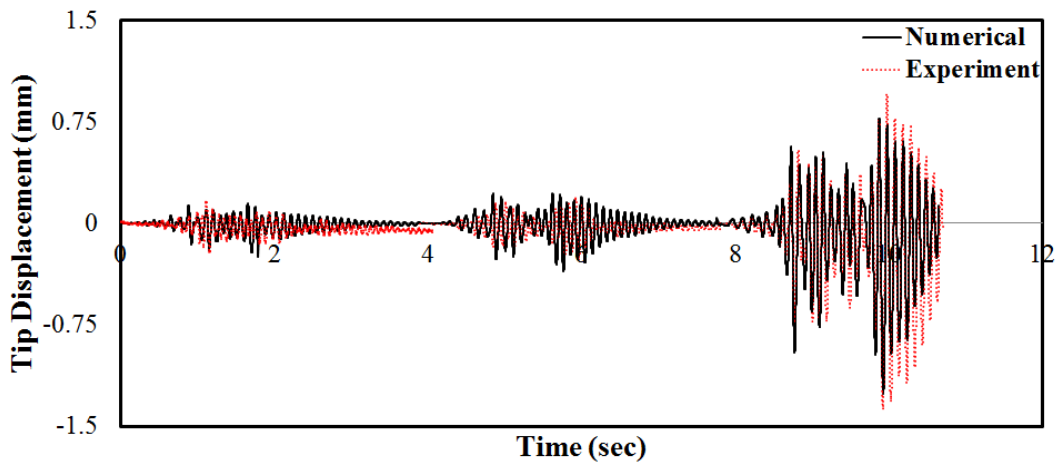


**Figure 6.8.** Comparison of Tip Displacement Demand Histories for Specimen 1 under the Effect of OBE, MDE and MCE Scenarios for Model 1

The predicted crack patterns after each hazard level are also compared with the experimentally observed cracks in Figure 6.10. The estimated crack lengths after the

OBE, MDE and the MCE earthquake scenarios were 725 mm, 905 mm and 1140 mm, respectively. On the contrary, the observed crack lengths were 400 mm, 550 mm and 1050 mm for the same hazard levels, respectively. Consequently, the numerical model always predicted the cracks longer than the observed ones. The ratios of the crack lengths (predicted / observed one) for the OBE, the MDE and the MCE are 1.81, 1.65 and 1.09, respectively. In addition, the numerically predicted cracks were more dispersed than the single (or few) cracking observed in the test. Besides, the body crack which appeared during the MDE earthquake scenario could not be predicted by the numerical analysis. Similar to the earthquake analyses, wider spread out of cracks were predicted by the numerical model than the observed ones (Figure 6.11). In summary, the numerical simulations were successful for estimating the base shear and the tip displacement capacities whereas they were not promising in forecasting the crack patterns except the MCE motion.

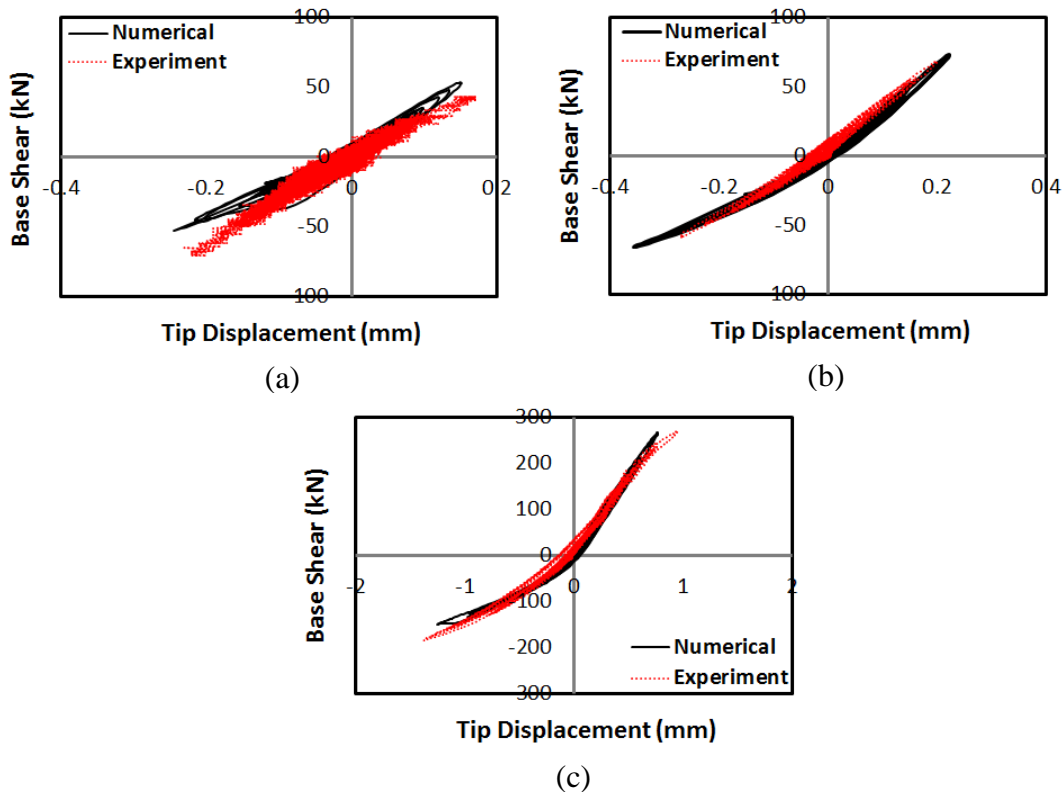


**Figure 6.9.** Comparison of Base Shear versus Tip Displacement Demand Histories for Specimen 1 under the Effect of (a) OBE, (b) MDE and (c) MCE Scenarios for Model 1

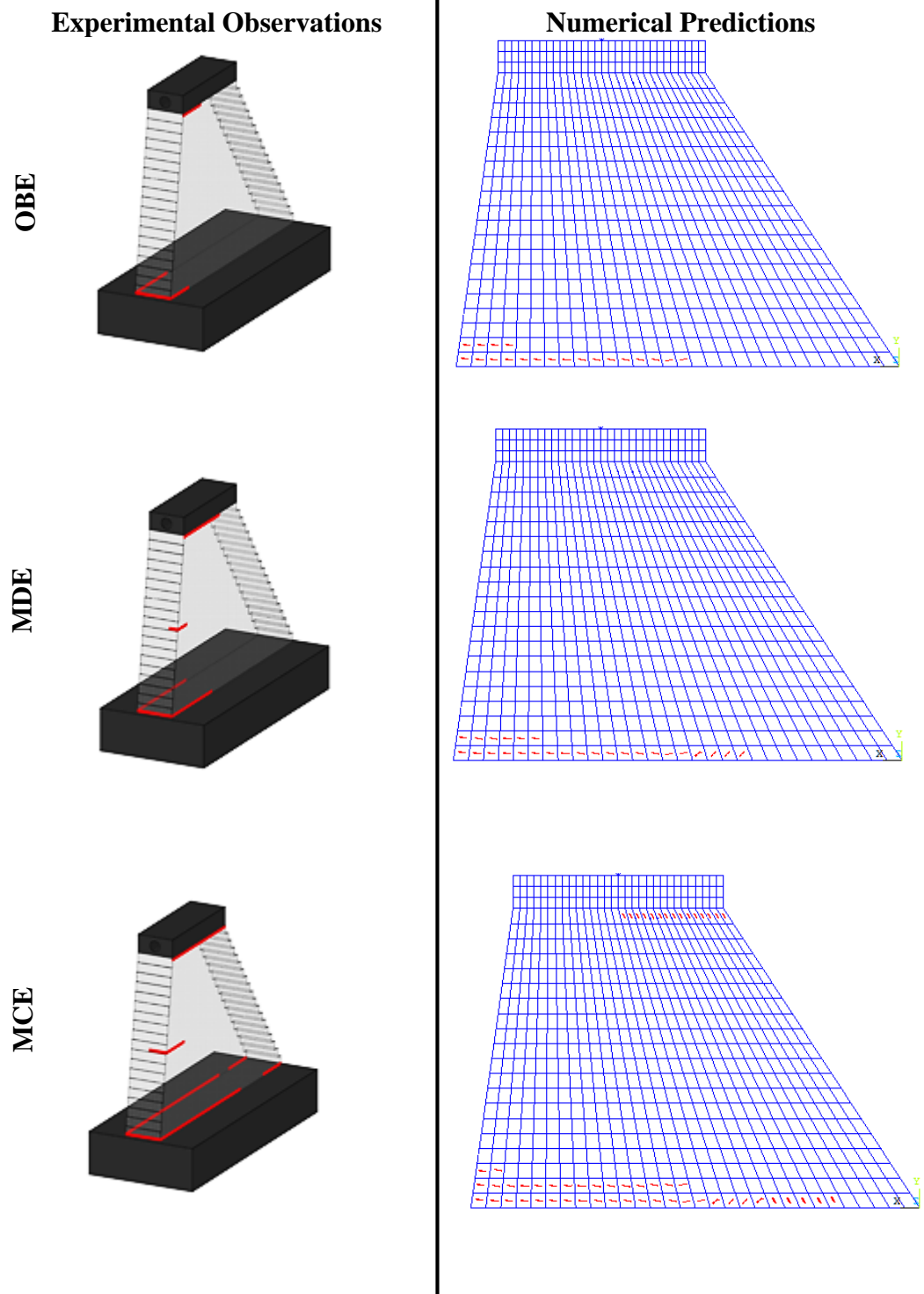


**Figure 6.10.** Comparison of Crack Patterns for Specimen 1 under the Effect of OBE, MDE and MCE Scenarios for Model 1

**Table 6.2.** Comparison of Base Shear Forces of Specimen 1 for Model 1  
(Maximum values are shown in red italics.)

Base Shear Force (kN)								
Experiment			Numerical			Percentage Error (%)		
<i>OBE</i>	<i>MDE</i>	<i>MCE</i>	<i>OBE</i>	<i>MDE</i>	<i>MCE</i>	<i>OBE</i>	<i>MDE</i>	<i>MCE</i>
<i>54.8</i>	<i>68.7</i>	<i>270.3</i>	52.5	73.3	268.3	<i>4.2</i>	<i>-6.7</i>	<i>0.7</i>
-44.6	-59.1	-184.2	-53.6	-65.8	-150.2	-20.2	-11.4	18.5

**Table 6.3.** Comparison of Tip Displacement of Specimen 1 for Model 1  
(Maximum values are shown in red italics.)

Tip Displacement (mm)								
Experiment			Numerical			Percentage Error (%)		
<i>OBE</i>	<i>MDE</i>	<i>MCE</i>	<i>OBE</i>	<i>MDE</i>	<i>MCE</i>	<i>OBE</i>	<i>MDE</i>	<i>MCE</i>
0.112	0.199	0.951	0.151	0.224	0.772	-34.5	-12.6	18.8
<i>-0.306</i>	<i>-0.270</i>	<i>-1.374</i>	-0.245	-0.357	-1.256	<i>20.0</i>	<i>-32.0</i>	<i>8.6</i>

### 6.3.2 RCC Gravity Dam : Specimen 2

The base shear force and tip displacement time series are compared with the experimentally obtained values in Figure 6.12 and Figure 6.13. The base shear-tip displacement curves are also compared with the experimental ones in Figure 6.14. In addition, the estimated crack patterns were also investigated in Figure 6.15. Finally, the complete capacity curve of the dam specimen, including the ascending and descending parts, was determined by conducting a pushover analysis (Figure 6.16).

The percentage errors in the base shear and tip displacement predictions obtained from numerical model are presented in Table 6.4 and Table 6.5, respectively. It can be observed that errors for the OBE motion were usually quite high. The most reasonable estimates of maximum demands in the order of 20% were observed during the MDE test. The accuracy of the MCE test estimations were better than the OBE but it had quite large errors (40 to 80 %) stating the failure of the model to estimate the maximum demands during the MCE motion. In addition, the errors in the maximum tip displacement predictions remained below 25% for the negative direction. The same conclusion for the tip displacements in the positive direction was valid. Similar to the first specimen, the frequency contents of both base shear and tip

displacement demands were similar to the experimental ones, especially under the effect of most demanding earthquake scenario MCE.

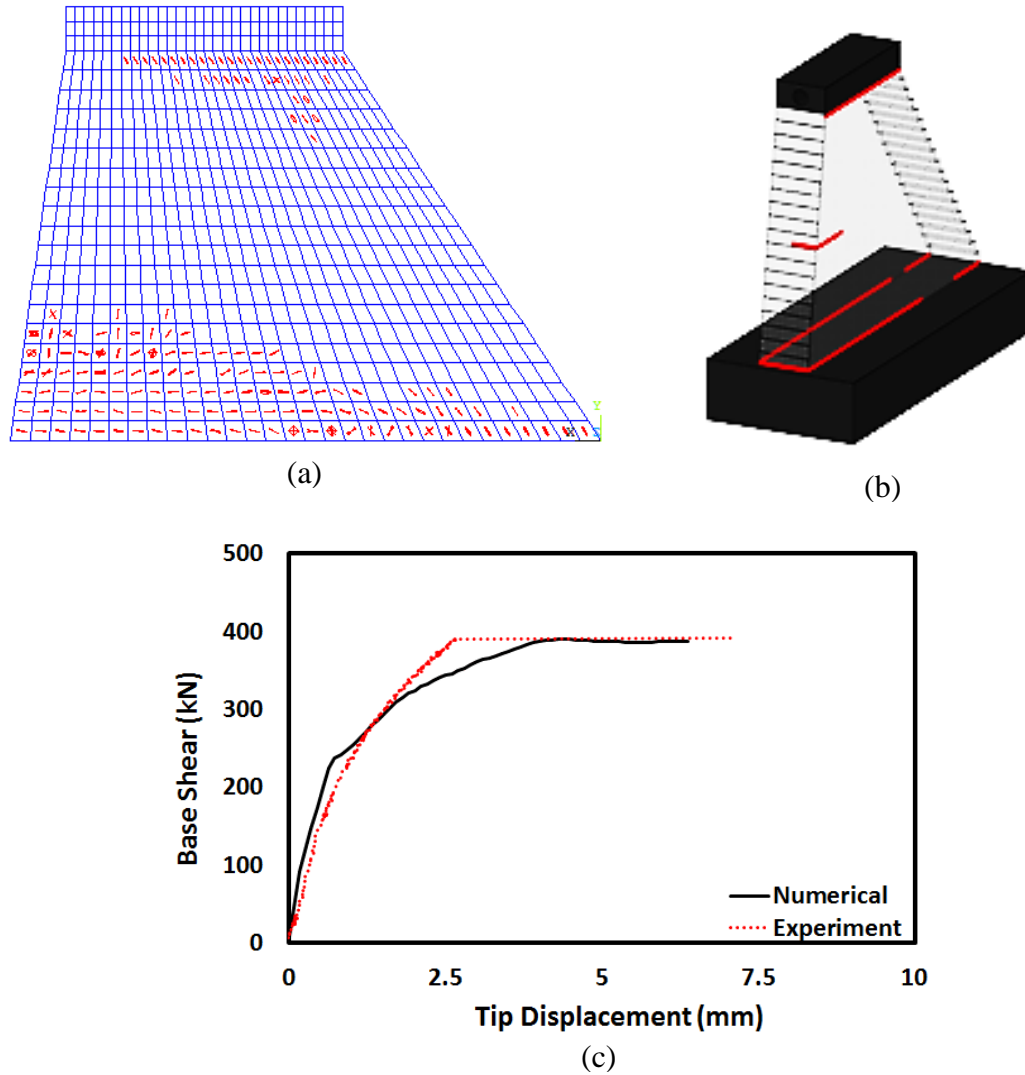


**Figure 6.11.** Comparison of Pushover Experiment for Specimen 1 from Model 1: (a) Crack Pattern from Numerical Model, (b) Crack Pattern from Experiment and (c) Capacity Curve

The comparisons of the estimated capacity curve with the experimentally obtained one shows that the numerical estimations matched the experimental values very well. In addition, the percentage errors in base shear and tip displacement capacities were detected to be less than 3% and 10%, respectively (Figure 6.16). It is worth noting that the displacement corresponding to the loss of lateral strength could also be detected with a good accuracy by the numerical model, which indicates that the

general demand parameters could be estimated with an acceptable error on computer environment for static loading conditions.

Figure 6.15 shows that the estimated crack lengths after the OBE, the MDE and the MCE earthquake scenarios were 450 mm, 590 mm and 1040 mm, respectively. On the contrary, the observed crack lengths were 200 mm, 700 mm and 900 mm for the same hazard levels, respectively. Similar to the first specimen, the numerical model predicted more spread out of cracks than the observed ones except for MDE scenario. This is a natural outcome of the smeared crack modeling as stated by Rots (1989). The ratios of the crack lengths (predicted / observed one) for OBE, MDE and MCE were 2.25, 0.84 and 1.16, respectively, stating an increasing accuracy of crack length estimations with increasing intensity of ground motions. It was also observed that the body crack that appeared during the MDE earthquake scenario could not be estimated by the numerical analysis.

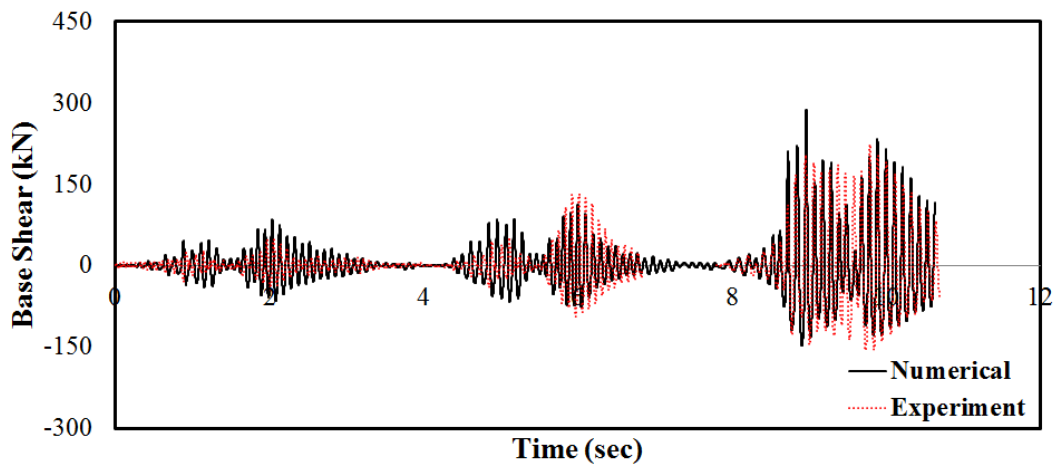


**Figure 6.12.** Comparison of Base Shear Demand Histories for Specimen 2 under the Effect of OBE, MDE and MCE Scenarios for Model 1

Similar to the ground motion simulations, considerably dispersed crack formations were predicted by the numerical model (Figure 6.16). The numerical model seems to indicate the formation of a base crack and an inclined crack resembling the observed failure mode. However, it is not possible to state that one can perfectly capture and

understand the expected cracking leading to the failure with the smeared crack model.

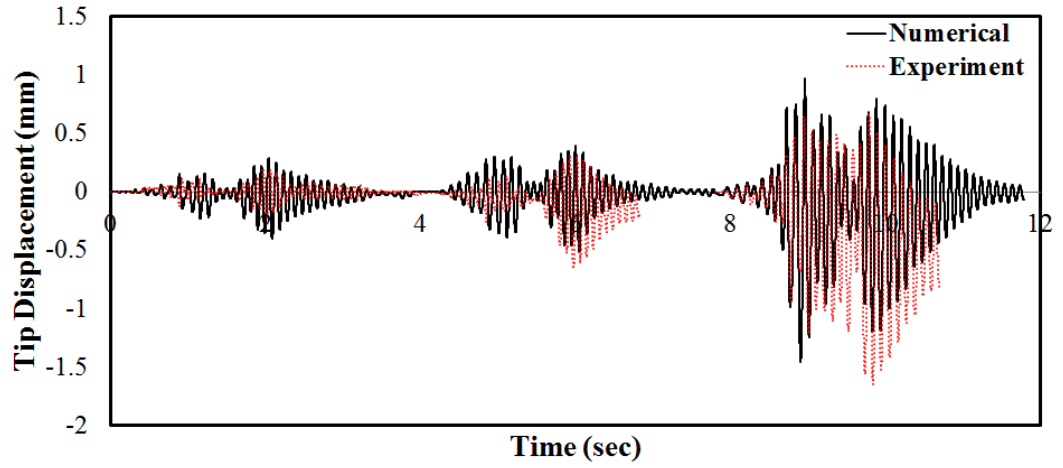


**Figure 6.13.** Comparison of Tip Displacement Demand Histories for Specimen 2 under the Effect of OBE, MDE and MCE Scenarios for Model 1

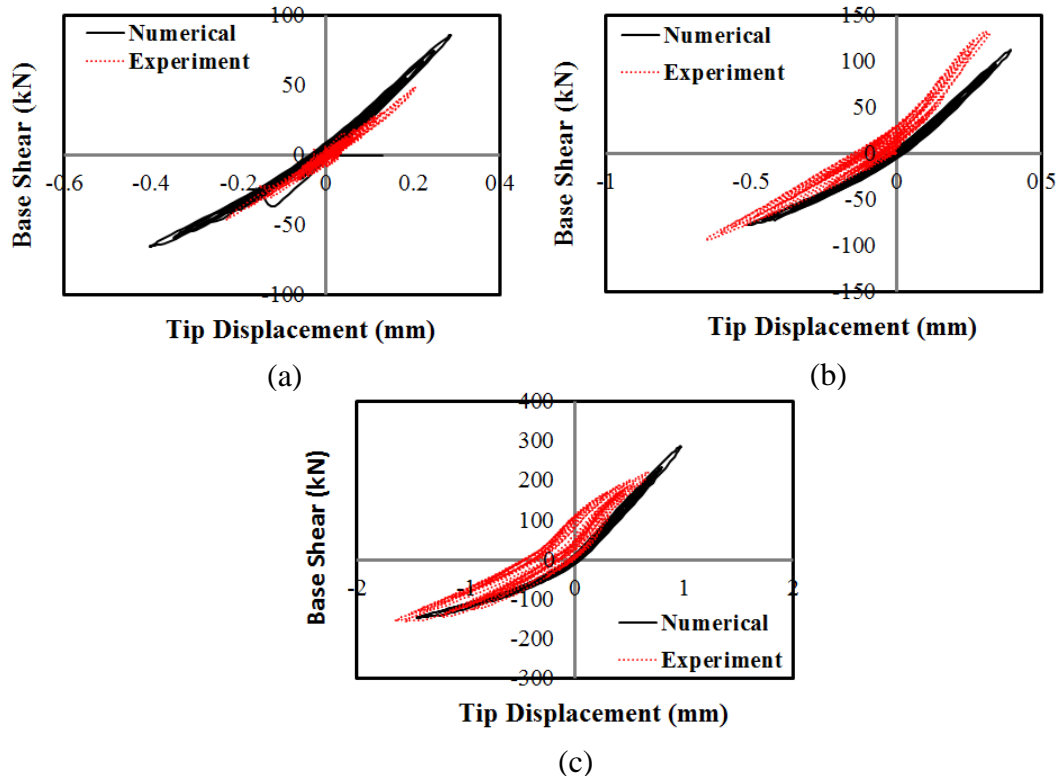


**Figure 6.14.** Comparison of Base Shear versus Tip Displacement Demand Histories for Specimen 2 under the Effect of (a) OBE, (b) MDE and (c) MCE Scenarios for Model 1

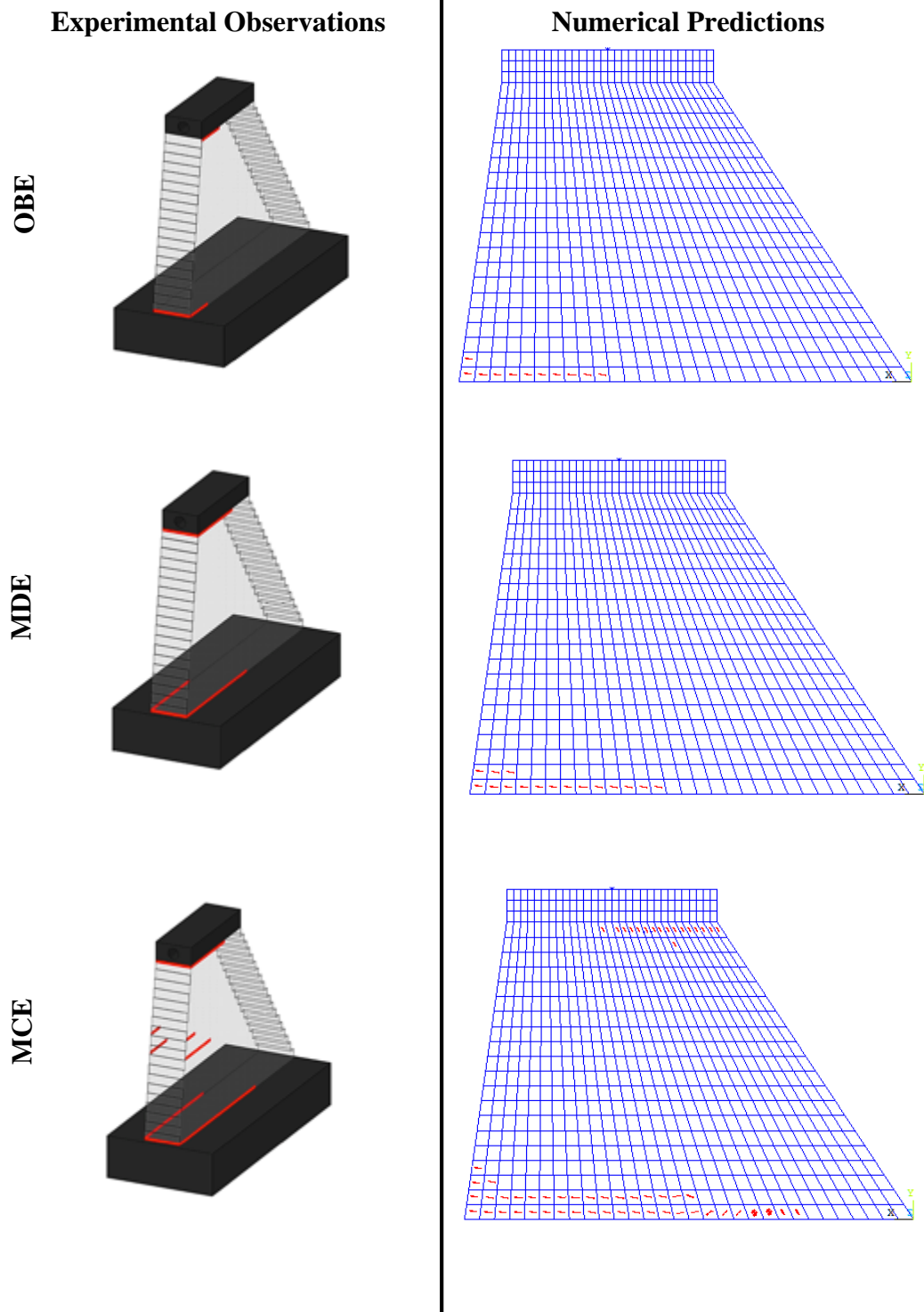


**Figure 6.15.** Comparison of Crack Patterns for Specimen 2 under the Effect of OBE, MDE and MCE Scenarios for Model 1



**Table 6.4.** Comparison of Base Shear Forces of Specimen 2 for Model 1  
(Maximum values are shown in red italics.)

Base Shear Force (kN)								
Experiment			Numerical			Percentage Error (%)		
<i>OBE</i>	<i>MDE</i>	<i>MCE</i>	<i>OBE</i>	<i>MDE</i>	<i>MCE</i>	<i>OBE</i>	<i>MDE</i>	<i>MCE</i>
<i>48.5</i>	<i>132.5</i>	<i>222.5</i>	86.1	112.4	286.4	<i>-77.5</i>	<i>41.4</i>	<i>33.7</i>
-45.9	-94.2	-156.1	-65.4	-77.7	-147.4	-42.5	-19.3	-83.5

**Table 6.5.** Comparison of Tip Displacement of Specimen 2 for Model 1  
(Maximum values are shown in red italics.)

Tip Displacement (mm)								
Experiment			Numerical			Percentage Error (%)		
<i>OBE</i>	<i>MDE</i>	<i>MCE</i>	<i>OBE</i>	<i>MDE</i>	<i>MCE</i>	<i>OBE</i>	<i>MDE</i>	<i>MCE</i>
0.206	0.322	0.674	0.287	0.394	0.971	-39.4	-22.6	-44.0
<i>-0.227</i>	<i>-0.656</i>	<i>-1.648</i>	-0.402	-0.510	-1.451	<i>-77.1</i>	<i>22.2</i>	<i>11.9</i>

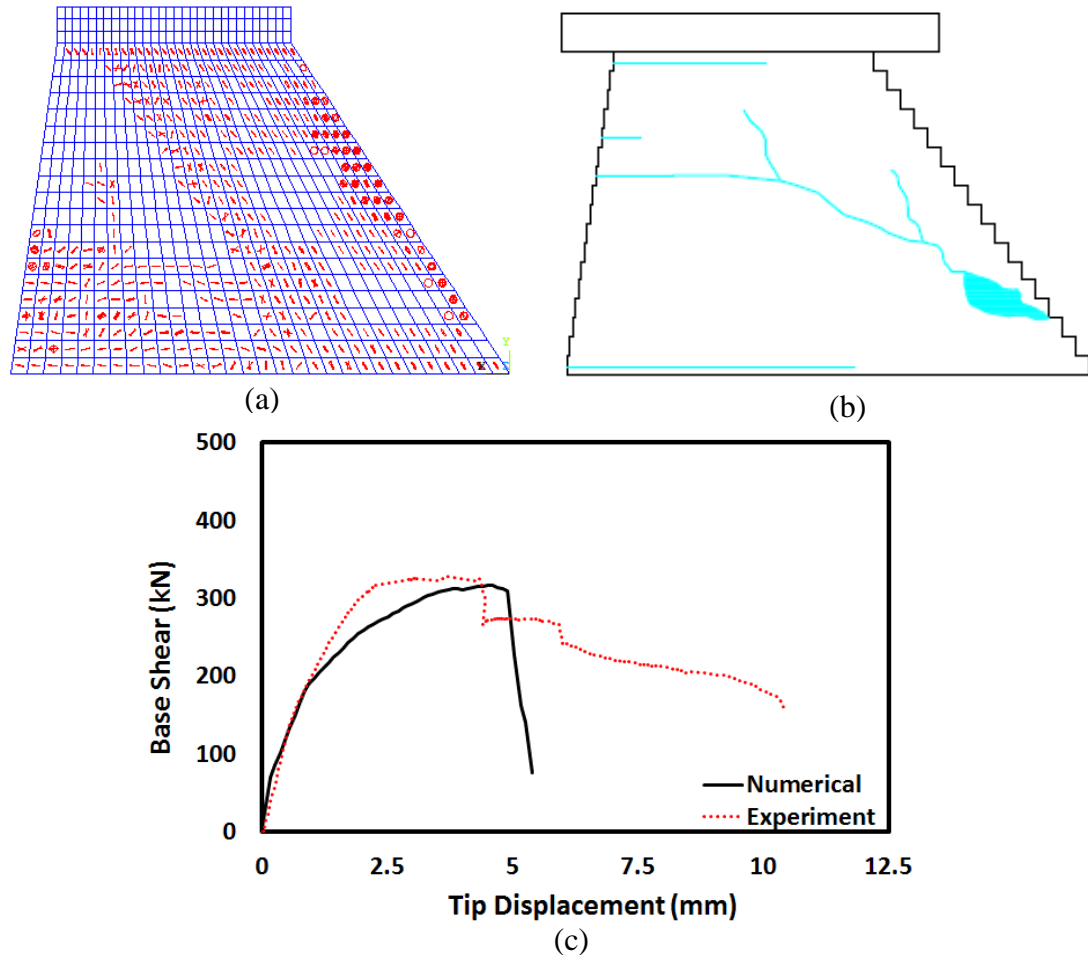


**Figure 6.16.** Comparison of Pushover Experiment for Specimen 2 from Model 1 : (a) Crack Pattern from Numerical Model, (b) Crack Pattern from Experiment and (c) Capacity Curve

### 6.3.3 RCC Gravity Dam : Specimen 3

The base shear force and tip displacement demands are compared with the experimentally obtained demands in Figure 6.17 and Figure 6.18. The base shear-tip displacement curves are also compared with the experimental ones in Figure 6.19. The estimated crack patterns are shown in Figure 6.20 and the complete capacity curve of the dam specimen from a pushover analysis is depicted in Figure 6.21. The percentage errors in the base shear and tip displacement predictions obtained from numerical model are presented in Table 6.6 and Table 6.7, respectively. These tables show that the maximum positive base shears during all earthquake scenarios were estimated with an error of approximately 30%. In contrast, the errors in base shear along negative direction were reasonable except MDE motion. However, the errors in the maximum tip displacement predictions were as high as 100%. Therefore, the tip displacement estimations were not acceptable other than the estimations of the MCE motion. In addition, the frequency contents of both base shear and tip displacement demands were less overlapping the experimental ones for the OBE and the MDE scenarios. The results for the most demanding earthquake scenario MCE were conforming well to the measured values. It can be stated that estimations of Model 1 for Specimen 3 was the least successful among the estimations obtained from 3 specimens.

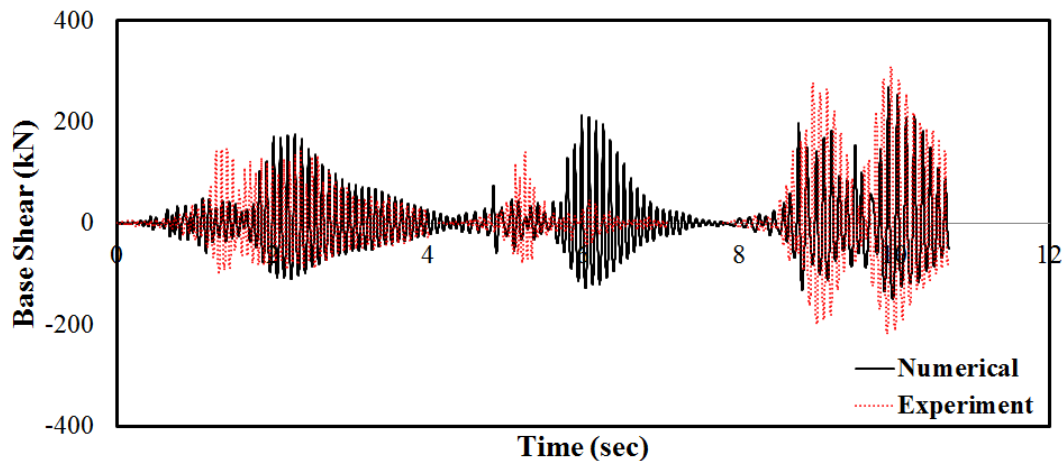


**Figure 6.17.** Comparison of Base Shear Demand Histories for Specimen 3 under the Effect of OBE, MDE and MCE Scenarios for Model 1

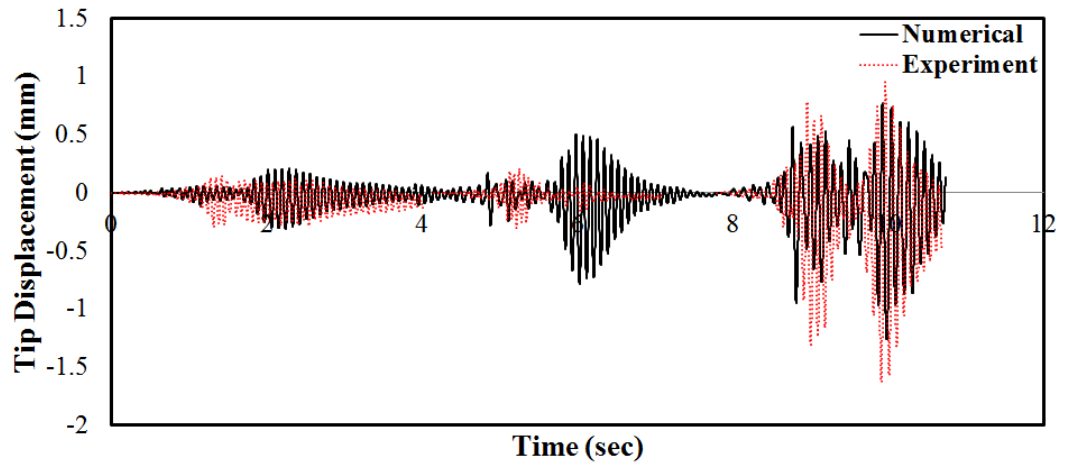


**Figure 6.18.** Comparison of Tip Displacement Demand Histories for Specimen 3 under the Effect of OBE, MDE and MCE Scenarios for Model 1

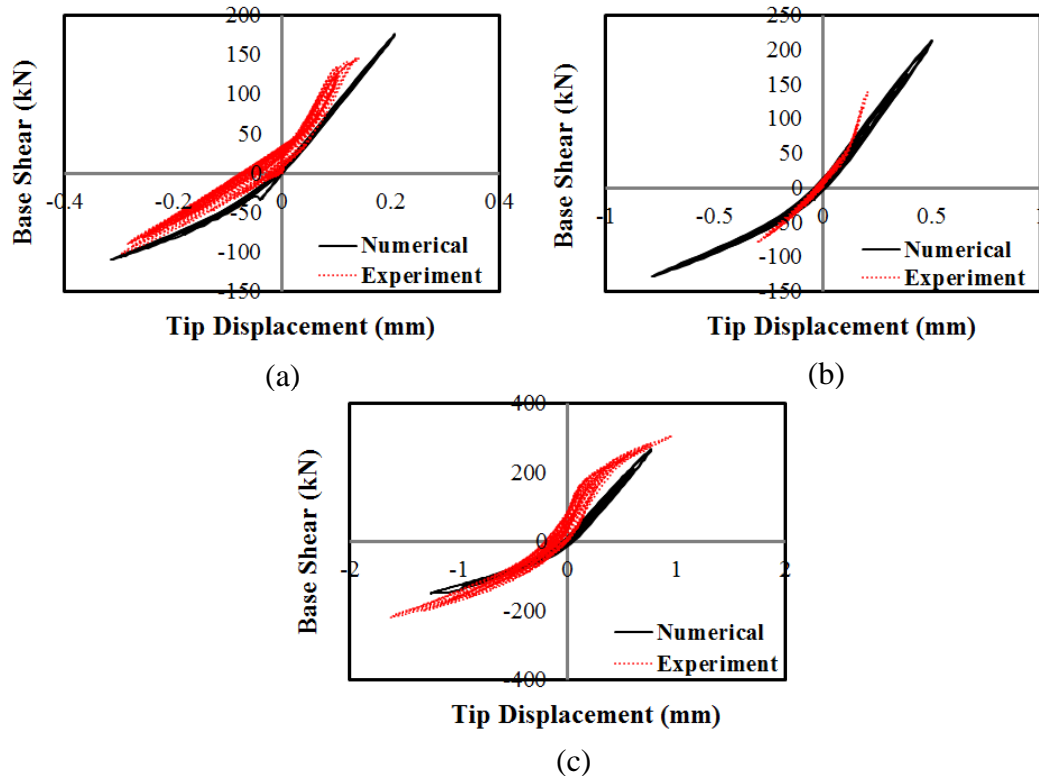


**Figure 6.19.** Comparison of Base Shear versus Tip Displacement Demand Histories for Specimen 3 under the Effect of (a) OBE, (b) MDE and (c) MCE Scenarios for Model 1

In Figure 6.20, it can be seen that the estimated crack lengths after OBE, MDE and MCE earthquake scenarios were 860 mm, 990 mm and 1180 mm, respectively. On the contrary, the observed crack lengths were 200 mm, 300 mm and 680 mm for the same hazard levels, respectively. The ratios of the crack lengths (predicted / observed one) for OBE, MDE and MCE were 4.30, 3.30 and 1.74, respectively. In addition, the numerically predicted cracks were wider spread-out to more than one line of elements. Besides, the body crack that appeared during MCE earthquake scenario could not be estimated by the numerical analysis.

The comparisons of the estimated capacity curve with the experimentally obtained revealed that the capacity curve could be determined within acceptable error limits. The base shear and tip displacement capacities were determined with an error of less than 15% and 10%, respectively (Figure 6.21). This result indicates the quite satisfactory outcomes from static simulations.

**Table 6.6.** Comparison of Base Shear Forces of Specimen 3 for Model 1  
(Maximum values are shown in red italics.)

Base Shear Force (kN)								
Experiment			Numerical			Percentage Error (%)		
<i>OBE</i>	<i>MDE</i>	<i>MCE</i>	<i>OBE</i>	<i>MDE</i>	<i>MCE</i>	<i>OBE</i>	<i>MDE</i>	<i>MCE</i>
<i>146.3</i>	<i>176.5</i>	<i>307.4</i>	176.1	214.0	150.2	<i>-20.4</i>	<i>27.5</i>	<i>12.7</i>
-101.1	-103.5	-219.0	-109.9	-128.0	-268.3	-7.8	-106.7	31.4

**Table 6.7.** Comparison of Tip Displacement of Specimen 3 for Model 1  
(Maximum values are shown in red italics.)

Tip Displacement (mm)								
Experiment			Numerical			Percentage Error (%)		
<i>OBE</i>	<i>MDE</i>	<i>MCE</i>	<i>OBE</i>	<i>MDE</i>	<i>MCE</i>	<i>OBE</i>	<i>MDE</i>	<i>MCE</i>
0.140	0.238	0.958	0.208	0.504	0.772	-48.1	-111.9	19.4
<i>-0.294</i>	<i>-0.435</i>	<i>-1.625</i>	-0.315	-0.783	-1.256	<i>-6.9</i>	<i>-80.0</i>	<i>22.7</i>

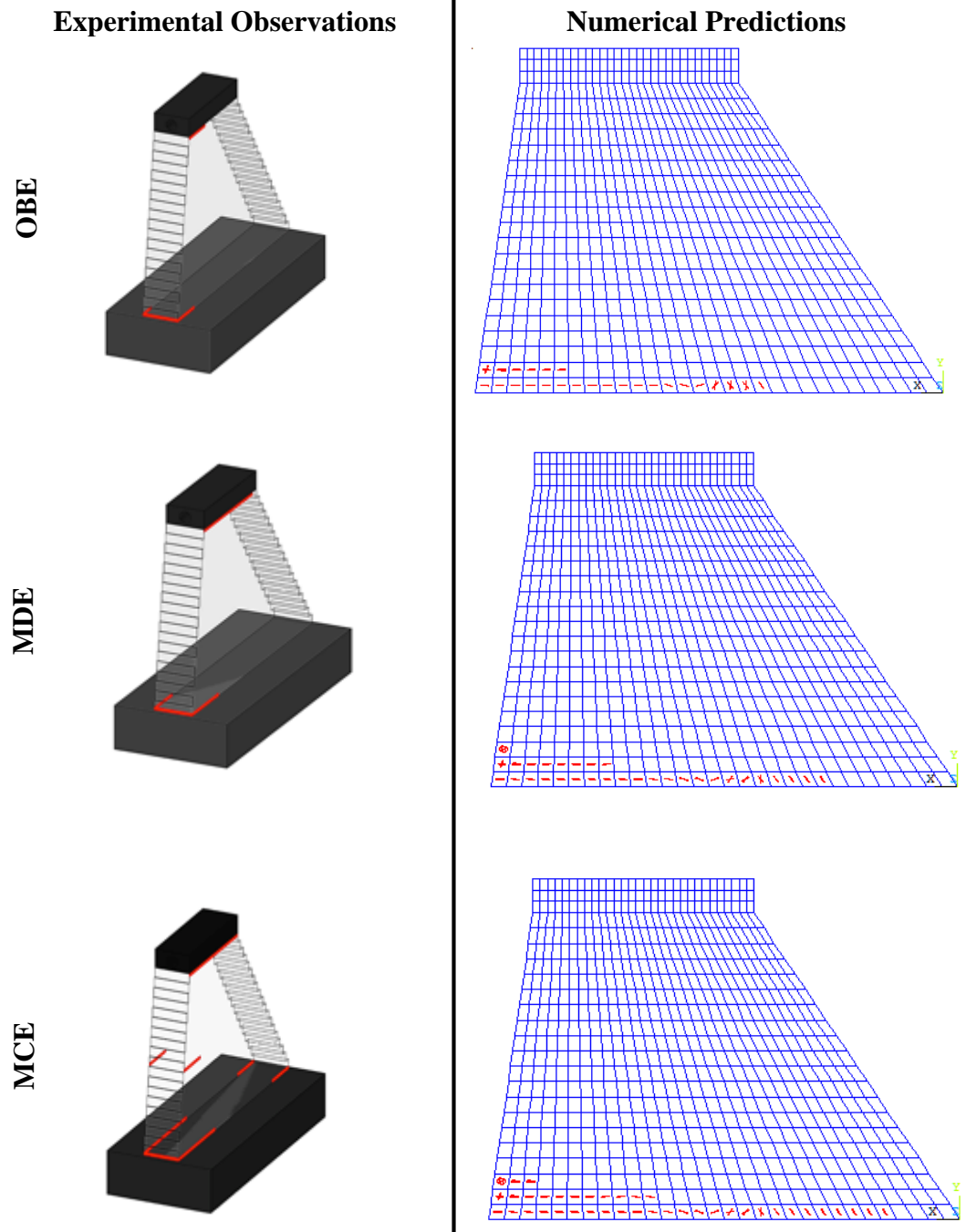


**Figure 6.20.** Comparison of Crack Patterns for Specimen 3 under the Effect of OBE, MDE and MCE Scenarios for Model 1

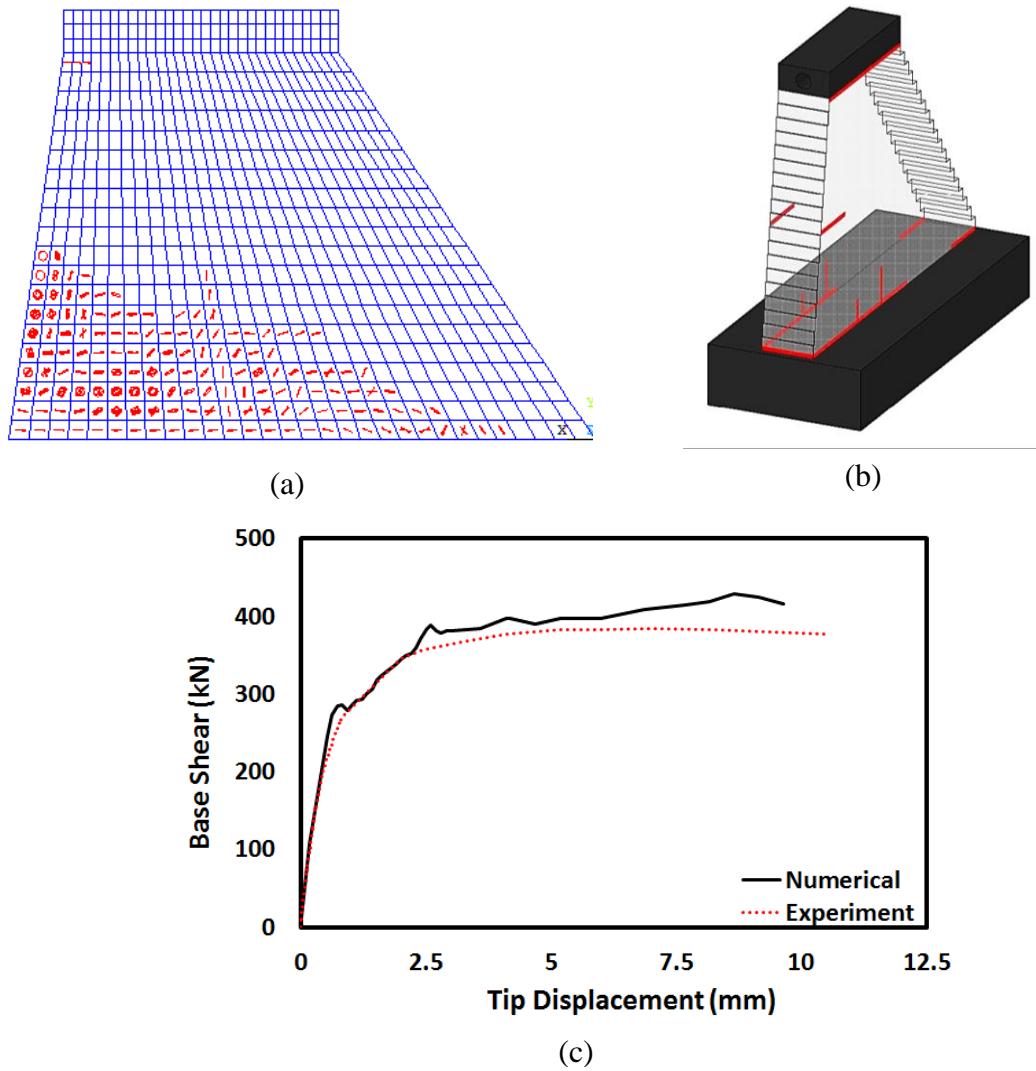


**Figure 6.21.** Comparison of Pushover Experiment for Specimen 3 from Model 1: (a) Crack Pattern from Numerical Model, (b) Crack Pattern from Experiment and (c) Capacity Curve

## 6.4 Numerical Simulation Summaries for Model 2

### 6.4.1 CVC Gravity Dam : Specimen 1

The numerical predictions of base shear force and tip displacement demands are shown in Figure 6.22 and Figure 6.23. The base shear versus tip displacement curves from numerical models are also compared with the experimental ones in Figure 6.24. In addition, the ability of the numerical model to estimate the crack patterns is also investigated in Figure 6.25. The full capacity curve of the dam specimen determined by conducting a pushover analysis is presented in Figure 6.26.

The percentage errors in the base shear and tip displacement demands from the analytical model are summarized in Table 6.8 and Table 6.9, respectively. From these tables, it can be inferred that except for the OBE motion, the base shear demands could be estimated within reasonable errors (less than 30%) for both direction of loading. In addition, the percentage errors in the tip displacement predictions were also less than 30% except for the OBE motion. It can be stated that the predictions were well conforming, in general, to the experimental ones except OBE motion for this method. The frequency contents of both base shear and tip displacement demands are compatible with the experimental ones, especially under the effect of most demanding earthquake scenario MCE, but the magnitudes of the selected demand parameters were predicted generally less than the observed ones similar to the results obtained in Section 6.3.1.

The comparisons of the estimated capacity curve with the experimentally obtained one showed that the numerical estimations were promising as far as the base shear and tip displacement capacities were concerned as the percentage errors in the base shear and the tip displacement capacities were detected to be less than 3% and 10%, respectively (Figure 6.26).

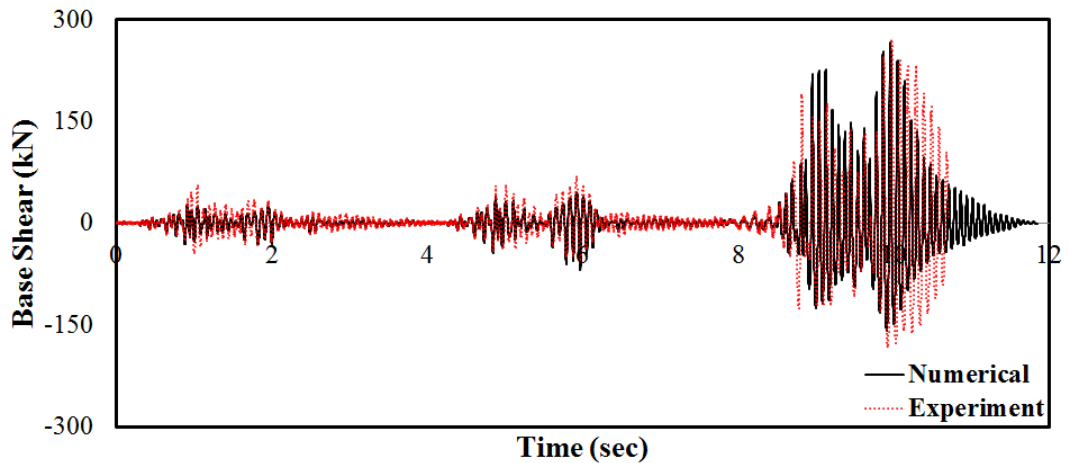


**Figure 6.22.** Comparison of Base Shear Demand Histories for Specimen 1 under the Effect of OBE, MDE and MCE Scenarios for Model 2

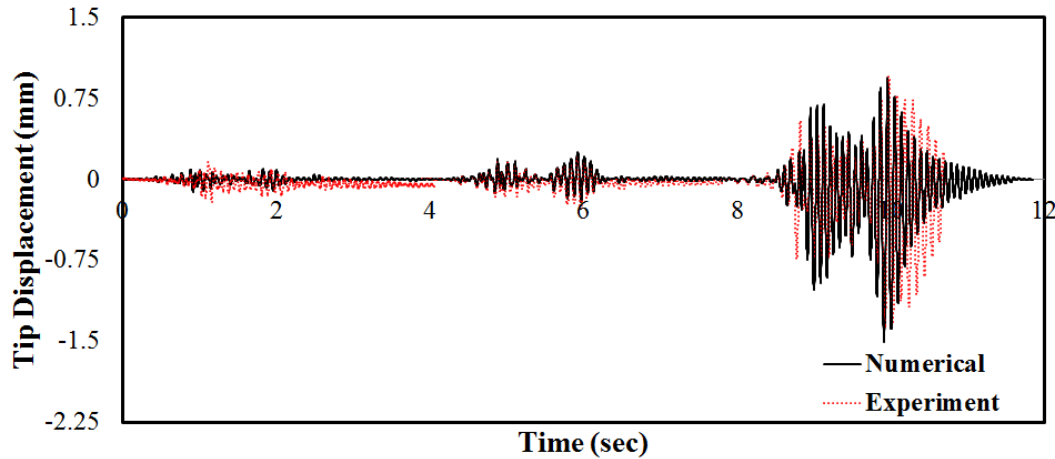


**Figure 6.23.** Comparison of Tip Displacement Demand Histories for Specimen 1 under the Effect of OBE, MDE and MCE Scenarios for Model 2

The predicted crack patterns after each hazard level are also compared with the experimentally observed cracks in Figure 6.25. It is apparent that the estimated crack lengths after the OBE, the MDE and the MCE earthquake scenarios were 0 mm, 270 mm and 910 mm, respectively. On the contrary, the observed crack lengths were 400 mm, 550 mm and 1050 mm for the same hazard levels, respectively. Contrary to Model 1, the numerical model predicted shorter cracks than the observed ones due to the base flexibility. The ratios of the crack lengths (predicted / observed) for the OBE, the MDE and the MCE were 0, 0.68 and 0.87, respectively. This model could not capture any cracking during the OBE earthquake scenario due to small base shear predictions delaying the cracking phenomenon. Besides, the body crack that appeared during MDE earthquake scenario could not be forecasted by the numerical analysis. In the MCE motion, the crack spreading was found to reach 4 layers of elements from the base. This result is due to the nature of smeared crack models in spreading the actual discrete cracks.

The comparisons of pushover analysis results are presented in Figure 6.26. The base shear and tip displacement capacities were estimated within acceptable limits, i.e. less than 10%. Such an excellent estimation for static tests is in well correlation with the previous results.



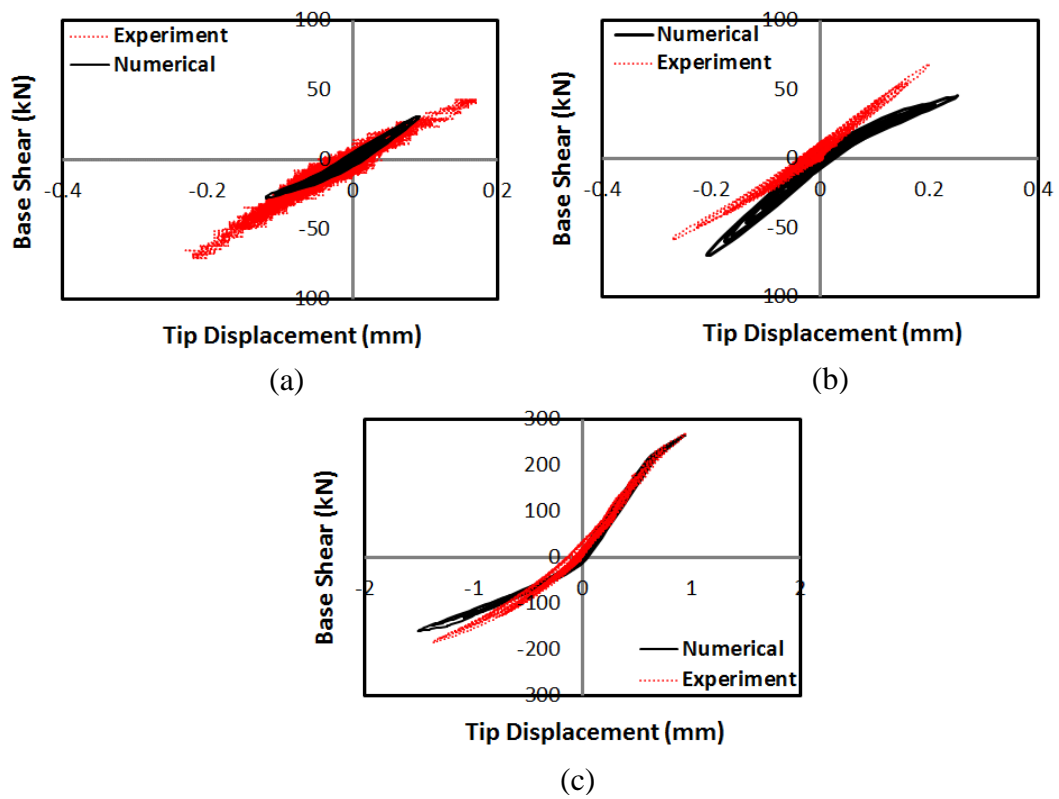


**Figure 6.24.** Comparison of Base Shear versus Tip Displacement Demand Histories for Specimen 1 under the Effect of (a) OBE, (b) MDE and (c) MCE Scenarios for Model 2

**Table 6.8.** Comparison of Base Shear Forces of Specimen 1 for Model 2  
(Maximum values are shown in red italics.)

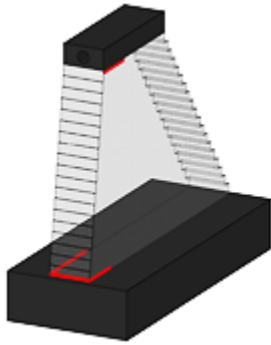
Base Shear Force (kN)								
Experiment			Numerical			Percentage Error (%)		
<i>OBE</i>	<i>MDE</i>	<i>MCE</i>	<i>OBE</i>	<i>MDE</i>	<i>MCE</i>	<i>OBE</i>	<i>MDE</i>	<i>MCE</i>
<i>54.8</i>	<i>68.7</i>	<i>270.3</i>	31.4	45.2	265.8	<i>42.6</i>	<i>34.3</i>	<i>1.7</i>
-44.6	-59.1	-184.2	-27.4	-70.0	-159.2	38.5	-18.5	<i>13.5</i>

**Table 6.9.** Comparison of Tip Displacement of Specimen 1 for Model 2  
(Maximum values are shown in red italics.)

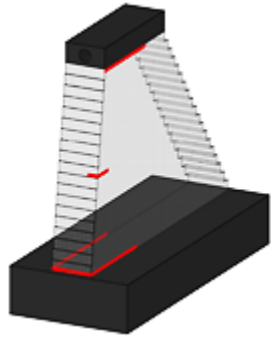
Tip Displacement (mm)								
Experiment			Numerical			Percentage Error (%)		
<i>OBE</i>	<i>MDE</i>	<i>MCE</i>	<i>OBE</i>	<i>MDE</i>	<i>MCE</i>	<i>OBE</i>	<i>MDE</i>	<i>MCE</i>
0.112	0.199	0.951	0.092	0.252	0.940	17.7	-26.8	1.1
<i>-0.306</i>	<i>-0.270</i>	<i>-1.374</i>	-0.120	-0.207	-1.507	<i>60.9</i>	<i>23.3</i>	<i>-9.6</i>

## Experimental Observations

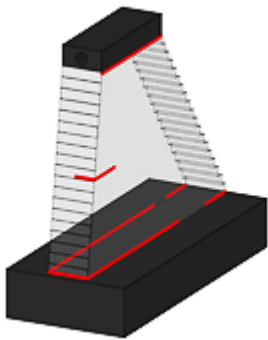
OBE



MDE



MCE



## Numerical Predictions

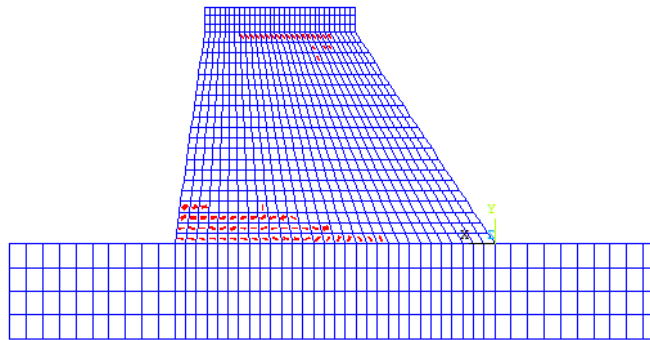
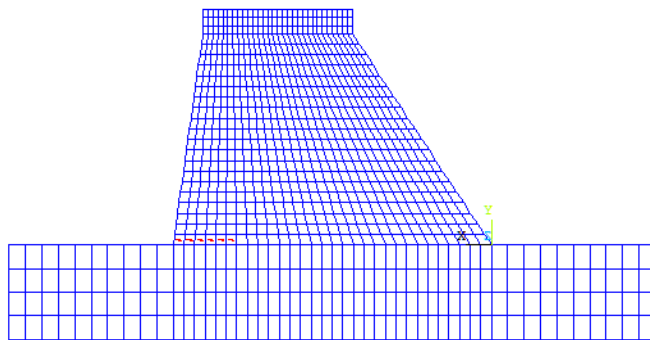
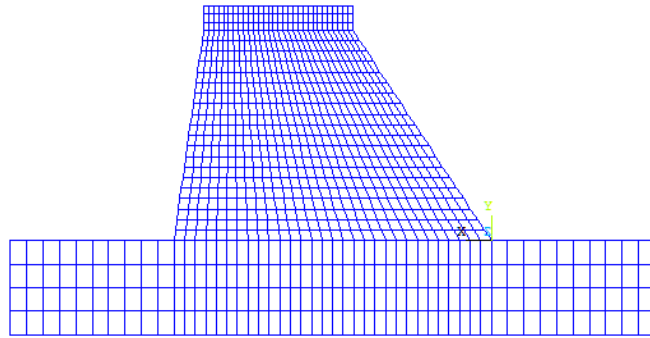


**Figure 6.25.** Comparison of Crack Patterns for Specimen 1 under the Effect of OBE, MDE and MCE Scenarios for Model 2

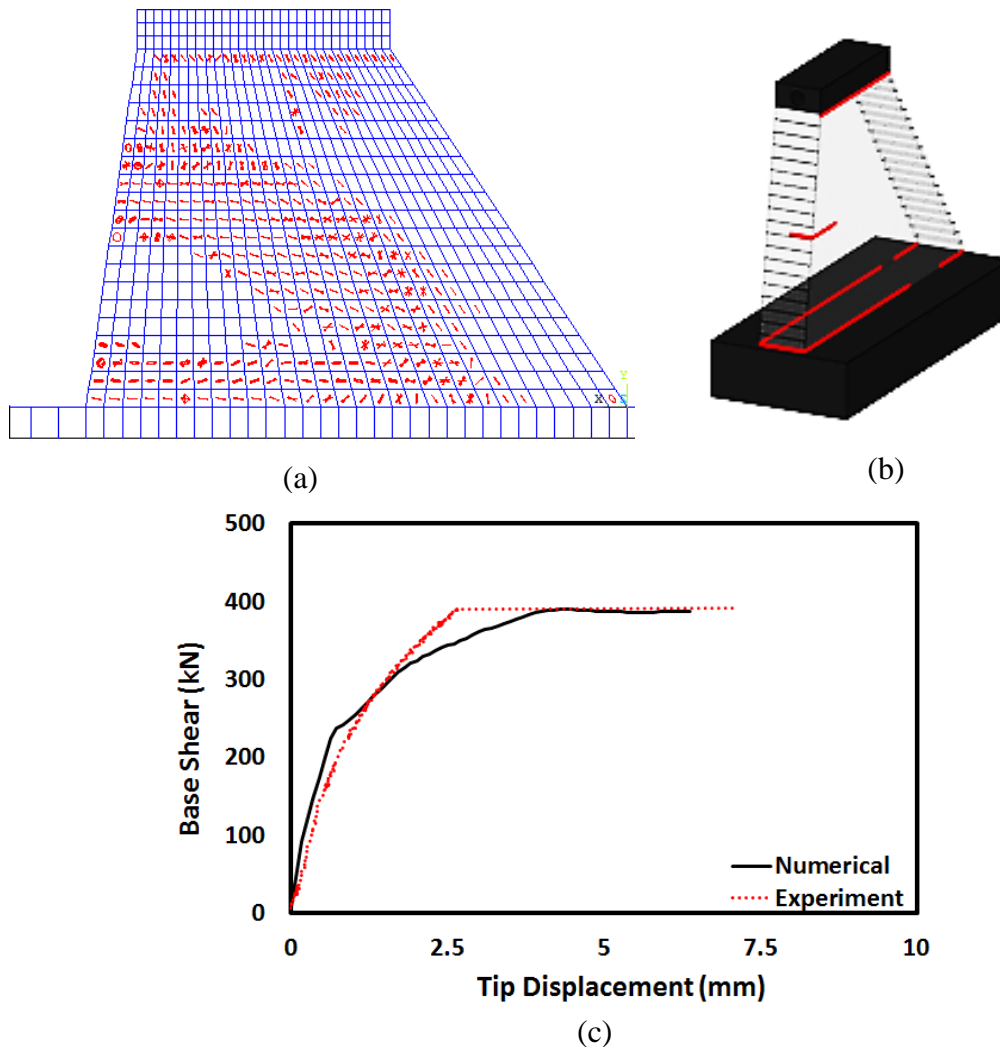


**Figure 6.26.** Comparison of Pushover Experiment for Specimen 1 from Model 2 : (a) Crack Pattern from Numerical Model, (b) Crack Pattern from Experiment and (c) Capacity Curve

#### 6.4.2 RCC Gravity Dam : Specimen 2

The base shear force and tip displacement demands are compared with the experimentally obtained demands in Figure 6.27 and Figure 6.28. The base shear-tip displacement curves are also presented by comparing them with the experimental ones in Figure 6.29. The estimated crack patterns are shown in Figure 6.30 along with the observed cracks. Finally, the complete capacity curve of the dam specimen from a pushover analysis is presented in Figure 6.31.

The percentage errors in the base shear and tip displacement predictions obtained from numerical model are presented in Table 6.10 and Table 6.11, respectively. These tables show that the maximum base shear during the OBE scenario was estimated with an error of approximately 50%. However, the percentage errors during most demanding earthquake scenarios, i.e. MDE and MCE, were about 20%. In addition, the errors in the maximum tip displacement predictions stay below 30% except for the OBE motion. Similar to the first specimen, the frequency contents of both base shear and tip displacement demands were similar to the experimental ones, best result obtained for the most demanding earthquake scenario MCE.

The comparisons of the estimated capacity curve with the experimentally obtained one show that the numerical estimations agree well with the experimental values. In addition, the percentage errors in base shear and tip displacement capacities were detected to be less than 20% (Figure 6.31). Although this method could not represent the failure displacement well, the predictions are close to the observed ones.

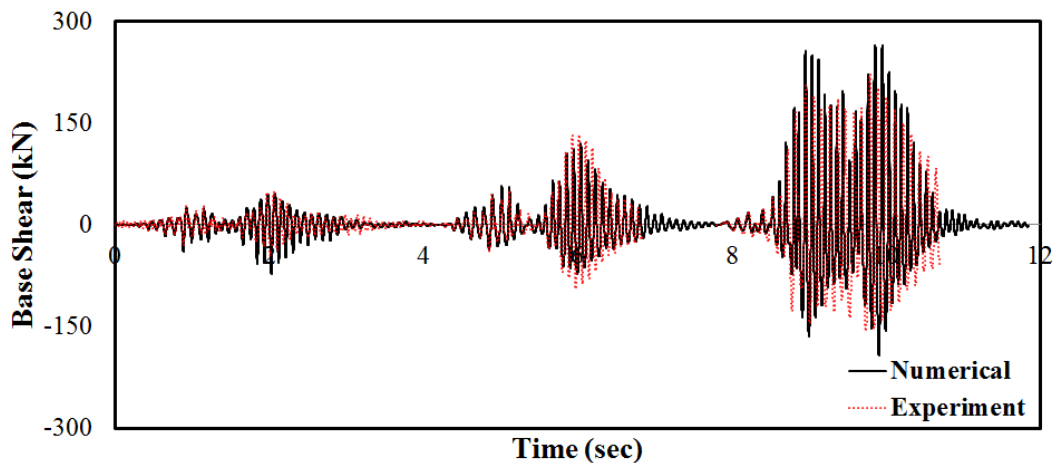


**Figure 6.27.** Comparison of Base Shear Demand Histories for Specimen 2 under the Effect of OBE, MDE and MCE Scenarios for Model 2

The estimated crack lengths after OBE, MDE and MCE earthquake scenarios are 270 mm, 450 mm and 860 mm, respectively (Figure 6.30). On the contrary, the observed crack lengths were 200 mm, 700 mm and 900 mm for the same hazard levels, respectively. Similar to the first specimen, the numerical model predicted longer cracks than the observed ones except for the MDE scenario. The ratios of the crack lengths (predicted / observed one) for the OBE, the MDE and the MCE are 1.35, 0.64

and 0.96, respectively. In addition, the numerically predicted cracks were usually continued in more than one set of integration points. As a final note, it should be stated that the body crack that appeared during MDE earthquake scenario could not be estimated by the numerical analysis.

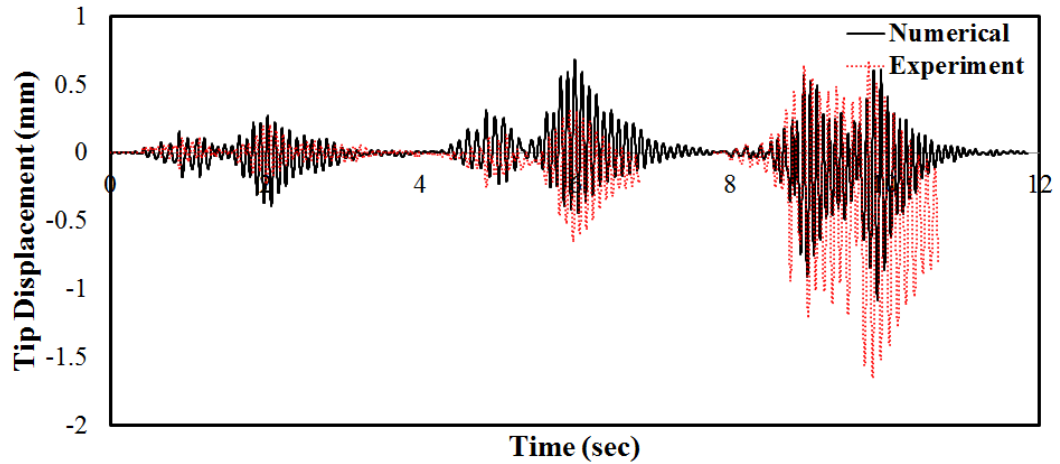


**Figure 6.28.** Comparison of Tip Displacement Demand Histories for Specimen 2 under the Effect of OBE, MDE and MCE Scenarios for Model 2

**Table 6.10.** Comparison of Base Shear Forces of Specimen 2 for Model 2  
(Maximum values are shown in red italics.)

Base Shear Force (kN)								
Experiment			Numerical			Percentage Error (%)		
<i>OBE</i>	<i>MDE</i>	<i>MCE</i>	<i>OBE</i>	<i>MDE</i>	<i>MCE</i>	<i>OBE</i>	<i>MDE</i>	<i>MCE</i>
<i>48.519</i>	<i>132.482</i>	<i>222.511</i>	72.127	119.950	264.510	<i>-48.656</i>	<i>9.460</i>	<i>-18.875</i>
-45.917	-94.239	-156.073	-45.882	-72.036	-192.050	0.076	23.561	-23.051

**Table 6.11.** Comparison of Tip Displacement of Specimen 2 for Model 2  
(Maximum values are shown in red italics.)

Tip Displacement (mm)								
Experiment			Numerical			Percentage Error (%)		
<i>OBE</i>	<i>MDE</i>	<i>MCE</i>	<i>OBE</i>	<i>MDE</i>	<i>MCE</i>	<i>OBE</i>	<i>MDE</i>	<i>MCE</i>
0.206	0.322	0.674	0.275	0.445	0.609	-33.279	-113.446	9.749
<i>-0.227</i>	<i>-0.656</i>	<i>-1.648</i>	-0.393	-0.687	-1.084	<i>-73.184</i>	<i>32.138</i>	<i>34.254</i>

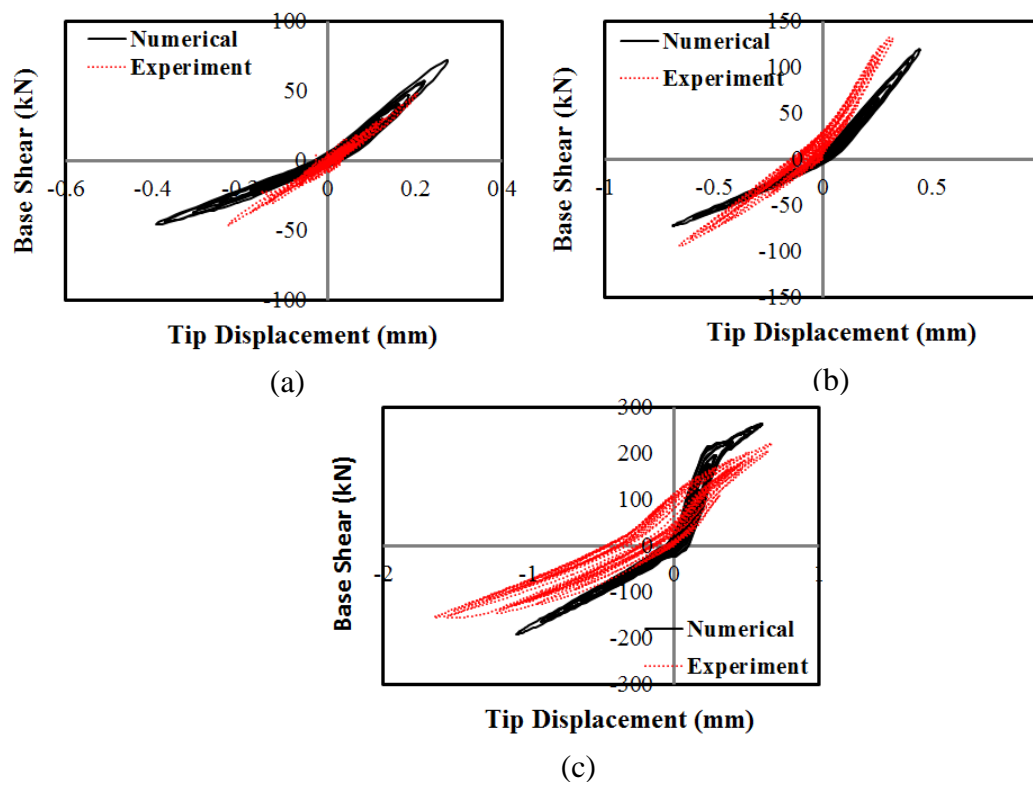


**Figure 6.29.** Comparison of Base Shear versus Tip Displacement Demand Histories for Specimen 2 under the Effect of (a) OBE, (b) MDE and (c) MCE Scenarios for Model 2

Similar to the earthquake analyses, wider spread-out of cracks are predicted by the numerical model than the observed ones (Figure 6.31). The numerical analysis matches both the displacement and base shear capacities of the dam specimen well. The agreement of the predicted displacement at the capacity loss with the experimental one is fairly well.

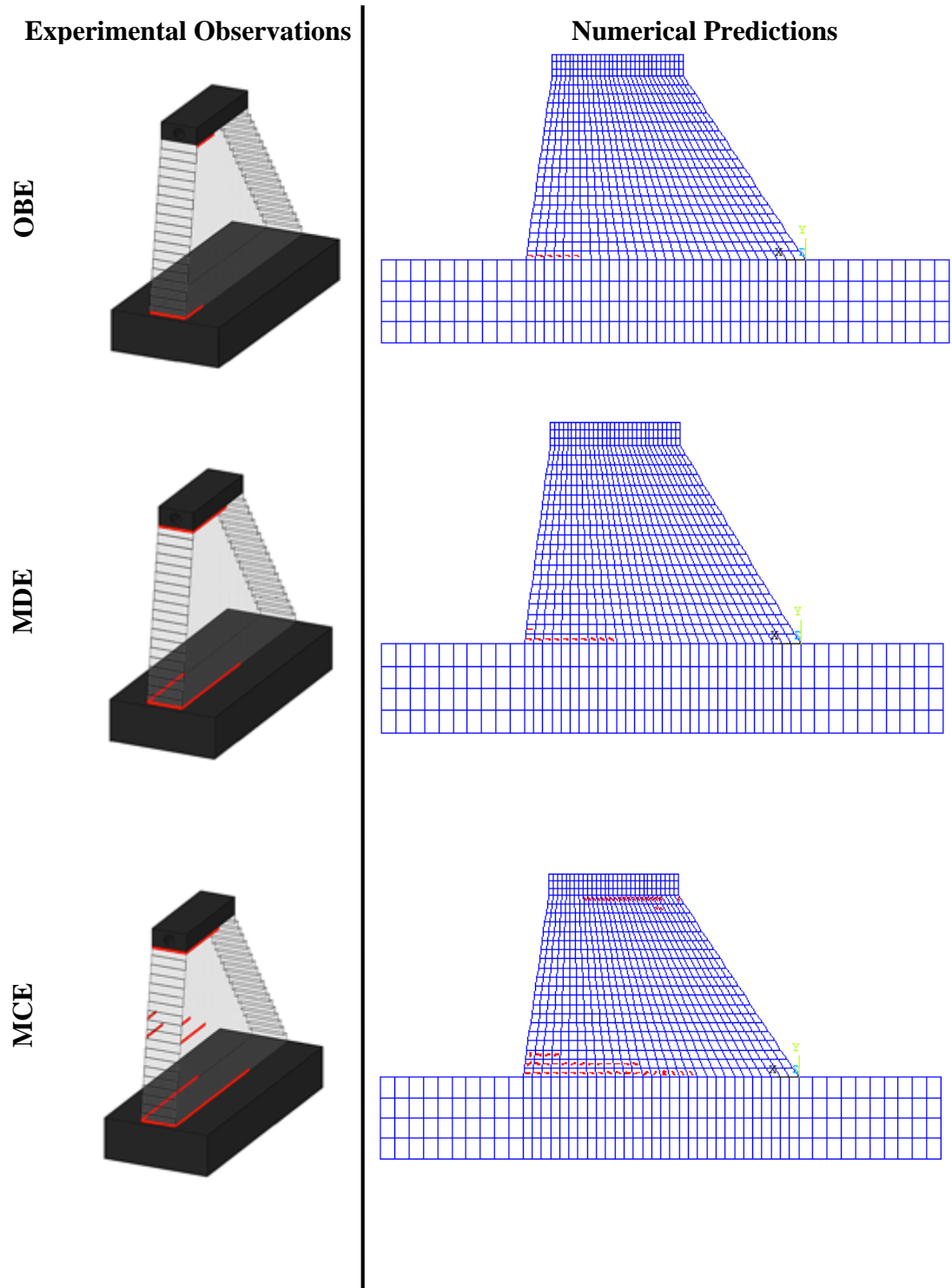


**Figure 6.30.** Comparison of Crack Patterns for Specimen 2 under the Effect of OBE, MDE and MCE Scenarios for Model 2

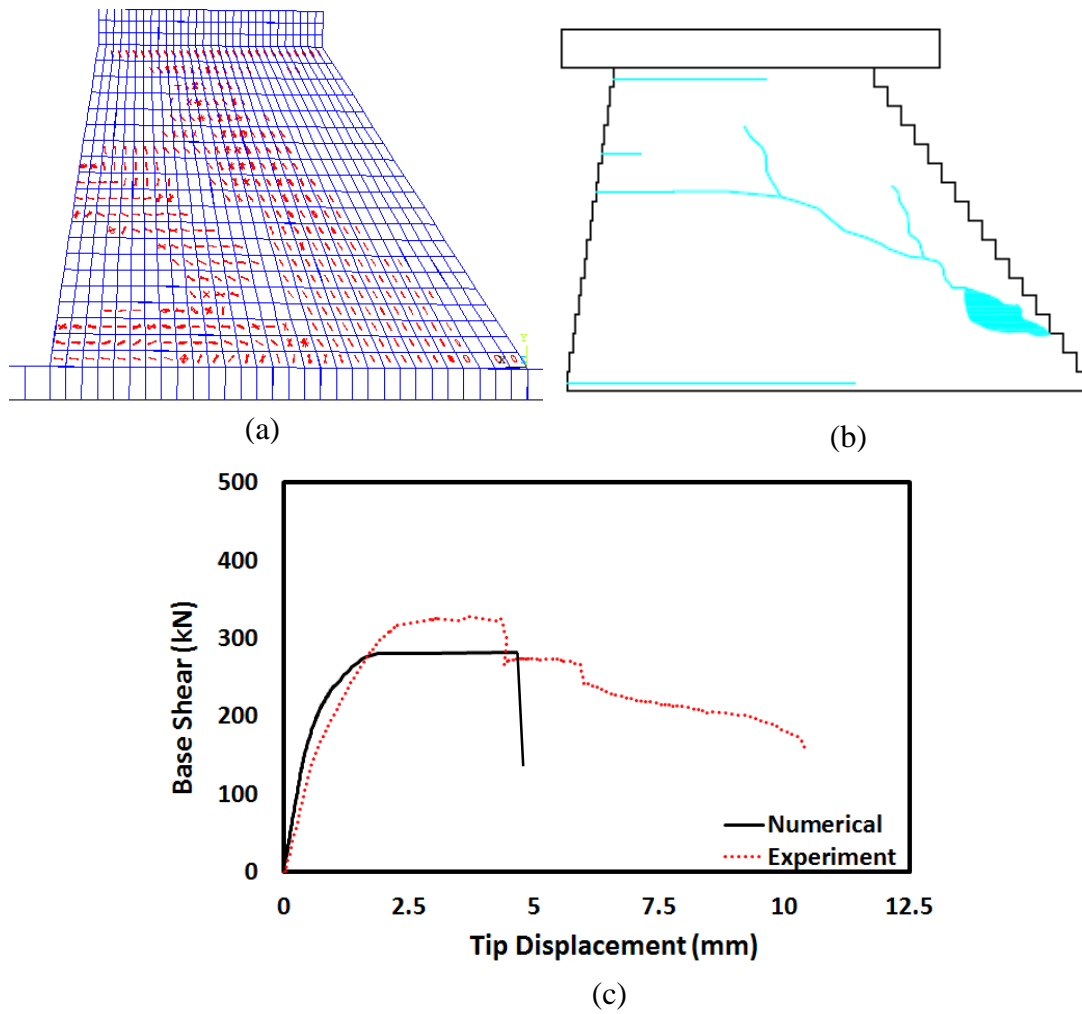


**Figure 6.31.** Comparison of Pushover Experiment for Specimen 2 from Model 2 : (a) Crack Pattern from Numerical Model, (b) Crack Pattern from Experiment and (c) Capacity Curve

### 6.4.3 RCC Gravity Dam : Specimen 3

The base shear force and tip displacement demands are compared with the experimentally obtained demands in Figure 6.32 and Figure 6.33. The base shear-tip displacement curves are also compared with the experimental ones in Figure 6.34. The estimated crack patterns are also shown in Figure 6.35 and the complete capacity curve of the dam specimen from a pushover analysis is shown in Figure 6.36. The percentage errors in the base shear and tip displacement predictions obtained from numerical model are presented in Table 6.12 and Table 6.13, respectively. These tables show that the maximum base shears in all directions were not estimated within



an acceptable error except the OBE motion. In addition, the errors in the maximum tip displacement predictions were as high as 110%. However, the tip displacement estimations were reasonable for the MDE and the MCE motion, having an error of 20%. In addition, like Model 1, the frequency contents of both base shear and tip displacement demands were inconsistent with the experimental ones except for the MCE motion. Nevertheless, the numerical simulations for the third specimen were the worse than the others.

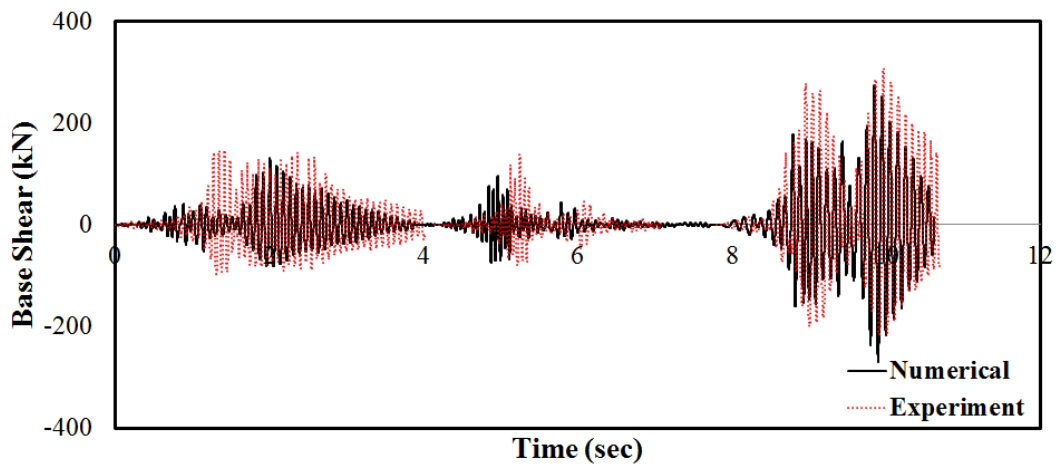


**Figure 6.32.** Comparison of Base Shear Demand Histories for Specimen 3 under the Effect of OBE, MDE and MCE Scenarios for Model 2

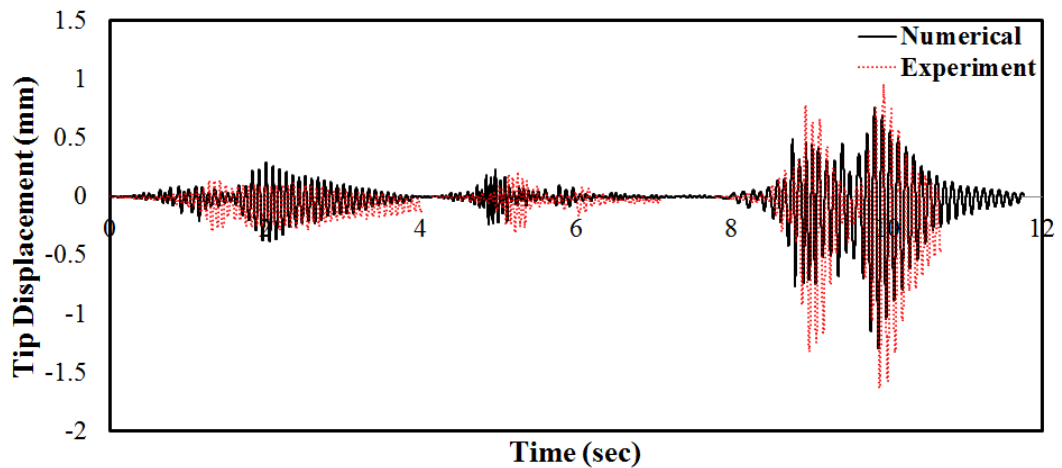


**Figure 6.33.** Comparison of Tip Displacement Demand Histories for Specimen 3 under the Effect of OBE, MDE and MCE Scenarios for Model 2

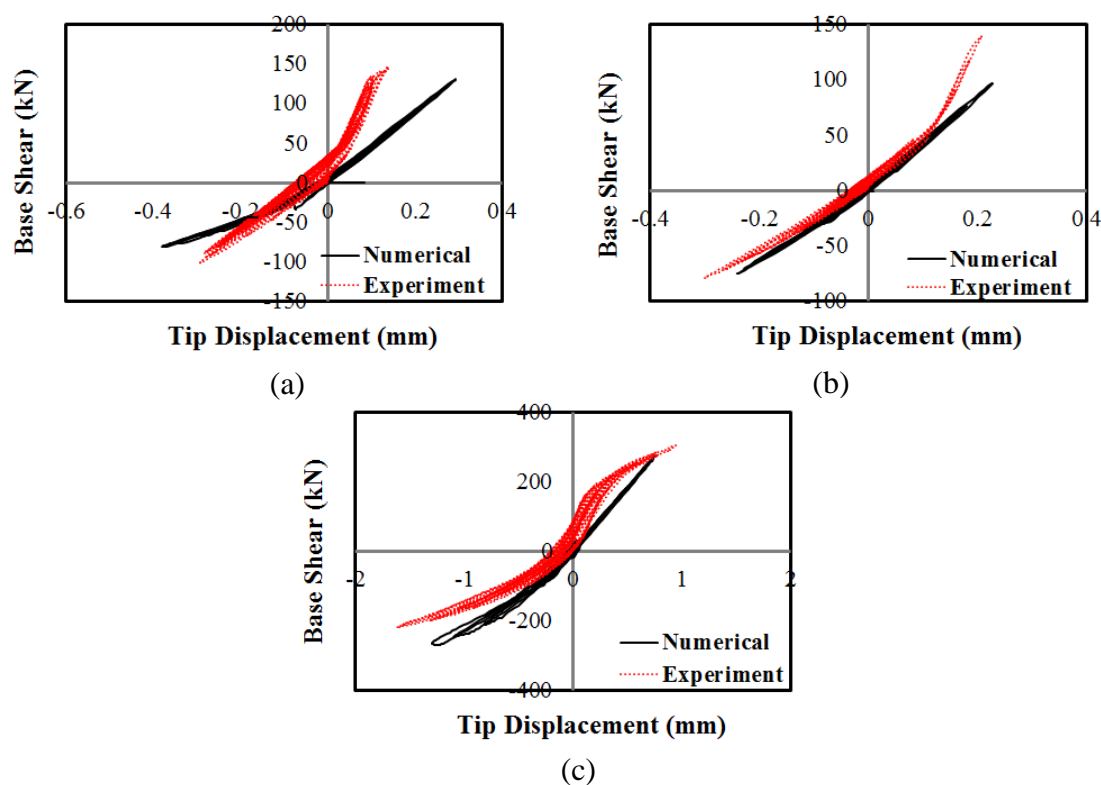


**Figure 6.34.** Comparison of Base Shear versus Tip Displacement Demand Histories for Specimen 3 under the Effect of (a) OBE, (b) MDE and (c) MCE Scenarios for Model 2

**Table 6.12.** Comparison of Base Shear Forces of Specimen 3 for Model 2  
(Maximum values are shown in red italics.)

Base Shear Force (kN)								
Experiment			Numerical			Percentage Error (%)		
<i>OBE</i>	<i>MDE</i>	<i>MCE</i>	<i>OBE</i>	<i>MDE</i>	<i>MCE</i>	<i>OBE</i>	<i>MDE</i>	<i>MCE</i>
<i>146.3</i>	<i>138.9</i>	<i>307.4</i>	130.8	97.0	269.5	<i>10.6</i>	<i>45.9</i>	<i>10.5</i>
-102.0	-78.9	-219.0	-81.4	-75.2	-275.2	20.2	-22.9	-23.0

**Table 6.13.** Comparison of Tip Displacement of Specimen 3 for Model 2  
(Maximum values are shown in red italics.)

Tip Displacement (mm)								
Experiment			Numerical			Percentage Error (%)		
<i>OBE</i>	<i>MDE</i>	<i>MCE</i>	<i>OBE</i>	<i>MDE</i>	<i>MCE</i>	<i>OBE</i>	<i>MDE</i>	<i>MCE</i>
0.140	0.208	0.958	0.292	0.228	0.759	-108.7	-9.2	20.7
<i>-0.294</i>	<i>-0.300</i>	<i>-1.625</i>	-0.380	-0.239	-1.296	<i>-29.0</i>	<i>20.3</i>	<i>20.2</i>

The estimated crack lengths after OBE, MDE and MCE earthquake scenarios were 140 mm, 450 mm and 725 mm, respectively (Figure 6.35).

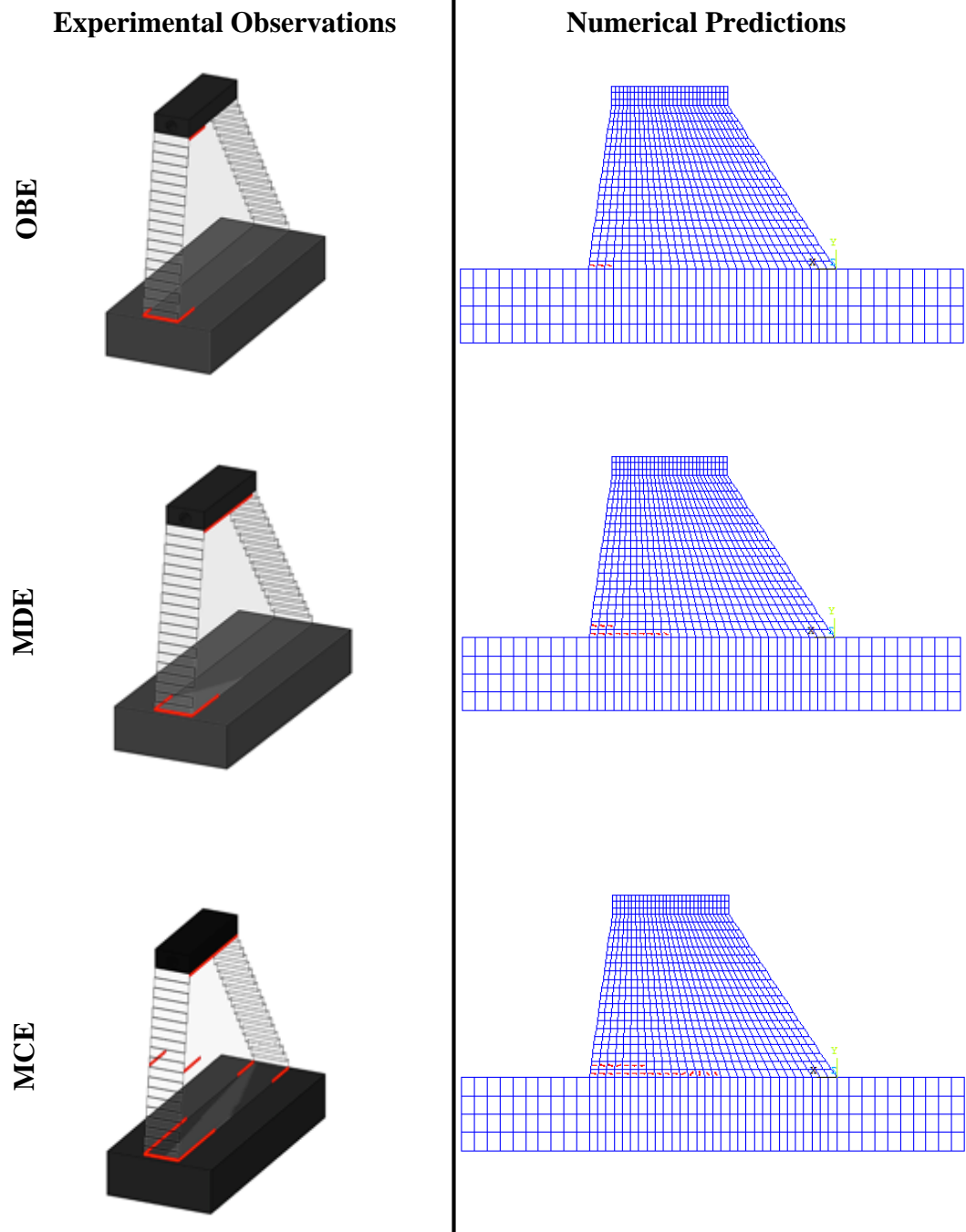


**Figure 6.35.** Comparison of Crack Patterns for Specimen 3 under the Effect of OBE, MDE and MCE Scenarios for Model 2

On the contrary, the observed crack lengths were 200 mm, 300 mm and 680 mm for the same hazard levels, respectively. The ratios of the crack lengths (predicted / observed one) for the OBE, MDE and MCE events were 0.70, 1.50 and 1.06, respectively. Besides, the body crack that appeared during MCE earthquake scenario could not be estimated by the numerical analysis. The comparisons of the estimated capacity curve with the experimentally obtained revealed that the capacity curve could be determined within acceptable error limits. The base shear and tip displacement capacities were determined with an error of less than 2% and 25%, respectively (Figure 6.36).

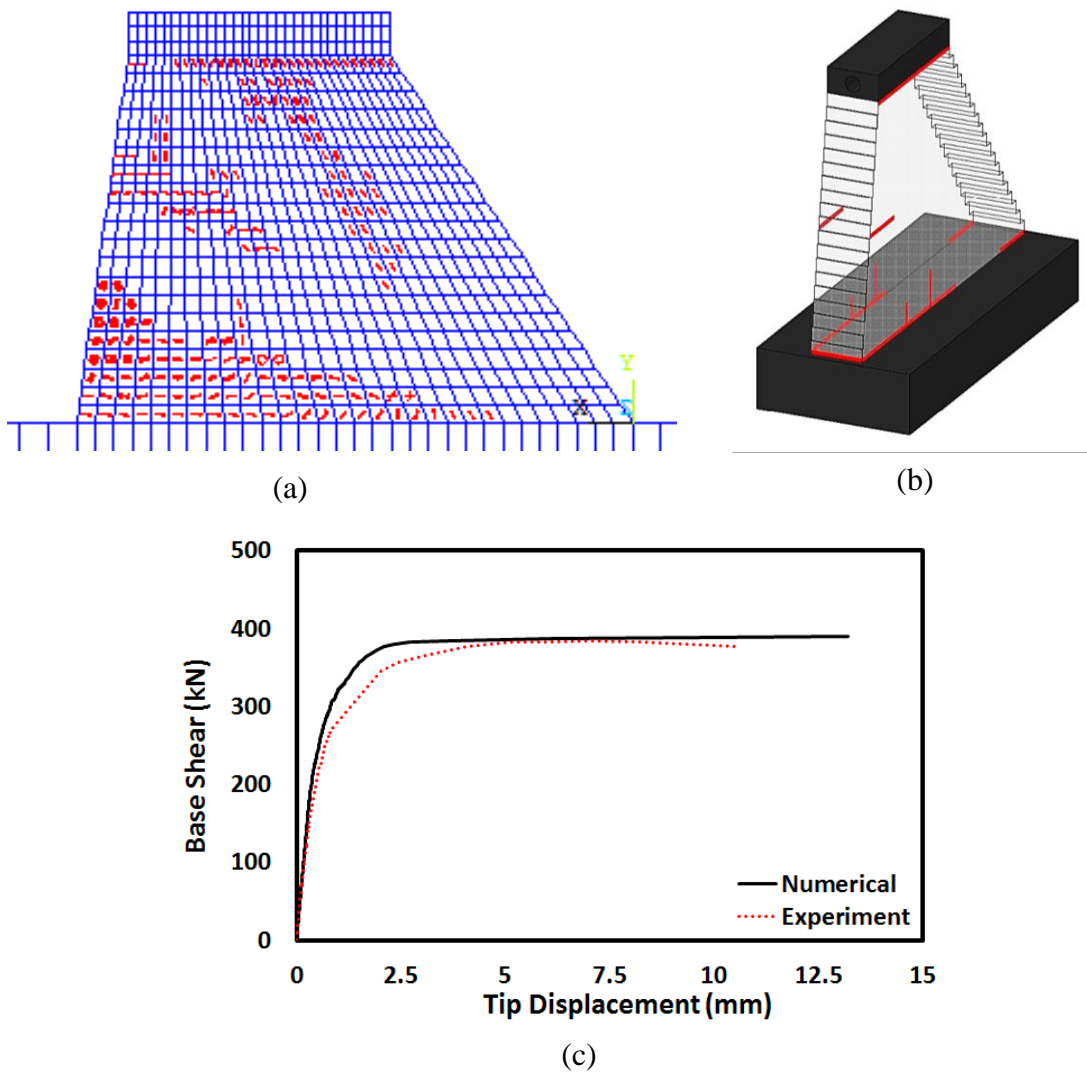


**Figure 6.36.** Comparison of Pushover Experiment for Specimen 3 from Model 2 : (a) Crack Pattern from Numerical Model, (b) Crack Pattern from Experiment and (c) Capacity Curve

## 6.5 Discussion of Numerical Simulation Results

In this part, the results of two different numerical modeling strategies are discussed based on the monitored base shear histories, tip displacement histories, capacity curves and the observed crack patterns. The ability of different modeling methods to predict the wave form of the base shear histories and the tip displacement histories are compared. Also, the success of these methodologies while predicting the maximum base shear and maximum tip displacement demands is discussed.

- Neither Model 1 nor Model 2 was determined to be explicitly better than the other one. One method could perform well for a specific case and could result in a large error for the other case. However, if to select one, Model 2 generally predicted the wave forms of aforementioned engineering demand parameters better than Model 1 as far as OBE and MDE motions were concerned. Yet, Model 1 matched the wave forms of base shear and tip displacement demands under the effect of MCE motions (Figure 6.37-Figure 6.39).
- One drawback of Model 2 was the adjustment of the spring constants. The target to match the fundamental period of the specimen could not uniquely be obtained. In other words, different pairs of compressive and tensile spring constants would lead to the same fundamental period as smaller tensile spring constants would result in reduced stiffness for the sake of more uplift deformations or comparable compressive and tensile spring constants would cause more base rotations. Apparently, the expected behavior was different for those two options. Therefore, the design engineers should be aware of the danger of using such spring models.
- The performances of Model 1 and Model 2 while predicting the maximum and minimum base shear demands were also motion- and specimen-dependent. However, in general, it could be inferred that Model 1 performed well for Specimen 1 during OBE motion and for Specimen 3 during MCE motion whereas the peak demands of base shear were forecasted better by Model 2 for all other cases.

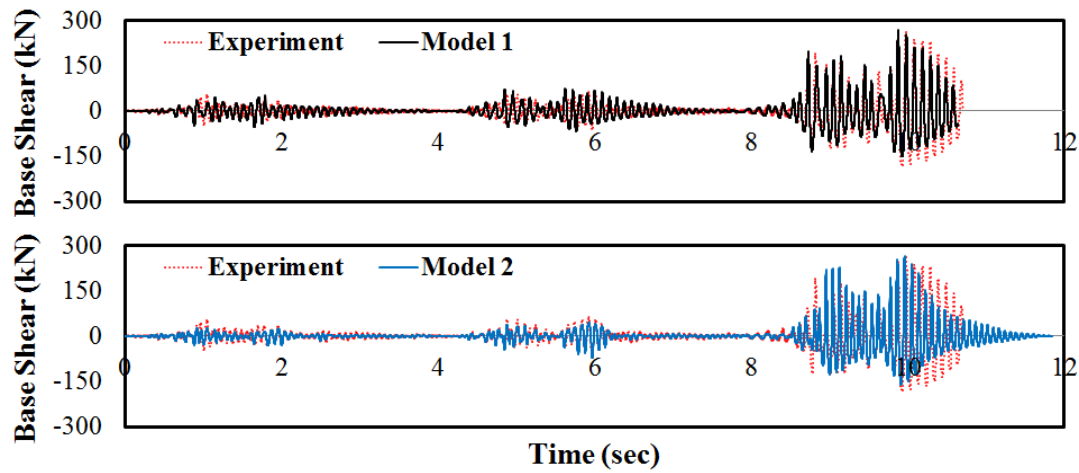


**Figure 6.37.** Comparison of Base Shear Demand Histories obtained from Model 1 and Model 2 for Specimen 1

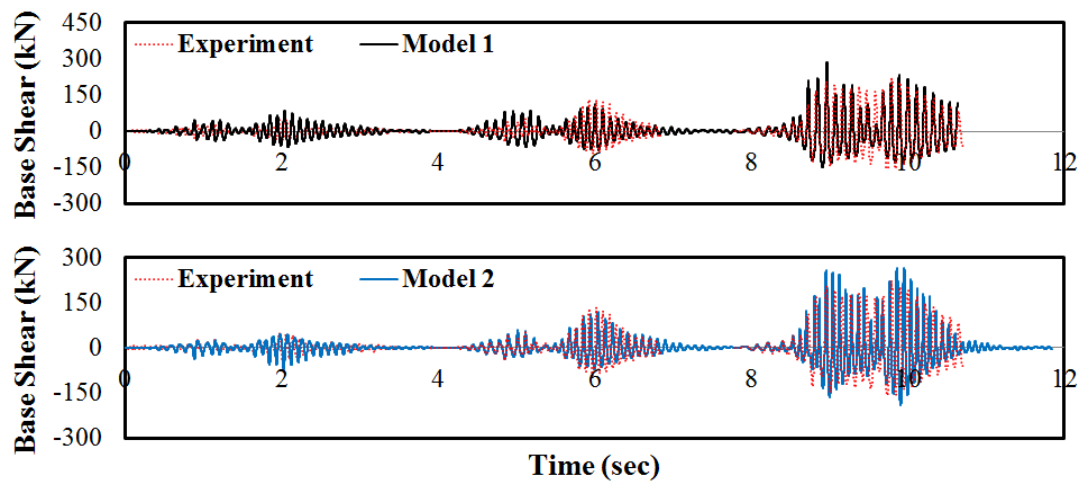


**Figure 6.38.** Comparison of Base Shear Demand Histories obtained from Model 1 and Model 2 for Specimen 2

- The crack lengths were mostly overestimated by Model 1 as this model had a fixed base assumption causing stress concentrations especially at the base. Contrary to Model 1, the crack lengths were usually underestimated by Model 2. However, both models accomplished to predict the crack lengths with sufficient accuracy for the most demanding earthquake scenario MCE.
- For both models, the cracks started to spread more around the previously opened cracks, which resulted in considerably more smeared cracking than the observed ones at final stages especially during pushover tests. This phenomenon was due to the deficiency of the smeared crack models. In

smear crack models, the nature of crack could not be modeled correctly due to the lack of physically opening motion. This shortcoming forced neighbor elements to easily crack due to the unavoidable redistribution of forces from the readily damaged (cracked) ones. Instead, in reality, the behavior around crack should be nearly rigid body motion with the crack opening and closing. Therefore, independent from the boundary conditions of these two methods, the crack spreading was more challenging to capture with the numerical models.

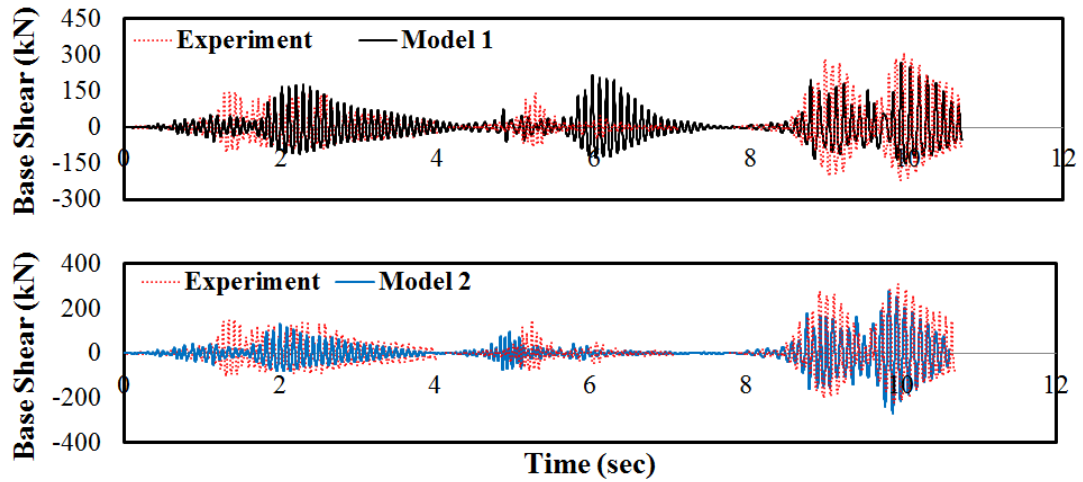


**Figure 6.39.** Comparison of Base Shear Demand Histories obtained from Model 1 and Model 2 for Specimen 3

- Both models succeeded to predict the base shear capacities of all specimens. The errors in base shear capacities were generally less than 10%. The performance of the numerical models for estimating the tip displacement capacity is also promising. However, the errors in the peak demand during nonlinear time history analyses were larger. This result implied that the numerical model had difficulties under the effect of cyclic loading but this deficiency was not so pronounced when a monotonic loading protocol was utilized. This observation was mainly due to the fact that the cyclic model required a more realistic hysteretic model, damping estimate (especially for cracks) and a failure criteria being capable of representing the stiffness degradation due to crack propagation reasonably, etc.

- In short, the numerical methods were more successful at predicting the global parameters such as the base shear force and the tip displacement compared to the crack patterns. Therefore, it was hard to reach definite conclusions on the failure modes of specimens. Consequently, the numerical models should be evaluated carefully at the design and evaluation stages and more realistic engineering demand parameters should be chosen for design and assessment procedures. In other words, the dam design practice also requires some displacement and/or base shear capacity limits commonly utilized in other types of structures like frame structures, tall buildings, etc.



## **CHAPTER 7**

### **CONCLUSION**

#### **7.1 Summary**

A total of three 1/75 scaled concrete dam specimens were tested by utilizing pseudo dynamic testing. Two of the specimens were constructed by using RCC and the other one was built by using CVC. All the specimens were tested for three different hazard levels, i.e. OBE, MDE and MCE. After these tests, a pushover test was also conducted to determine the full capacity curve and the possible failure mechanism of each specimen.

The application of the pseudo-dynamic testing to a distributed mass system requires a unique procedure. This procedure for dynamic testing of gravity dams are presented in Chapter 2. The proposed method incorporates both static (gravity+hydrostatic loads) and dynamic (inertial+hydrodynamic loads) testing. However, there are some assumptions involved to simplify the distributed system to a single-degree-of-freedom system in order possibly to apply pseudo-dynamic testing. These assumptions and the justifications are presented in Chapter 2. The application of the procedure to the specimens to be tested is also summarized in this chapter and the outline of the procedure is also demonstrated.

After the presentation of the necessary background for the pseudo-dynamic testing procedure, the material mix designs required during the preparation of each specimen and the effect of scaling on the material properties are investigated in Chapter 3. The compressive stress-strain curves were also determined and the effect of aggregate scaling on the fracture energy, strain energy and the stress-strain characteristics were discussed. In the scope of this chapter, the cementitious material amounts required for the planned specimens are also tabulated.

In Chapter 4, the details of the test setup along with the instrumentation intended to be used during testing are presented. After that, the validation for the pseudo-dynamic system was carried out by conducting two different tests on an L-shaped steel frame. The fundamental period of the verification frame was arranged such that it gave a close match to the expected fundamental period of the scaled dam specimens. Finally, the properties of each specimen and the details of specimen preparation were also summarized.

In the next chapter, the results from the testing of three scaled dam models by using the PSD method are presented. All specimens were tested under the effect of three different ground motions corresponding to OBE, MDE and MCE hazard levels. Then, the capacity curve of each specimen was determined by conducting a pushover test. The experimental observations along with the recorded engineering demand parameters like the base shear force, tip and base displacements, etc. are utilized to explain the observed behavior and to compare the seismic performances of each specimen.

In Chapter 6, the viability of the numerical prediction of the test results, hence the nonlinear behavior of a dam monolith, using a commercially available FE software was investigated. In order to account for the unintended base flexibility, two different modeling strategies were employed to simulate the experimentally observed behavior of each test specimen. In Model 1, all specimens were assumed to have a fixed base and the flexibility due to the base and the foundation rotations were taken into account by softening the modulus of elasticity of each specimen. In Model 2, the foundation of the dam was also included in the numerical model and vertical base springs were placed under the foundation to reflect the uplift motion. The ability of each model to predict the crack patterns, force and displacement demands were compared.

## **7.2 Conclusions**

In literature, there is a limited number of experimental research on dams despite of the necessity of testing the seismic response of CVC and RCC gravity dams. Therefore, this dissertation aimed to propose a new approach for testing the seismic

performance of gravity dams. The following conclusions are drawn in the light of the experimental and analytical studies:

### **I. Materials:**

- It was detected that the strain capacity of the CVC cylinders was more than the strain capacities of RCC25 cylinders at 7<sup>th</sup> day (Figure 3.13). Also, the strain at ultimate strength of CVC cylinders was more. However, the stress-strain curves of the CVC and RCC25 cylinders are similar at 28<sup>th</sup> day as far as the ascending portions of the curves are concerned except for the softening regions, which was steeper for the RCC cylinders. This discrepancy would be related to the layered nature of the RCC cylinders.
- The effect of aggregate scaling on the stress-strain curve characteristics was the increase in the strain energy due to their softer descending regions, i.e. scaled CVC cylinders had about 25% more strain energy with respect to the unscaled CVC cylinders (Figure 3.14 and Table 3.19). This observation was probably due to the relatively more cement paste amount inside the scaled CVC cylinders and more aggregate surface area from using no coarse aggregates in the scaled CVC mixture.
- The percentage difference in the ultimate strain (strain at 85% capacity drop) was determined as only 15% between the scaled and unscaled CVC cylinders. In addition, the error in the fracture energy due to scaling process was found to be in the order of about 25%.

### **II. Experimental Results:**

- The effect of the material type (CVC or RCC) on the specimen behavior and base shear capacity of the specimens was negligible if the compressive strength values were similar (Figure 5.50).

The type of material had no significant effect on the crack formations, propagations and lengths (Figure 5.14 and Figure 5.48

- **Figure 5.48).**

- The effect of compressive/tensile strength on the behavior of dam specimens was more pronounced on the ultimate displacement capacity than the base shear capacity. The differences in the lateral load capacity and the ultimate tip displacement between Specimen 1 and 2 were about 20% and more than 200%, respectively.
- The stiffness of the base of each dam specimen was reduced due to major base cracks especially at the upstream face. However, none of the specimens showed pure sliding motion, i.e. a time period in which zero stiffness was detected (spike-type motions in base deformation records). Therefore, it could be concluded that the base application (surface roughening) would prevent base sliding type failure modes.
- All specimens were identified to have similar damping ratios independent from their material properties. These identified damping ratios were close to the damping ratio values recommended by USACE (2003) (Figure 5.15, Figure 5.35 and Figure 5.49) except for MCE motion. The identified damping ratio for the MCE motion was seemed to be slightly smaller than USACE (2003) recommended 7% material damping.
- The hysteresis loops in the lateral load-tip displacement curves were narrow for all specimens as the crack opening/closing cycles were not sufficient to dissipate large energy when no sliding was present. In fact, it was observed that this mechanism was only capable of producing 2 to 4% damping.
- The period of each specimen had a tendency to increase during consecutive earthquake load applications. The initial period of each specimen had increased nearly 1.6 times during the last motion, MCE. This observation was nearly the same for each specimen. More importantly, the deviations in periods during the same motion was not more than 20%. This observation was vital as the verification of the test method was totally dependent on the performed linear analysis.

### **III. Numerical Results:**

- Neither fixed base assumption with softer modulus of elasticity (Model 1) nor numerical model with base springs (Model 2) was determined to be superior numerical model for predicting the specimen behaviour. One method could

perform well for a specific case and could result in a large error for other case.

- The crack lengths were mostly overestimated by Model 1 as this model had a fixed base assumption causing stress concentrations especially at the base. Contrary to Model 1, the crack lengths were usually underestimated by Model 2. However, both models accomplished to predict the crack lengths successfully for the most demanding earthquake scenario MCE.
- Numerical models estimated a more distributed crack pattern compared to the observed ones. In addition, the predicted cracked regions were significantly larger. This phenomenon was due to the deficiency of the smeared crack models. In the smeared crack models, the nature of crack could not be modeled correctly due to the lack of physically opening motion. Therefore, independent from the boundary conditions of these two methods, the crack formations were more intensive in numerical models. As a remedy, interface elements could be utilized.
- Both models were successful in predicting the full-capacity curves of all specimens. However, the peak demands during nonlinear time history analyses were estimated with a larger margin of errors. This result implied that the numerical model had difficulties under the reversible loadings but this deficiency was not so pronounced when a monotonic loading protocol was utilized. Therefore, the numerical methods were more skilled while predicting the global parameters like base shear, tip displacement, etc. Yet, they were not evolved enough to predict the crack patterns under the cyclic loading. Consequently, the numerical models should be evaluated carefully at the design and evaluation stages and more realistic engineering demand parameters should be chosen during these procedures.

### **7.3 Future Study**

Based on the conclusions from this work, following future studies are recommended:

- Cohesive zone material could be used to take the possibility of base sliding into account along with smeared crack continuum models. In this way, both

failure modes, i.e. sliding and body damage, could be incorporated in the numerical model.

- The dam specimens could be tested only for a specific ground motion level, especially under the effect of the MCE motion, to come up with a better identification for the damping ratio.
- Pseudo dynamic testing algorithm could be modified to incorporate simultaneous solution of the equation motion considering hydrodynamic effects and base flexibility due to foundation. In this way, the requirement of a single piston acting on the test specimen can be removed.
- Further tests on scaled dam specimens with different geometry and various ground motions should be conducted to further understand the influence of dam geometry and ground motion on the seismic response of concrete gravity dams.

## REFERENCES

- ABAQUS (2012), “ABAQUS/CAE Use Manual”, SIMULIA.
- ACI 207 (1999), “Roller - Compacted Mass Concrete”, ACI Committee.
- Akkar, S. (2010), “Probabilistic Seismic Risk Analysis of Melen Dam for Design Spectrum Calculations”, Report No: 2010-03-03-1-01-04, METU (in Turkish).
- Akkose, M. and Simsek, E. (2010), “Non-Linear Seismic Response of Concrete Gravity Dams to Near-Fault Ground Motions including Dam-Water-Sediment-Foundation Interaction”, *Applied Mathematical Modelling*, **34**, 3685–3700.
- American Concrete Institute (ACI 318), “Building Code Requirements for Structural Concrete”, Farmington Hills.
- ANSYS Inc. (2010.a), “Basic Analysis Guide for ANSYS 13”, SAS IP Inc.
- ANSYS Inc. (2010.b), “Element Reference for ANSYS 13”, SAS IP Inc.
- ANSYS Inc. (2010.c), “Structural Analysis Guide for ANSYS 13”, SAS IP Inc.
- ANSYS Inc. (2010.d), “Theory Reference for the Mechanical APDL and Mechanical Applications ANSYS 13”, SAS IP Inc.
- Arabshahi, H. and Lotfi, V. (2008), “Earthquake Response of Concrete Gravity Dams including Dam–Foundation Interface Nonlinearities”, *Engineering Structures*, **30**, 3065-3073.
- Arıcı, Y. (2016), “Barajların Analizi için Sonlu Eleman Yazılımı Hazırlanması”, TUBITAK Üniversite Sanayi İşbirliği Projeleri, Report: , (in Turkish).
- ASTM C 42 (1994), “Standard Test Method for Obtaining and Testing Drilled Cores and Sawed Beams of Concrete”, Annual Book of ASTM Standards.
- ASTM C 127-12 (2012), “Standard Test Method for Density, Relative Density (Specific Gravity), and Absorption of Coarse Aggregate”, Annual Book of ASTM Standards.
- ASTM C 128-12 (2012), “Standard Test Method for Density, Relative Density (Specific Gravity), and Absorption of Fine Aggregate”, Annual Book of ASTM Standards.
- ASTM C 150-12 (2012), “Standard Specification for Portland Cement”, Annual Book of ASTM Standards.

- ASTM C 618-12 (2012), “Standard Specification for Coal Fly Ash and Raw or Calcined Natural Pozzolan for Use in Concrete”, Annual Book of ASTM Standards.
- Baba, K. (1980), “Model and Full-scale Concrete Dam Studies in Japan”, *Proceedings of Research Conference on Earthquake Engineering*, Skopje, Yugoslavia.
- Banerjee, A., Paul, D.K. and Dubey, R.N. (2014), “Modelling Issues in the Seismic Analysis of Concrete Gravity Dams”, *Dam Engineering*, **24**(2), 1-23.
- Basili, M. and Nuti, C. (2011), “A Simplified Procedure for Base Sliding Evaluation of Concrete Gravity Dams under Seismic Action”, *ISRN Civil Engineering*.
- Basu, U. and Chopra, A.K. (2003), “Perfectly Matched Layers for Time-harmonic Elastodynamics of Unbounded Domains: Theory and Finite-element Implementation”, *Computer Methods in Applied Mechanics and Engineering*, **192**, 1337-1375.
- Bernal, D. and Youssef, A. (1998), “A Hybrid Time Frequency Domain Formulation for Non-Linear Soil-structure Interaction”, *Earthquake Engineering and Structural Dynamics*, **27**, 673-685.
- Bertero V.V., Aktan A.E., Charney F.A. and Sause R. (1984), “Earthquake Simulation Tests and Associated Studies of a 1/5th-scale Model of a 7-story R/C Frame–wall Test Structure”, Report No: *UCB/EERC-84/05*, University of California, Berkeley, California.
- Bhattacharjee, S.S. and Leger, P. (1994), “Application of NFLM Models to Predict Cracking in Concrete Gravity Dams”, *Journal of Structural Engineering ASCE*, **120**(4), 1255-1271.
- Bhattacharjee, S.S. and Leger, P. (1995), “Fracture Response of Gravity Dams due to Rise of Reservoir Elevation”, *Journal of Structural Engineering ASCE*, **121**(9), 1298- 1305.
- Binici, B., Aldemir, A. and Gharibdoust, A. (2016), “Effect of Base Roughness on Seismic Response of Concrete Gravity Dams”, *10<sup>th</sup> ICOLD European Club Symposium*, Antalya, Turkey.
- Bougacha, S. and Tassoulas, J.L. (1992), “Effects of Sedimentary Material on the Response of Concrete Gravity Dams”, *Earthquake Engineering and Structural Dynamics*, **20**(9), 849-858.



- Bougacha, S. and Tassoulas, J.L. (2006), “Dam-Water-Sediment-Rock Systems: Seismic Analysis”, *Soil Dynamics and Earthquake Engineering*, **26**(6), 680-693.
- Calayir, Y, Dumanoglu, A.A. and Bayraktar, A. (1996), “Earthquake Analysis of Gravity Dam-Reservoir Systems using the Eulerian and Lagrangian Approaches”, *Computers and Structures*, **59**(5), 877-890.
- Carter, B. (2008), “Structures and land forms: Faults [online]. Available from <http://itc.gsw.edu/faculty/bcarter/geomorph/struct/fault1.htm> [cited 18 August 2013].
- Červenka, V., Jendele, L. and Červenka, J. (2016), “ATENA Program Documentation Part 1: Theory”, Červenka Consulting.
- Chen, W.F. (1982), “Plasticity in Reinforced Concrete”, McGraw-Hill Inc., New York.
- Chopra, A.K. (1967). “Hydrodynamic Pressures on Dams during Earthquakes”, *Journal of Engineering Mechanics ASCE*, **93**(6), 205-224.
- Chopra, A.K. (1978), “Earthquake Resistant Design of Concrete Gravity Dams”, *Journal of Structural Division*, **104**(6), 953–971.
- Chopra, A.K. (2012), “Dynamics of Structures: Theory and Applications to Earthquake Engineering”, 4<sup>th</sup> Edition, Prentice Hall, Upper Saddle River, New Jersey.
- Chopra, A.K. and Chakrabarti, P. (1970), “A Computer Program for Earthquake Analysis of Dams”, Report No: *EERC-70-05*, Earthquake Engineering Research Center, University of California, Berkeley, California.
- Chopra, A.K. and Chakrabarti, P. (1971), “The Koyna Earthquake of December, 11 1967 and the Performance of Koyna Dam”, Report No: *EERC-71-01*, Earthquake Engineering Research Center, University of California, Berkeley, California.
- Chopra, A.K. and Wang, J. (2008), “Analysis and Response of Concrete Arch Dams Including Dam-Water-Foundation Rock Interaction to Spatially-Varying Ground Motions”, Report No: *UCB/EERC-2008-03*, Earthquake Engineering Research Center, University of California, Berkeley, California.
- Chopra, A.K., Chakrabarti, P. and Gupta, S. (1980), “Earthquake Response of Concrete Gravity Dams including Hydrodynamic and Foundation Interaction

- Effects”, Report No: *UCB/EERC-80-01*, Earthquake Engineering Research Center, University of California, Berkeley, California.
- Clough, R.W. (1980), “Nonlinear Mechanisms in the Seismic Response of Arch Dams”, *Proceedings of International Research Conference on Earthquake Engineering*, Skopje, Yugoslavia
- Clough, R.W., Raphael, J.M. and Mojtahedi, S. (1973), “ADAP – A Computer Program for Static and Dynamic Analysis of Arch Dams”, Report No: *EERC-73-14*, Earthquake Engineering Research Center, University of California, Berkeley, California.
- Cook R.D., D.S. Malkus, M.E. Plesha and R.J. Witt (2002), “Concepts and Applications of Finite Element Analysis”, 4<sup>th</sup> Edition, John Wiley and Sons Inc., New Jersey, USA.
- Dasgupta, G. and Chopra, A.K. (1979), “Dynamic Stiffness Matrices for Viscoelastic Half Planes”, *Journal of Engineering Mechanics Division, ASCE*, **105**(5), 729-745.
- Day, R.L. (1994), “Strength Measurement of Concrete using Different Cylinder Sizes: A Statistical Analysis”, *Cement, Concrete, and Aggregates, CCAGPD*, **16**(1), 21-30.
- Donlon, W.P. (1989), “Experimental Investigation of the Nonlinear Seismic Response of Concrete Gravity Dams”, Ph.D. Thesis, California Institute of Technology, California, USA.
- Donlon, W.P. and Hall, J.F. (1991), “Shaking Table Study of Concrete Gravity Dam Monoliths”, *Earthquake Engineering and Structural Dynamics*, **20**(8), 769–786.
- Duron, Z.H. (1987), “Experimental and Finite Element Studies of a Large Arch Dam”, Report No: *EERL 87-02*, Earthquake Engineering Research Laboratory, California Institute Technology, Pasadena, California.
- Dursun, B. and Gokcol, C. (2011), “The role of hydroelectric power and contribution of small hydropower plants for sustainable development in Turkey”, *Renewable Energy*, **36**, 1227-1235.
- Elkhoraibi T. and Mosalam K.M. (2007), “Towards Error-free Hybrid Simulation using Mixed Variables”, *Earthquake Engineering and Structural Dynamics*, **36**(11), 1497–1522.

- Federal Energy Regulatory Commission (FERC) (1999), “Engineering Guidelines for the Evaluation of Hydropower Projects”, Office of Energy Projects.
- Fenves, G. and Chopra, A.K. (1983), “Effects of Reservoir Bottom Absorption on Earthquake Response of Concrete Gravity Dams”, *Earthquake Engineering and Structural Dynamics*, **11**(6), 809-829.
- Fenves, G. and Chopra, A.K. (1984.a), “EAGD-84: A Computer Program for Earthquake Response Analysis of Concrete Gravity Dams”, Report No: *UCB/EERC-734*, Earthquake Engineering Research Center, University of California, Berkeley, California.
- Fenves, G. and Chopra, A. K. (1984.b), “Earthquake Analysis and Response of Concrete Gravity Dams”, Report No: *UCB/EERC-84/10*, Earthquake Engineering Research Center, University of California, Berkeley, California.
- Fenves, G. and Chopra, A.K. (1984.c), “Earthquake Analysis of Concrete Gravity Dams including Reservoir Bottom and Dam-Water-Foundation Rock Interaction”, *Earthquake Engineering and Structural Dynamics*, **12**(5), 663-680.
- Fenves, G. and Chopra, A.K. (1985.a), “Simplified Earthquake Analysis of Concrete Gravity Dams: Separate Hydrodynamic and Foundation Interaction Effects”, *Journal of Engineering Mechanics*, **111**(6), 715-735.
- Fenves, G. and Chopra, A.K. (1985.b), “Simplified Earthquake Analysis of Concrete Gravity Dams: Combined Hydrodynamic and Foundation Interaction Effects”, *Journal of Engineering Mechanics*, **111**(6), 736-756.
- Fenves, G. and Chopra, A.K. (1986), “Simplified Analysis for Earthquake Resistant Design of Concrete Gravity Dams”, Report No: *UCB/EERC-85-10*, Earthquake Engineering Research Center, University of California, Berkeley, California.
- Ferro, A.N. (2013), “Nonlinear Dynamic Soil-Structure Interaction in Earthquake Engineering”, Ph.D. Thesis, École Centrale Paris, Paris, France.
- Fok, K., Hall, J.F. and Chopra, A.K. (1986), “EACD-3D A Computer Program for Three-dimensional Earthquake Analysis of Concrete Dams”, Report No: *UCB/EERC-86/09*, University of California, Berkeley, California.
- Fronteddu, L., Leger, P. and Tinawi, R. (1998), “Static and Dynamic Behavior of Concrete Lift Joint Interfaces”, *Journal of Structural Engineering (ASCE)*, **124**(12), 1418:1430.

- Fuller, W.B. and Thompson, S.E. (1907), “The Laws of Proportioning Concrete”, *Transactions of the ASCE*, 159.
- General Directorate of State Hydraulic Works, <http://www.dsi.gov.tr/baraj-arama>, last visited 28.10.2015.
- Ghaemian, M and Ghobarah, A. (1998), “Staggered Solution Schemes for Dam-Reservoir Interaction”, *Journal of Fluids and Structures*, **12**(7), 933-948.
- Ghanaat, Y. (2004), “Failure Modes Approach to Safety Evaluation of Dams”, *13<sup>th</sup> World Conference on Earthquake Engineering*, Vancouver, B.C., Canada.
- Gogoi, I. and Maity, D. (2005), “Seismic Safety of Aged Concrete Gravity Dams Considering Fluid-Structure Interaction”, *Journal of Earthquake Engineering*, **9**(5), 637-656.
- Gutierrez, A.J. and Chopra, A.K. (1976), “A Substructure Method for Earthquake Analysis of Structure-soil Interaction”, Report No: *UCB/EERC-76/09*, University of California, Berkeley, California.
- Hall, J.F. (1998), “Efficient Non-Linear Seismic Analysis of Arch Dams”, *Earthquake Engineering and Structural Dynamics*, **27**, 1425-1444.
- Hall, J.F. and Chopra, A.K. (1980), “Dynamic Response of Embankment, Concrete Gravity and Arch Dams including Hydrodynamic Interaction”, Report No: *UCB/EERC-80-39*, Earthquake Engineering Research Center, University of California, Berkeley, California.
- Hamad, A.J. (2015), “Size and Shape Effect of Specimen on the Compressive Strength of HPLWFC Reinforced with Glass Fibres”, *Journal of King Saud University – Engineering Sciences*, online.
- Harris, D.W. Snorteland, N., Dolen, T. and Travers, F. (2000), “Shaking Table 2D Models of a Concrete Gravity Dam”, *Earthquake Engineering and Structural Dynamics*, **29**(6), 769–787.
- Hatanaka, M. (1955), “Fundamental Considerations on the Earthquake Resistant Properties of Earth Dam”, Disaster Prevention Research Institute, Bulletin No:11, Kyoto, Japan.
- Hui, P.K. (1992), “Dynamic behaviour of base cracked gravity dam by the way of the hybrid frequency time domain procedure”, M.S. Thesis, The University of British Columbia, Canada.

- International Commission on Large Dams (ICOLD), [http://www.icold-cigb.org/gb/world\\_register/general\\_synthesis.asp?IDA=206](http://www.icold-cigb.org/gb/world_register/general_synthesis.asp?IDA=206), last visited 28.10.2015.
- Jackson, J. (2012), “Earthquake hazards and large dams in western China”, Probe International Report.
- Javanmardi, F., Leger, P. and Tinawi, R. (2005), “Seismic Structural Stability of Concrete Gravity Dams Considering Transient Uplift Pressures in Cracks”, *Engineering Structures*, **27**, 616-628.
- Keightley, W.O. (1964), “A Dynamic Investigation of Bouquet Canyon Dam”, Earthquake Engineering Research Laboratory, California Institute Technology, Pasadena, California.
- Klieger, P. and Lamond, J.F. (1994), “Significance of tests and properties of concrete and concrete-making concrete”, ASTM Publication Code Number (PCN): 04-169030-07, Philadelphia, USA.
- Ko, H.Y. (1988), “Summary of the State-of-the-art in Centrifuge Model Testing”, Centrifuges in Soil Mechanics, S.C. James, ed., A.A. Balkema, Rotterdam, The Netherlands.
- Kuo, J.S.H. (1982), “Fluid – structure Interactions: Added Mass Computations for Incompressible Fluid”, Report No: *UCB/EERC-82/09*, University of California, Berkeley, California.
- Kurt, E.G., Binici, B., Kurc, O., Canbay, E., Akpınar, U. and Özcebe, G. (2011), “Seismic Performance of a Deficient Reinforced Concrete Test Frame with Infill Walls”, *Earthquake Spectra*, **27**(3), 817-838.
- Lee, J. and Fenves, G.L. (1998), “A Plastic-Damage Concrete Model for Earthquake Analysis of Dams”, *Earthquake Engineering and Structural Dynamics*, **27**, 937:956.
- Lim, W.Z., Xiao, R.Y. and Chin, C.S. (2012), “A Comparison of Fluid-Structure Interaction Methods for a Simple Numerical Analysis of Concrete Gravity-Dam”, *Proceedings of the 20<sup>th</sup> UK Conference of the Association for Computational Mechanics in Engineering*, The University of Manchester, Manchester, UK, 321-324.
- Løkke, A. and Chopra, A.K. (2013), “Response Spectrum Analysis of Concrete Gravity Dams including Dam-Water-Foundation Interaction”, Report No:

- 2013/17, Pacific Earthquake Engineering Research Center, University of California, Berkeley, California.
- Lotfi, V., Roesset, J. M., and Tassoulas, J. L. (1987), “A Technique for the Analysis of the Response of Dams to Earthquakes”, *Earthquake Engineering and Structural Dynamics*, **15**, 463-490.
- Lubliner, J., Oliver, J., Oller, S. and Onate, E. (1989), “A Plastic-Damage Model for Concrete”, *International Journal of Solids and Structures*, **25**(3), 299:326.
- Mahin, S.A., Shing, P.B., Thewalt, C.R. Sz Hanson, R.D. (1989). “Pseudodynamic Test Method: Current Status and Future Directions”, *Journal of Structural Engineering*, **115**(8), 2113-2128.
- Maia, N.M.M. and Silva, J.M.M. (1997), “Theoretical and Experimental Modal Analysis”, Research Studies Press, John Wiley, New York.
- Medina F. and Dominguez, J. (1989), “Boundary Elements for the Analysis of the Seismic Response of Dams including Dam-water-foundation Interaction Effects”, *Engineering Analysis with Boundary Elements*, **6**(3), 152:157.
- Medina, F., Dominguez, J., and Tassoulas, J. (1990), “Response of Dams to Earthquakes including Effects of Sediments”, *Journal of Structural Engineering ASCE*, **116**(11), 3108–3121.
- Megally, S.H. (1998), “Punching Shear Resistance of Concrete Slabs to Gravity and Earthquake”, Ph.D. Thesis, The University of Calgary, Canada.
- Mehta, P.K. and Monteiro, P.J.M., (2014), “Concrete: Microstructure, Properties, and Materials”, McGraw-Hill, fourth edition.
- Mills-Bria, B., Nuss, L. and Chopra, A.K. (2008), “Current Methodology at the Bureau of Reclamation for the Nonlinear Analyses of Arch Dams Using Explicit Finite Element Techniques”, *The 14<sup>th</sup> World Conference on Earthquake Engineering*, Beijing, China.
- Molina F.J, Verzeletti G., Magonette G., Buchet P.H. and Geradin M. (1999), “Bi-directional Pseudodynamic Test of a Full-size Threestorey Building”, *Earthquake Engineering and Structural Dynamics*, **28**(12), 1541–1566.
- Molina, F.J., Pegon, P. and Verzeletti, G. (1999), “Time - Domain Identification from Seismic Pseudo Dynamic Test Results on Civil Engineering Specimens”, *2nd International Conference on Identification in Engineering Systems*, 29–31 March 1999, University of Wales, Swansea.

- Moradloo, J., Ahmadi, M.T. and Vahdani, S. (2008), “Nonlinear Dynamic Analysis of Concrete Arch Dam considering Large Displacements”, *14<sup>th</sup> World Conference on Earthquake Engineering*, Beijing, China.
- Mridha, S. and Maity, D. (2014), “Experimental Investigation on Nonlinear Dynamic Response of Concrete Gravity Dam-Reservoir System”, *Engineering Structures*, **80**, 289–297.
- Nakashima, M., Kaminosono, T., Ishida, M, Ando, K. (1990). “Integration Techniques for Substructure Pseudo Dynamic Test”, *4<sup>th</sup> US National Conference on Earthquake Engineering*, Palm Springs, California.
- Nawy, E.G. (2008), “Concrete Construction Engineering Handbook”, Second Edition, CRC Press, Boca Raton, USA.
- Niwa, A. and Clough, R.W. (1980), “Shaking Table Research on Concrete Dam Models”, Report No: *UCB/EERC-80/06*, Earthquake Engineering Research Center, University of California, Berkeley, California.
- Nuss, L.K., Matsumoto, N. and Hansen, K.D. (2012), “Shaken but not Stirred Earthquake Performance of Concrete Dams”, *32<sup>nd</sup> Annual USSD Conference*, New Orleans, Louisiana.
- Ouzandja, D., Benkechida, F., Ouzandja, T. and Belhaded, H. (2014), “Study of Dynamic Soil-Structure Interaction of Concrete Gravity Dams”, *2<sup>nd</sup> European Conference on Earthquake Engineering and Seismology*, Istanbul, Turkey.
- Ozcan, S. (2008), “Bonding Efficiency Of Roller Compacted Concrete With Different Bedding Mixes”, M.S. Thesis, Middle East Technical University, Ankara, Turkey.
- Phansri, B., Charoenwongmit, S., Yooprasertchai, E., Park, K., Warnitchai, P. and Shin, D. (2015), “An Experimental Study on Shaking Table Tests on Models of a Concrete Gravity Dam”, *KSCE Journal of Civil Engineering*, **19**(1),142-150.
- Plizzari, G., Waggoner, F. and Saouma, V.E. (1995), “Centrifuge Modeling and Analysis of Concrete Gravity Dams”, *Journal of Structural Engineering ASCE*, **121**(10), 1471-1479.
- Proulx, J. and Paultre, P. (1997), “Experimental and Numerical Investigation of Dam – Reservoir – Foundation Interaction for a Large Gravity Dam”, *Canadian Journal of Civil Engineering*, **24**(1): 90-105.

- Raphael, J.M., (1971), “The Optimum Gravity Dam”, *Proceedings of Conference on Rapid Construction of Concrete Dams*, ASCE, New York, 221-247.
- Raphael, J.M., (1984), “Tensile strength of concrete”, *Journal of American Concrete Institute*, **81**(2), 158–165.
- Rots, J.G. (1989), “Various Crack Concepts for Curved Fracture in Concrete”, *Proceedings of the 7<sup>th</sup> International Conference on Fracture*, Houston, USA.
- Saouma, V., Broz, J., Brühwiler, E. and Boggs, H. (1991), “Effect of Aggregate and Specimen Size on Fracture Properties of Dam Concrete”. *Journal of Materials in Civil Engineering (ASCE)*, **3**(3):204 –218.
- Sevim, B., Altunsik, A.C., Bayraktar, A., Akkose, M. and Calayir, Y. (2011), “Water Length and Height Effects on the Earthquake Behavior of Arch Dam-Reservoir-Foundation Systems”, *KSCE Journal of Civil Engineering*, **15**(2), 295-303.
- Slowik, V. And Saouma, V.E. (2000), “Water Pressures in Propagating Concrete Cracks”, *Journal of Structural Engineering ASCE*, **126**(2), 235-242.
- Soysal, B.F., Binici, B. and Arıcı, Y. (2016), “Investigation of the Relationship of Seismic Intensity Measures and the Accumulation of Damage on Concrete Gravity Dams using Incremental Dynamic Analysis”, *Earthquake Engineering and Structural Dynamics*, **45**, 719–737.
- Takanashi K., Udagawa K., Seki M., Okada T. and Tanaka H. (1975). “Nonlinear Earthquake Response Analysis of Structures by a Computer-Actuator On-line System”, *Bulletin of Earthquake Resistant Structure Research Center*, **8**, 1-17.
- Takata, T. and Kuribayashi, E. (1961), “Studies on Stress Analysis for Dam by Photo Elastic Method, a Large Centrifugal Type Loading Apparatus and its Application Experimental Tests”, *Journal of Research, Public Works Research Institute*, **4**(13), 1-24.
- Taylor, R.L., Beresford, P.J. and Wilson, E.L. (1976), “A non-conforming Element for Stress Analysis”, *International Journal for Numerical Methods in Engineering*, **10**(6), 1211-1219.
- Tinawi R., Leger P., Leclerc M. and Cipolla G. (2000), “Seismic Safety of Gravity Dams: From Shake Table Experiments to Numerical Analyses”, *Journal of Structural Engineering (ASCE)*, **126**(1), 518-529.
- TNO DIANA. (2008). User’s Manual R. 9.3.



- Tsai, C.S. and Lee, G.C. (1991), "Time-Domain Analyses of Dam-Reservoir System II: Substructure Method", *Journal of Engineering Mechanics*, **117**(9), 2007:2026.
- Tsai, C.S., Lee, G.C. and Ketter, R.L. (1990.a), "A Semi-Analytical Method for Time-Domain Analyses of Dam-Reservoir Interactions", *International Journal of Numerical Methods in Engineering*, **29**(5), 913:933.
- Tsai, C.S., Lee, G.C. and Yeh, C.S. (1990.b), "Transient Responses of 3D Fluid Structure Interactions", *Advances in Boundary Elements Methods in Japan and USA*, **7**, 183:199.
- Uchita, Y., Shimpo, T. and Saouma, V. (2005), "Dynamic Centrifuge Tests of Concrete Dam", *Earthquake Engineering and Structural Dynamics*, **34**(12), 1467–1487.
- Uji, K. (2005), "Roller Compacted Concrete Dam and Utilization of Fly Ash in Japan", *JSCE-VIFCEA Joint Seminar on Concrete Engineering in Vietnam and Workshop*, Vietnam.
- Ulusal Barajlar Kongresi (UBK) (2012), "Beton Barajlar Tasarım İlkeleri Rehberi", Devlet Su İşleri Genel Müdürlüğü, s.81.
- United States Army Corps of Engineering (USACE) (1994), "Arch Dam Design", Report No: *EM 1110-2-2201*, Washington, DC.
- United States Army Corps of Engineering (USACE) (2003), "Time History Dynamic Analysis of Concrete Hydraulic Structures", Report No: *EM 1110-2-6051*, Washington, DC.
- Vandegrift, D. Jr. and Schindler, A.K. (2006), "The Effect of Test Cylinder Size on the Compressive Strength of Sulfur Capped Concrete Specimens", Project No: *IR-6-01*, Highway Research Center and Department of Civil Engineering, Auburn University.
- Wang, J. and Chopra, A.K. (2008), "EACD-3D: A Computer Program for Three Dimensional Earthquake Analysis of Concrete Dams Considering Spatially - Varying Ground Motion", Report No: *UCB/EERC-2008/04*, Earthquake Engineering Research Center, University of California, Berkeley, California.
- Westergaard, H.M. (1933), "Water pressures on dams during earthquakes", *Transactions of the American Society of Civil Engineers*, **98**, 418–433.

- Wilcoski, J., Hall, R.L., Matheu, E.E., Gambill, J.B. and Chowdhury, M.R. (2001), "Seismic Testing of a 1/20 Scale Model of Koyna Dam", Technical Report ERDC TR-01-17, U.S. Army Corps of Engineers, Engineering Research and Development Center: Washington, USA.
- Willam, K.J., and E.D. Warnke (1975), "Constitutive Model for the Triaxial Behavior of Concrete", *Proceedings of International Association for Bridge and Structural Engineering*, **19**, ISMES, Bergamo, Italy.
- Yilmazturk, S.M., Arici, Y. and Binici, B. (2015), "Seismic Assessment of a Monolithic RCC Gravity Dam including Three Dimensional Dam-Foundation-Reservoir Interaction", *Engineering Structures*, **100**, 137-148.
- Yucel, A.L. (2013), "Seismic Analysis of Concrete Gravity Dams including Dam-Foundation-Reservoir Interaction", M.S. Thesis, Middle East Technical University, Ankara, Turkey.

## APPENDIX A

### FORMULATIONS FOR SIMPLIFIED METHOD FOR DAMS

#### A.1. Separate Hydrodynamic Effects

The excitation – frequency dependent modal coordinates for the exact interaction between dam body and the compressible fluid could be determined from Eq. A.1. The terms  $M_1$ ,  $C_1$  and  $K_1$  are the generalized mass, damping and stiffness of the fundamental mode (Eq. A.1.a-d).

$$\bar{Y}_1(\omega) = \frac{-[L_1 + B_0(\omega)]}{-\omega^2\{M_1 + Re[B_1(\omega)]\} + i\omega\{C_1 - Im[B_1(\omega)]\} + K_1} \quad (A.1)$$

$$M_1 = \iint \{m_x(x, y)[\phi_{x_1}^x(x, y)]^2 + m_y(x, y)[\phi_{x_1}^y(x, y)]^2\} dx dy \quad (A.1.a)$$

$$C_1 = 2M_1\xi_1\omega_1 \quad (A.1.b)$$

$$K_1 = \omega_1^2 M_1 \quad (A.1.c)$$

$$L_1 = \iint m_x(x, y)\phi_{x_1}^x(x, y) dx dy \quad (A.1.d)$$

where  $m_x(x, y)$  and  $m_y(x, y)$  are the densities of dam material in x and y directions, respectively.  $\omega_1$  is the fundamental natural vibration frequency of the dam on rigid foundation.  $\xi_1$  is the damping ratio of the fundamental vibration mode.

The hydrodynamic terms in Eq. A.1 are defined as

$$B_j(\omega) = \int_0^H \bar{p}_j(y, \omega)\phi_{x_1}^x(0, y) dy \quad j = 0, 1 \quad (A.2)$$

where H is the depth of water,  $\bar{p}_0(y, \omega)$  and  $\bar{p}_1(y, \omega)$  are the response function for hydrodynamic pressure on the upstream face due to horizontal ground acceleration of a rigid dam and acceleration of a dam in its first fundamental mode of vibration, respectively (Eq. A.2.a).

$$\bar{p}_j(y, \omega) = 2\rho H \sum_{n=1}^{\infty} \frac{\mu_n(\omega)^2}{H[\mu_n(\omega)^2 - (\omega q)^2] + i(\omega q)} \frac{I_{jn}(\omega)}{\sqrt{\mu_n(\omega)^2 - \frac{\omega^2}{c^2}}} Y_n(y, \omega) \quad j = 0, 1 \quad (A.2.a)$$

in which  $I_{jn}(\omega) = \frac{1}{H} \int_0^H f_i(y) Y_n(y, \omega) dy \quad j = 0, 1$

In above equations,  $f_0(y) = 1$  and  $f_1(y) = \phi^x_1(0, y)$ ,  $\rho$  is the density of water,  $C$  is the velocity of pressure waves in water,  $q$  is the damping coefficient for the sediments,  $\mu_n(\omega)$  are the complex-valued and frequency dependent eigenvalues of the impounded water. The eigenvalues and eigenvectors of the impounded water are defined by Eq. A.3 and Eq. A.4, respectively.

$$e^{2i\mu_n(\omega)H} = -\frac{\mu_n(\omega) - \omega q}{\mu_n(\omega) + \omega q} \quad (\text{A.3})$$

$$Y_n(y, \omega) = \frac{1}{2\mu_n(\omega)} \{ [\mu_n(\omega) + \omega q] e^{i\mu_n(\omega)y} + [\mu_n(\omega) - \omega q] e^{-i\mu_n(\omega)y} \} \quad (\text{A.4})$$

The effect of absorption of sediments at the reservoir base can be reflected to the analytical model by two different parameters namely the damping coefficient ( $q$ ) and the wave reflection coefficient ( $\alpha$ ). They are related to each other by Eq. A.5. The wave reflection coefficient is a more physically meaningful parameter for analytical models as it is the ratio of the amplitude of the reflected hydrodynamic pressure waves to the amplitude of a vertically propagating pressure wave at the reservoir bottom.

$$\alpha = \frac{1 - qC}{1 + qC} \quad (\text{A.5})$$

where  $q = \frac{\rho}{\rho_r} * C_r = \frac{\rho}{\rho_r} * \sqrt{\frac{E_r}{\rho_r}}$  in which  $\rho_r$  and  $E_r$  are the density and the modulus of elasticity of the sediment.

The modal coordinates for frequency-independent hydrodynamic terms are given in Eq. A.6.

$$\bar{Y}_1(\omega) = \frac{-\tilde{L}_1}{-\omega^2 \tilde{M}_1 + i\omega \tilde{C}_1 + K_1} \quad (\text{A.6})$$

where  $\tilde{C}_1$ ,  $\tilde{L}_1$ , and  $\tilde{M}_1$  are defined as follows:

$$\tilde{M}_1 = M_1 + Re \left\{ \int_0^H m_a(y) [\phi^x_1(0, y)]^2 dy \right\} = M_1 + Re\{B_1(\bar{\omega}_r)\} \quad (\text{A.6.a})$$

$$\tilde{C}_1 = C_1 - \omega Im \left\{ \int_0^H m_a(y) [\phi^x_1(0, y)]^2 dy \right\} = C_1 - \bar{\omega}_r Im\{B_1(\bar{\omega}_r)\} \quad (\text{A.6.b})$$

$$\tilde{L}_1 = L_1 + \int_0^H m_a(y) [\phi^x_1(0, y)]^2 dy = L_1 + B_0(\bar{\omega}_r) \quad (\text{A.6.c})$$

where  $m_a(y)$  is the added mass due to the hydrodynamic effects calculated from  $m_a(y) = \frac{\bar{p}_1(y, \bar{\omega}_r)}{\phi^{x_1}(0, y)}$ .  $m_a(y)$  is complex-valued mass for absorptive reservoir bottom. Its real part is the added mass and its complex part contributes to the damping.

The decreased natural vibration frequency of the equivalent SDFS,  $\bar{\omega}_r$ , can be calculated by Eq. A.7.

$$\bar{\omega}_r = \frac{\omega_1}{\sqrt{1 + \frac{Re[B_1(\bar{\omega}_r)]}{M_1}}} \quad (A.7)$$

where  $\omega_1$  is the fundamental natural vibration frequency of dam on rigid foundation rock with empty reservoir.

The increased damping of the equivalent SDFS,  $\bar{\xi}_r$ , can be calculated by Eq. A.8.

$$\bar{\xi}_r = \frac{\bar{\omega}_r}{\omega_1} \xi_1 + \xi_r \quad (A.8)$$

where  $\xi_r$  is the added damping due to both reservoir interaction and reservoir bottom absorption and it is defined as Eq. A.8.a.  $\xi_1$  is the viscous damping of dam without water in its fundamental vibration frequency.

$$\xi_r = -\frac{1}{2} \frac{1}{M_1} \left( \frac{\bar{\omega}_r}{\omega_1} \right)^2 Im\{B_1(\bar{\omega}_r)\} \quad (A.8.a)$$

## A.2. Separate Foundation Flexibility Effects

The inclusion of foundation flexibility during the time history analysis requires the determination of complete equation of motion consisting of the horizontal translation ( $u_o(t)$ ) and rotation ( $\theta(t)$ ) at the dam base and the overturning moment ( $M(t)$ ) and base shear ( $V(t)$ ) stemmed from the foundation flexibility (Eq. A.9.a-c).

$$M_1 \ddot{Y}_1(t) + C_1 \dot{Y}_1(t) + K_1 Y_1(t) + L_1 \ddot{u}_o(t) + L_1^\theta \ddot{\theta}(t) = -L_1 a_g(t) \quad (A.9.a)$$

$$L_1 \ddot{Y}_1(t) + m_t \ddot{u}_o(t) + K_1 Y_1(t) + L_\theta^x \ddot{\theta}(t) + V(t) = -m_t a_g(t) \quad (A.9.b)$$

$$L_1^\theta \ddot{Y}_1(t) + L_\theta^x \ddot{u}_o(t) + I_t \ddot{\theta}(t) + M(t) = -L_\theta^x a_g(t) \quad (A.9.c)$$

where  $m_t$  is the total mass of the dam monolith,  $I_t$  is the mass moment of inertia of the dam monolith about the centroid of its base given by Eq. A.9.d.

$$I_t = \iint \left\{ m_x(x, y) y^2 + m_y(x, y) \left( \frac{b}{2} - x \right)^2 \right\} dx dy \quad (\text{A.9.d})$$

where  $b$  is the width of the base,  $m$  is the density,  $L_1^\theta$  and  $L_\theta^x$  are given in Eq. A.9.e and Eq. A.9.f, respectively.

$$L_1^\theta = \iint \left\{ m_x(x, y) y \phi_1^x(x, y) + m_y(x, y) \left( \frac{b}{2} - x \right) \phi_1^x(x, y) \right\} dx dy \quad (\text{A.9.e})$$

$$L_\theta^x = \iint m_x(x, y) y dx dy \quad (\text{A.9.f})$$

The base displacement and rotation are related to the base shear and overturning moment demands by the frequency dependent complex stiffness matrix given in Eq. A.10.

$$\begin{bmatrix} K_{VV}(\omega) & K_{VM}(\omega) \\ K_{MV}(\omega) & K_{MM}(\omega) \end{bmatrix} * \begin{bmatrix} \bar{u}_o(\omega) \\ \bar{\theta}(\omega)b \end{bmatrix} = \begin{bmatrix} \bar{V}(\omega) \\ \frac{\bar{M}(\omega)}{b} \end{bmatrix} \quad (\text{A.10})$$

In Eq. 2.10, the coupling impedances are equal to each other and all of the variables are obtained by using Fourier transformation, i.e.  $u_o(t) = \bar{u}_o(\omega)e^{i\omega t}$ . Dasgupta and Chopra (1979) suggest a method to evaluate the compliance functions at uniformly spaced nodal points on the flexible foundation, which is assumed to be homogeneous, isotropic and viscoelastic half-plane. After that, these compliance functions are inverted to obtain the dynamic stiffness matrix of uniformly distributed nodal points on the foundation. The dynamic stiffness matrix given in Eq. A.10 is calculated from this dynamic stiffness matrix by utilizing constraint matrix for the rigid dam base. The details of this procedure can be found in Dasgupta and Chopra (1979).

The analytical solution for the modal coordinate under the effect of a harmonic ground acceleration, i.e.  $a_g(t) = e^{i\omega t}$  can be obtained by Eq. A.11. In obtaining Eq. A.11, the mass related terms ( $m_t$ ,  $L_\theta^x$  and  $I_t$ ) are assumed to be first mode dominant. With this assumption, the modal coordinates, complicated by the higher mode contributions to  $m_t$ ,  $L_\theta^x$  and  $I_t$ , can be calculated. The validation of these assumptions can be found in Fenves and Chopra (1985.a).

$$Y_1(\omega) = \frac{-L_1}{-\omega^2 M_1 + i\omega C_1 + K_1 - \omega^2 M_1 \left(1 + \frac{i2\xi_1 \omega}{\omega_1}\right) F(\omega)} \quad (\text{A.11})$$

$$\text{where } (\omega) = \frac{\frac{K_{VV}(\omega)}{m_1^* \omega_1^2} + \frac{K_{MM}(\omega)}{m_1^* \omega_1^2} \left(\frac{b}{h_1^*}\right)^2 - 2 \frac{K_{VM}(\omega)}{m_1^* \omega_1^2} \left(\frac{b}{h_1^*}\right)}{\frac{K_{VV}(\omega)}{m_1^* \omega_1^2} \frac{K_{MM}(\omega)}{m_1^* \omega_1^2} \left(\frac{b}{h_1^*}\right)^2 - \left[\frac{K_{VM}(\omega)}{m_1^* \omega_1^2} \left(\frac{b}{h_1^*}\right)\right]^2}, m_1^* = \frac{L_1^2}{M_1} \text{ and } h_1^* = \frac{L_1 \theta}{L_1}.$$

The complex-valued term  $F(\omega)$  is purely related to the foundation-dam interaction. It decreases the effective stiffness of the dam and its complex part also changes the damping properties of the system. Physically, these effects make sense as the deformations in the flexible base dam will be greater than its rigid based counterpart due to the foundation flexibility. And, the effective damping should also be different from the rigid base case because of the material damping at the intersection between the dam and foundation region and because of the radiation.

In all of the above equations, the coupling terms in the impedance matrix are included although there is a consensus on neglecting those terms for high-rise buildings. Fenves and Chopra (1985.a) show that the inclusion of these coupling terms in the analyses decreases the demands owing to the additional radiation damping (Figure A.1).

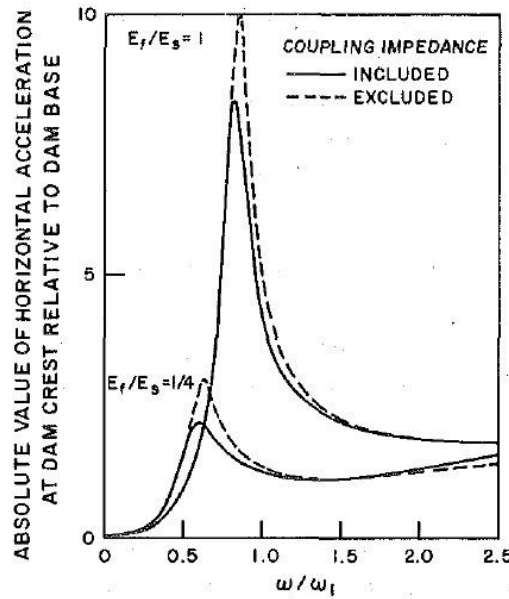


**Figure A.1.** Effect of Coupling Impedance on Response of Dams on Flexible Foundation Due to Harmonic Ground Excitation (Fenves and Chopra 1985.a)

The properties of SDFS are calculated by modifying the properties of an empty and rigid based dam-reservoir-foundation system. Therefore, the modal coordinate for the equivalent SDFS becomes

$$\bar{Y}_1(\omega) = \left(\frac{\bar{\omega}_f}{\omega_1}\right)^2 \frac{-L_1}{-\omega^2 M_1 + i\omega\{2\bar{\xi}_f M_1 \bar{\omega}_f\} + \bar{\omega}_f^2 M_1} \quad (\text{A.12})$$

The decreased natural vibration frequency of the equivalent SDFS,  $\bar{\omega}_f$ , can be calculated by Eq. A.13.

$$\bar{\omega}_f = \frac{\omega_1}{\sqrt{1 + Re[F(\bar{\omega}_f)]}} \quad (\text{A.13})$$

where  $\omega_1$  is the fundamental natural vibration frequency of dam on rigid foundation rock with empty reservoir and rigid base.

If the maximum response of the equivalent SDFS (Eq. A.12) is equated to the exact solution obtained at the natural vibration frequency of the equivalent SDFS,  $\bar{\omega}_f$ , (Eq. A.13), the damping ratio of the equivalent SDFS,  $\bar{\xi}_f$ , can be calculated (Eq. A.14).

$$\bar{\xi}_f = \left(\frac{\bar{\omega}_f}{\omega_1}\right)^3 \xi_1 + \xi_f \quad (\text{A.14})$$

where  $\xi_f$  is the added damping due to foundation flexibility and it is defined as Eq. A.14.a.  $\xi_1$  is the viscous damping of dam body material without water in its fundamental vibration frequency.

$$\xi_f = -\frac{1}{2} \frac{1}{M_1} \left(\frac{\bar{\omega}_f}{\omega_1}\right)^2 Im\{F(\bar{\omega}_f)\} \quad (\text{A.14.a})$$

### A.3. Combined Hydrodynamic and Foundation Flexibility Effects

Fenves and Chopra (1985.b) combine their findings for separate actions of reservoir-dam and foundation-dam interactions and present the frequency response function for the modal coordinate as follows:



$$Y_1(\omega) = \frac{-[L_1 + B_o(\omega)]}{-\omega^2\{M_1 + Re[B_1(\omega)]\} + i\omega\{C_1 - Im[B_1(\omega)]\} + K_1 - \omega^2 M_1 \left(1 + \frac{i2\xi_1\omega}{\omega_1}\right)} [F(\omega) + F_r(\omega)] \quad (A.15)$$

$$F_r(\omega) = \frac{\frac{B_{00}(\omega)K_{VV}(\omega)}{m^*_{\omega_1} m^*_{\omega_1}\omega_1^2} + \frac{B_{0\theta}(\omega)K_{MM}(\omega)}{m^*_{\omega_1} h^*_{\omega_1} m^*_{\omega_1}\omega_1^2} \left(\frac{b}{h^*_{\omega_1}}\right)^2 - 2\frac{B_{00}(\omega)K_{VM}(\omega)}{m^*_{\omega_1} h^*_{\omega_1} m^*_{\omega_1}\omega_1^2} \left(\frac{b}{h^*_{\omega_1}}\right)}{\frac{K_{VV}(\omega)K_{MM}(\omega)}{m^*_{\omega_1}\omega_1^2 m^*_{\omega_1}\omega_1^2} \left(\frac{b}{h^*_{\omega_1}}\right)^2 - \left[\frac{K_{VM}(\omega)}{m^*_{\omega_1}\omega_1^2} \left(\frac{b}{h^*_{\omega_1}}\right)\right]^2} \quad (A.15.a)$$

$$B_{00}(\omega) = \int_0^H \bar{p}_0(y, \omega) dy \quad (A.15.b)$$

$$B_{0\theta}(\omega) = \int_0^H y \bar{p}_0(y, \omega) dy \quad (A.15.c)$$

$$B_{\theta\theta}(\omega) = \int_0^H y \bar{p}_0^\theta(y, \omega) dy \quad (A.15.d)$$

$$\bar{p}_0^\theta(y, \omega) = 2\rho H \sum_{n=1}^{\infty} \frac{\mu_n(\omega)^2}{H[\mu_n(\omega)^2 - (\omega q)^2] + i(\omega q)} \frac{I_{\theta n}(\omega)}{\sqrt{\mu_n(\omega)^2 - \frac{\omega^2}{c^2}}} Y_n(y, \omega) \quad (A.15.e)$$

$$I_{\theta n}(\omega) = \frac{1}{H} \int_0^H y Y_n(y, \omega) dy \quad (A.15.f)$$

For an empty reservoir case ( $F_r(\omega) = 0$ ,  $B_o(\omega) = 0$  and  $B_1(\omega) = 0$ ), Eq. A.15 reduces to Eq. A.12. Or, if the foundation has a high rigidity ( $E_f = \infty$ ,  $F(\omega) = 0$  and  $F_r(\omega) = 0$ ), Eq. A.15 becomes equal to Eq. A.1. Note that the water-foundation coupling term,  $F_r(\omega)$ , exists only when reservoir-foundation-dam interaction is considered simultaneously.

Then, an equivalent SDFS lying on a rigid foundation is also formed instead of the real system dealing with the foundation-reservoir-dam interaction simultaneously, just like the previous separate interaction examples. Consequently, the properties of the equivalent SDFS can be obtained from

$$\bar{\omega}_1 = \omega_1 \frac{1}{\sqrt{1 + \frac{Re[B_1(\bar{\omega}_1)]}{M_1}}} \left( \frac{1}{\sqrt{1 + Re[F(\bar{\omega}_1)]}} \right) \quad (A.16)$$

As Eq. A.16 is an implicit equation, the frequency of the equivalent system is only calculated by carrying out an iterative procedure. However, one more simplification is also possible by keeping in mind that the first term in Eq. A.16 is purely related to the added hydrodynamic mass and the second term stems from the foundation interaction. Therefore, it is wise to calculate those terms at their corresponding frequencies like  $Re[B_1(\bar{\omega}_1)] \cong Re[B_1(\bar{\omega}_r)]$  and  $Re[F_1(\bar{\omega}_1)] \cong Re[F_1(\bar{\omega}_f)]$  (Eq. A.17).

$$\bar{\omega}_1 = \omega_1 \frac{1}{\sqrt{1 + \frac{Re[B_1(\bar{\omega}_r)]}{M_1}}} \left( \frac{1}{\sqrt{1 + Re[F(\bar{\omega}_f)]}} \right) \quad (A.17)$$

Eq. A.17 can also be reduced to Eq. A.18 by utilizing Eq. A.7 and Eq. A.13.

$$\bar{\omega}_1 = \left( \frac{\bar{\omega}_r}{\omega_1} \right) \left( \frac{\bar{\omega}_f}{\omega_1} \right) \omega_1 \quad (A.18)$$

Therefore, the equivalent SDFS' fundamental frequency can be found by factoring the fundamental natural vibration frequency of a dam on rigid foundation rock with empty reservoir condition. This factorization, generally, causes a reduction in the fundamental vibration frequency.

Before calculating the damping term for the equivalent SDFS, the equation for modal coordinates should be derived. This is because; the damping is obtained by equating the equivalent systems response (Eq. A.19) to the exact response (Eq. A.15) at the equivalent systems fundamental frequency, i.e.  $\bar{Y}(\bar{\omega}_1) = Y(\bar{\omega}_1)$  (Eq. A.20).

$$\bar{Y}_1(\omega) = \left( \frac{\bar{\omega}_f}{\omega_1} \right)^2 \frac{-\bar{L}_1}{-\omega^2 \bar{M}_1 + i\omega\{2\bar{\xi} \bar{M}_1 \bar{\omega}_1\} + \bar{\omega}_1^2 \bar{M}_1} \quad (A.19)$$

where  $\bar{M}_1 = M_1 + Re\{B_1(\bar{\omega}_r)\}$  and  $\bar{L}_1 = L_1 + B_0(\bar{\omega}_1)$ .

The increased damping of the equivalent SDFS,  $\bar{\xi}$ , can be calculated by Eq. A.20.

$$\bar{\xi} = \left( \frac{\bar{\omega}_r}{\omega_1} \right) \left( \frac{\bar{\omega}_f}{\omega_1} \right)^3 \xi_1 + \frac{1}{\left( \frac{\bar{\omega}_f}{\omega_1} \right)^2} \xi_r(\bar{\omega}_1) + \frac{1}{\left( \frac{\bar{\omega}_r}{\omega_1} \right)^2} \xi_f(\bar{\omega}_1) \quad (A.20)$$

where the additional damping due to dam-reservoir ( $\xi_r(\bar{\omega}_1)$ ) and dam-foundation ( $\xi_f(\bar{\omega}_1)$ ) interactions are defined by

$$\xi_r(\bar{\omega}_1) = -\frac{1}{2} \frac{1}{M_1} \left( \frac{\bar{\omega}_1}{\omega_1} \right)^2 Im\{B_1(\bar{\omega}_1)\} \quad (A.20.a)$$

$$\xi_f(\bar{\omega}_1) = -\frac{1}{2} \left( \frac{\bar{\omega}_1}{\omega_1} \right)^2 Im\{F(\bar{\omega}_1)\} \quad (A.20.b)$$

Fenves and Chopra (1985.b) determine the independent variables for both  $\xi_r(\bar{\omega}_1)$  and  $\xi_f(\bar{\omega}_1)$  and conclude that  $\xi_r(\bar{\omega}_1)$  is sensitive to  $E_f/E_s$  ratio (Figure A.2.a) and

$\xi_f(\bar{\omega}_1)$  depends on  $H/H_s$  and wave reflection coefficient ( $\alpha$ ) (Figure A.2.b). The computation of these damping ratios for different conditions in a simplified procedure is inconvenient. Consequently, Fenves and Chopra (1985.a) simplify the damping ratio contributions of reservoir and foundation interactions given by Eq. A.21.a-b. Thus, Eq. A.20 becomes Eq. A.22.

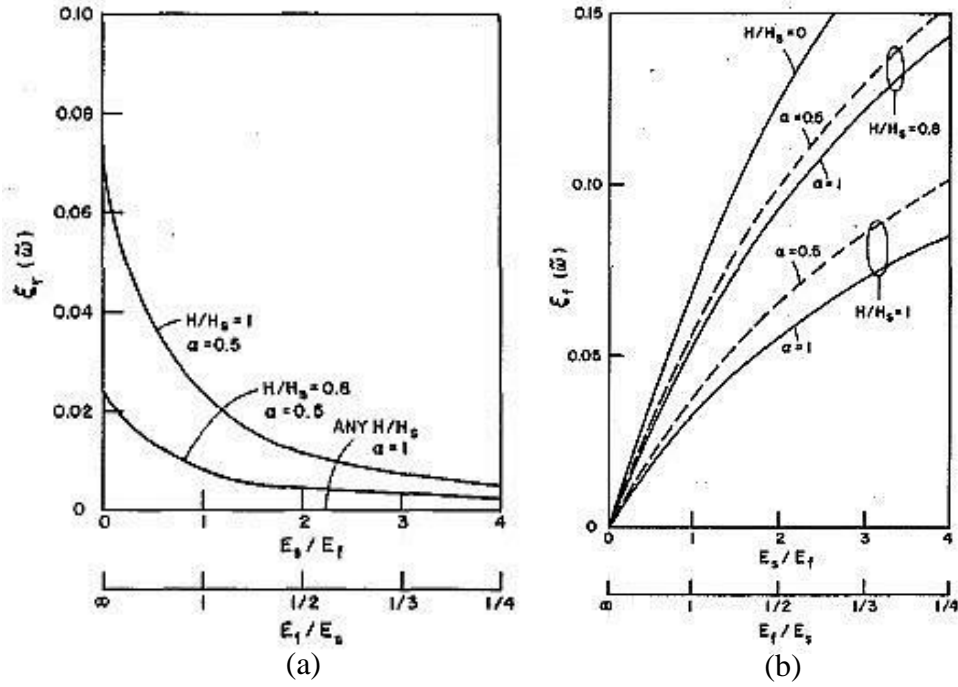


**Figure A.2.** Additional Damping for  $E_s=27,500$  MPa and  $\eta_f=0.10$  due to (a) Dam-Reservoir ( $\xi_r(\bar{\omega}_1)$ ) and (b) Dam-Foundation ( $\xi_f(\bar{\omega}_1)$ ) Interactions [Fenves and Chopra 1985.b]

$$\xi_r(\bar{\omega}_1) \cong \left(\frac{\bar{\omega}_f}{\omega_1}\right)^2 \xi_r \quad (\text{A.21.a})$$

$$\xi_f(\bar{\omega}_1) \cong \left(\frac{\bar{\omega}_r}{\omega_1}\right)^2 \xi_f \quad (\text{A.21.b})$$

where  $\xi_r = -\frac{1}{2} \frac{1}{M_1} \left(\frac{\bar{\omega}_r}{\omega_1}\right)^2 \text{Im}\{B_1(\bar{\omega}_r)\}$  and  $\xi_f = -\frac{1}{2} \left(\frac{\bar{\omega}_f}{\omega_1}\right)^2 \text{Im}\{F(\bar{\omega}_f)\}$

$$\bar{\xi} = \left(\frac{\bar{\omega}_r}{\omega_1}\right) \left(\frac{\bar{\omega}_f}{\omega_1}\right)^3 \xi_1 + \xi_r + \xi_f \quad (\text{A.22})$$

The simplified damping ratio causes overestimates the response quantities for non-absorptive reservoir bottom ( $\alpha=1$ ) whereas it underestimates the response for absorptive reservoir bottom ( $\alpha=0.5$ ) (Figure A.3).

Fenves and Chopra (1985.b) test the equivalent SDFS' performance by comparing the horizontal acceleration estimations of the exact and equivalent system (Figure A.4).

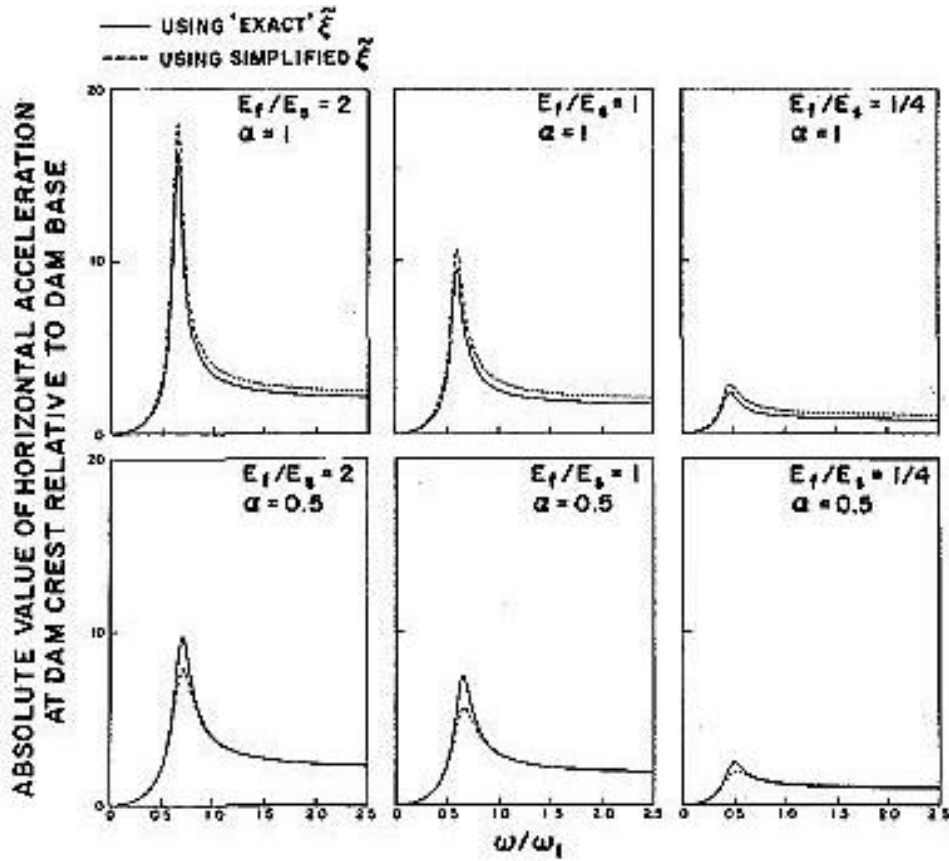


**Figure A.3.** Comparison of Equivalent SDFS Response due to Harmonic Horizontal Ground Motions using Exact Damping and Simplified Damping [Fenves and Chopra 1985.b]

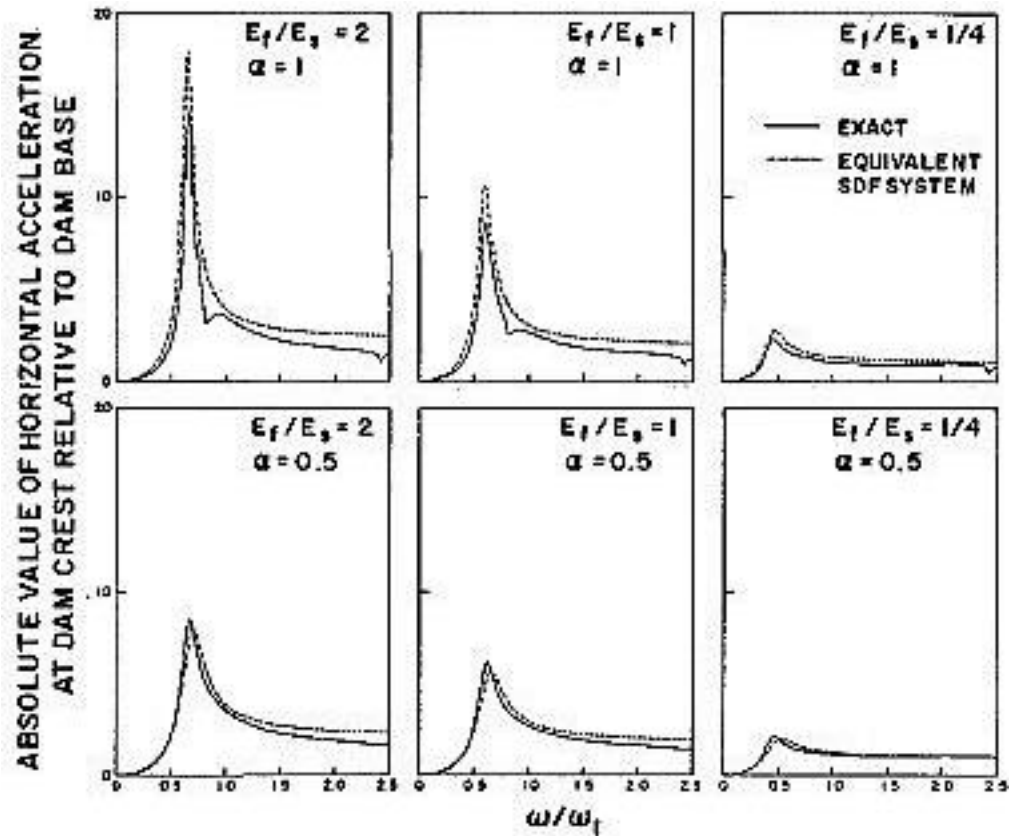


**Figure A.4.** Comparison of Horizontal Acceleration Responses of Equivalent SDFS and Exact System due to Harmonic Horizontal Ground Motions [Fenves and Chopra 1985.b]

Therefore, the foundation-reservoir-dam interaction could be taken into account by simplifying the complex-valued and frequency-dependent hydrodynamic and foundation flexibilities to real-valued and frequency-independent values (Fenves and Chopra 1985.a and 1985.b). The comparison of results obtained both from exact and the equivalent systems are very promising.



## APPENDIX B

### DEMAND HISTORIES FOR CVC SPECIMEN

#### B.1. OBE Motion

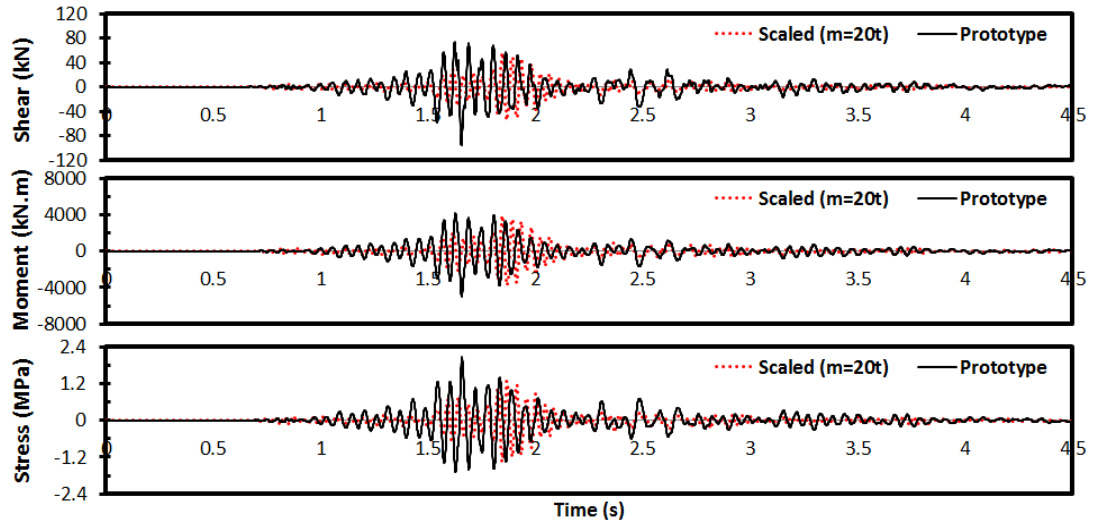


**Figure B.1.** Comparison of the Analysis Results for OBE Motion with Numerical Mass of 20t : (a) Base Shear, (b) Overturning Moment and (c) Vertical Stress at Toe

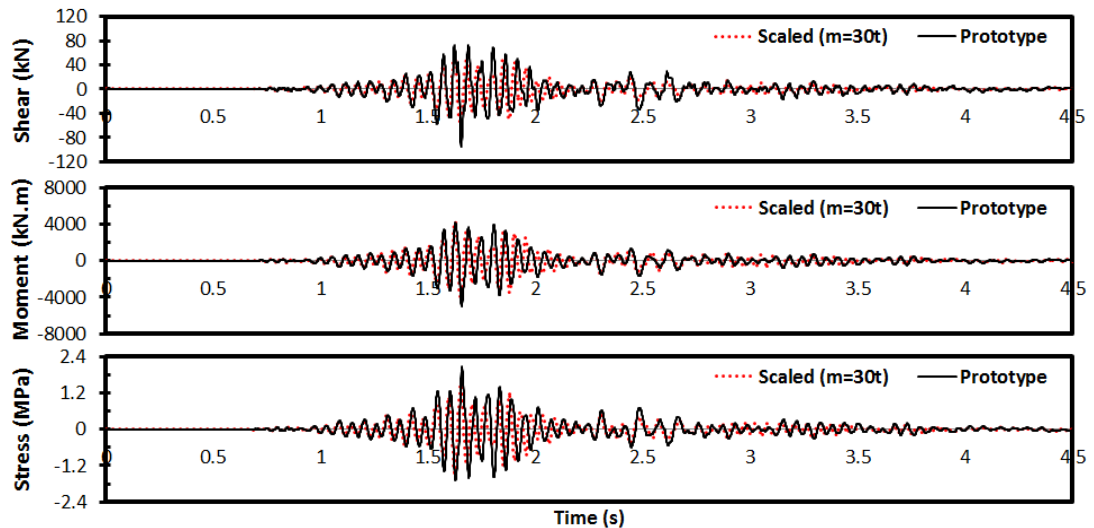


**Figure B.2.** Comparison of the Analysis Results for OBE Motion with Numerical Mass of 30t : (a) Base Shear, (b) Overturning Moment and (c) Vertical Stress at Toe

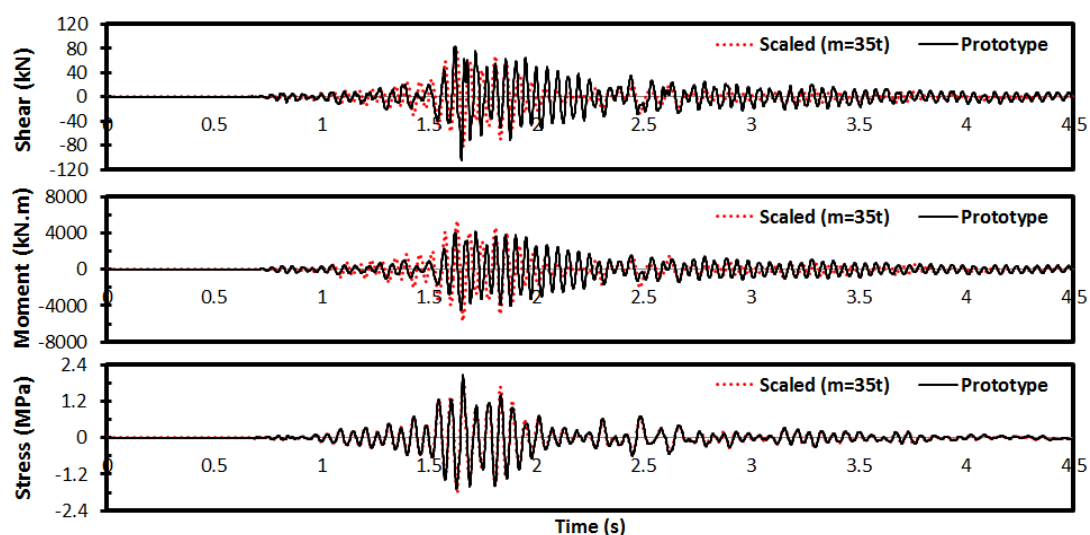


**Figure B.3.** Comparison of the Analysis Results for OBE Motion with Numerical Mass of 35t : (a) Base Shear, (b) Overturning Moment and (c) Vertical Stress at Toe

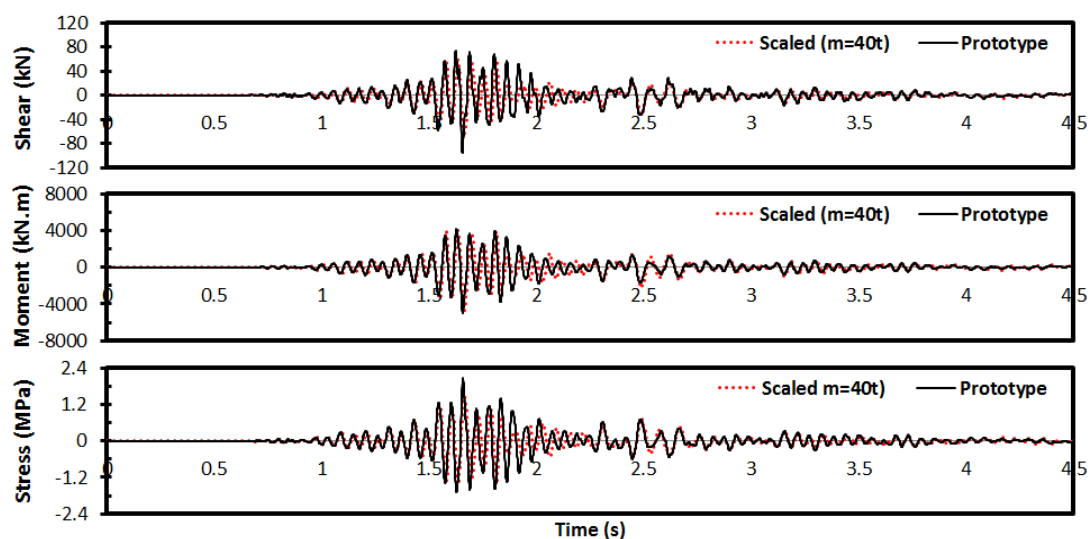


**Figure B.4.** Comparison of the Analysis Results for OBE Motion with Numerical Mass of 40t : (a) Base Shear, (b) Overturning Moment and (c) Vertical Stress at Toe



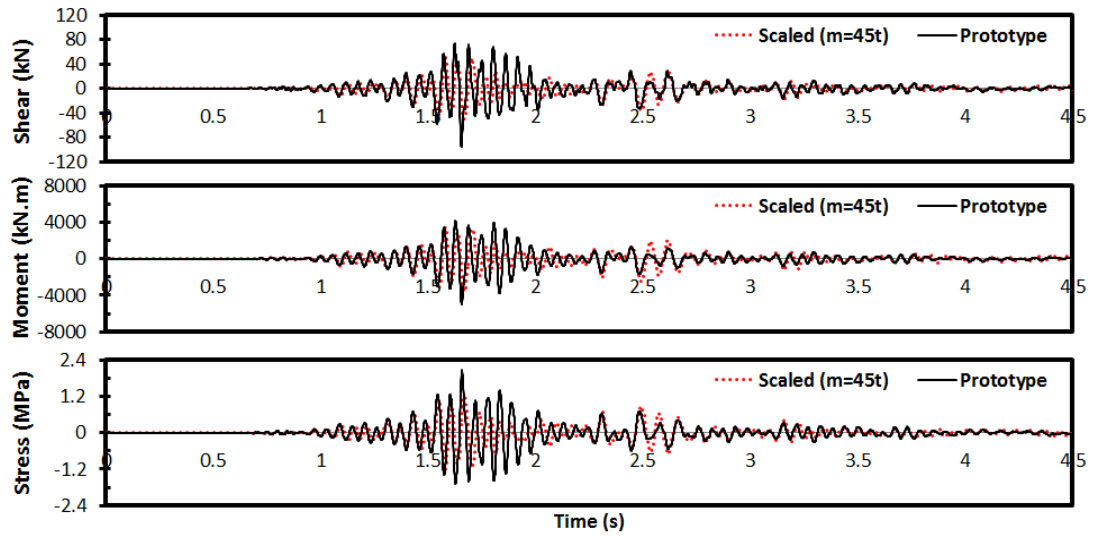


**Figure B.5.** Comparison of the Analysis Results for OBE Motion with Numerical Mass of 45t : (a) Base Shear, (b) Overturning Moment and (c) Vertical Stress at Toe

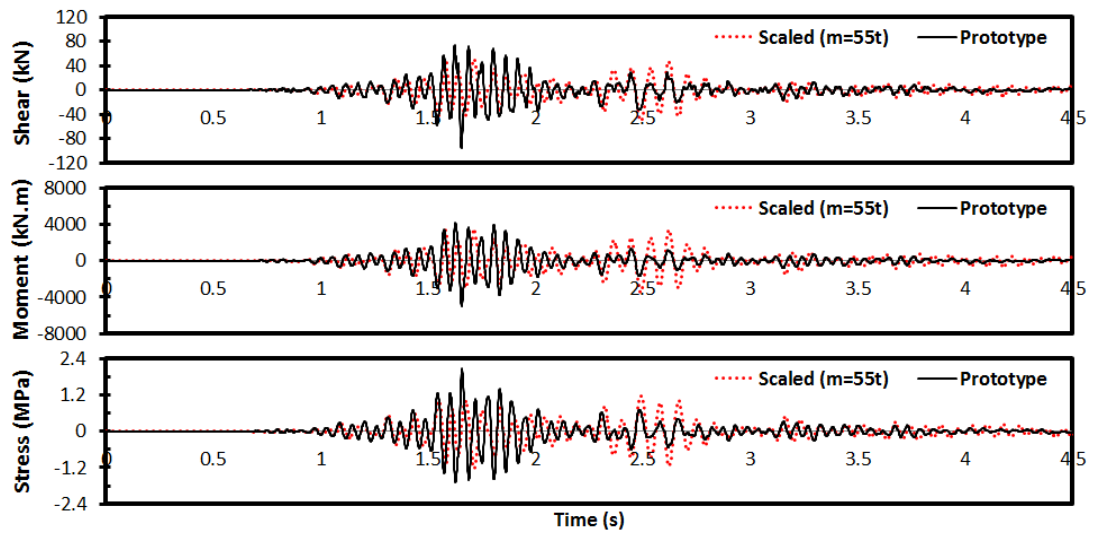


**Figure B.6.** Comparison of the Analysis Results for OBE Motion with Numerical Mass of 55t : (a) Base Shear, (b) Overturning Moment and (c) Vertical Stress at Toe

## B.2. MDE Motion

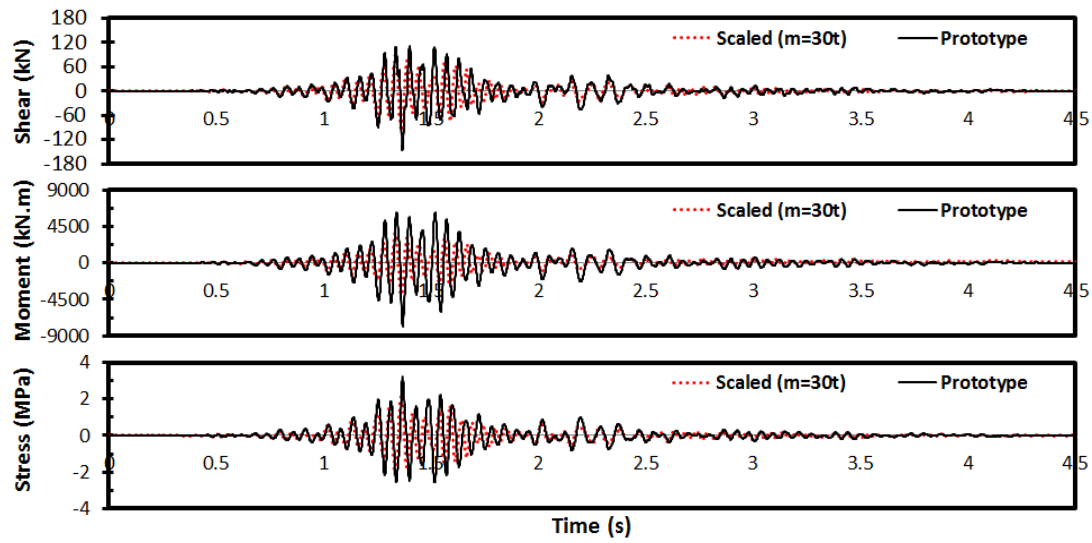


**Figure B.7.** Comparison of the Analysis Results for MDE Motion with Numerical Mass of 30t : (a) Base Shear, (b) Overturning Moment and (c) Vertical Stress at Toe

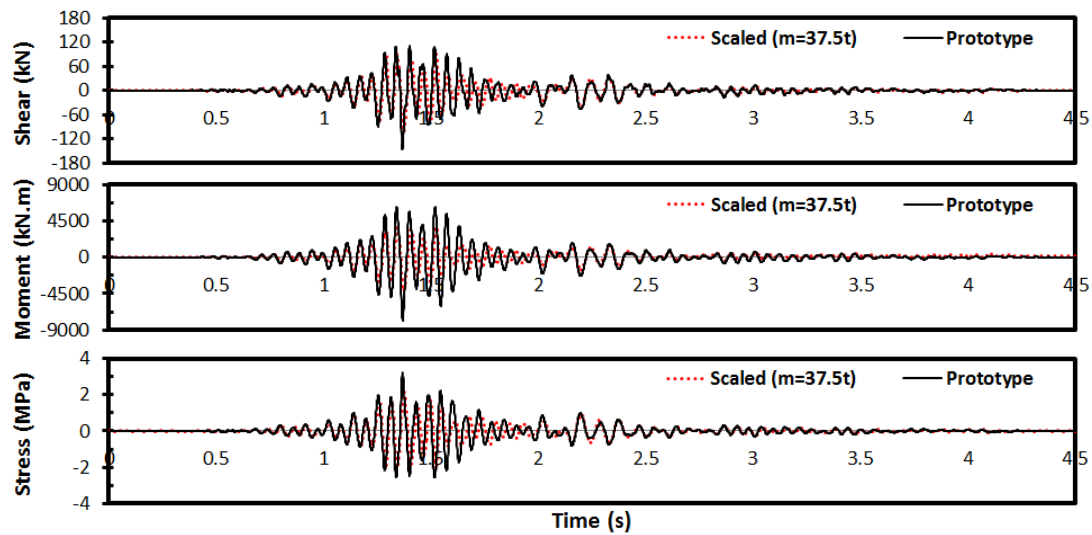


**Figure B.8.** Comparison of the Analysis Results for MDE Motion with Numerical Mass of 37.5t : (a) Base Shear, (b) Overturning Moment and (c) Vertical Stress at Toe

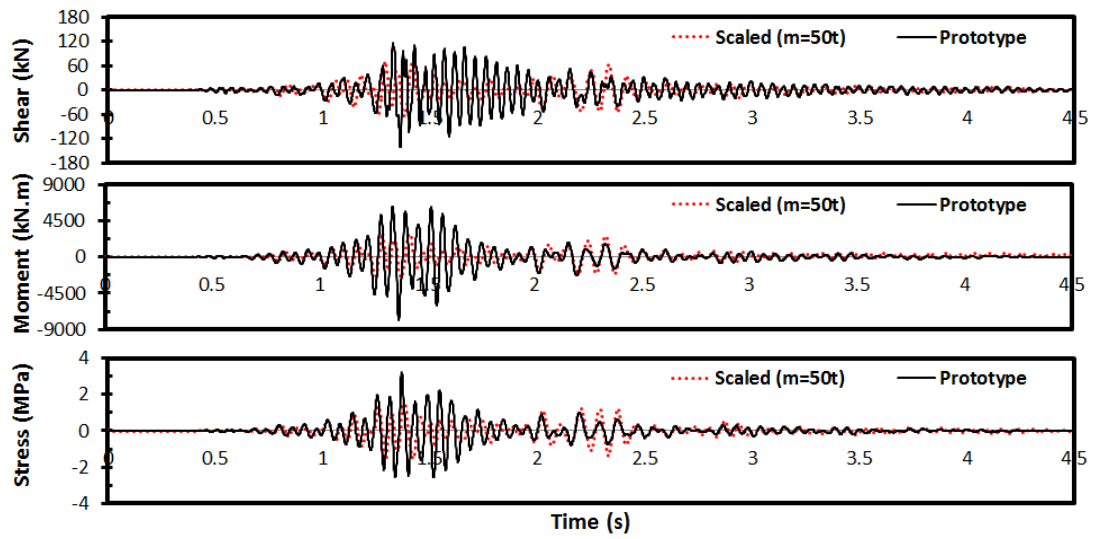


**Figure B.9.** Comparison of the Analysis Results for MDE Motion with Numerical Mass of 50t : (a) Base Shear, (b) Overturning Moment and (c) Vertical Stress at Toe

### B.3. MCE Motion

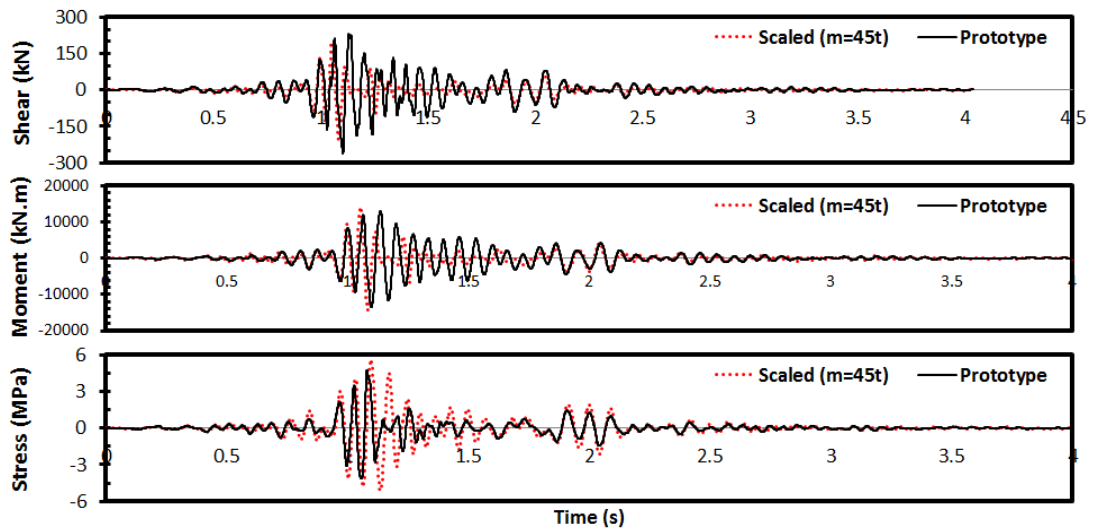


**Figure B.10.** Comparison of the Analysis Results for MDE Motion with Numerical Mass of 45t : (a) Base Shear, (b) Overturning Moment and (c) Vertical Stress at Toe

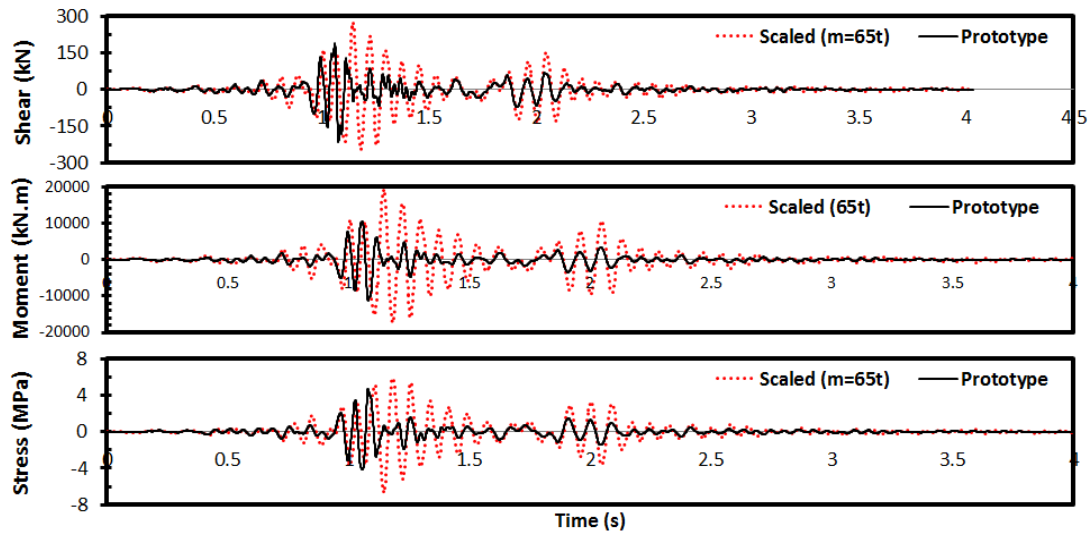


**Figure B.11.** Comparison of the Analysis Results for MCE Motion with Numerical Mass of 65t : (a) Base Shear, (b) Overturning Moment and (c) Vertical Stress at Toe

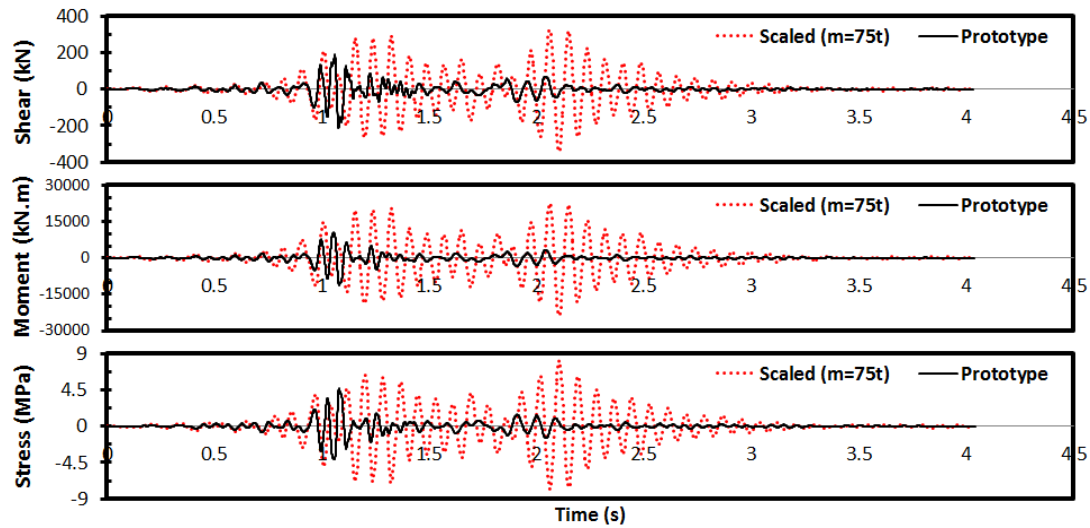


**Figure B.12.** Comparison of the Analysis Results for MCE Motion with Numerical Mass of 75t : (a) Base Shear, (b) Overturning Moment and (c) Vertical Stress at Toe

## APPENDIX C

### DEMAND HISTORIES FOR RCC SPECIMEN

#### C.1. OBE Motion

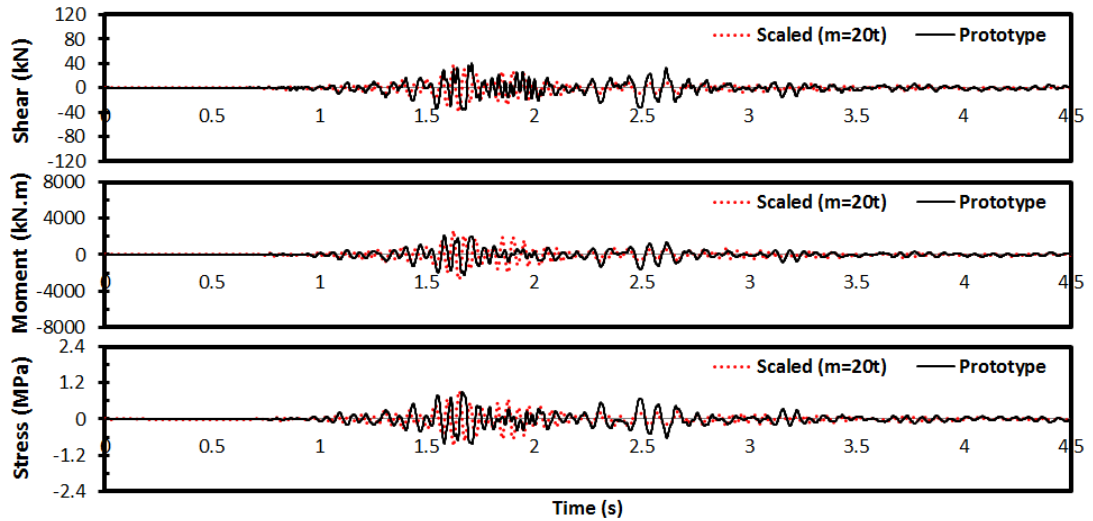


**Figure C.1.** Comparison of the Analysis Results for OBE Motion with Numerical Mass of 20t : (a) Base Shear, (b) Overturning Moment and (c) Vertical Stress at Toe

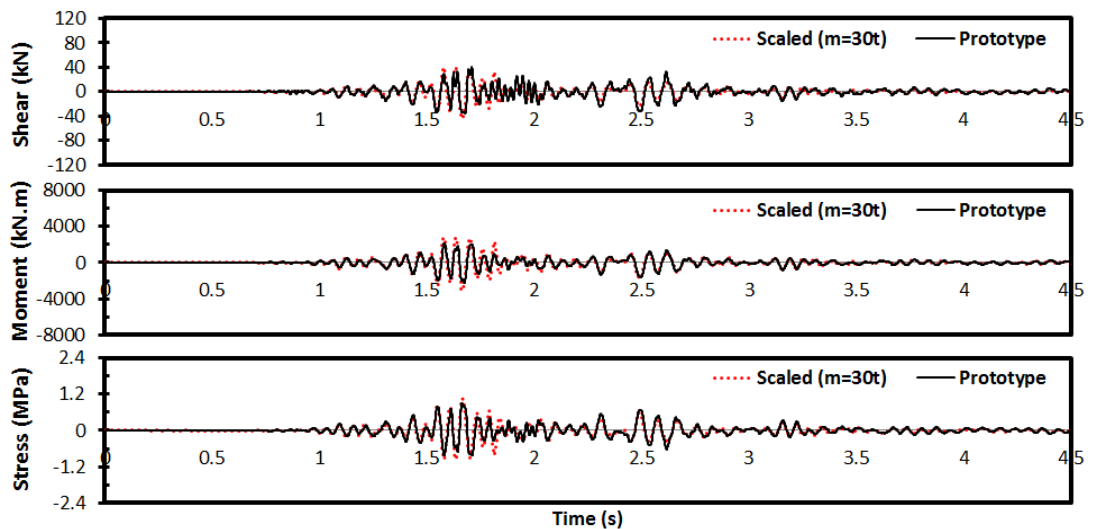


**Figure C.2.** Comparison of the Analysis Results for OBE Motion with Numerical Mass of 30t : (a) Base Shear, (b) Overturning Moment and (c) Vertical Stress at Toe

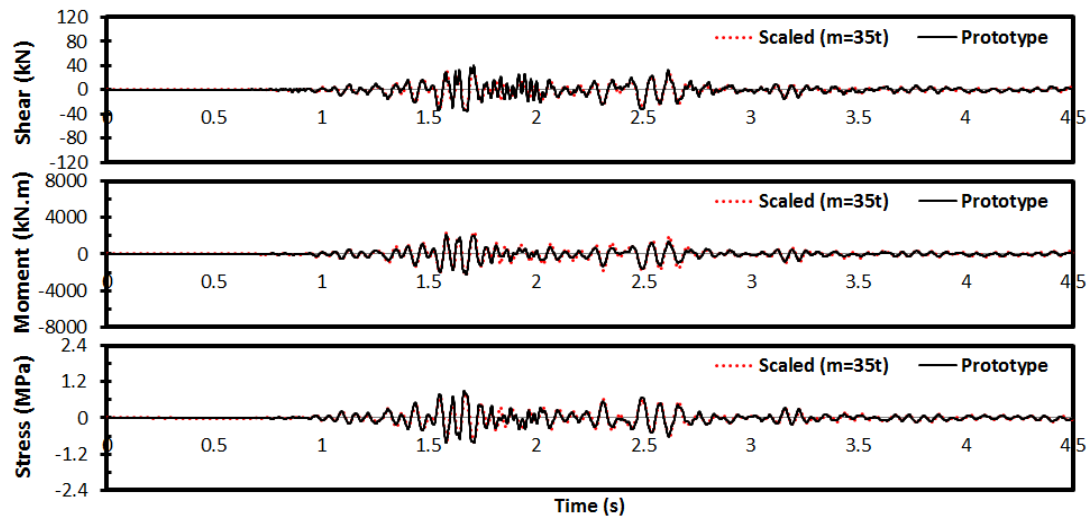


**Figure C.3.** Comparison of the Analysis Results for OBE Motion with Numerical Mass of 35t : (a) Base Shear, (b) Overturning Moment and (c) Vertical Stress at Toe

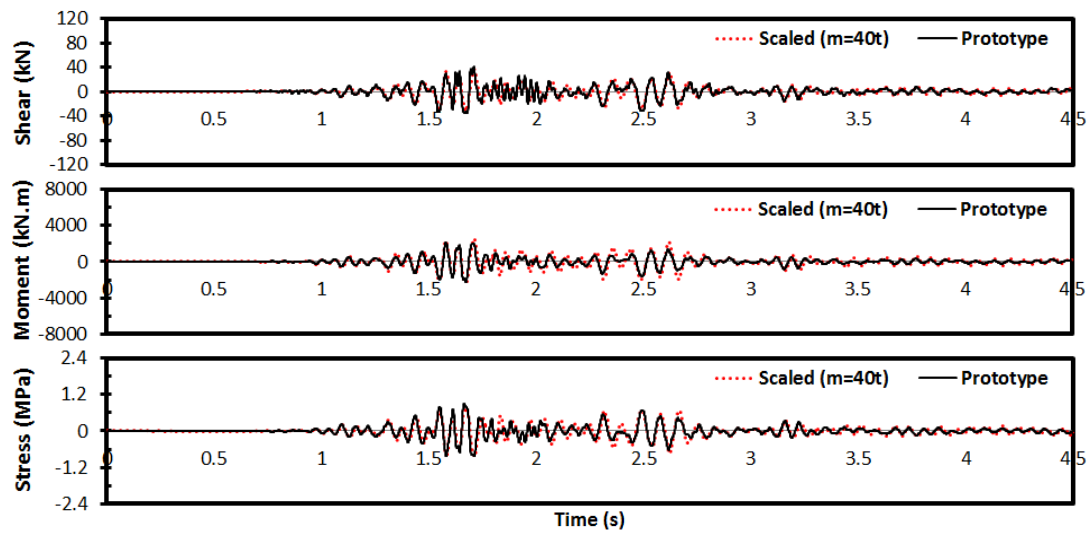


**Figure C.4.** Comparison of the Analysis Results for OBE Motion with Numerical Mass of 40t : (a) Base Shear, (b) Overturning Moment and (c) Vertical Stress at Toe

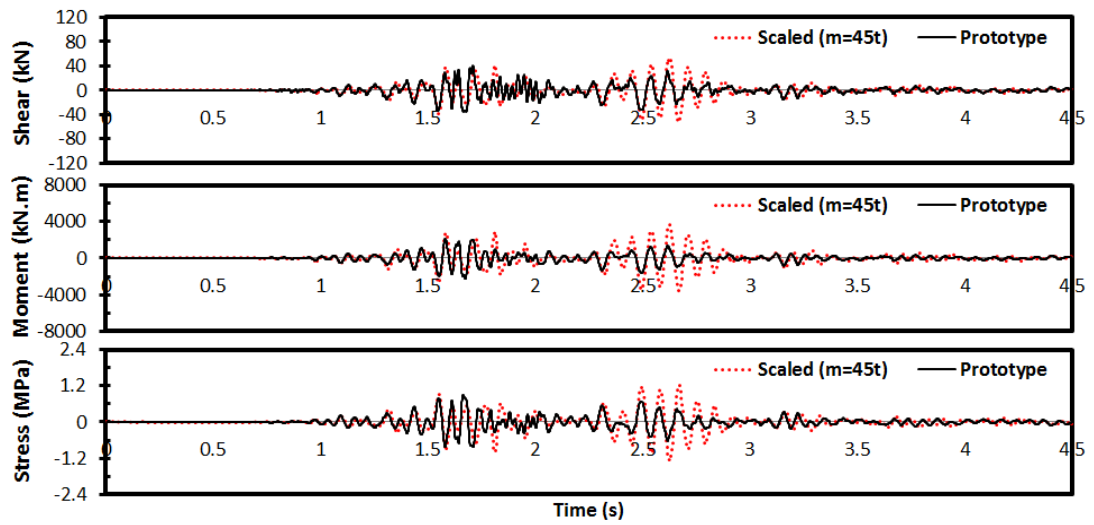


**Figure C.5.** Comparison of the Analysis Results for OBE Motion with Numerical Mass of 45t : (a) Base Shear, (b) Overturning Moment and (c) Vertical Stress at Toe

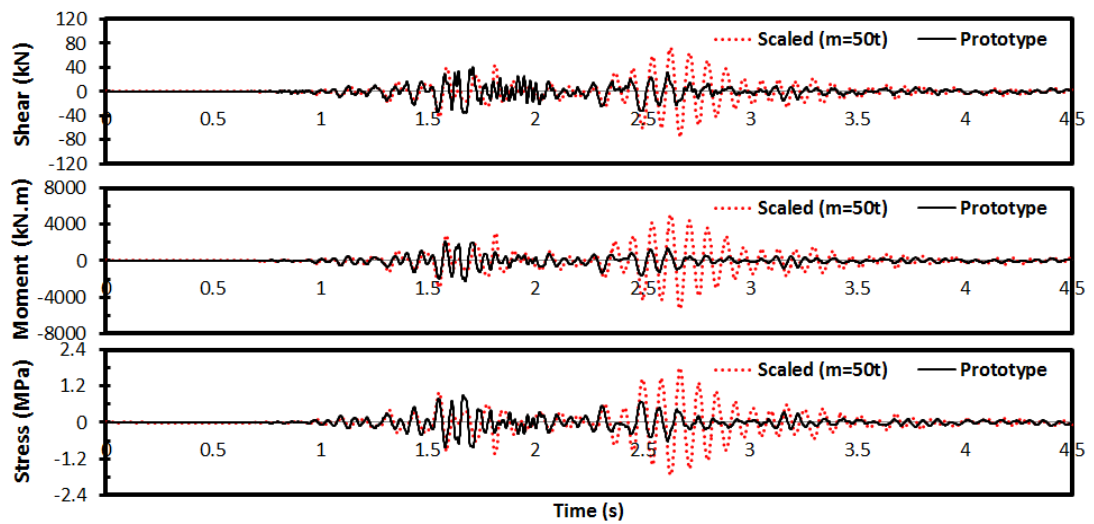


**Figure C.6.** Comparison of the Analysis Results for OBE Motion with Numerical Mass of 50t : (a) Base Shear, (b) Overturning Moment and (c) Vertical Stress at Toe

## C.2. MDE Motion

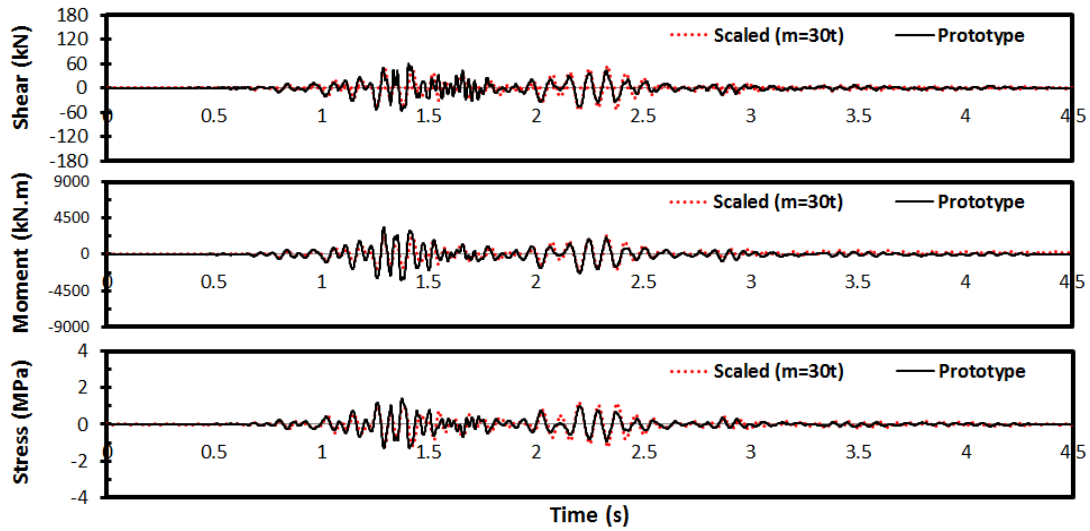


**Figure C.7.** Comparison of the Analysis Results for MDE Motion with Numerical Mass of 30t : (a) Base Shear, (b) Overturning Moment and (c) Vertical Stress at Toe

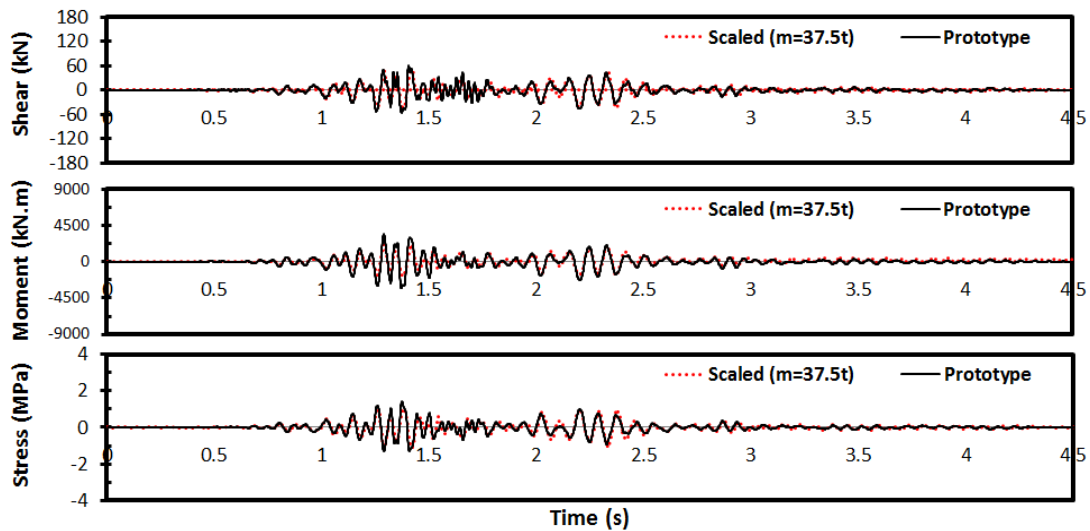


**Figure C.8.** Comparison of the Analysis Results for MDE Motion with Numerical Mass of 37.5t : (a) Base Shear, (b) Overturning Moment and (c) Vertical Stress at Toe



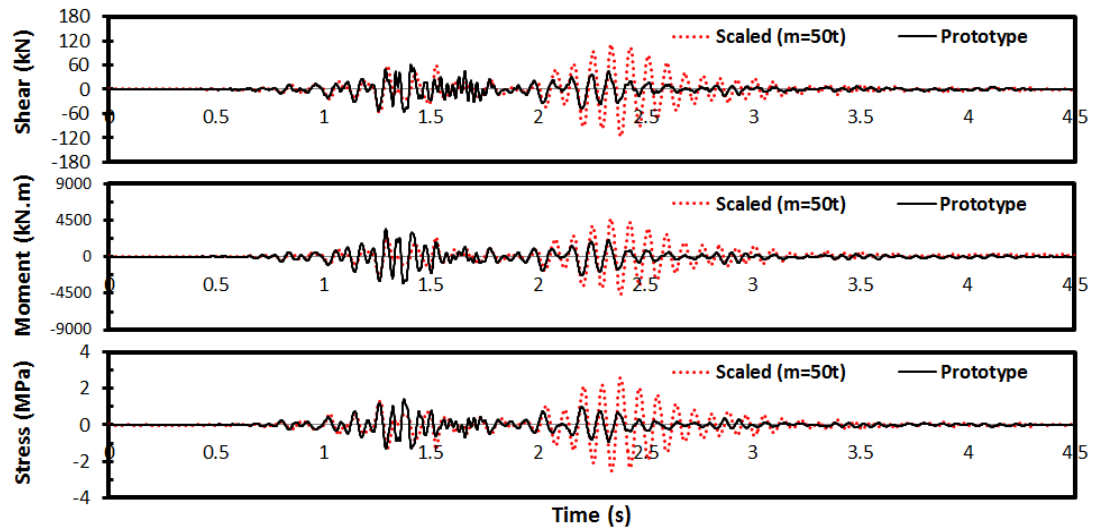


**Figure C.9.** Comparison of the Analysis Results for MDE Motion with Numerical Mass of 50t : (a) Base Shear, (b) Overturning Moment and (c) Vertical Stress at Toe

### C.3. MCE Motion

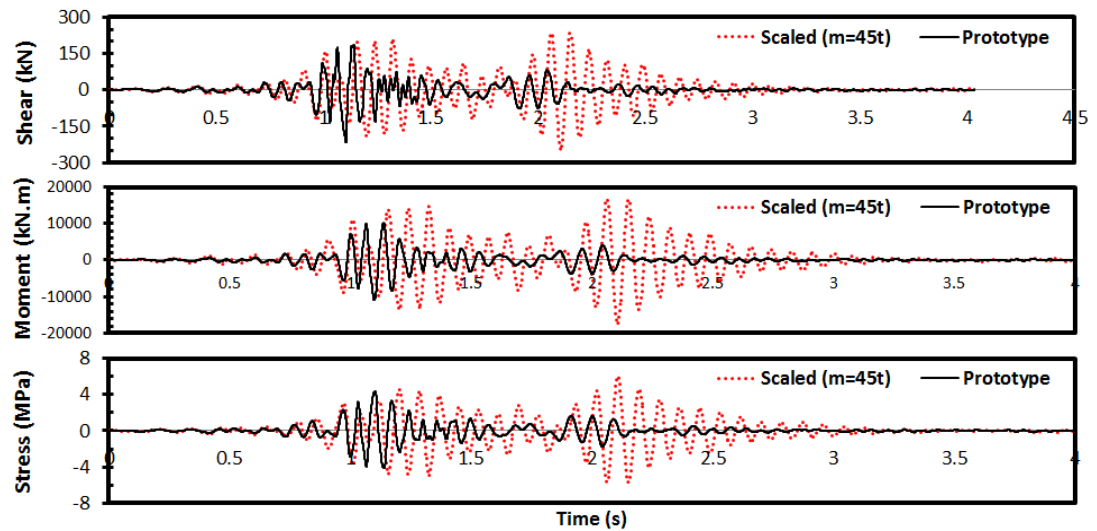


**Figure C.10.** Comparison of the Analysis Results for MCE Motion with Numerical Mass of 45t : (a) Base Shear, (b) Overturning Moment and (c) Vertical Stress at Toe

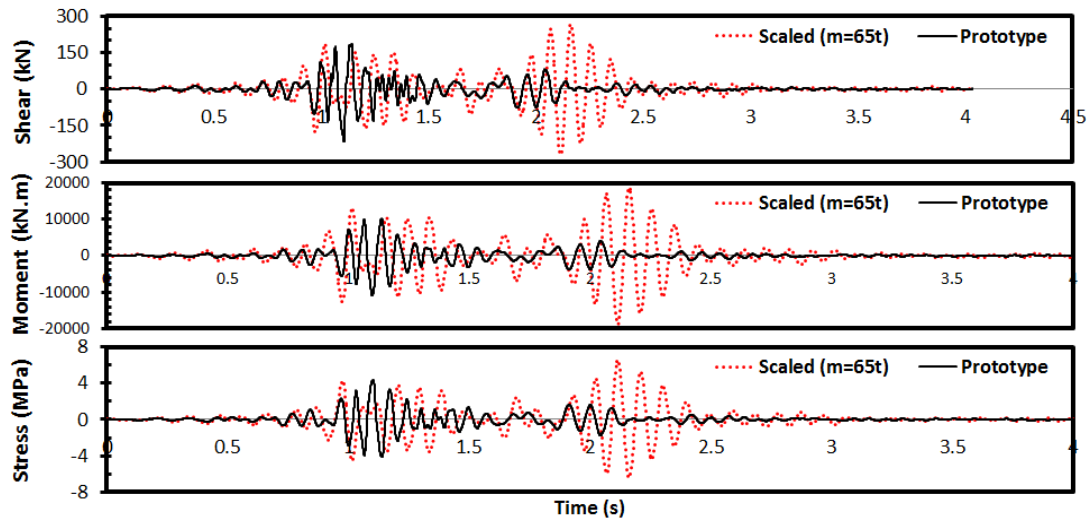


**Figure C.11.** Comparison of the Analysis Results for MCE Motion with Numerical Mass of 65t : (a) Base Shear, (b) Overturning Moment and (c) Vertical Stress at Toe

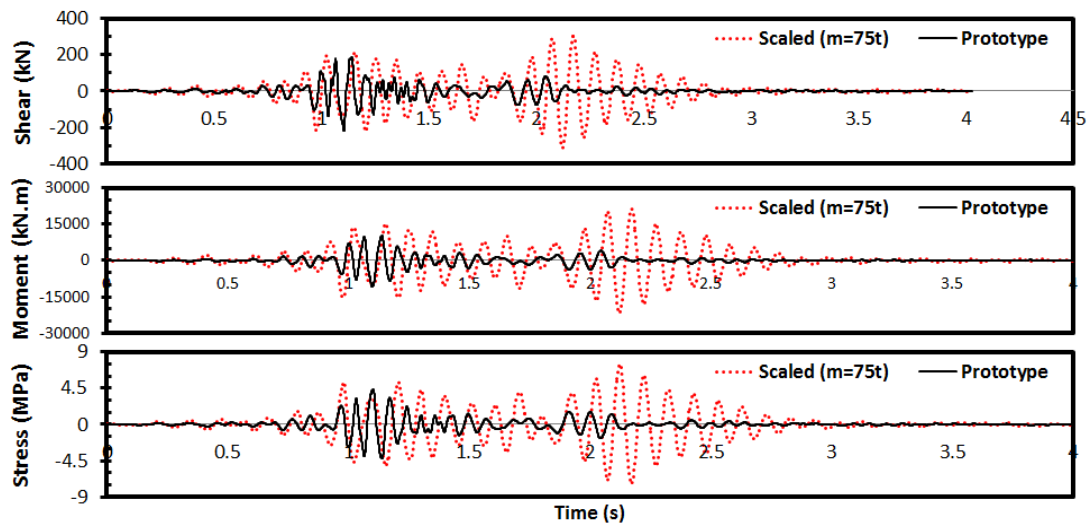


**Figure C.12.** Comparison of the Analysis Results for MCE Motion with Numerical Mass of 75t : (a) Base Shear, (b) Overturning Moment and (c) Vertical Stress at Toe

## APPENDIX D

### DETAILS FOR PUSHOVER TESTS

Pushover tests were conducted in a one-way cyclic manner. This is because; the axial load on each specimen was applied by utilizing prestressed rods attached to the foundation block. The drawback of this type of loading was the fact that the prestressing forces could change with the application of lateral displacements and, for some loading, it could cause excessive axial loads on the tested specimen. In fact, this phenomenon would result in erroneous observations as more axial load increases the base resistance for sliding and the compressive stresses could also rise due to excessive axial load. Therefore, the initial axial load level during pushover tests were reduced (less than 400kN) and the specimen were pushed till the target axial load level of 400kN was attained. Then, the specimen was brought to zero lateral load position, the axial load was decreased to a lower value. And the specimen was pushed more. As an example, the pushover curve and base shear – base displacement curve for Specimen 1 (CVC) are presented in Figure D.1 and Figure D.2, respectively.

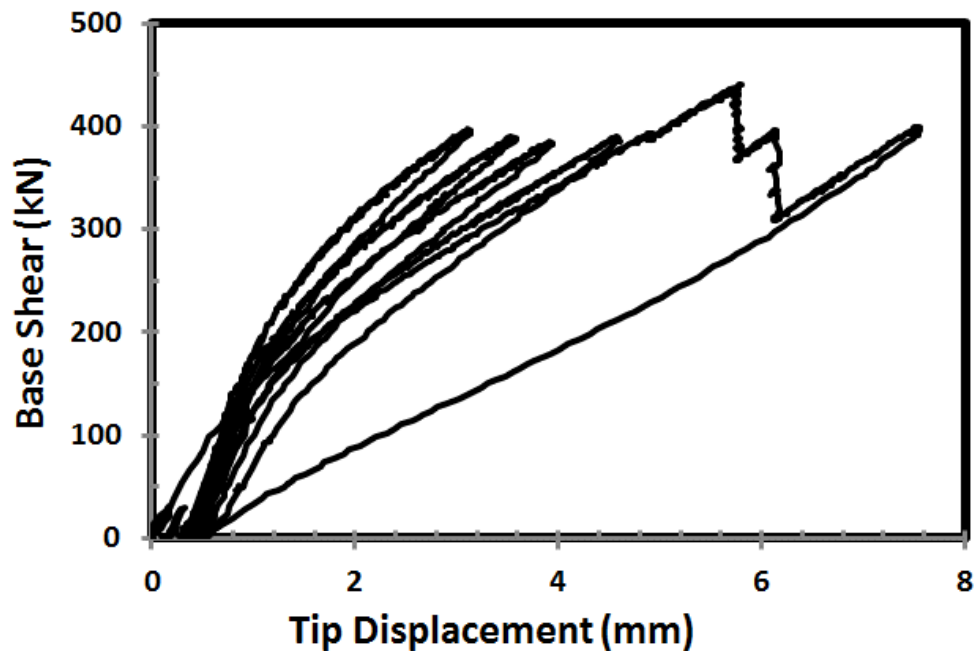


**Figure D.1.** Pushover Curve for Specimen 1

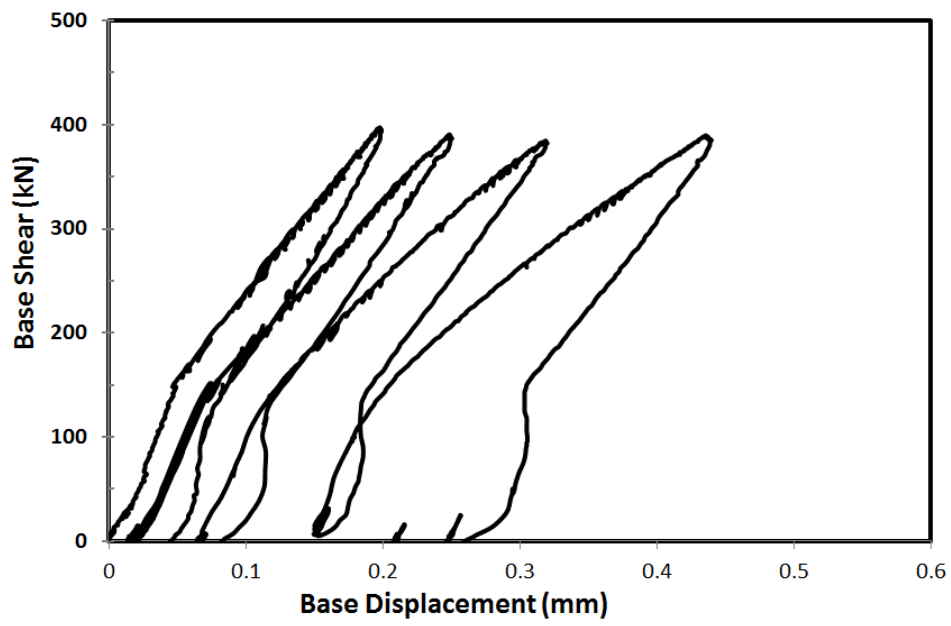


**Figure D.2.** Base Shear versus Base Displacement Curve for Specimen 1

## APPENDIX E

### DETAILS FOR THE FAILURE SURFACE

#### E.1. CCC Domain

In this domain, the principal stress state,  $F$ , and failure surface,  $S$ , are defined as summarized in Eq. E.1 and E.2 (ANSYS 2010.d).

$$F_1 = \frac{1}{\sqrt{15}} \left( \sqrt{(\sigma_1 - \sigma_2)^2 + (\sigma_2 - \sigma_3)^2 + (\sigma_3 - \sigma_1)^2} \right) \quad (E.1)$$

$$S_1 = \frac{2r_2(r_2^2 - r_1^2)\cos\eta + r_2(2r_1 - r_2)\sqrt{4(r_2^2 - r_1^2)\cos^2\eta + 5r_1^2 - 4r_1r_2}}{4(r_2^2 - r_1^2)\cos^2\eta + (r_2 - 2r_1)^2} \quad (E.2)$$

where  $\cos\eta$ ,  $r_1$ ,  $r_2$  and  $\xi$  are determined by using Eq. E.3-E.6,  $\sigma_h$  is the hydrostatic stress state,  $\eta$  is the angle of similarity,  $a_0$ ,  $a_1$ ,  $a_2$ ,  $b_0$ ,  $b_1$ , and  $b_2$  are coefficients to be determined,  $\sigma_i$  ( $i=1, 2, 3$ ) are the principal stresses and  $f_c$  is the compressive strength.

$$\cos\eta = \frac{2\sigma_1 - \sigma_2 - \sigma_3}{\sqrt{2}\sqrt{(\sigma_1 - \sigma_2)^2 + (\sigma_2 - \sigma_3)^2 + (\sigma_3 - \sigma_1)^2}} \quad (E.3)$$

$$r_1 = a_0 + a_1\xi + a_2\xi^2 \quad (E.4)$$

$$r_2 = b_0 + b_1\xi + b_2\xi^2 \quad (E.5)$$

$$\xi = \frac{\sigma_h}{f_c} \quad (E.6)$$

The angle of similarity,  $\eta$ , is purely associated with the ratios of principal stresses. For instance, all stress states with  $\sigma_1 = \sigma_2 > 0 > \sigma_3$  constitute  $\eta = 0^\circ$  and every stress state with  $\sigma_3 > 0 > \sigma_2 = \sigma_1$  form  $\eta = 60^\circ$ . All other stress states fall between  $\eta = 0^\circ$  and  $\eta = 60^\circ$ . Likewise, failure surfaces for  $\eta = 0^\circ$  and  $\eta = 60^\circ$  coincide with  $r_1$  and  $r_2$ , respectively (Eq. E.2). This phenomenon is more apparent if Figure E.1 is investigated. In Figure E.1, the failure surface profiles are depicted. The details about Willam-Warnke failure criteria could be found in Chen (1982).

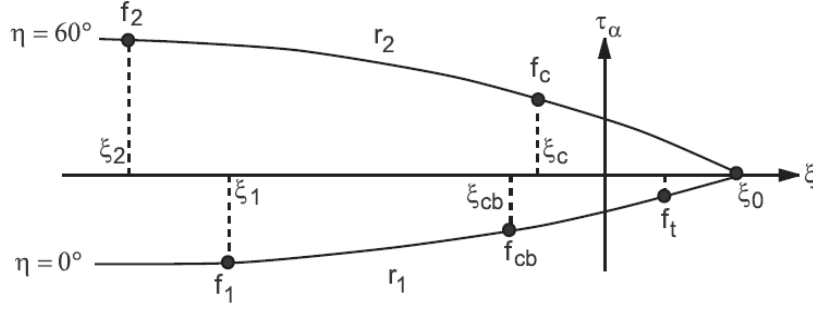


**Figure E.1.** Profile Views of the Failure Surface [ANSYS 2010.d]

In this domain, the material crushes when Eq. 6.7 is satisfied.

## E.2. CCT Domain

The principal stress state,  $F$ , and failure surface,  $S$ , for CCT domain are presented in Eq. E.7 and E.8.

$$F_2 = \frac{1}{\sqrt{15}} \left( \sqrt{(\sigma_2 - \sigma_3)^2 + \sigma_2^2 + \sigma_3^2} \right) \quad (E.7)$$

$$S_2 = \left( 1 - \frac{\sigma_1}{f_t} \right) \frac{2p_2(p_2^2 - p_1^2) \cos \eta + p_2(2p_1 - p_2) \sqrt{4(p_2^2 - p_1^2) \cos^2 \eta + 5p_1^2 - 4p_1 p_2}}{4(p_2^2 - p_1^2) \cos^2 \eta + (p_2 - 2p_1)^2} \quad (E.8)$$

where  $\cos \eta$ ,  $p_1$ ,  $p_2$  and  $\chi$  are defined in Eq. E.9 –E.12,  $\eta$  is the angle of similarity,  $a_0$ ,  $a_1$ ,  $a_2$ ,  $b_0$ ,  $b_1$ , and  $b_2$  are coefficients to be determined and  $\sigma_i$  ( $i=2$  and  $3$ ) are the principal stresses.

$$\cos \eta = \frac{2\sigma_1 - \sigma_2 - \sigma_3}{\sqrt{2} \sqrt{(\sigma_1 - \sigma_2)^2 + (\sigma_2 - \sigma_3)^2 + (\sigma_3 - \sigma_1)^2}} \quad (E.9)$$

$$p_1 = a_0 + a_1 \chi + a_2 \chi^2 \quad (E.10)$$

$$p_2 = b_0 + b_1 \chi + b_2 \chi^2 \quad (E.11)$$

$$\chi = \frac{1}{3} (\sigma_2 + \sigma_3) \quad (E.12)$$

Cracking is the mode failure for this domain as far as Eq. 6.7 is satisfied. Cracking occurs along a direction perpendicular to the first principal stress,  $\sigma_1$ , (ANSYS 2010.d). The details on crushing phenomenon in this domain could be found in Willam and Warnke (1975).

### E.3. CTT Domain

The principal stress state,  $F$ , and failure surface,  $S$ , for this domain could be determined by utilizing Eq. E.13 and E.14.

$$F_3 = \sigma_i \quad \text{for } i = 1 \text{ and } 2 \quad (\text{E.13})$$

$$S_3 = \frac{f_t}{f_c} \left( 1 + \frac{\sigma_3}{f_c} \right) \quad (\text{E.14})$$

where  $\sigma_i$  ( $i=1, 2$  and  $3$ ) are the principal stresses,  $f_c$  is the compressive strength and  $f_t$  is the tensile strength.

In this domain, crack lying on a plane perpendicular to the first principal direction nucleates provided that Eq. 6.7 is satisfied for only  $\sigma_1$ . Or, two cracks could be formed on planes perpendicular to the first and second principal directions if both  $\sigma_1$  and  $\sigma_2$  satisfy Eq. 6.7. The details on crushing phenomenon in this domain could be found in Willam and Warnke (1975).

### E.4. TTT Domain

The principal stress state,  $F$ , and failure surface,  $S$ , for the fourth domain are obtained by using Eq. E.15 and E.16.

$$F_4 = \sigma_i \quad \text{for } i = 1, 2 \text{ and } 3 \quad (\text{E.15})$$

$$S_4 = \frac{f_t}{f_c} \quad (\text{E.16})$$

where  $\sigma_i$  ( $i=1, 2$  and  $3$ ) are the principal stresses,  $f_c$  is the compressive strength and  $f_t$  is the tensile strength.

In this domain, only cracking is possible since there exist no compressive principal stresses. At most, three cracking planes appear at each quadrature point provided that Eq. 6.7 is satisfied.





## CURRICULUM VITAE

### a) PERSONAL DETAILS :

*Date of Birth* : 7/09/1984  
*Place of Birth* : ANKARA  
*Nationality* : Turkish  
*Marital Status* : Single  
*Gender* : Male

### b) EDUCATION :

- |                       |   |                 |
|-----------------------|---|-----------------|
| <b>1) 1998 – 2002</b> | Cankaya Anadolu Lisesi<br>High School Degree<br>Graduated with high honor<br>CGPA : 4.88/5.00   | Ankara – Turkey |
| <b>2) 2002 – 2007</b> | Middle East Technical University<br>B.S. in Civil Engineering Department<br>CGPA : 3.86/4.00<br>Rank : 1 <sup>st</sup> among 221 students | Ankara – Turkey |
| <b>3) 2007 – 2010</b> | Middle East Technical University<br>M.Sc. in Civil Engineering Department<br>CGPA : 4.00/4.00   | Ankara – Turkey |
| <b>4) 2010 – 2016</b> | Middle East Technical University<br>Ph.D. in Civil Engineering Department<br>CGPA : 4.00/4.00   | Ankara – Turkey |

### c) WORK EXPERIENCE :

- |                          |  |                 |
|--------------------------|--|-----------------|
| <b>1) 2016 – Present</b> | Hacettepe University<br>Civil Engineering Department<br>Teaching Assistant             | Ankara – Turkey |
| <b>2) 2007 – 2016</b>    | Middle East Technical University<br>Civil Engineering Department<br>Teaching Assistant | Ankara – Turkey |

#### d) PUBLICATIONS :

##### 1. Peer Reviewed International Journal Papers :

- a) Akkar, S., Aldemir, A., Askan, A., Bakır, S., Canbay, E., Demirel, I.O., Erberik, M.A., Gülerce, Z., Gülkan, P., Kalkan, E., Prakash, S., Sandikkaya, M.A., Sevilgen, V., Ugurhan, B., Yenier, E. (2011), “8 March 2010 Elazığ-Kovancılar (Turkey) Earthquake: Observations on Ground Motions and Building Damage”, *Seismological Research Letters*, **82**(1), 42-58.
- b) Aldemir, A., Erberik, M.A., Demirel, I.O. and Sucuoglu, H. (2013), “Seismic Performance Assessment of Unreinforced Masonry Buildings with a Hybrid Modeling Approach”, *Earthquake Spectra*, **29**(1), 33–57.
- c) Arici, Y., Binici, B. and Aldemir, A. (2014), “Comparisons of Expected Damage Patterns from Two and Three Dimensional Nonlinear Dynamic Analyses of an RCC Dam”, *Structure and Infrastructure Engineering*, **10**(3), 305-315.
- d) Aldemir, A., Binici, B., Arici, Y., Kurc, O. and Canbay, E. (2015), “Pseudo-dynamic Testing of a Concrete Gravity Dam”, *Earthquake Engineering and Structural Dynamics*, **44**, 1747-1763.
- e) Aldemir, A., Binici, B., Canbay, C. and Yakut, A. (2015), “Lateral Load Testing of an Existing Two Story Masonry Building up to Near Collapse”, *Bulletin of Earthquake Engineering*, published online.
- f) Aldemir, A., Yilmaztürk, S.M., Yücel, A.R., Binici, B., Arıcı, Y. and Akman, A. (2015), “Beton Barajların Deprem Davranışlarının İncelenmesinde Kullanılan Analiz Metotları”, *IMO Teknik Dergi*, **427**, 6943-6968.

##### 2. Non-peer Reviewed Journal Papers :

- a) Aldemir, A., Binici, B. ve Akman, A. (2014), “Dinamik Benzeri Deney Yöntemiyle Beton Performansının İncelenmesi”, *Teknik Müşavir Dergisi*, **31**, 18-23.

##### 3. International Conference Papers :

- a) Erberik, M.A., Aldemir, A., and Ay, B.Ö. (2009), “A Critique on the Turkish Earthquake Code Regulations Regarding Masonry Construction”, *8<sup>th</sup> International Seminar on Structural Masonry*, 5 – 7 November 2009, Istanbul, Turkey.
- b) Akpınar, U., Aldemir, A. and Binici, B. (2011), “Different Analysis Strategies for Roller Compacted Concrete Dam Design”, *5<sup>th</sup> International Conference on Advanced Computational Engineering and Experimenting*, 3 – 6 July 2011, Algarve, Portugal.
- c) Aldemir, A., Akpınar U., Arıcı, Y. and Binici, B. (2012), “Seismic Design and Performance of an High RCC Dam”, *15<sup>th</sup> World Conference on Earthquake Engineering*, 24 – 28 September 2012, Lisboa, Turkey.
- d) Binici, B., Arıcı, Y., Aldemir, A. and Akpınar, U. (2012), “Two and Three Dimensional Nonlinear Dynamic Analysis of an RCC Dam”, *10<sup>th</sup>*

- International Congress on Advances in Civil Engineering*, 17 - 19 October 2012, Ankara, Turkey.
- e) Demirel, I.O., Aldemir, A. and Erberik, M.A. (2012), "A New Computational Method for the Assessment of URM Buildings", *10<sup>th</sup> International Congress on Advances in Civil Engineering*, 17 - 19 October, Ankara 2012, Turkey.
  - f) Binici, B., Arici, Y. and Aldemir, A. (2012), "Comparisons of Two and Three Dimensional Nonlinear Dynamic Analyses Results of a Roller Compacted Concrete Dam", *Research, Development, and Practice in Structural Engineering and Construction*, 28 November – 02 December 2012, Perth, Australia.
  - g) Aldemir, A., Binici, B., Canbay, E., Kurç, Ö. and Arıcı, Y. (2013), "Seismic Performance Evaluation of a Concrete Gravity Dam by using Pseudo Dynamic Testing", *The 2013 World Conference on Advances in Structural Engineering and Mechanics*, 8 – 12 September 2013, Jeju, Korea.
  - h) Aldemir, A., Erdil, B., Demirel, I.O., Yakut, A. and Binici, B. (2014), "Damage from Two Consecutive Earthquakes at City of Van (Turkey)", *10<sup>th</sup> National Conference on Earthquake Engineering*, 21 – 25 July 2014, Alaska, USA.
  - i) Demirel, I.O., Aldemir, A., Yakut, A. and Binici, B. (2014), "Comparison of Analytical and Observed Damages on a Commercial RC Building", *10<sup>th</sup> National Conference on Earthquake Engineering*, 21 – 25 July 2014, Alaska, USA.
  - j) Binici, B., Canbay, E., Yakut, A. and Aldemir, A. (2015), "Lateral Load On Site Testing of a Two Story Masonry Building up to Near Collapse", *10<sup>th</sup> Pacific Conference on Earthquake Engineering*, 06 – 08 November 2015, Sydney, Australia.
  - k) Aldemir, A., Binici, B., Yakut, A. and Canbay, E., (2015), "Identifying Masonry Buildings under High Seismic Risk", *10<sup>th</sup> Pacific Conference on Earthquake Engineering*, 06 – 08 November 2015, Sydney, Australia.
  - l) Binici, B., Canbay, E., Ducia, F., Ozcebe, G. and Aldemir, A. (2015), "Seismic Behavior of Double Walls with Continuity Reinforcement", *11<sup>th</sup> Canadian Conference on Earthquake Engineering*, 21 – 24 July 2015, Victoria, Canada.
  - m) Aldemir, A., Binici, B. and Canbay, E. (2015), "Comparisons of Pseudo Dynamic Test Results and Numerical Results of an RCC Dam Model", *11<sup>th</sup> Canadian Conference on Earthquake Engineering*, 21 – 24 July 2015, Victoria, Canada.

#### 4. National Conference Papers :

- a) Aldemir, A. ve Binici, B. (2011), "Koçak Kemer Beton Barajı Sismik Performansının İncelenmesi", *2. Su Yapıları Sempozyumu*, 16 - 18 Eylül 2011, Diyarbakır, Türkiye.
- b) Aldemir, A., Erberik, M.A. ve Sucuoğlu, H. (2011), "Tuğla Yığma Duvarlar için Performansa Dayalı Bir Değerlendirme Yöntemi", *1.*

*Türkiye Deprem Mühendisliği ve Sismoloji Konferansı*, 11 - 14 Ekim 2011, Ankara, Türkiye.

- c) Aldemir, A., Binici, B. ve Arıcı, Y. (2012), “Silindirle Sıkıştırılmış Beton Bir Barajın Deprem Güvenliğinin Çeşitli Seviye Modeller ile İrdelenmesi”, 3. *Ulusal Baraj Güvenliği Sempozyumu*, 10 – 12 Ekim 2012, Eskişehir, Türkiye.
- d) Aldemir, A., Binici, B., Canbay, E., Kurç, Ö. ve Arıcı, Y. (2013), “Dinamik Benzeri Yöntemlerle Bir Beton Ağırlık Barajın Sismik Performansının Değerlendirilmesi”, 2. *Türkiye Deprem Mühendisliği ve Sismoloji Konferansı*, 25 – 27 Eylül 2013, Hatay, Türkiye.
- e) Aldemir, A. ve Binici, B. (2013), “Dinamik Benzeri Deneylerle Beton Ağırlık Baraj Sismik Performansının İncelenmesi”, 3. *Su Yapıları Sempozyumu*, 7 - 8 Aralık 2013, Ankara, Türkiye.
- f) Aldemir, A. ve Binici, B., (2014), “Dinamik Benzeri Deney Yöntemiyle SSB ve Geleneksel Beton Baraj Performanslarının İncelenmesi”, 2. *Barajlar Kongresi*, 13-15 Şubat 2014, İstanbul, Türkiye.
- g) Binici, B. ve Aldemir, A., (2014), “Analitik Modellerin Beton Ağırlık Baraj Sismik Davranışını Taklit Etmekteki Verimliliğinin İrdelenmesi”, 4. *Ulusal Baraj Güvenliği Sempozyumu*, 9 – 11 Ekim 2014, Elazığ, Türkiye.

## 5. Reports :

- a) Bakır, S., Canbay, E., Erberik, M.A., Gülerce, Z., Aldemir, A. ve Demirel, İ.O. (2010), “8 Mart 2010 Başyurt-Karakoçan (Elazığ) Depremi Ön İnceleme Raporu”, Rapor No: METU/EERC 2011-02, Deprem Mühendisliği Araştırma Merkezi, Orta Doğu Teknik Üniversitesi.
- b) Sandıkkaya, M.A., Senyurt, M., Aldemir, A., Akın, E., Sisi, A.A., Binici, B., Canbay, E., Akkar, S. (2011), “19 Mayıs 2011 Kütahya Depremi Raporu”, Deprem Mühendisliği Araştırma Merkezi, Orta Doğu Teknik Üniversitesi.
- c) “23 Ekim 2011  $M_w$  7.2 Van Depremi Sismik Ve Yapısal Hasara İlişkin Saha Gözlemleri”, Rapor No: METU/EERC 2011-04, Deprem Mühendisliği Araştırma Merkezi, Orta Doğu Teknik Üniversitesi.
- d) “9 Kasım 2011  $M_w$  5.6 Van - Edremit Depremi Sismik ve Yapısal Hasara İlişkin Gözlemler”, Rapor No: METU-EERC / İMO 2012-01, Deprem Mühendisliği Araştırma Merkezi, Orta Doğu Teknik Üniversitesi.

## 6. Chapter in a Book:

- a) Akpınar, U., Aldemir, A. and Binici, B. (2013), “Different Analysis Strategies for Roller Compacted Concrete Dam Design”, *Design and Analysis of Materials and Engineering Structures: Advanced Structured Materials*, **32**, 117-134.